NISTIR 8395

Low-GWP Alternative Refrigerant Blends for HFC-134a: Interim Report

Strategic Environmental Research and Development Program
Project: WP 19-1385

Principal Investigators:
Piotr A. Domanski
Mark O. McLinden

Co-Authors:
Valeri I. Babushok
Ian H. Bell
Tara J. Fortin
Michael J. Hegetschweiler
Mark A. Kedzierski
Dennis K. Kim
Lingnan Lin
Gregory T. Linteris
Stephanie L. Outcalt
Richard A. Perkins
Aaron Rowane
Harrison Skye

This publication is available free of charge from:
https://doi.org/10.6028/NIST.IR.8395

National Institute of Standards and Technology
U.S. Department of Commerce

NISTIR 8395

Low-GWP Alternative Refrigerant Blends for HFC-134a: Interim Report

Interim Report
Strategic Environmental Research and Development Program
Project: WP 19-1385

Piotr A. Domanski, Valeri I. Babushok, Michael J. Hegetschweiler,
Lingnan Lin, Mark A. Kedzierski, Gregory T. Linteris, Harrison Skye
Building Energy and Environment Division
Engineering Laboratory

Mark O. McLinden, Ian H. Bell, Tara J. Fortin,
Stephanie Outcalt, Richard A. Perkins, Aaron Rowane
Applied Chemicals and Materials Division
Material Measurement Laboratory

This publication is available free of charge from:
https://doi.org/10.6028/NIST.IR.8395

October 2021

U.S. Department of Commerce
Gina M. Raimondo, Secretary

National Institute of Standards and Technology
James K. Olthoff, Performing the Non-Exclusive Functions and Duties of the Under Secretary of Commerce for Standards and Technology & Director, National Institute of Standards and Technology

National Institute of Standards and Technology Interagency or Internal Report 8395
Natl. Inst. Stand. Technol. Interag. Intern. Rep. 8395, 177 pages (October 2021)

This publication is available free of charge from:
https://doi.org/10.6028/NIST.IR.8395

Abstract

This project addresses the objectives of the Statement of Need number WPSON-17-20 "No/Low Global Warming Potential Alternatives to Ozone Depleting Refrigerants." Its goal is to identify and demonstrate performance of low global-warming-potential (GWP), non-flammable refrigerants to replace HFC-134a in military environmental control units (ECUs). This project is a follow-on to the limited-scope project WP-2740, which used thermodynamic cycle simulation models alone to screen over 100 000 refrigerant blends and identified over 20 candidate HFC-134a replacements. In this study we narrow the pool of blend candidates down to three 'best' fluids, verify experimentally their flammability behavior, demonstrate their performance through tests in a military ECU in environmental chambers over a wide range of operating conditions, and extrapolate the laboratory-measured performance to ECUs equipped with optimized heat exchangers through first-principles-based simulations combined with machine-learning optimization methods.

This Interim Report documents the work leading to the selection of three 'best' blends. This work included refrigerant blend tests in a laboratory mini-breadboard heat pump apparatus, fundamental measurements and modeling of thermophysical properties, two-phase heat-transfer performance, and flammability behavior.

Key Words

Air conditioning; Coefficient of performance; Cycle simulation; Flammability; Refrigerants; Vapor compression; Volumetric capacity.

Table of Contents

Abstract ..... **i**
Key Words ..... **i**
List of Tables ..... **iii**
Nomenclature ..... **viii**
Acknowledgements ..... **ix**
1. Objective **1**
2. Technical Approach **2**
3. Results and Discussion **3**
3.1. Task 1: Experimental Measurements of Blend Properties and Development of Mixture Equation of State **3**
3.1.1. Purpose and Approach. 3
3.1.2. Vapor-Liquid Equilibrium (VLE) Measurements. 5
3.1.3. Pressure-Density-Temperature (P, ρ, T, x) Measurements. 5
3.1.4. Speed of Sound Measurements. 6
3.1.5. Thermal Conductivity Measurements. 7
3.1.6. Viscosity Measurements. 7
3.1.7. Model Development (Subtask 1c). 7
3.2. Task 2: Flammability Testing **11**
3.2.1. Introduction 11
3.2.2. E681 tests and Japanese High-Pressure Gas Law tests 12
3.2.3. Improvements in Predictive Model 20
3.2.4. Interpretation of E681 and JHPGL Experimental Results 22
3.2.5. Coordination with Full-Scale Testing 25
3.2.6. Summary of Flammability Work to Date 26
3.3. Task 3: Testing of Selected Blends in a Mini-Breadboard Heat Pump **27**
3.3.1. Test Apparatus 27
3.3.2. Test Protocol 29
3.3.3. Model simulation of tests 31
3.3.4. Test Results and CYCLE_D-HX Model Validation 32
3.4. Task 4: Refrigerant Forced-Convection Heat-Transfer Testing **39**
3.4.1. Test Apparatus 39
3.4.2. Data Analysis and Correlation Development 42
3.5. Task 5: Selection of Final Blends for Testing in Military ECU **46**

3.5.1. Evaluation of "New" Fluids 46
3.5.2. Selection of Four Blends for Testing in Mini-Breadboard Heat Pump..... 48
3.5.3. Selection of Three Blends for Testing in ECU..... 49
4. Conclusions to Date 51
5. Literature Cited 54
Appendix A: Details of Experiments and Modeling 60
A.1. Task 1 - Details of Thermophysical Properties Measurements and Modeling.... 60
A.1.1. Vapor-Liquid Equilibria 60
A.1.2. Density (*P, ρ, T, x*) Measurements 68
A.1.3. Liquid-Phase Speed of Sound..... 91
A.1.4. Liquid-phase Thermal Conductivity..... 115
A.1.5. Mixture Preparation..... 124
A.2. Task 2 - Flammability Experiments and Test Data 128
A.2.1. ASHRAE Standard 34 E681 Test Data 128
A.2.2. Japanese High-Pressure Gas Law Test..... 131
A.2.3. Constant Volume (2 L) Laminar Burning Velocity Measurements 139
A.3 Task 4 - Tabulated Flow-Boiling Heat-Transfer Measurements..... 149

List of Tables

Table 3.1-1. Refrigerant blend properties measured in the current work. 4
Table 3.1-2. Interaction parameters used in this work (note: the order of components is significant) 8
Table 3.1-3. Coefficients for entropy scaling of thermal conductivity data (Eq. 3.1-5)..... 10
Table 3.2-1. Modeling and test results for candidate blends (reactants at 296 K, 101 kPa, and 50 % r.h.)..... 14
Table 3.3-1. MBHP: HFC-134a baseline test operating targets and control parameters..... 30
Table 3.3-2. MBHP: Test targets and parameters..... 31
Table 3.3-3. MBHP: Executed test matrix..... 31
Table 3.5-13.5-2. Selected "best" blends from the limited-scope project (sorted by GWP) [3] 49
Table A.1-1. Measured vapor-liquid equilibria (VLE) data for the system R-1234yf/134a at a molar composition of (0.320/0.680). 62
Table A.1-2. Measured vapor-liquid equilibria (VLE) data for the system R-1234yf/134a at a molar composition of (0.647/0.353). 63
Table A.1-3. Measured vapor-liquid equilibria (VLE) data for the system R-134a/1234ze(E) at a molar composition of (0.334/0.666)..... 64
Table A.1-4. Measured vapor-liquid equilibria (VLE) data for the system R-134a/1234ze(E) at a molar composition of (0.663/0.337)..... 64
Table A.1-5. Measured vapor-liquid equilibria (VLE) data for the system R-1234yf/1234ze(E) at a molar composition of (0.324/0.676)..... 65

Table A.1-6. Measured vapor-liquid equilibria (VLE) data for the system R-1234yf/1234ze(E) at a molar composition of (0.638/0.362)..... 66
Table A.1-7. Measured vapor-liquid equilibria (VLE) data for the system R125/1234yf at a molar composition of (0.349/0.651). 67
Table A.1-8. Measured vapor-liquid equilibria (VLE) data for the system R-125/1234yf at a molar composition of (0.664/0.336). 67
Table A.1-9. Measured (P, ρ, T, x) data for the system R-1234yf/134a at a molar composition of (0.33634/0.66366). 72
Table A.1-10. Measured (P, ρ, T, x) data for the system R-1234yf/134a at a molar composition of (0.64709/0.35291)..... 76
Table A.1-11. Measured (P, ρ, T, x) data for the system R-134a/1234ze(E) at a molar composition of (0.33250/0.66750)..... 79
Table A.1-12. Measured (P, ρ, T, x) data for the system R-134a/1234ze(E) at a molar composition of (0.66356/0.33644)..... 82
Table A.1-13. Measured (P, ρ, T, x) data for the system R-1234yf/1234ze(E) at a molar composition of (0.33584/0.66416)..... 85
Table A.1-14. Measured (P, ρ, T, x) data for the system R-1234yf/1234ze(E) at a molar composition of (0.66660/0.33340)..... 88
Table A.1-15. Measured speed of sound data for the system R-1234yf/134a at a molar composition of (0.33634/0.66366)..... 96
Table A.1-16. Measured speed of sound data for the system R-1234yf/134a at a molar composition of (0.64709/0.35291)..... 99
Table A.1-17. Measured speed of sound data for the system R-134a/1234ze(E) at a molar composition of (0.32916/0.67084)..... 101
Table A.1-18. Measured speed of sound data for the system R-134a/1234ze(E) at a molar composition of (0.63688/36312)..... 105
Table A.1-19. Measured speed of sound data for the system R-1234yf/1234ze(E) at a molar composition of (0.33584/0.66416)..... 110
Table A.1-20. Measured speed of sound data for the system R-1234yf/1234ze(E) at a molar composition of (0.66660/0.33340)..... 113
Table A.1-21. Representative thermal conductivity data measured for the system R-1234yf/134a at a molar composition of (0.320/0.680). 118
Table A.1-22. Representative thermal conductivity data measured for the system R-1234yf/134a at a molar composition of (0.647/0.353). 119
Table A.1-23. Representative thermal conductivity data measured for the system R-134a/1234ze(E)) at a molar composition of (0.334/0.666)..... 120
Table A.1-24. Representative thermal conductivity data measured for the system R-134a/1234ze(E)) at a molar composition of (0.663/0.337)..... 121
Table A.1-25. Representative thermal conductivity data measured for the system R-1234yf/1234ze(E) at a molar composition of (0.323/0.677)..... 122
Table A.1-26. Representative thermal conductivity data measured for the system R-1234yf/1234ze(E) at a molar composition of (0.642/0.358)..... 123
Table A.2-1. E681 test results for R-513A, NIST-ternary blend, R-450A, R-515B, and blends of R-1234yf/134a at a molar composition of (0.26/0.74), (0.28/0.72), and (0.30/0.70)..... 128

Table A.2-2. Japanese High-Pressure Gas Law test results obtained at NIST for: R-513A, NIST-ternary blend, R-450A, R-515B, and blends of R-1234yf/134a, all with dry or 50 % r.h. air as listed. 133
Table A.2-3. Fitting parameters for the variation of SL with ϕ , T_u and P for experimental burning velocity data obtained in 2-L experiment from pressure rise data for R-152a/134a and R-152a/1234yf mixtures. Data presented for 298 K, 101 kPa initial conditions, and dry air (<2% r.h.) of wet air (50 % r.h.) as noted. 144
Table A.2-4. Experimental burning velocity data obtained in 2-L experiment from pressure rise data for R-152a/134a and R-152a/1234yf mixtures. Data presented for 298K, 101 kPa initial conditions, dry air (<2% r.h.) and wet air (50 % r.h.) as noted. Blend compositions given in mole fraction. 145
Table A.3-1. Measured flow-boiling heat-transfer data for R-515B, R-450A, R-513A, and HFC-134a. 149

List of Figures

Figure 1.0-1. Project tasks 1
Figure 3.1-1. Measured (P, ρ, T, x) points for the R-1234yf/1234ze(E) blend at a composition of (0.6666/0.3334) molar; left: pressure versus temperature; right: density versus temperature; ◊, measured points; line, phase boundary; *, critical point. 5
Figure 3.1-2. Measured speed of sound points for the R-1234yf/1234ze(E) blend at a composition of (0.6666/0.3334) mole fraction; left: pressure versus temperature; right: sound speed versus temperature; symbols are measured points and lines connect points along an isochore; red line is phase boundary. 6
Figure 3.1-3. Deviation plots for the measured experimental data with the mixture EOS using the parameters from Table 3.1-2. The different plot symbols indicate the two compositions measured here; the vertical lines indicate the mixture critical temperature. Literature data are shown as light grey + markers (some literature data have deviations outside the range of the figures). 9
Figure 3.1-4. Entropy scaling model for the thermal conductivity of the three blends studied here; (a) plus-scaled thermal conductivity λ+ as a function of reduced scaled residual entropy s+, the different symbols denote the different measured blends; (b) relative deviations in λ+. 10
Figure 3.2-1. Left image: schematic of ASTM 681 test vessel; Right two images: visual images from HFC-32/HFC-134a blend (0.35 /0.65 mass fraction) below and above the lean flammability limit [20, 21] 13
Figure 3.2-2. Equilibrium explosion pressure of candidate blends (Tern-1, R-513A, R-450A, and R-515B) together with experimental results in the JHPGL test as a function of blend volume fraction in air (50 % r.h.). 16
Figure 3.2-3. Explosion pressure of candidate blends in JHPGL test as a function of blend volume fraction in air (left frame: dry air; right, moist). 17
Figure 3.2-4. Explosion pressure of candidate blends (Tern-1, R-513A, R-450A, and R-515B) in JHPGL test as a function of blend volume fraction in air (solid lines: dry air; dashed lines: moist air; note different scales). 18

Figure 3.2-5. Explosion pressure in the JHPGL test for binary blends of HFC-134a with HFO-1234yf as function of volume fraction the blend in air. Different curves show results for varying volume fractions of HFC-134a/HFO-1234yf in the blend (left frame: dry air; right: moist). 19
Figure 3.2-6. Peak explosion pressure in the JHPGL test for binary blends of HFC-134a with HFO-1234yf as function the volume fraction of HFC-134a in the blend, for moist (50 % r.h.) and dry (< 2 % r.h.) air. 19
Figure 3.2-7. Laminar burning velocity of R-152a/134a (left frame) and R-152a/1234yf (right frame) mixtures with air as a function of the equivalence ratio. 21
Figure 3.2-8. Calculated vs. measured laminar burning velocity (peak over all ϕ) of twenty-one refrigerant/N_2/O_2 flames for which experimental data are available in the literature [46-48]. 21
Figure 3.2-9. Overall chemical reaction ω_{psr} as a function of volume fraction in air determined via perfectly stirred reactor simulations for the blend R-1234yf/134a. Each curve refers to one blend ratio: top curve, 100% HFO-1234yf, bottom curve 100 % HFC-134a; Frames: 0 % r.h. (dry), 50 % r.h., and 100 % r.h. 22
Figure 3.2-10. Peak (over all ϕ for each blend) chemical reaction ω_{psr} as a function of volume fraction of HFC-134a in the blend of R-1234yf/134a. Individual curves are shown for varying water vapor in the air (0 %, 50 %, 75 % and 100 % r.h.) 23
Figure 3.2-11. Explosion pressure in the JHPGL test vs. overall chemical reaction ω_{psr} (both peak over all ϕ) for R-513A, R-450A, R-515B and the Tern-1 blend and the R-1234yf/134a blends at increasing HFC-134a volume fraction. Dotted line is a polynomial fit to all the data to aid in visualization. (Initial conditions: 296 K, 101 kPa, 50 % r.h.) 24
Figure 3.2-12. Peak (over all ϕ for each blend) chemical reaction ω_{psr} for R-513A, R-450A, R-515B and the NIST blend. Data are shown for the Nominal, WCF, and WCFF compositions in air (T = 296 K) and 0 %, 50 %, and 100 % r.h. 25
Figure 3.3-1. Photos of the MBHP test apparatus. 27
Figure 3.3-2. Schematic of the MBHP test apparatus. 28
Figure 3.3-3. MBHP: Schematics of annular heat exchanger including (a) refrigerant tube lengths, (b) cross section of annular heat exchanger, (c) detailed cross-section of microfin tube, and (d) helix angle of microfins. 29
Figure 3.3-4. Cooling COP for HFC-134a and the replacement candidates (a) without LLSL-HX and (b) with LLSL-HX. 34
Figure 3.3-5. Cooling volumetric capacity for HFC-134a and the replacement candidates (a) without LLSL-HX and (b) with LLSL-HX. 34
Figure 3.3-6. Compressor isentropic efficiency (a) without LLSL-HX and (b) with LLSL-HX. 35
Figure 3.3-7. Compressor volumetric efficiency (a) without LLSL-HX and (b) with LLSL-HX. 35
Figure 3.3-8. Compressor speed (a) without LLSL-HX and (b) with LLSL-HX. 36
Figure 3.3-9. R-450A measurement and model prediction of: (a) evaporator and 38
Figure 3.4-1. Schematic of flow boiling test apparatus. 40
Figure 3.4-2. Cross section of flow-boiling test section. 41
Figure 3.4-3. Detailed schematic of test section (counterflow) 41
Figure 3.4-4. Comparison between measured Nusselt numbers and those predicted by the Hamilton et al. correlation[59] 44

Figure 3.4-5. Comparison between measured Nusselt numbers and those predicted by the new correlation given by Eq. (3.4-5). 45
Figure A.1-1. Schematic of instrument for vapor liquid equilibria measurements. 60
Figure A.1-2. Two-sinker densimeter. 68
Figure A.1-3. Sinkers in the two-sinker densimeter (shown removed from the measuring cell). 69
Figure A.1-4. Dual-path, pulse-echo, speed of sound instrument. 92
Figure A.1-5. Instrument rack for the pulse-echo speed of sound instrument. 93
Figure A.1-6. Schematic diagram of the measuring cell inside the pressure vessel. 94
Figure A.1-7. Circuit diagram of the Wheatstone bridge and long and short hot wire arrangement 116
Figure A.1-8. Effect of density on the thermal conductivity for binary mixtures of R-1234yf, R-134a, and R-1234ze(E) at temperatures ranging from 200 K to 340 K. 117
Figure A.2-1. Spherical 2-L chamber for JHPGL tests and constant volume method laminar burning velocity measurements. 131
Figure A.2-2. Plumbing schematic diagram for 2-L chamber. 132
Figure A.2-3. Experimental pressure trace P, flame radius rf, flame stretch rate κ, and gas temperature (unburned Tu and burned Tb) as a function of time. 141
Figure A.2-4. Three-dimensional plot of burning velocity as a function of pressure P and unburned gas temperature Tu. 142

List of Acronyms

AC	air conditioning
AHRI	Air-Conditioning, Heating and Refrigeration Institute
ANSI	American National Standards Institute
ARL	Army Research Laboratory
ASHRAE	American Society of Heating Refrigerating and Air-Conditioning Engineers
ASTM	American Society for Testing and Materials
CFC	chlorofluorocarbon
COP	coefficient of performance
ECU	environmental control unit
GWP	global warming potential
HFC	hydrofluorocarbon
HFO	hydroflouroolefin
HTF	heat-transfer fluid
HVAC	heating, ventilating and air-conditioning
ISO	International Organization for Standardization
JHPGL	Japanese High-Pressure Gas Law Test
LBV	laminar burning velocity
MBHP	mini breadboard heat pump
NBP	normal boiling point
NSD	no statistical difference

Nomenclature

Symbols

A_c cross-sectional area (m^2)

B_{nd} local Bond number = $(\rho_l - \rho_v)ge D_h/(\sigma N)$, (-)

Bo local boiling number = $\frac{q''}{G_r i_{fg}}$, (-)

c_p specific heat (J kg^{-1} K^{-1})

C coefficients given in Eq. (3.4.5)

D_e equivalent inner diameter of smooth tube (m)

D_h hydraulic diameter of micro-fin tube (m)

e fin height (mm)

g acceleration due to gravity (m/s^2)

G total mass velocity (kg m^{-2} s^{-1})

$h_{2\phi}$ local two-phase heat-transfer coefficient (W $m^{-2}K^{-1}$)

i_{fg} latent heat of vaporization (J kg^{-1})

k refrigerant thermal conductivity (W m^{-1} K^{-1})

N total number of microfins in cross section (-)

Nu local Nusselt number based on D_h

$\dot{m}$ mass flow rate (kg s^{-1})

M_w molar mass (g $mole^{-1}$)

p wetted perimeter (m)

P local fluid pressure (Pa)

Pr liquid refrigerant Prandtl number = $\left.\frac{c_p \mu}{k}\right|_{r,l}$, (-)

Q_{vol} volumetric capacity (kJ m^{-3})

q'' local heat flux based on tube inner surface area (W m^{-2})

Re all liquid, refrigerant Reynolds number based on D_h, $\mathrm{Re} = \frac{G_r D_h}{\mu_{r,l}}$

s distance between fins (mm)

T temperature (K)

t_b bottom thickness of fin (mm)

t_w tube wall thickness (mm)

U expanded relative uncertainty (%)

x_q thermodynamic mass quality (-)

z axial distance (m)

Greek Symbols

α helix angle (°), learning rate

β fin angle (°)

ϕ fuel-air equivalence ratio

ΔL incremental length (m)

ΔT_s T_s - T_w (K)

μ viscosity (Pa·s)
ν specific volume, $x_q \nu_v + (1-x_q)\nu_l$ (m^3 kg^{-1})
ρ density (kg m^{-3})
σ surface tension (kg s^{-2})
ω overall chemical rate (s^{-1})

Subscripts
b bubble point
c critical condition
d dew point
f water
i inside, inlet
l liquid
o outlet, exit
p prediction, single component
psr perfectly stirred reactor
r refrigerant
s saturated state
v vapor
w heat transfer surface

Acknowledgements

This work was supported by the Strategic Environmental Research and Development Program; Project WP19-1385: WP-2740 Follow-On: Low-GWP Alternative Refrigerant Blends for HFC-134a

1. Objective

This work addresses the objectives of the Statement of Need number WPSON-17-20 "No/Low Global Warming Potential Alternatives to Ozone Depleting Refrigerants." It seeks to identify and experimentally demonstrate the performance and flammability behavior of three non-flammable refrigerant blends that can potentially replace HFC-134a in military environmental control units (ECUs). The selected fluids should have zero ozone depletion potential (ODP) and a global warming potential (GWP) less than that of HFC-134a. The selection criteria also include COP, volumetric capacity (Q_{vol}), and toxicity.

This work is a follow-on of the limited-scope project WP-2740, which screened over 100 000 refrigerant blends using thermodynamic cycle simulation models and identified candidate HFC-134a replacements[1]. The current project narrows the pool of blend candidates down to three 'best' fluids, experimentally verifies their flammability behavior, and demonstrates their performance through tests in a military ECU in environmental chambers over a wide range of operating conditions.

To facilitate authoritative narrowing of the set of over 20 candidates to three 'best' blends for ECU testing, we carried out the following five tasks involving novel hydrofluoroolefin (HFO) fluids (Figure 1.0-1):

- Task 1: Fundamental measurements and modeling of thermophysical properties
- Task 2: Tests and modeling of flammability behavior
- Task 3: Preliminary performance tests in a mini-breadboard heat pump apparatus
- Task 4: Heat-transfer performance measurements and modeling
- Task 5: Selection of final blends for testing in military ECU

This Interim Report (Task 6) documents the results of Tasks 1 through 5. Tests of the selected three blends in the ECU will be carried out as Task 7 within the next stage of this project.

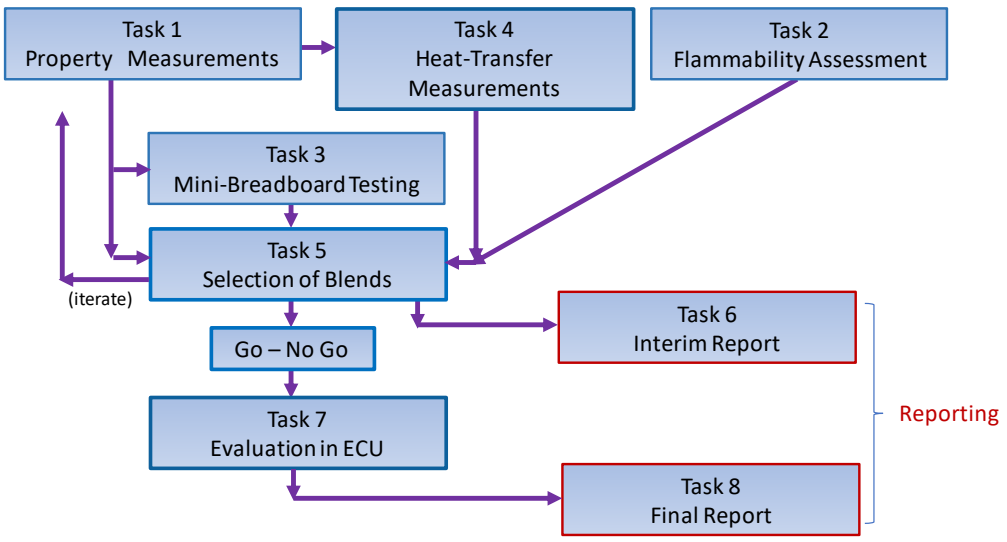

Figure 1.0-1. Project tasks

2. Technical Approach

Prior work [2] demonstrated that all single-component refrigerants that could serve—from the performance stand-point—as a replacement for HFC-134a are at least mildly flammable. For this reason, both the limited-scope project and the present work evaluate refrigerant binary and ternary blends to explore the possibility of formulating a non-flammable blend that would satisfy the requirements of military ECU systems.

The limited-scope project identified over 20 candidate low-GWP blends following an exhaustive search and evaluation of over 100 000 two- and three-component blends among a slate of 13 single-component refrigerants, subsequently expanded to 14 refrigerants [1, 3]. The limited-scope project was limited to computer simulations, while the present work will provide experimental results.

The candidate blends from the limited-scope project are listed here in Table 3.5-1. It was apparent that several of these candidate blends were very close in composition to existing compounds already included in ASHRAE Standard 34, so those similar blends, namely R-450A, R-513A, and R-515B, were adopted.

Up to this point of the present project, we have selected three ‘best’ blends for ECU testing. The selection of the ‘best’ blends was based on (1) non-flammability; (2) minimum GWP; (3) maximum coefficient of performance (COP); and (4) the volumetric capacity (Q_{vol}) matching that of the baseline HFC-134a, where the Q_{vol} of an air-conditioning system is a figure of merit related to the size of the compressor. The larger Q_{vol}, the smaller the compressor needs to be for a given cooling capacity. This selection process was aided by laboratory measurements of refrigerant thermophysical properties, two-phase heat transfer performance, flammability behavior, and cycle performance tests in a mini-breadboard heat pump (laboratory vapor-compression test apparatus).

The next stage of the project will focus on testing of the three ‘best’ low-GWP blends and the baseline HFC-134a in a military ECU installed in environmental chambers over a wide range of operating conditions. These tests will involve ‘soft optimization’ of the ECU, which will entail a modification of the expansion device and optimization of refrigerant charge for each blend. Following these tests, we will extrapolate the ECU performance measurements with simulations using a detailed, first-principles-based system model to predict the performance potential of competing blends in a system with an optimized evaporator and condenser.

3. Results and Discussion

3.1. Task 1: Experimental Measurements of Blend Properties and Development of Mixture Equation of State

3.1.1. Purpose and Approach.

A mixture equation of state (EOS) providing validated thermodynamic properties and separate transport property models are needed for conducting the MBHP tests (Task 3), refrigerant two-phase heat-transfer tests (Task 4), and ECU tests (Task 7). Updated properties will also be implemented in the NIST heat exchanger and ECU simulation models (Task 7).

The simulation of cycle performance, the analysis of laboratory measurements in equipment, and heat-transfer experiments in support of cycle simulation modeling require thermodynamic and transport properties of the blends. The thermodynamic properties are expressed in terms of an "equation of state," which is a mathematical model representing, in a consistent way, all of the thermodynamic properties of a pure fluid or blend. The properties of a refrigerant blend are given by a combination of the constituent pure fluids in the blend plus additional terms representing the mixture. The transport properties of thermal conductivity and viscosity are represented by separate models, also by combining pure-fluid models with mixture terms.

Any equation of state or transport property model (for a pure fluid or mixture) requires experimental data to fit adjustable parameters and validate its accuracy. While pure-fluid EOS are available and generally adequate for the new low-GWP refrigerants, this is not the case for refrigerant blends. This task has carried out the measurements necessary to define the mixture terms in the EOS and transport property models. These terms are expressed in terms of binary pairs of components; a mixture of the components A, B, and C, for example, is expressed in terms of the binary pairs A/B, A/C, and B/C. Thus, the present measurements were carried out on binary mixtures, even though ternary (three-component) mixtures are also among the "best" blends. The mixture parameters used in the simulations in the limited-scope study were based on limited experimental data from the literature or, in some cases, were entirely predicted.

Measurements at two levels of effort were carried out. For three binary pairs (R-1234yf/134a, R-134a/1234ze(E), R-1234yf/1234ze(E)) that appear in multiple "best" blends, comprehensive measurements were carried out in Subtask 1a. These included vapor-liquid equilibrium (VLE) measurements; pressure-density-temperature-composition (P, ρ, T, x) data in the single-phase and supercritical regions; speed of sound in the single-phase liquid region; viscosity in the single-phase liquid region; and thermal conductivity in the single-phase liquid region. Limited measurements (i.e., only vapor-liquid equilibrium) were carried out on additional binary pairs in Subtask 1b (R-125/1234yf, R-227ea/1234ze(E), R-152a/1234yf). For each blend, measurements were carried out at nominal compositions of (0.33/0.67) and (0.67/0.33) mole fraction. These measurements were designed to yield an optimal data set for the purposes of fitting mixture EOS and transport property models. The measurements are summarized in Table 3.1-1. The remainder of this section provides an overview of the measurements and modeling results, with details given in Appendix A.1.

Table 3.1-1. Refrigerant blend properties measured in the current work.

Blend	Composition (mole frac)	*T*-range (K)	*P*-range (MPa)	Number of points*
Vapor-Liquid Equilibria (VLE)				
R-1234yf/134a	(0.320/0.680)	270 – 360	0.28 – 3.10	10
R-1234yf/134a	(0.647/0.353)	270 – 360	0.29 – 3.05	10
R-134a/1234ze(E)	(0.334/0.666)	270 – 360	0.22 – 2.61	10
R-134a/1234ze(E)	(0.663/0.337)	270 – 360	0.24 – 2.84	10
R-1234yf/1234ze(E)	(0.324/0.676)	270 – 360	0.23 – 2.56	10
R-1234yf/1234ze(E)	(0.638/0.362)	270 – 360	0.26 – 2.74	10
R-125/1234yf	(0.349/0.651)	270 – 335	0.39 – 2.21	10
R-125/1234yf	(0.664/0.336)	270 – 335	0.49 – 2.70	10
R-227ea/1234ze(E)	†	†	†	†
R-152a/1234yf	†	†	†	†
(*P*, *ρ*, *T*, *x*)—Liquid and Vapor Phases and Supercritical States				
R-1234yf/134a	(0.3363/0.6637)	230 – 400	0.04 – 11.7	124
R-1234yf/134a	(0.6471/0.3529)	230 – 400	0.04 – 10.6	105
R-134a/1234ze(E)	(0.3325/0.6675)	230 – 400	0.04 – 20.5	94
R-134a/1234ze(E)	(0.6636/0.3364)	230 – 400	0.04 – 21.5	81
R-1234yf/1234ze(E)	(0.3358/0.6642)	230 – 400	0.04 – 11.4	116
R-1234yf/1234ze(E)	(0.6666/0.3334)	230 – 400	0.04 – 10.5	109
Speed of Sound—Liquid Phase				
R-1234yf/134a	(0.3363/0.6637)	230 – 345	0.35 – 13.0	78
R-1234yf/134a	(0.6471/0.3529)	235 – 310	0.66 – 11.6	40
R-134a/1234ze(E)	(0.3292/0.6708)	235 – 345	0.53 – 51.4	141
R-134a/1234ze(E)	(0.6369/0.3631)	230 – 345	0.13 – 50.3	163
R-1234yf/1234ze(E)	(0.3358/0.6642)	230 – 345	0.26 – 11.3	71
R-1234yf/1234ze(E)	(0.6666/0.3334)	230 – 335	0.45 – 12.0	60
Thermal Conductivity—Liquid Phase				
R-1234yf/134a	(0.320/0.680)	200 – 340	0.95 – 12.05	379
R-1234yf/134a	(0.647/0.353)	200 – 340	1.03 – 12.00	403
R-134a/1234ze(E)	(0.334/0.666)	200 – 340	0.96 – 50.32	350
R-134a/1234ze(E)	(0.663/0.337)	200 – 340	0.97 – 50.14	335
R-1234yf/1234ze(E)	(0.323/0.677)	200 – 340	1.02 – 12.33	352
R-1234yf/1234ze(E)	(0.642/0.358)	200 – 340	0.89 – 12.10	341

*Distinct (*T*, *P*) state points; multiple replicate measurements were made at each state point.
†Measurements on two compositions of this blend were in progress as this report was being written.

3.1.2. Vapor-Liquid Equilibrium (VLE) Measurements.

The measurement of vapor-liquid equilibrium is the mixture analog of vapor pressure for a pure component. VLE data are the most important type of data needed for fitting a mixture EOS. They indicate, for example, the departure from ideal behavior and the presence or absence of azeotropes. Measurements of the bubble-point pressure as a function of temperature and liquid-phase composition (P, T, x) were made here. Conceptually, the measurement is very simple: load a liquid sample of known composition into a closed volume (i.e., "measuring cell"), bring the measuring cell to some temperature, and when the temperature has stabilized, measure the pressure. The VLE instrument and measurement details are described in Appendix A.1.1.

3.1.3. Pressure-Density-Temperature (P, ρ, T, x) Measurements.

The present measurements utilized a two-sinker densimeter with a magnetic suspension coupling. This type of instrument applies the Archimedes (buoyancy) principle to provide an absolute determination of the density. This general type of instrument is described by Wagner and Kleinrahm,[4] and the instrument used here is described in detail by McLinden and Lösch-Will,[5] and only a brief description is given here. Two sinkers of nearly the same mass and same surface area, but very different volumes, were each weighed with a high-precision balance while they were immersed in the sample of unknown density. (The sinkers are shown in Figure A.1-3.) The fluid density ρ is given by:

$$r = \frac{\left(m_1 - m_2\right) - \left(W_1 - W_2\right)}{\left(V_1 - V_2\right)}, \tag{3.1-1}$$

where m and V are the mass and volume of the sinkers, W are the balance readings, and the subscripts refer to the two sinkers. One sinker was made of tantalum (m = 60.094 633 g, V = 3.60 872 cm^3) and the other of titanium (m = 60.075 386 g, V = 13.315 284 cm^3). A magnetic suspension coupling transmitted the gravity and buoyancy forces on the sinkers to the balance, thus isolating the fluid sample from the balance. The two-sinker method largely cancels out systematic errors in the weighing and from many other sources. Figure 3.1-1 illustrates the range of the measurements for one blend composition as an example.

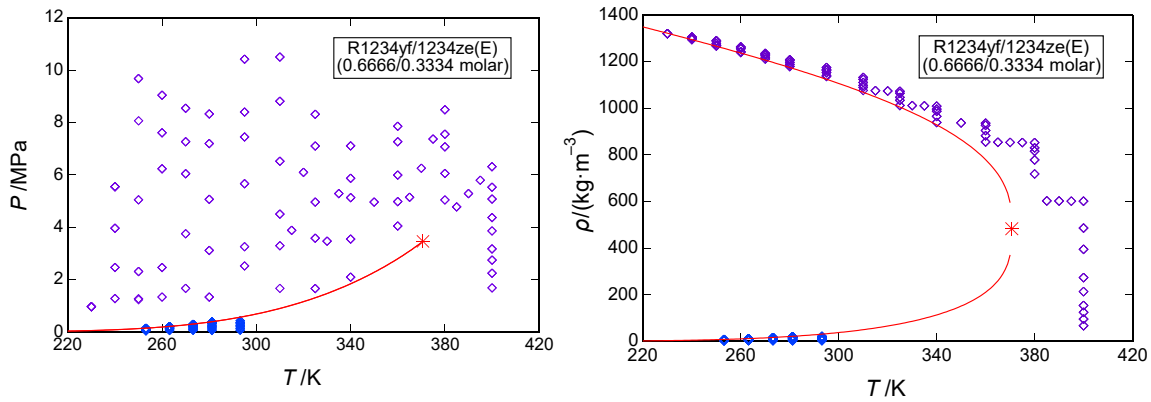

Figure 3.1-1. Measured (P, ρ, T, x) points for the R-1234yf/1234ze(E) blend at a composition of (0.6666/0.3334) molar; left: pressure versus temperature; right: density versus temperature; ◊, measured points; line, phase boundary; *, critical point.

3.1.4. Speed of Sound Measurements.

The speed of sound is closely related to heat capacity, and either speed of sound or heat capacity data are important for obtaining the correct values for enthalpy and entropy, which are needed for cycle calculations. Enthalpy and entropy cannot be measured directly, and speed of sound can be measured much more accurately than heat capacity, which is the reason for including speed of sound.

The speed of sound was measured over a wide range of temperature and pressure in a dual-path, pulse-echo-type instrument. In this technique, a piezoelectric transducer of single-crystal quartz is located within a sample volume of the test fluid. It is excited with a sinusoidal burst near the crystal resonance frequency, thus emitting ultrasonic pulses from each face of the crystal which travel through the fluid sample, reflect off planar surfaces at each end of the sample volume, and return to the transducer, which also serves as the detector. The difference in the arrival times of the echo signals give the speed of sound by

$$w = \frac{2(L_2 - L_1)}{\Delta t} \tag{3.1-2}$$

where w is the speed of sound, L_1 and L_2 are the path lengths, and Δt is the time difference. The differential nature of this technique cancels end effects and improves the accuracy. The instrument, measurement sequence, and uncertainties are described in Appendix A.1.3.

An example of the measurements carried out is depicted

Figure 3.1-2. The measured data, as well as the relative, combined, expanded (k = 2) uncertainty in the speed of sound for each point, are reported in Appendix A.1.3. For both the (P, ρ, T) and sound speed measurements, the maximum pressure was restricted to no more than 12 MPa to avoid possible polymerization of HFO-1234yf.

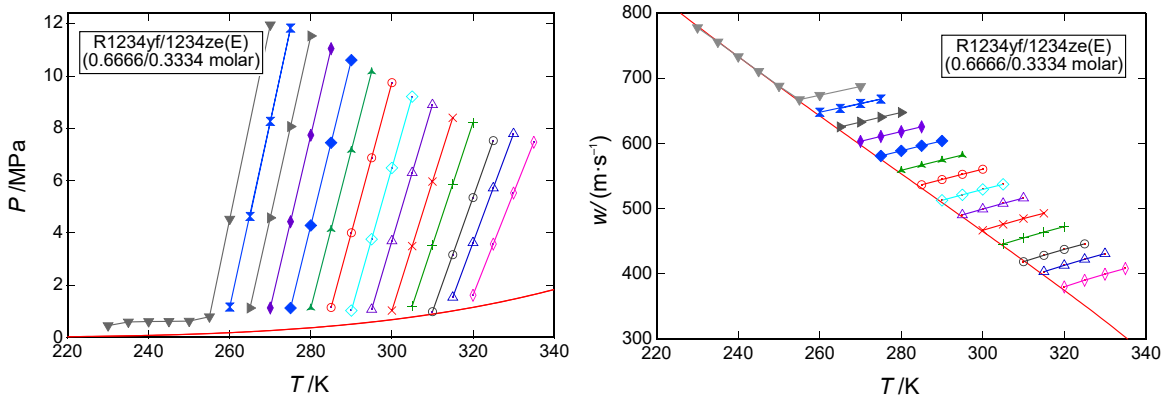

Figure 3.1-2. Measured speed of sound points for the R-1234yf/1234ze(E) blend at a composition of (0.6666/0.3334) mole fraction; left: pressure versus temperature; right: sound speed versus temperature; symbols are measured points and lines connect points along an isochore; red line is phase boundary.

3.1.5. Thermal Conductivity Measurements.

Thermal conductivity cannot be calculated from an equation of state but is important for the analysis of heat-transfer behavior. Here, the thermal conductivity was measured with the transient hot-wire technique, whereby a voltage pulse lasting about 1 s is applied to a fine wire immersed in the fluid under test; this heats the surrounding fluid and the temperature rise is monitored (using the same wire, which also serves as a resistance thermometer) to extract thermal conductivity. The wire approximates a line source and the ideal temperature rise, ΔT_{id}, is given by

$$\Delta T_{\mathrm{id}} = \frac{q}{4\pi\lambda}\left[\ln(t) + \ln\left(\frac{4a}{r_0^{\,2} C} \right) \right] = \Delta T_{\mathrm{w}} + \sum_{i=1}^{10} \delta T_i \,, \tag{3.1-3}$$

where q is the power applied per unit length, t is the elapsed time, r_0 is the radius of the hot wire, $C = 1.781...$ is the exponential of Euler's constant, λ is the thermal conductivity of the fluid, and $a = \lambda/(\rho C_p)$ is the thermal diffusivity of the fluid, where ρ and C_p are the fluid density and isobaric specific heat capacity.[6] The form of Eq. (3.1-3) is that of a line, where the thermal conductivity can be found from the slope and the thermal diffusivity can be found from the intercept. The summation term accounts for deviations from the ideal model. These measurements provided the data necessary for development of a model for the thermal conductivity of refrigerant blends. The instrument, measurement sequence, and uncertainties are described in Appendix A.1.4; the measured data are also tabulated in Appendix A.1.4.

3.1.6. Viscosity Measurements.

Viscosity data cannot be calculated from an equation of state but are important for the analysis of heat-transfer behavior. Measurement of the viscosity of three refrigerant blends, at two compositions each, will be carried out in the second phase of the project.

3.1.7. Model Development (Subtask 1c).

The data measured in Subtasks 1a and 1b were fitted to thermodynamic and transport property models with results provided in the form of files compatible with the NIST REFPROP database. Data are compared to existing models in REFPROP. The form of the model will be optimized and the data refit to the optimized model before the detailed system modeling of Task 7.

Mixture EOS for thermodynamic properties. The experimental data collected thus far have been compared against the default thermodynamic models implemented in NIST REFPROP 10.0. Significant differences were identified for the binary mixtures R-1234yf/1234ze(E) and R-1234yf/134a. For that reason, the interaction parameters for these blends were refit by applying the approach of Bell and Lemmon[7]. This approach uses evolutionary optimization to fit the mixture interaction parameters to minimize deviations in bubble-point pressure, as is detailed in Appendix A.1.6. The model implements the reducing functions (explained in Appendix A.1.6) of Kunz and Wagner[8]; and this is referred to as the "XR0" model in REFPROP. The result of the fitting is the set of new interaction parameters given in Table 3.1-2. The parameters for R-134a/1234ze(E) and R-125/R1234yf were not updated at this time.

Table 3.1-2. Interaction parameters used in this work (note: the order of components is significant)

Binary Pair	$\beta_{T,ij}$	$\gamma_{T,ij}$	$\beta_{V,ij}$	$\gamma_{V,ij}$	F_{ij}
R-1234yf/1234ze(E)*	1.000555	0.992815	1.0	1.0	0.0
R-1234yf/134a*	0.999557	0.986956	1.0	1.0	0.0
R-134a/1234ze(E)†	1.0	0.992	1.0	1.0	0.0
R-125/1234yf†	1.0	0.999	1.0	1.0	0.0

*updated values for the mixture interaction parameters
†mixture interaction parameters from REFPROP 10.0

Deviations of the data with the updated models are shown in Figure 3.1-3. By tuning the interaction parameters, the deviations in bubble-point pressure (i.e., VLE data) have been reduced to within or near their experimental uncertainty. The density data are also well represented, except for densities in the critical region, where the uncertainties are larger due to the propagation of uncertainty in pressure measurement through to the combined expanded (k = 2) uncertainty. On the other hand, the adjustment of the interaction parameters to reduce deviations in bubble-point pressure did have a negative effect on the reproduction of the speed of sound, although all the speed of sound deviations are within 2% with the updated parameters, and most are within 1%. Considering the combined expanded uncertainty of the speed of sound measurements is approximately 0.07 %, there remains an opportunity to update the mixture models to yield a better representation of the caloric properties by better reproduction of the speed of sound data. This is perhaps not a surprising result because the current mixture model for refrigerants, that of Lemmon and Jacobsen[9], was developed in the early 2000s with virtually no speed of sound data as input. This is a target for the second phase of the project in which we will generate reference thermodynamic models, with the goal being to reproduce all experimental data measured in this project to within their experimental uncertainties.

Thermal conductivity model. We have applied the modified entropy scaling approach to model the measured thermal conductivity data. Entropy scaling is a relatively new approach for the modeling of transport properties and is based on the idea that entropy (a thermodynamic property), when scaled in an appropriate way, is a measure of the structure of the fluid phase. Thus, transport properties can be expressed in terms of this scaled entropy, rather than as a function of, for example, the temperature and density. This approach connects the transport properties (e.g., thermal conductivity and viscosity) to the thermodynamic properties (which are represented by an equation of state). The power of entropy scaling is that it allows an accurate representation of the transport properties with far fewer experimental data needed as input to the model compared to traditional models.

The thermal conductivity λ is non-dimensionalized to the plus-scaled thermal conductivity λ^+ as defined by

$$\lambda^+ = \lambda/\left(k_B(\rho N_A)^{2/3}\sqrt{RT/M}\right) \times (s^+)^{2/3} \quad (3.1\text{-}4)$$

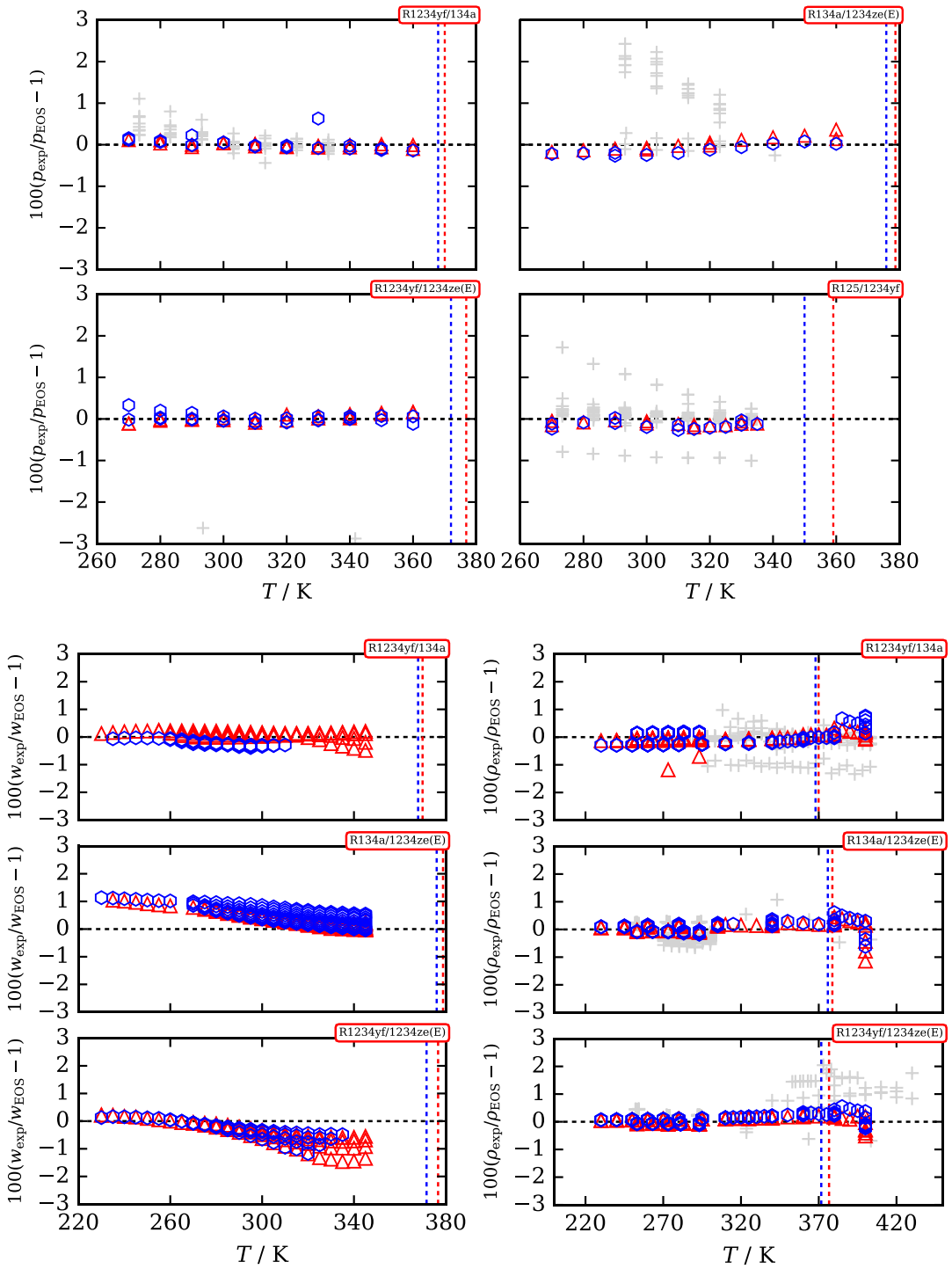

Figure 3.1-3. Deviation plots for the measured experimental data with the mixture EOS using the parameters from Table 3.1-2. The different plot symbols indicate the two compositions measured here; the vertical lines indicate the mixture critical temperature. Literature data are shown as light grey + markers (some literature data have deviations outside the range of the figures).

λ^+ is a function of the reduced scaled residual entropy s^+, with a factor including the molar density ρ, Boltzmann constant k_B, Avogadro's constant N_A, temperature T, and molar mass M. All dimensional quantities are expressed in base-SI units (kg, m, Pa, etc.). The origins of this scaling are described in Appendix A.1-6.

In these scaled coordinates, the experimental mixture thermal conductivity data fall very nearly along a single curve, as shown in Figure 3.1-4. The curve is given by a simple polynomial fitted to the experimental data by unweighted linear least squares:

$$\lambda^+ = \sum_i c_i \, (s^+)^i \tag{3.1-5}$$

where the coefficients c_i are given in Table 3.1-3, and the deviations are shown in Figure 3.1-4.(b). The average absolute deviation is 1.32 % and the central 95.5 percentiles of the signed relative errors (approximately equivalent to a 95 % confidence interval) span the range -2.82 % to 2.98 %. This quality of fit is rather remarkable given that a total of six mixtures formed of three different components are collapsed to a single curve with no empirical tuning parameters. While this interim correlation was fitted to only liquid phase data, with a dilute-gas model and a critical enhancement model, its range of validity can be extended to the entire phase diagram, from dilute gas to the melting line.

Table 3.1-3. Coefficients for entropy scaling of thermal conductivity data (Eq. 3.1-5).

i	c_i
0	15.19495
1	-6.29123
2	2.74329
3	-0.12635

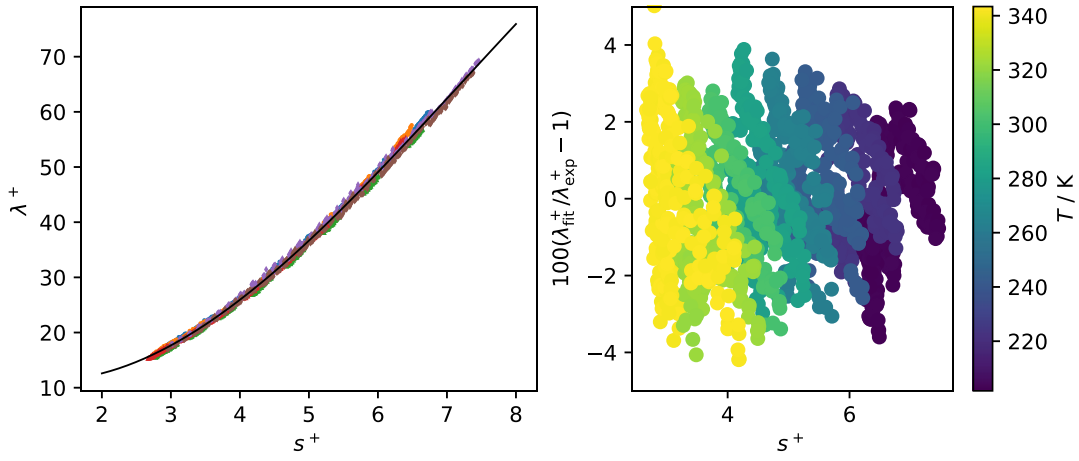

Figure 3.1-4. Entropy scaling model for the thermal conductivity of the three blends studied here; (a) plus-scaled thermal conductivity λ+ as a function of reduced scaled residual entropy *s*+, the different symbols denote the different measured blends; (b) relative deviations in λ+.

3.2. Task 2: Flammability Testing

3.2.1. Introduction

It is essential that any low-GWP replacement for HFC-134a be non-flammable. This is challenging, however, since for molecules containing only hydrogen, fluorine, and carbon, there is a trade-off between GWP and flammability. The common changes to the molecules (adding hydrogen atoms or double bonds) to make them more reactive in the troposphere and hence lower their atmospheric lifetime (which lowers GWP), also makes them more flammable. Thus, one desires to make the molecules, or mixtures of compounds, have the lowest GWP possible while still maintaining non-flammable behavior. A further challenge arises, however, in that flammable behavior is not a distinct boundary, but depends upon the environment to which the refrigerant is exposed. As described by Williams [10], flame stabilization requires that the characteristic chemical reaction rate be fast enough to keep up with the flow/transport field in which the refrigerant is reacting. For compounds that are clearly flammable or non-flammable, for example methane or CO_2, their behavior in air is consistent among common configurations. But for compounds of intermediate flammability, for example mixtures of CO_2 and CH_4, or pure HFO-1234yf, their behavior will be very sensitive to the flame/fire configuration. For example, in recent full-scale tests in a 50 m^3 module [11], stable flames of HFO-1234yf and air could not be initiated with a high-voltage spark ignition system typical of that used in the small-scale E681 test [12]. In contrast, using a glow-plug ignition source, turbulent flames of HFO-1234yf and air in an HVAC duct were achieved by Papas et al. [13], with turbulent flame speeds much higher than previously reported laminar burning velocities.

There are two goals of the present refrigerant flammability work. The first is to assess experimentally the flammability of the candidate blends predicted to be non-flammable (as determined by ASHRAE Standard 34 [12]) in the previous limited-scope project. In the preliminary work, an empirical model of flammability based on the adiabatic flame temperature and the fluorine to hydrogen ratio of the reactants was used to create a flammability index [14] and rank a list of candidate blends with regard to their flammability. All of the candidate blends selected for further study in the MBHP or ECU were predicted to be non-flammable. Nonetheless, it is essential that the candidate blends be tested in experiments to verify that the predictions were accurate. It is expected, however, that the fire threats in the DOD applications will be much more aggressive than in typical HVAC applications, and a more conservative flammability test would be desirable.

The second goal of the present work is to use the experimental flammability test results, together with flame modeling, to predict, for a given blend, if it will be flammable in the fire threats of interest to the DOD. Researchers at the Army Research Laboratory (ARL) have developed a representative scenario, in which an incendiary projectile impacts a coil filled with refrigerant. In such a test, ignition sources are abundant, and it is required that the resulting refrigerant-air cloud not support a self-propagating flame. Predicting the behavior of candidate lower-GWP refrigerant blends in that test is challenging. Of course, all candidate blends could be tested at full-scale, but this would be prohibitively expensive and time consuming. It is desired to predict the full-scale behavior based on laboratory-scale test results. While challenging, such a prediction is not unprecedented. For example, the behavior

of HFC fire suppressant agents in the FAA Aerosol Can Test [15] has many similarities as will be discussed below.

The approach for flammability assessment is as follows. First, the flammability of the candidate blends must be experimentally tested. Since the empirical model for refrigerant flammability in the limited-scope project was developed based upon the data in the ASHRAE Standard 34 database, the modified ASTM E681 specified in Standard 34 is used to experimentally verify the predicted performance of the candidate blends. Next, a more stringent test is applied. For this purpose we adopt a modified version of the Japanese High-Pressure Gas Law (JHPGL) test [16], as described below. Development of the kinetic model of combustion of the refrigerant-air flames is discussed, and the model is used to interpret the experimental data available to date. Finally, an approach for connecting the small-scale tests to the full-scale live-fire tests to be conducted at ARL is described, with the goal of properly interpreting those results and minimizing the number of tests necessary to ensure non-flammable behavior of the selected blends.

3.2.2. E681 tests and Japanese High-Pressure Gas Law tests

E681: Experimental Results. For HVAC applications, the flammability of a refrigerant is assessed via ANSI/ASHRAE Standard 34 [17] or the very similar ISO Standard 817 [18]. A flammability rating of Class "1" to "3" is assigned, based on its heat of combustion, lower flammability limit, and laminar burning velocity. In the ASHRAE standard, Class 3 fluids, termed "higher flammability," exhibit flame propagation at 60 °C and 101.3 kPa and have a heat of combustion greater than 19 MJ/kg *or* a lower flammability limit (LFL) less than 0.10 kg/m^3. Class 2 fluids, "lower flammability" have a heat of combustion less than 19 MJ/kg *and* an LFL greater than 0.10 kg/m^3. Class 1 fluids exhibit "no flame propagation" when tested at 60 °C and 101.3 kPa. Class "2L" fluids also have a maximum burning velocity less than 10 cm/s. For the present discussion, we focus on the distinction between Class 1 and Class 2L.

Flame propagation and the lower flammability limit in ASHRAE Standard 34 are determined by the test method specified in ASTM E681 [19], with slight modifications. A schematic of the E681 test vessel is shown in Figure 3.2-1. In the test, the refrigerant and air are introduced into a 12 L glass sphere, which is closed by a spring-loaded stopper at the top. A 15 kV AC source provides a spark (spark duration 0.4 s) to tungsten electrodes (1 mm diameter, 6.4 mm gap) located 1/3 diameter from the bottom of the vessel. If a flame forms and extends upwards and outwards from the spark to the walls of the flask and subtends an angle equal to or greater than 90° as measured from the point of ignition, there is "flame propagation." Tests are conducted at 60 °C with air at 50 % relative humidity (r.h.) at 23 °C (0.0088 g H_2O/g air).

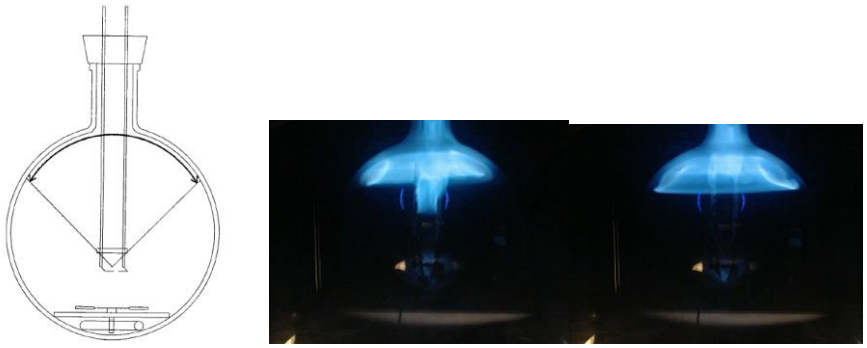

Figure 3.2-1. Left image: schematic of ASTM 681 test vessel; Right two images: visual images from HFC-32/HFC-134a blend (0.35 /0.65 mass fraction) below and above the lean flammability limit [20, 21].

The ASHRAE Standard 34/ASTM E681 tests for the present work were performed by an outside testing laboratory under contract to NIST. This contractor was selected because they have extensive experience with the test [21] and have provided a substantial number of the data in the ASHRAE Standard 34 database. Considering that there is significant variability in the test approaches that can affect the quantitative results [21, 22], it was useful to select a contractor likely to provide a test approach consistent with the existing database. This was important since the present test results are being compared to flammability predictions from our earlier work [1, 14], which was developed based on the existing ASHRAE Standard 34 database.

It was originally expected that all mixtures selected for further study would need to be tested by the outside contractor. However, over the course of the project, it was apparent that several of the candidate blends were very close in composition to existing compounds for which applications to ASHRAE 34 had recently been made, so those similar blends (R-450A, R-513A, and R-515B) were adopted. A side benefit is that they would not need to be tested again via the contracted E681 experiments, freeing up some of those tests for other compounds of interest.

The results of the contracted E681 tests are listed in Section A.2.1 of Appendix A. Table 3.2-1 below summarizes the results of the E681 tests and lists the existing flammability ratings [14] for R-513A, R-450A, and R-515B from the ASHRAE Standard 34 database ($P_{\max}$ and ω_{psr} are discussed below). All of the candidate blends are flammability Class 1. The last three mixtures, blends of HFO-1234yf and HFC-134a, were tested at increasing concentration of HFC-134a until a Class 1 rating was achieved. These tests will be used to connect E681 experiments, JHPGL experiments, and simulations to full-scale results, as discussed below.

Table 3.2-1. Modeling and test results for candidate blends (reactants at 296 K, 101 kPa, and 50 % r.h.).

Name	Blend (mole%)	Std.34 Class	$\overline{\Pi}$ †	P_{max} [bar]	ω_{psr} [s^{-1}]
Tern-1	R1234yf/134a/1234ze(E) (32/52/16)	1 [E]	-1.2	0.451	86
R-513A	R1234yf/134a (53.2/46.8)	1 *	-0.5	0.474	99
R-450A	R1234ze(E)/134a (53.3/44.7)	1 *	-0.2	0.262	110
R-515B	R1234ze(E)/227ea (93.85/6.15)	1 *	2.0	1.56	166
YF/134a-30	R1234yf/134a (70/30)	1 [E]	1.7	1.27	166
YF/134a-28	R1234yf/134a (72/28)	2L [E,e]	1.9	-	169
YF/134a-26	R1234yf/134a (74/26)	2L [E,e]	2.1	-	177

* from Std. 34 database

† flammability index from ref. [14]

[E] from contracted E681 testing

[e] estimate based on E681 testing and consideration of similar compounds

E681: Interpretation of E681 Results in Regard to Large-Scale Behavior. The E681 test, as modified by ASHRAE Standard 34, is widely used in the HVAC industry and is believed to be sufficiently conservative to provide safe application of refrigerants in those settings. It may not, however, be appropriate for the much more stringent non-flammable requirements of DOD applications. As described above, flammability is a continuum, and only becomes a discrete rating when some criterion is applied. As an example, the 90° flame angle criterion is used in the ASHRAE Standard 34 to distinguish between "flame propagating" and "non-flame propagating." This is illustrated in Figure 3.2-1, in which the left and right flame images (with flame angles of 85° and 95°, respectively) are for refrigerant concentrations in air that are just below and above the lean flammability limit. To an observer, these flames might both appear to be "flammable," and hence the 90° criterion may not be appropriate for more energetic, turbulent-ignition scenarios such as in the Army Research Laboratory ARL live-fire tests.

The selection of the 90° criterion is informative for the present discussion. Richard and co-workers [23] conducted experiments in larger, 200 L vessels in which the walls did not constrain the effects of buoyancy on the flame propagation. They found that some flames propagated and consumed all the fuel in the vessel while others self-extinguished and failed to propagate. The successful flame propagation in the 200 L vessel correlated with those flames in the 12 L vessel that had a flame angle of 90° or greater, validating the 90° criterion in the ASHRAE Standard 34/E681 test. Note that as an additional measure of safety, the ASHRAE Standard 34 test is conducted with gases at 60 °C, i.e., a more flammable condition, so that a non-flammable rating obtained at the test condition is conservative. Nonetheless, concerns have been raised with regard to the 90° criterion. For example, only two refrigerant blends were used, i.e., R-152a/134a and R-152a/125, and it is unclear if the

behavior will be the same for different chemical classes of refrigerants, e.g., HFOs vs HFCs. Also, the stretched burning velocity and critical flame radius for flame propagation are known to depend on the Lewis number of the mixture [24, 25], which can vary for different blend components.

The challenge in the present work is to find a relevant flammability criterion in small-scale tests that properly captures the important flame dynamics in the full-scale, live-fire tests of interest to the Department of Defense, which is characterized by strong, multiple ignition sites (due to projectile impact), heated product gases from ancillary combustion (from the pyrotechnic charge) and shock-induced heating, and turbulence. The next section presents the rational for selecting the Japanese High-Pressure Gas Law (JHPGL) test, and some experimental results from it with the candidate blends and R-1234yf/134a mixtures.

Japanese High-Pressure Gas Law Test: Relevance. A modified version of the Japanese High-Pressure Gas Law (JHPGL) test (documented in the appendix of ref. [16]) has been selected to provide a more stringent, reduced-scale flammability test for refrigerants exposed to live-fire tests at full scale. The experiment uses a 2 L stainless steel spherical pressure vessel into which the premixed gases are introduced using the partial pressure method. A thin platinum wire energized by a continuous 100 VAC source provides ignition. The explosion pressure P_{max} (i.e., the maximum pressure in the vessel for any value of fuel-air equivalence ratio ϕ) provides the metric for flammability. The experiment is described in detail in previous work [16, 26-28] and in Section A.2.2 of Appendix A, and has been used to understand HFC refrigerant flammability [16, 26] as well as HFC fire-suppressant performance in aircraft fire-suppression applications [27, 28]. Modifications from the original standard are the use of pressure rather than temperature as the flammability metric, and a modified ignitor configuration to allow insertion through a single port.

The test indicates wider flammability limits than the ASHRAE Standard 34 E681 test for the following reasons. The exploding platinum wire sprays droplets of molten platinum through the chamber [29], providing numerous ignition sites by catalytic surfaces, and the turbulent flow field accelerates the flame speed and minimizes stretch-induced extinction of the nascent flames [30] at early times. The constant volume combustion chamber also provides compressive heating, which increases reactivity. In previous work, flammability in the JHPGL test was shown to accurately predict flammability of HFC/hydrocarbon/air mixtures in the very intense conditions of the FAA Aerosol Can Test (FAA-ACT). In that test, a 10 m^3 pressure vessel is used to mimic the inside of an airliner cargo-bay, in which an aerosol spray can explodes due to the heat of a cargo-bay fire. In the FAA-ACT, a fast-acting valve releases the contents of the simulated aerosol can (454 g of propane, ethanol, and water) across a 15 kV continuous AC spark ignitor, into the chamber which has been prefilled with a mixture of air and an HFC fire *suppressant* (e.g., HFC-125, 2-BTP, Novec 1230, etc.). The contents of the aerosol can form an intense propane/ethanol/water turbulent spray flame at the ignitor location, and the question is whether the flame propagates into the air/HFC end-gases in the chamber. The pressure rise in the chamber due to reaction of the aerosol can contents (and sometimes HFC suppressant) creates a temperature rise of 100 °C to 250 °C. The similarities with the ARL live-fire refrigerant-coil test include: strong ignition source, temperature rise due to compressive heating, reactive intermediates supplied by strong

combustion of an adjacent flame, and basically the same type of reactants (HFCs, HFOs, etc. mixed with air) in the end gases, which may or may not be ignited. The FAA-ACT also provides extra water (i.e., mixed with the fuel), enhancing the reactivity of the HFC compounds. The fact that the JHPGL test could accurately predict which fire suppressants (and blends) agents would combust in the end-gases of the FAA-ACT [28] gives confidence that it is a good small scale test for predicting the behavior of similar compounds in the ARL live-fire refrigerant tests.

Japanese High-Pressure Gas Law Test: Experimental Results. The JHPGL as used provides the peak pressure rise in the vessel as a function of blend volume fraction in the air. Figure 3.2-2 shows, for the four candidate blends, the measured peak pressure as a function of refrigerant volume fraction in moist (50% r.h.) air (lower curves) together with the calculated [31] equilibrium explosion pressures for the same mixtures. Equilibrium values are about 10 bar for all blends, varying about 1% between the candidate blends, and by about 1% for varying water vapor in the air (0 % to 100 % r.h.). The equilibrium value assumes complete reaction to most stable products with no heat losses. For typical fast hydrocarbon flames, 90 % of the equilibrium value can be attained [27]. For slower flames, the pressure rise is a smaller fraction of equilibrium, for example about 50 % for HFO-1234yf. Fusing of the Pt wire causes a pressure rise of 0.033 bar +/- 0.013 bar [16]. Thus, the candidate blends have pressure rises of 2 % to 13 % of the equilibrium values.

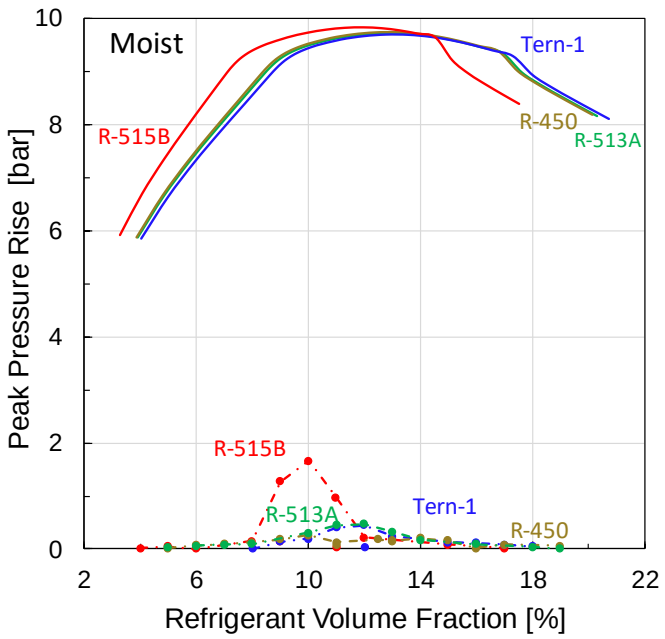

Figure 3.2-2. Equilibrium explosion pressure of candidate blends (Tern-1, R-513A, R-450A, and R-515B) together with experimental results in the JHPGL test as a function of blend volume fraction in air (50 % r.h.).

The experimentally observed peak pressure rise for the four candidate blends is given in Section A.2.2 of Appendix A and shown graphically in Figure 3.2-3 for dry and moist air. Focusing on the moist air results (right frame), the peak pressure for the four agents: R-450A, Tern-1, and R-513A is low (0.262, 0.451, and 0.474) bar, but higher for R-515B, about

1.6 bar. Details of the results for individual blends are shown in Figure 3.2-4 (note difference in scales). While these data may appear noisy, it is important to keep in mind that these are very low pressure rises, at the lower end of the dynamic range of the piezo-electric dynamic pressure transducer. Also, the stochastic nature of the exploding-wire ignition system creates variability in the results. The individual results in Figure 3.2-4 illustrate the effects of water vapor, which are small for R-450A and R-515B, and larger for R-513A and the Tern-1 blend.

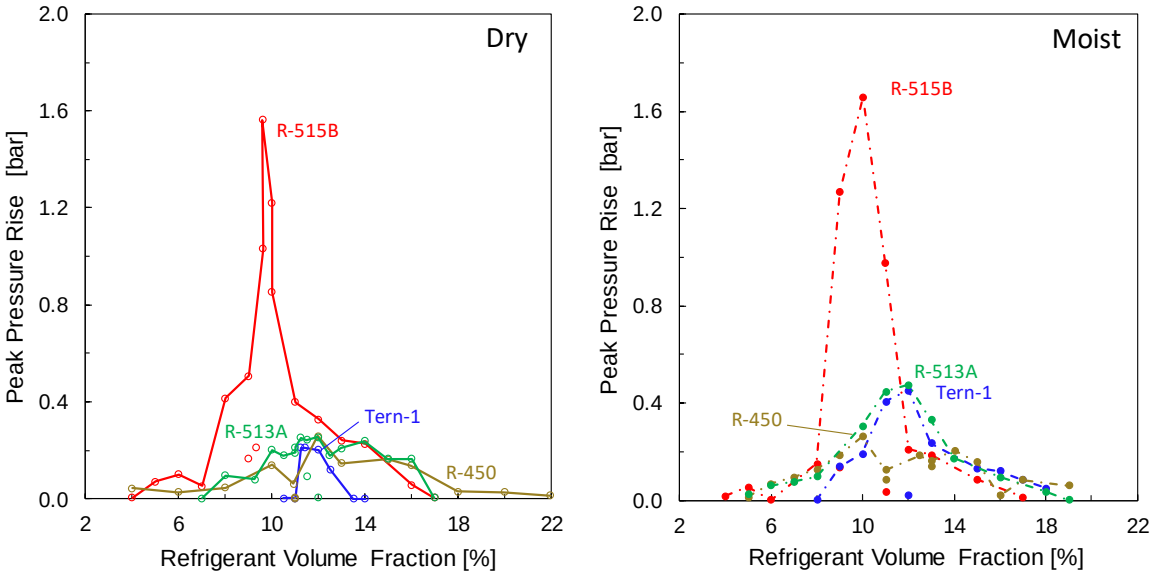

Figure 3.2-3. Explosion pressure of candidate blends in JHPGL test as a function of blend volume fraction in air (left frame: dry air; right, moist).

While the results of the tests for the candidate blends are useful and illuminating, there is value in conducting tests in which the blend components are more systematically varied. To do this, we considered a binary blend of HFC-134a with HFO-1234yf, with increasing mole fraction of the less-flammable component (HFC-134a) up to 100 %. Figure 3.2-5 shows the JHPGL explosion pressure as a function of blend volume fraction in the air; each curve refers to a particular HFC-134a volume fraction in the blend (left frame: dry air; right frame: moist air, 50 % r.h.). Figure 3.2-6 shows the peak values from Figure 3.2-5 as a function of the volume fraction of HFC-134a in the blend. For pure HFO-1234yf flames, moist flames have about 25 % higher peak pressure than do dry flames. For both moist and dry air, the peak pressure drops off steadily until about 50/50 volume fraction, after which the reduction in peak pressure with increasing HFC-134a is small. That is, after about 60 % HFC-134a volume fraction, there appears to be no additional benefit of adding this component to HFO-1234yf, in this experimental configuration.

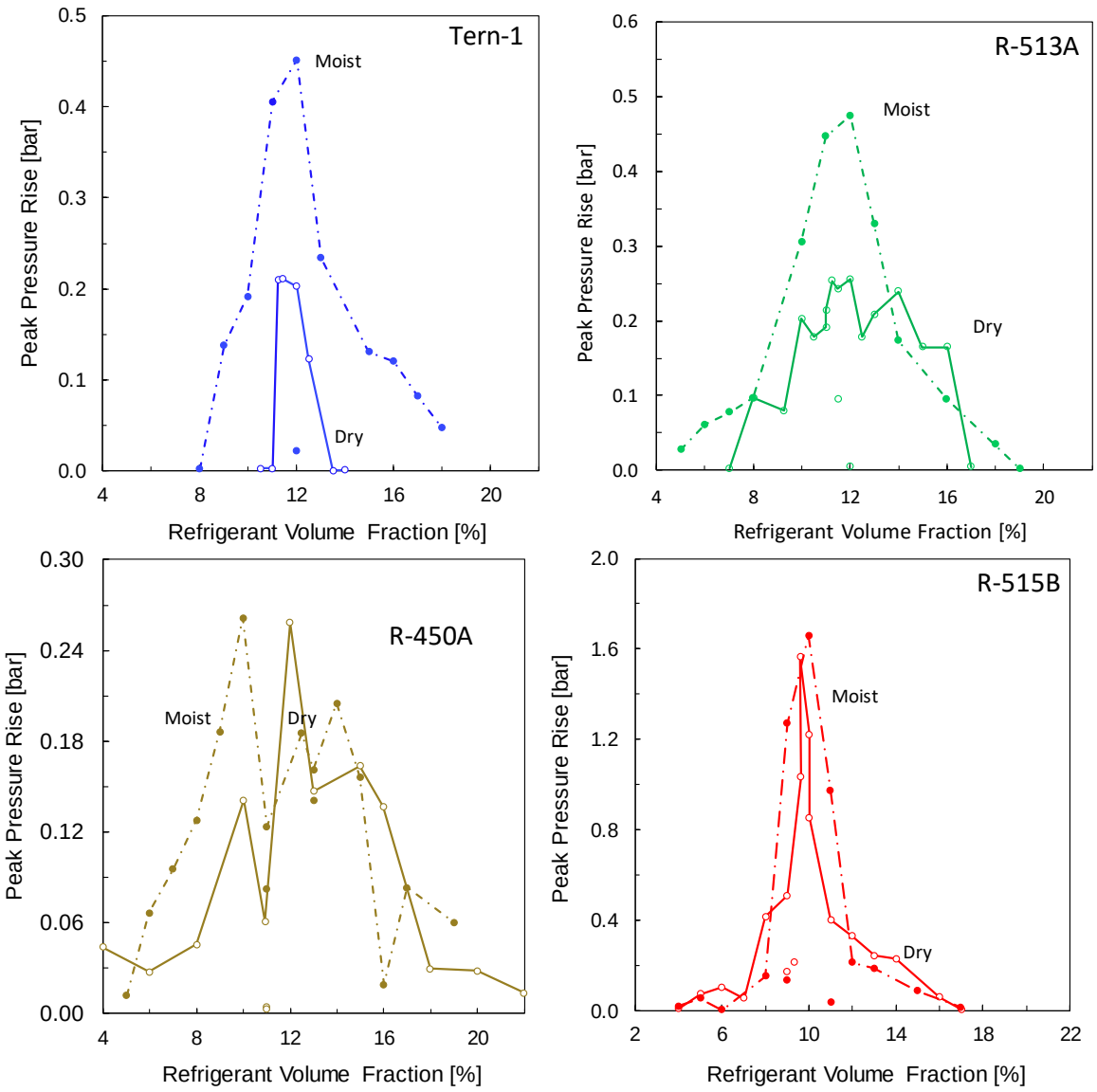

Figure 3.2-4. Explosion pressure of candidate blends (Tern-1, R-513A, R-450A, and R-515B) in JHPGL test as a function of blend volume fraction in air (solid lines: dry air; dashed lines: moist air; note different scales).

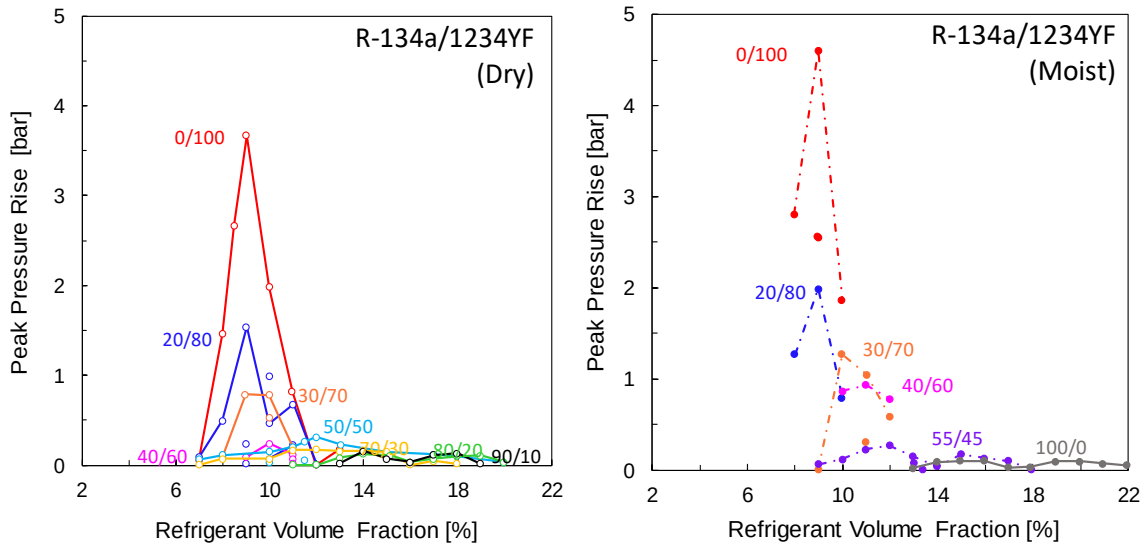

Figure 3.2-5. Explosion pressure in the JHPGL test for binary blends of HFC-134a with HFO-1234yf as function of volume fraction the blend in air. Different curves show results for varying volume fractions of HFC-134a/HFO-1234yf in the blend (left frame: dry air; right: moist).

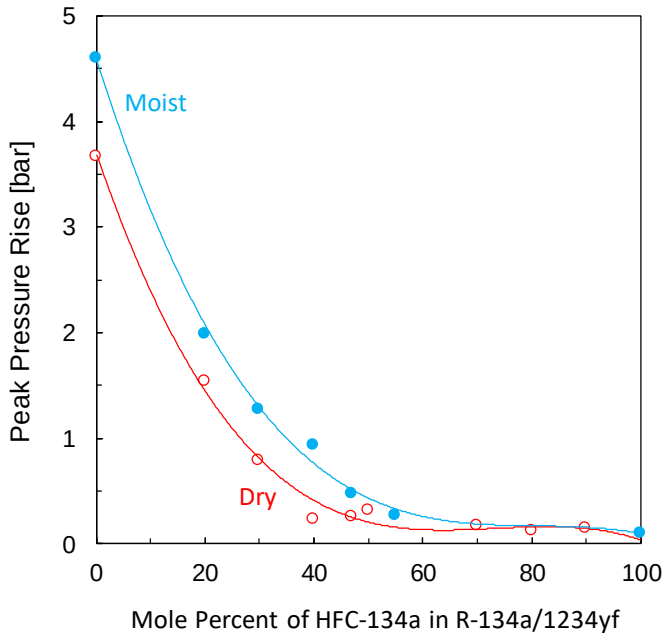

Figure 3.2-6. Peak explosion pressure in the JHPGL test for binary blends of HFC-134a with HFO-1234yf as function the volume fraction of HFC-134a in the blend, for moist (50 % r.h.) and dry (< 2 % r.h.) air.

3.2.3. Improvements in Predictive Model

Recent work at NIST has had the goal of developing the predictive capability for flammability. A reasonable surrogate for flammability is the laminar burning velocity S_u^0, which is defined as the rate of propagation of a 1-D, planar, adiabatic, combustion wave through a mixture of combustible gases. It is a useful flammability metric since it is a fundamentally based parameter incorporating the effects of overall reaction rate, heat release, and molecular transport for the fuel-oxidizer mixture. It is used as a scaling parameter for turbulent flame speed [32] and as an input to full-scale explosion models [33, 34]. It is correlated with minimum ignition energy, flame quenching diameter, and lean flame extinction, and is a metric used in existing and developing codes and standards for refrigerant flammability [17, 18]. In the present work, we adopt burning velocity, along with the overall chemical rate as determined in a stirred-reactor, since both have proven useful for understanding the behavior of near-limit flames of fluorinated compounds, alone with air, or in hydrocarbon-air mixtures [15, 35-43]. Calculating either the burning velocity or the overall chemical rate requires a detailed kinetic model of the combustion of the fluorinated compounds.

Early work at NIST developed a detailed kinetic model for HFC fire suppressants [44, 45] and recent work has extended it to flames of pure refrigerants and air [46-48]. In the present project, the mechanism was further refined and updated with new rates and thermodynamic data appearing in the literature. As a result, the mechanism can accurately predict the existing experimental burning velocity data in the literature for one- and two-carbon HFCs [47] and fluoropropenes (HFOs) [48]. Since it has not been extensively tested with data for blends of refrigerants, the present work collected new burning velocity data for R-152a/134a, and R-152a/1234yf blends. Also, since the burning velocity of either HFO-1234yf or HFC-134a with air at 298 K is too low to measure in normal-gravity experiments, the addition of a more reactive HFC, in this case HFC-152a, allows one to more readily obtain data on their combustion behavior. The mechanism was then used to calculate the burning velocity *a priori* for the experimental conditions to assess its predictive ability.

Experimental Data for Model Validation. As described in Section A.2.3 of the Appendix, the 2 L chamber was used with a spark ignition system to collect the chamber pressure P as a function of time t, from which the burning velocity is determined using a thermodynamic model [49]. Figure 3.2-7 shows the burning velocity as a function of refrigerant volume fraction [50] (points: experimental data, dotted lines: cubic fit to experimental data, solid lines: numerical predictions). The different curves in each frame are for R-152a/134a blends at (1.00/0.0), (0.80/0.20), (0.50/0.50) volume fractions (left frame), and R-152a/1234yf blends at (1.00/0.0), (0.50/0.50), (0.40/0.60), and (0.30/0.70) volume fraction. The air in these tests was dry (< 2 % r.h. at 23 °C) except for the one curve for at R-152a/1234yf (0.40/0.60), for which the r.h. was about 50 %. The dotted lines are cubic fits to the experimental data. As indicated, the mechanism does a very good job of predicting the burning velocity for these conditions. A similar comparison has been performed for other refrigerants [46-48]. The different data sets on each frame correspond to different molar ratios of the two constituents, as indicated on the curve labels. The experimental data are the points, the dotted lines cubic fits to the experimental data, and the solid lines the numerical modeling predictions.

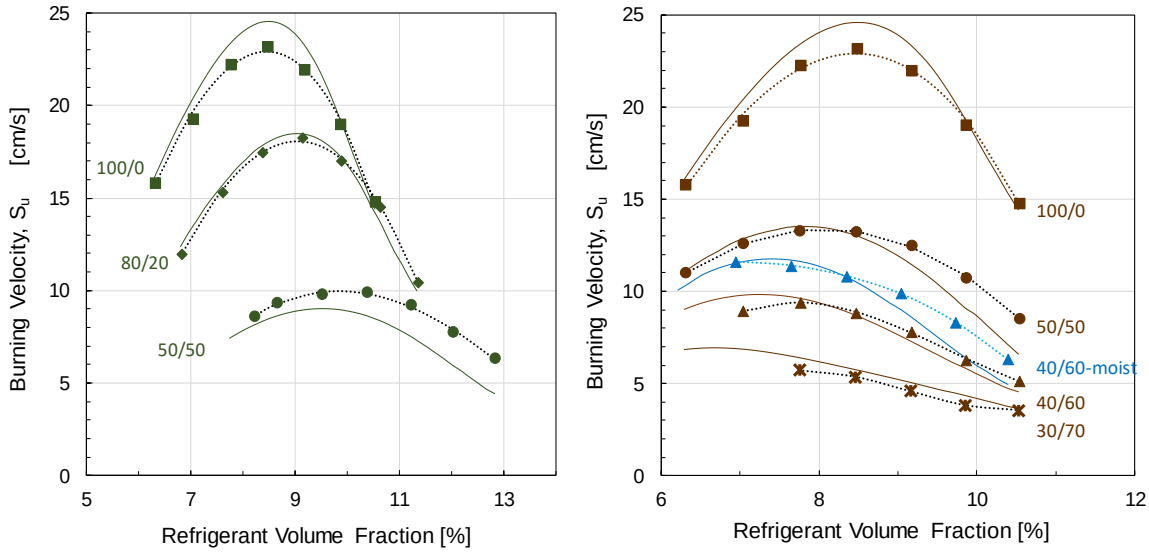

Figure 3.2-7. Laminar burning velocity of R-152a/134a (left frame) and R-152a/1234yf (right frame) mixtures with air as a function of the equivalence ratio.

Figure 3.2-8. summaries the predictions of the present model vs. the experimental results, indicating that the predictive ability of the model is good. Hence, the kinetic model should be a useful tool for understanding the present candidate blends (since all of the constituents of the blends are included in the kinetic model).

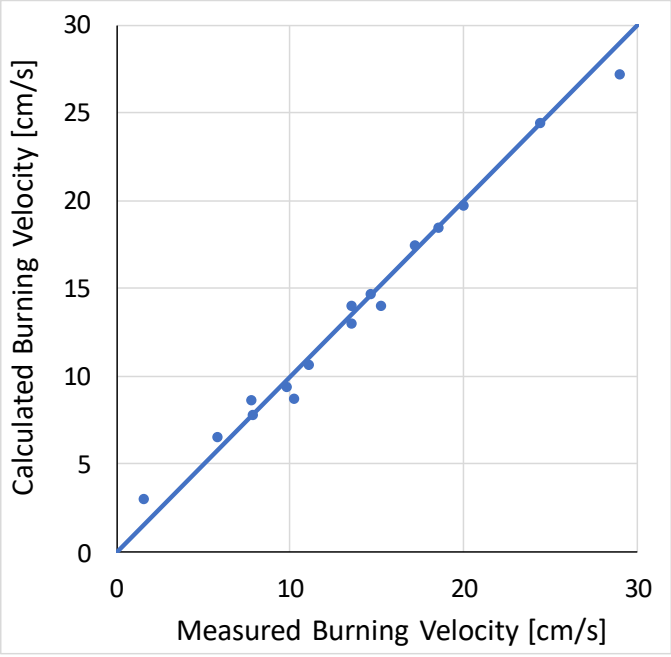

Figure 3.2-8. Calculated vs. measured laminar burning velocity (peak over all ϕ) of twenty-one refrigerant/N_2/O_2 flames for which experimental data are available in the literature [46-48].

3.2.4. Interpretation of E681 and JHPGL Experimental Results

The results in the JHPGL test as well as in the E681 test can be interpreted using the kinetic model as a tool. A useful metric is the overall reaction rate of the mixtures, at the conditions of interest (e.g., initial *T*, *P*, humidity, etc.). Simulations (or experiments) of the blow-out condition of a perfectly stirred reactor (PSR) can be used to obtain an estimate of the overall chemical rate ω_{psr}. This rate can be used, among other things, to estimate the laminar burning velocity [51], the flammability limits [16], and the extinction conditions of full-scale fires [39]. For example, in Figure 3.2-9, the overall chemical rate ω_{psr} calculated for the mixture R-1234yf/134a is shown as a function of the volume fraction of the blend (i.e., fuel). Increasing volume fractions of HFC-134a in the blend reduces ω_{psr}, and the effect of humidity is shown by the three frames (0 % r.h., 50 % r.h., and 100 % r.h.). Of particular interest is the peak value of ω_{psr} for each blend. These are shown in Figure 3.2-10 with one curve for each value of the humidity in the air. As indicated, increasing water vapor (0 % to 100 % r.h.) increases the peak overall reactivity by a factor of 2.5 for HFO-1234yf and 1.8 for HFC-134a. Moreover, as shown in Figure 3.2-9, at 50 % r.h. the ω_{psr} has broad plateaus, whereas at 0 and 100 % r.h. there are distinctive peaks. This behavior is expected to be exhibited for all HFC blends.

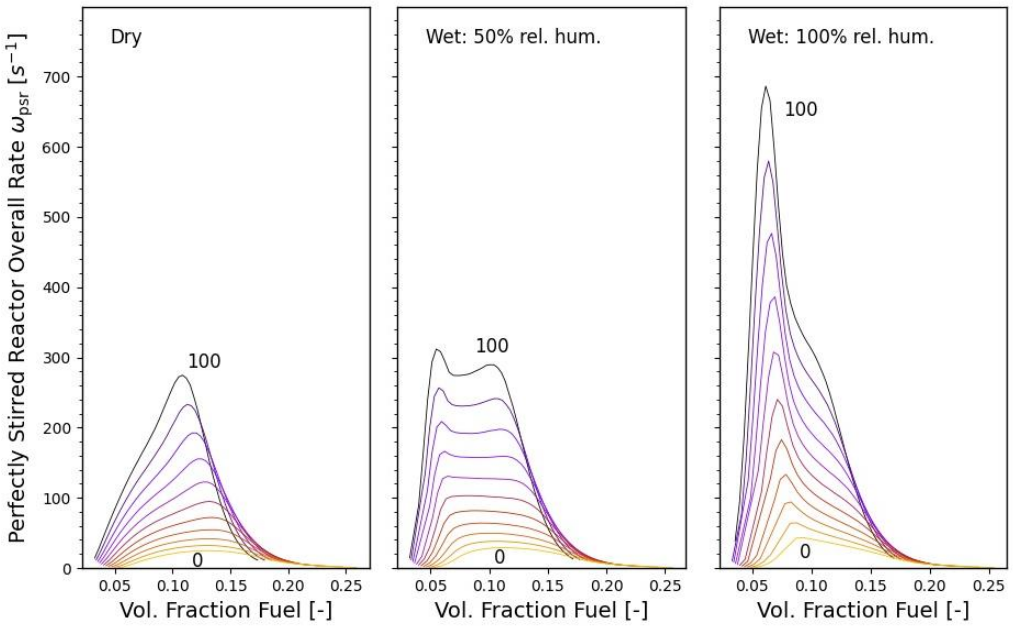

Figure 3.2-9. Overall chemical reaction ω_{psr} as a function of volume fraction in air determined via perfectly stirred reactor simulations for the blend R-1234yf/134a. Each curve refers to one blend ratio: top curve, 100% HFO-1234yf, bottom curve 100 % HFC-134a; Frames: 0 % r.h. (dry), 50 % r.h., and 100 % r.h.

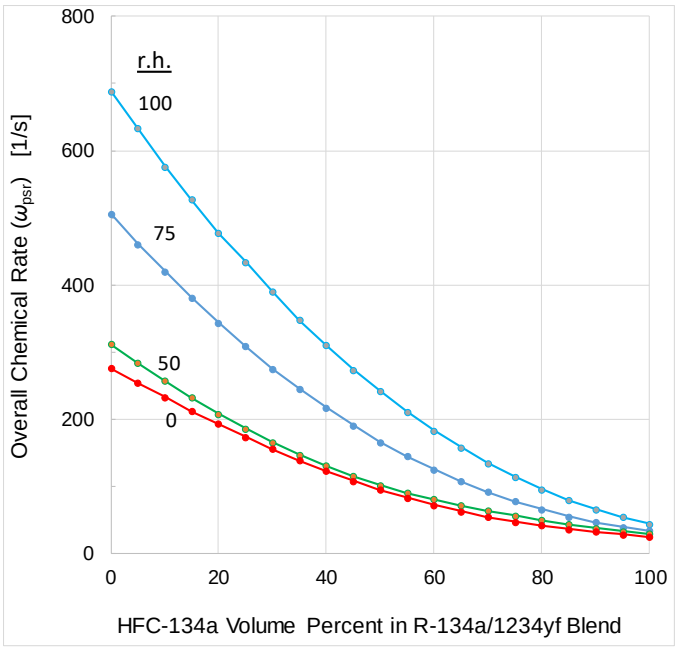

Figure 3.2-10. Peak (over all ϕ for each blend) chemical reaction ω_{psr} as a function of volume fraction of HFC-134a in the blend of R-1234yf/134a. Individual curves are shown for varying water vapor in the air (0 %, 50 %, 75 % and 100 % r.h.)

The overall chemical rate ω_{psr} provides a useful metric for examining the flammability of refrigerant blends. It can be used to compare alternative flame-suppressant agents, examine their flammability with respect to concentration in the air, discern the effects of humidity, and compare with experimental results. It is used in the section below to interpret the experimental results in the E681 and JHPGL tests.

Figure 3.2-11 shows the explosion pressure in the JHPGL test vs. the Overall Chemical Rate ω_{psr} for data from the candidate blends ("×" markers) and the R-1234yf/134a blends ("○" markers) (from Table 3.2-1). Blue points have an ASHRAE Standard 34 Class 1 rating, and the blue box bounds the locus of those mixtures; the orange points are class 2L. As indicated, there is a good correlation between the explosion pressure and ω_{psr}. As described above, the three blends Tern-1, R-513A, and R-450A have about the same explosion pressure and ω_{psr}. The blend R-515B, while it has a Class 1 rating, is likely at the limit of this rating because the 70/30 R1234yf/134a blend is just at the Class 1 limit (i.e., 72/28 and 74/26 had flame angles > 90° and hence were not Class 1). Thus, the three metrics, ASHRAE Standard 34 rating, JHPGL test explosion pressure, and ω_{psr} are related as shown in Figure 3.2-11. For a Class 1 rating, the explosion must be less than 1.41 bar ±0.14 bar and $\omega_{psr} < 166\ s^{-1}$. The important point is that ω_{psr} is a parameter based in physics that can be calculated for a mixture and can be used to correlate experimental flammability results between test methods, or with full-scale test results.

Interpretation of Results with Regard to the Full-Scale Live-Fire Tests. As shown in Figure 3.2-11, the JHPGL test explosion pressure and ω_{psr} are useful scales for characterizing blends. The next step is to understand, for the live-fire tests, what degree of flammability is

acceptable. A straightforward way to do that would be do live-fire tests with mixtures of R-1234yf/134a at varying mole fractions of HFC-134a. The mixture ratio that provides non-flammable behavior in that test can be used with Figure 3.2-11 to quantify the corresponding JHPGL test explosion pressure limit and ω_{psr} limit.

The overall chemical rate ω_{psr} can also be used to explore other features of the blends. For example, Figure 3.2-12 shows ω_{psr} for the candidate blends for different levels of water vapor in the air (0 %, 50 %, and 100 % r.h.) Data are shown for the nominal blend (Nom), worst-case fractionation WCF (from uncertainty in the blend components), and worst-case fractionation for flammability WCFF (from different vaporization rates for leaking blend components of liquid agent at the WCF). As indicated, for most blends, the differences in Nom., WCF, and WCFF are small, except for the case of R-450A, for which the WCFF is quite different from the WCF (although the Class 1 rating is still maintained for the WCFF). In the DOD application, the concern is with rapid loss of refrigerant charge, so WCF is the mixture of interest. A humidity level of 50 % r.h. was selected for the JHPGL tests as listed in the comparisons in Table 3.2-1. Nonetheless, as discussed for the R-1324yf/134a blend in Figure 3.2-10, Figure 3.2-12 shows that for the candidate blends, although there is predicted to be a small effect of humidity at 50 % r.h., there is predicted to be a large effect of humidity at 100 % r.h.

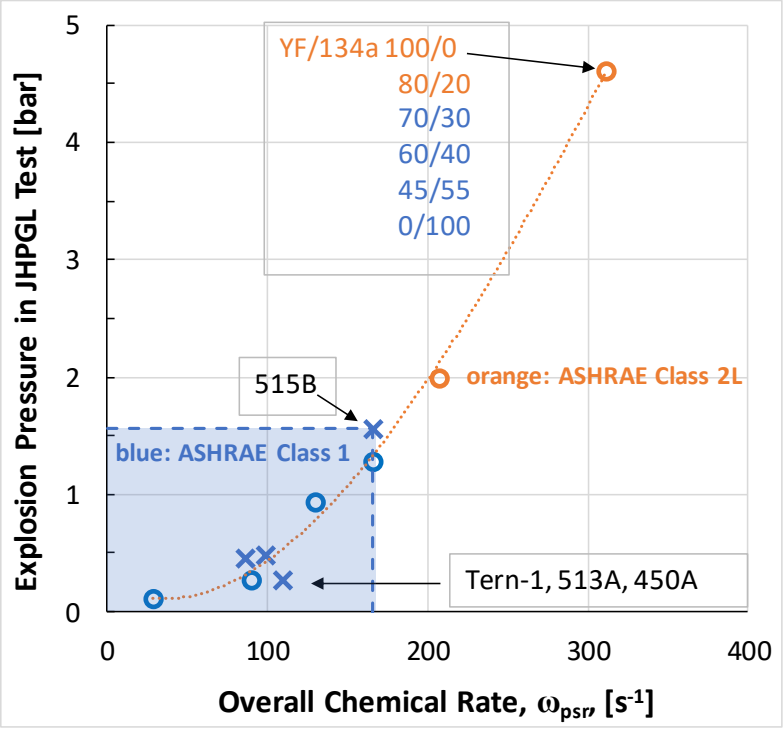

Figure 3.2-11. Explosion pressure in the JHPGL test vs. overall chemical reaction ω_{psr} (both peak over all ϕ) for R-513A, R-450A, R-515B and the Tern-1 blend and the R-1234yf/134a blends at increasing HFC-134a volume fraction. Dotted line is a polynomial fit to all the data to aid in visualization. (Initial conditions: 296 K, 101 kPa, 50 % r.h.)

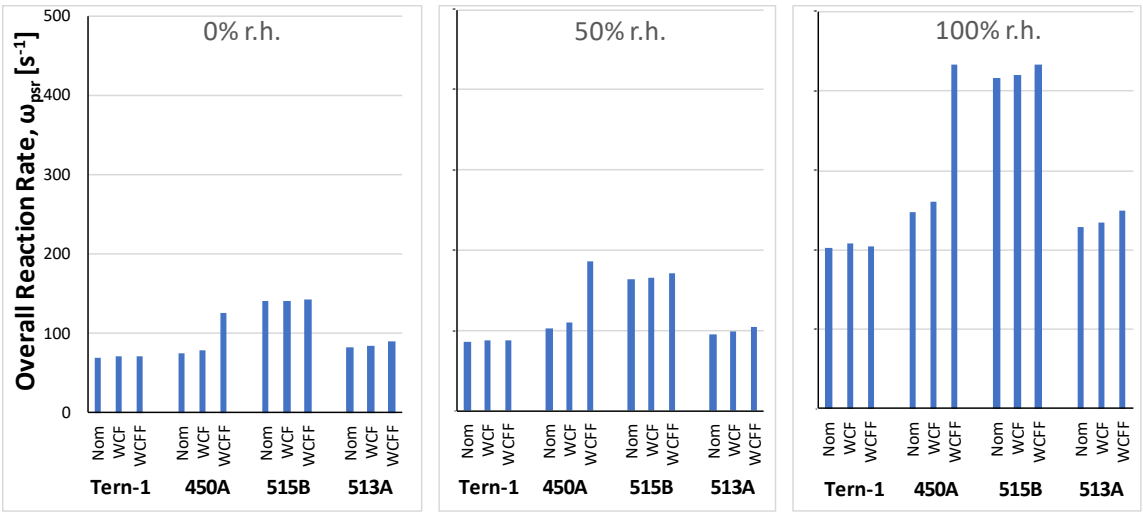

Figure 3.2-12. Peak (over all ϕ for each blend) chemical reaction ω_{psr} for R-513A, R-450A, R-515B and the NIST blend. Data are shown for the Nominal, WCF, and WCFF compositions in air (T = 296 K) and 0 %, 50 %, and 100 % r.h.

3.2.5. Coordination with Full-Scale Testing

The live-fire tests at ARL have been delayed due to COVID-19 related shutdowns. NIST will work with the engineers at ARL to provide input on potentially useful tests to conduct, as well as provide interpretation using the computational tools that have been developed. For example, based on the results to date:

1. The three blends, Tern-1, R-513A, and R-450A are expected to behave similarly and have the most promising behavior with respect to flammability. R-515B, while nonflammable in the E681 test, it is close to the border of flammability.
2. Levels of humidity above 0.014 moles H_2O/mole air (50 % r.h. at 23 °C) may significantly increase the flammability of the blends.
3. HFC-134a should be tested at high ambient temperature and high humidity as a benchmark. Following that, tests with increasing amounts of added HFO-1234yf would be very valuable.

Recommendations concerning a proposed test matrix with ARL engineers will be discussed. The results of the present tests and calculations will be used as input. The goal is to minimize the number of full-scales tests while extracting as much information as possible from the tests. It is possible that the ASHRAE Standard 34 Class 1 flammability rating will be sufficient to ensure non-flammability in the live-fire tests. It is also possible that a more stringent criterion, for example something close to the behavior of Tern-1, R-513A and R-450A in Figure 3.2-11 ($P_{max} < 0.3$ bar and $\omega_{psr} < 110$ s^{-1}) will be required. With a few live-fire tests, it should be possible to bound and understand the problem, and additional tests would provide higher levels of confidence in the findings and conclusions.

3.2.6. Summary of Flammability Work to Date

All of the four candidate blends are non-flame propagating in the modified E681 test specified in ASHRAE Standard 34. In a more stringent test, the Japanese high-pressure gas law test (JHPGL), the explosion pressure in a 2 L combustion chamber with a fused platinum wire ignition source, is used as a metric for flammability. Three of four candidate blends (Tern-1, R-513A, R-450A) had similar pressure rise (0.451, 0.474, and 0.262 bar), while one (R-515B) had a higher pressure rise (1.56 bar). Tests with binary blends of HFC-134a and HFO-1234yf with increasing fraction of HFC-134a showed that an HFC-134a mole fraction of 0.30 was required to pass the E681 tests, and at this composition, the explosion pressure in the JHPGL test was 1.27 bar. Hence, it appears that the R-515B blend is close the edge of passing the E681 test, while the other blends pass the test more easily.

A recently developed and validated kinetic model of combustion for one-, two-, and three-carbon HFC and HFO refrigerants was further improved and validated. For this purpose, burning velocity data were obtained in the 2 L chamber from the rate of pressure rise (using a spark ignition system). For binary blends of R-152a/134a and R-152a/1234yf, the experimentally derived burning velocity agreed well with the predictions from detailed numerical simulations. This adds confidence to the kinetic model.

The kinetic model was subsequently used to estimate the overall chemical reaction rate of the candidate blends. Both the E681 flame propagating/non-propagating boundary, as well as the JHPGL test explosion pressure were well correlated with the calculated overall reaction rate for each blend. The overall reaction rate is easily calculated for any arbitrary mixtures of interest. It is a fundamentally based parameter that can be used to correlate experimental flammability results between test methods, or with full-scale test results.

An important question is how well the live-fire tests at the Army Research Laboratory will compare with the small-scale E681, the JHPGL tests, and the calculated overall rate. It is unclear *a priori* if the live-fire tests will require lower or higher levels of flammability than the E681. For example, turbulence can increase flame speed of premixed flames, but high velocities can strain flames and extinguish them. If live-fire tests can be conducted for the mixtures of HFC-134a/HFO-1234yf at increasing mole fraction of HFC-134a until acceptable flammability occurs, it will presumably be possible to correlate the behavior in the three metrics (E681, JHPGL test, and calculated overall reaction rate), greatly reducing the number of required tests and increasing the information available from each test.

3.3. Task 3: Testing of Selected Blends in a Mini-Breadboard Heat Pump

The Mini-Breadboard Heat Pump (MBHP) was used to experimentally evaluate HFC-134a and four candidate low-GWP blends: R-513A, R-450A, R-515B, and Tern-1. Section 3.5.2 details how these blends were selected. The purpose of these tests was to validate the CYCLE_D-HX simulation model[52, 53] used in the limited-scope project[1] and qualify the three 'best' blends for testing in a military ECU (Task 7).

Note the MBHP measurements were de facto 'drop-in tests' and do *not* show the absolute performance potential for each fluid, since the MBHP hardware was not optimized for each fluid. The limited-scope project simulations included hardware optimized for each fluid, and thus provide a more equitable fluid comparison.

3.3.1. Test Apparatus

The NIST MBHP is a laboratory, modular heat-pump system for measuring performance of refrigerants. This system is extensively instrumented. The refrigerant circuit includes a variable-speed, oil-lubricated, reciprocating compressor powered by an electric motor and inverter, where the speed controls cooling/heating capacity. The evaporator and condenser are single circuits (no parallel tube branches). The heat exchangers' size can be adjusted by changing the number of active refrigerant tubes, which enables control of the heat flux. The evaporator and condenser are of the annular design arranged in the counter-current configuration; the refrigerant flows in the enhanced inner tube (copper), while the heat-transfer fluid (HTF) flows in the smooth annular space. An electronic expansion valve (EEV) regulates the evaporator-exit superheat. A liquid-line/suction-line heat exchanger (LLSL-HX) can be optionally included in the refrigerant circuit. The small internal volume of this apparatus facilitates testing fluids that are only available in small quantities. A chiller removes heat from the condenser, and a water heater applies a load to the evaporator. More details about the test apparatus are available in [55].

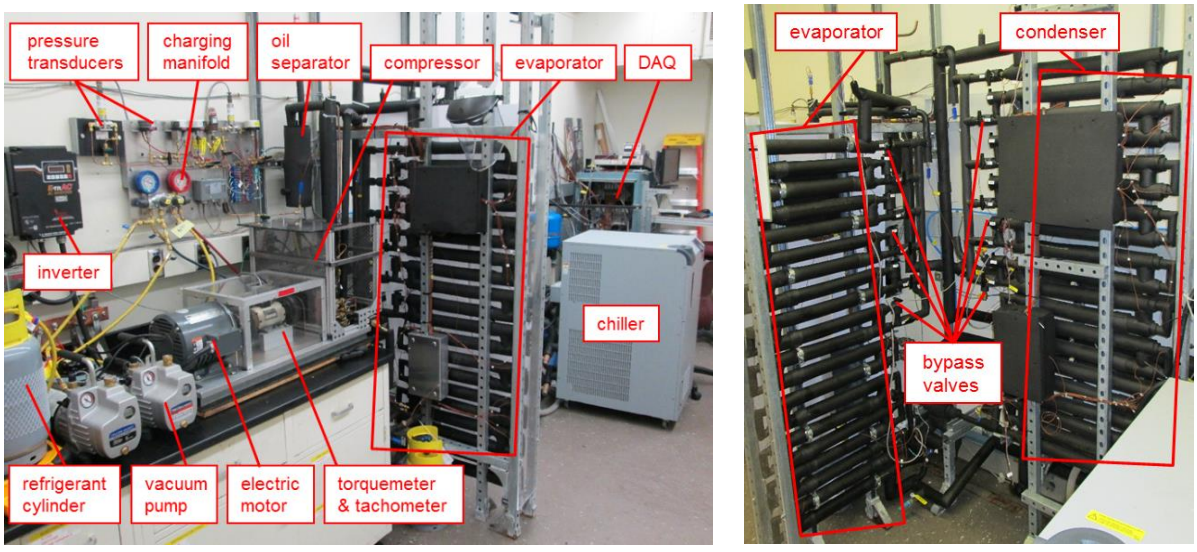

Figure 3.3-1. Photos of the MBHP test apparatus.

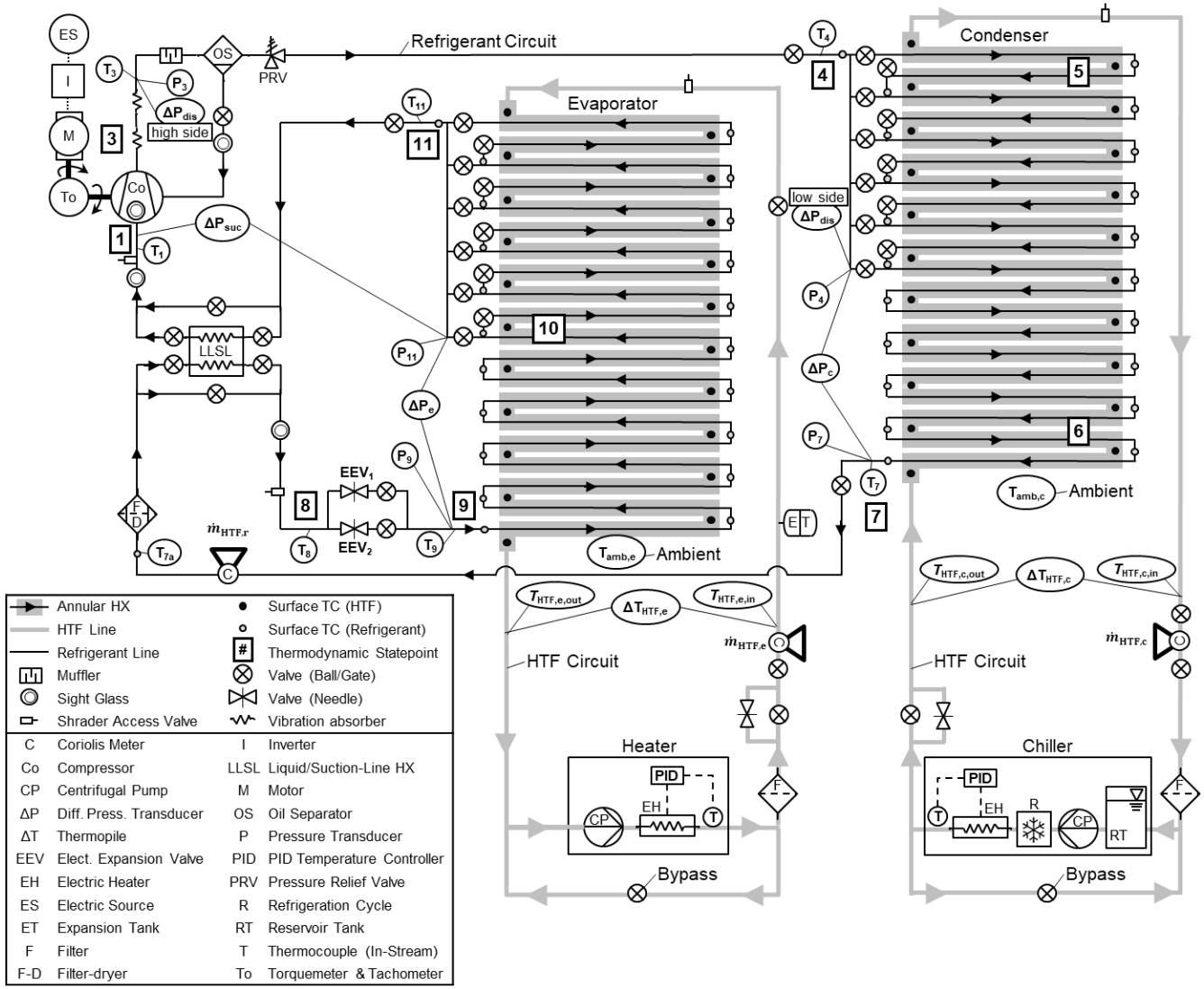

Figure 3.3-2. Schematic of the MBHP test apparatus.

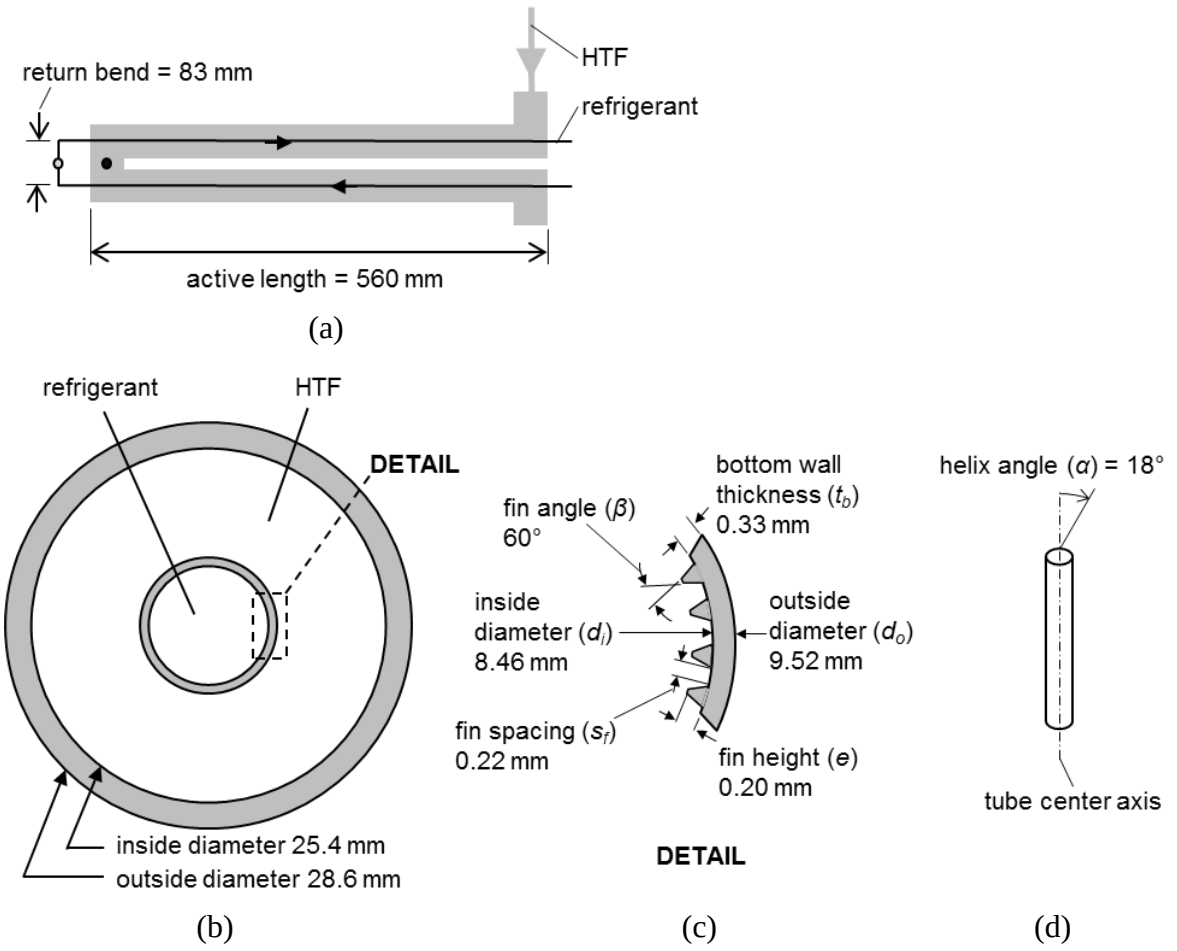

Figure 3.3-3. MBHP: Schematics of annular heat exchanger including (a) refrigerant tube lengths, (b) cross section of annular heat exchanger, (c) detailed cross-section of microfin tube, and (d) helix angle of microfins.

3.3.2. Test Protocol

The first baseline tests with HFC-134a established the control parameter settings required to reach the operating targets listed in Table 3.3-1. The HTF inlet temperatures were set to achieve refrigerant average saturation temperatures of 40 °C in the condenser and 8 °C in the evaporator, which are typical for air-source heat pumps operating at the Cooling A rating test [54]. The compressor speed was controlled to generate a cooling capacity of 1.5 kW. Condenser and evaporator dewpoint temperature drops of 2 K were targeted since the CYCLE_D-HX model showed the HFC-134a mass flux was optimal under these conditions (the mass flux was high enough for good heat transfer but with only moderate pressure drop penalty). These dewpoint temperature drops were also used in the limited-scope project[1]. These dewpoint temperature changes were obtained using 10 evaporator tubes and 16 condenser tubes. A refrigerant charge of 1420 g produced the targeted subcooling of 5 K. Extensive tests showed that an evaporator-exit superheat of 15 K yielded the best repeatability for the system without the LLSL-HX. A lower evaporator-exit superheat of 8 K was used with the LLSL-HX to achieve nominally equivalent compressor suction superheat (which correlated to repeatability), and because the lower superheat resulted in lower LLSL-HX energy

imbalance. The condenser HTF was distilled water and the evaporator HTF was a potassium formate brine (Dynalene HC40) whose capacitance was measured and reported in [55].

After establishing the baseline conditions and heat exchanger sizes, HFC-134a and the four replacement candidates were tested at varied capacity (Table 3.3-2, Table 3.3-3) to quantify performance over a range of heat and mass fluxes, for a total of 121 tests. Test conditions were repeated to quantify representative average performance and to bring the 95 % confidence for COP to the (0.5 to 1.0) % range, where the variation was largely driven by test-to-test differences in compressor efficiency (more details given in Section 3.3.4). The tests were primarily carried out at (1.3, 1.5 and 1.7) kW capacity. Additional tests at higher capacities of (1.9 and 2.0) kW were also performed for HFC-134a, R-513A, and R-450A, but these two test points were abandoned for Tern-1 and R-515B because it became clear the refrigerant mass flux and pressure drop too high to represent realistic conditions for a system with optimization of evaporator and condenser refrigerant tube circuitry.

The condenser and evaporator HTF inlet temperatures and number of tubes were fixed for all tests at the values established in the baseline tests. For every test the compressor speed was set to reach the target capacity, and the refrigerant charge was adjusted to achieve the target subcooling. All fluids were tested with and without the LLSL-HX. Energy imbalance between the refrigerant and HTF in the condenser and evaporator was less than 5 %.

Table 3.3-1. MBHP: HFC-134a baseline test operating targets and control parameters.

#	Operating parameter target	Value	Control Parameter	Value
1	Avg. saturation temp - cond.	40 °C	HTF inlet temp: cond.	32.7 °C
2	Avg. saturation temp - evap.	8 °C	HTF inlet temp: evap.	28.0 °C
3a	Cooling capacity (w/o LLSL-HX)	1.5 kW	Compressor speed (w/o LLSL-HX)	14.5 Hz
3b	Cooling capacity (w/ LLSL-HX)	1.5 kW	Compressor speed (w/ LLSL-HX)	13.5 Hz
4	Dewpoint temp. drop - cond.	2 K	Number of tubes: cond.	16
5	Dewpoint temp. drop – evap.	2 K	Number of tubes: evap.	10
6	Subcooling	5 K	Refrigerant charge	1420 g
7a	Superheat – w/o LLSL-HX	15 K	EEV opening	--
7b	Superheat – w/ LLSL-HX	8 K	EEV opening	--

Table 3.3-2. MBHP: Test targets and parameters.

Parameter	Unit	Tol.	Value				
Cooling capacity	kW	±2 %	1.3	1.5	1.7	1.9	2.0
HTF temperature change: evap.	K	±0.02	8.67	10.00	11.33	12.67	13.33
HTF inlet temp: cond.	°C	±0.2			32.7		
HTF inlet temp: evap.	°C	±0.3			27.9		
HTF flowrate: cond.	g/s	±0.3			97.6		
HTF flowrate: evap.	g/s	±0.3			56.3		
Number of tube circuits: cond.	--	--			1		
Number of tube circuits: evap.	--	--			1		
Number of tubes: cond.	--	--			16		
Number of tubes: evap.	--	--			10		
Subcooling: cond. out	K	±0.5			5		
Superheat: evap. out (w/ LLSL-HX)	K	±1.0			15		
Superheat: evap. out (w/o LLSL-HX)	K	±1.0			8		
Energy imbalance: cond.	%	±5			0		
Energy imbalance: evap.	%	±5			0		

Table 3.3-3. MBHP: Executed test matrix.

	Cooling capacity [kW]				
	1.3	1.5	1.7	1.9	2.0
Fluid	Number of tests: without (with) LLSL-HX				
HFC-134a	4 (4)	4 (4)	4 (4)	4 (4)	3 (2)
R-513A	3 (2)	3 (2)	3 (2)	3 (2)	--
R-450A	4 (3)	4 (3)	4 (3)	1 (0)	--
Tern-1	4 (3)	4 (3)	4 (3)	--	--
R-515B	4 (3)	4 (3)	4 (3)	--	--

3.3.3. Model simulation of tests

CYCLE_D-HX is a semi-theoretical model that simulates performance of a vapor-compression cycle for specified temperature profiles of the heat source and heat sink. The evaporator and condenser refrigerant saturation conditions (e.g. temperature, pressure) can optionally be predicted based on physical models of the two-phase heat transfer and pressure drop. To utilize this feature, CYCLE_D-HX requires, as a preliminary step, simulating of a 'reference case' to calculate the thermal resistance on the HTF side and to establish

correlations for refrigerant heat transfer and pressure drop in the heat exchangers[52, 53]. The inputs for the 'reference case' simulation are based on measured data for the reference fluid and also include the geometry parameters characterizing the evaporator and condenser: refrigerant tube inner diameter and length, number of tubes, number of circuits, and indication of whether the tube is smooth or enhanced (Figure 3.3-3). Further, the model can leverage this feature to optimize refrigerant tube circuitry for each fluid, enabling the equitable comparison of fluid performance potential shown in the limited-scope project[1].

Each experimental test was simulated using CYCLE_D-HX to verify the model's predictive capability. Model inputs included measurements for: HTF inlet and outlet temperatures, refrigerant superheat and subcooling, compressor volumetric and isentropic efficiencies, pressure drops in the suction and discharge lines, and the target cooling capacity. The model then predicted the cycle thermodynamic states and the resulting COP and volumetric capacity (Q_{vol}). The model's tube circuit optimization feature was not used for simulation of the experimental tests since the tests had fixed evaporator and condenser tube circuitry (Table 3.3-2).

The baseline tests listed in Table 3.3-1 were the basis for two 'reference cases', one each for the cycle with and without the LLSL-HX. The use of two 'reference cases' was necessitated by the different superheats, 15 K and 8 K, respectively, used in the cycle without and with LLSL-HX, respectively. Relying on a single 'reference case' could result in inadequate performance predictions because CYCLE_D-HX, as a simplification, estimates the pressure drop and heat transfer in the superheat section based on the values calculated for the two-phase section. The effect of the superheat section is partially corrected for in the 'reference' HTF-side thermal resistance and refrigerant-side pressure drop multiplication factor. However, the accuracy of this correction diminishes if the superheat is different than that used to establish the 'reference', so we created two unique 'references' for tests with and without the LLSL-HX.

3.3.4. Test Results and CYCLE_D-HX Model Validation

It is critical to note that the MBHP measurements reported here were taken primarily for validating the CYCLE_D-HX simulation results from the limited-scope project[1], rather than to provide the absolute performance potential of the candidate low-GWP fluids. While the MBHP tests were controlled to achieve a similar heat flux through the evaporator (a key requirement for a fair experiment-based comparison of different fluids[56]), all MBHP hardware was fixed for all tests, which constituted 'drop-in' testing. Such testing may not affect the results significantly for fluids having similar volumetric capacities, however, its effect on results may increase exponentially for large disparities in Q_{vol}. In such a case, the system performance can be impacted to a significant degree through a performance degradation of the compressor and heat exchangers, which were optimized for the reference refrigerant. The CYCLE_D-HX validation concept relies on the assumption that if the model can correctly predict the MBHP 'drop-in' test results, it's predictions from the limited-scope project for optimized systems can be considered as verified.

Test Results. The HFC-134a replacement candidate's performances were evaluated based on cooling COP (Figure 3.3-4) and Q_{vol} (Figure 3.3-5). The COP and Q_{vol} data were correlated

to capacity with a linear regression, and the figures show the individual measurements (symbols), curve fits (short-dashed lines), 95 % confidence intervals of the fit (long-dashed lines). When fluid is described here as having higher tested COP (or Q_{vol}) than another fluid, the curve fit value is higher, and the confidence intervals don't overlap. If the confidence intervals overlap, the average performances of the fluids have no statistical difference (NSD).

The following results summary applies to both tests without and with the LLSL-HX:

- COP (Figure 3.3-4)
  - HFC-134a had higher COP than all replacement candidates for all capacities.
  - R-515B had lower COP than all other fluids for all capacities.
  - At 1.3 kW, R-513A, R-450A, and Tern-1 had NSD in COP.
  - At (1.5 and 1.7) kW, R-513A and Tern-1 had NSD in COP, but both had higher COP than R-450A.
- Q_{vol} (Figure 3.3-5)
  - HFC-134a and R-513A had the highest Q_{vol} (NSD between them), followed by Tern-1, R-450A, and R-515B.

For all tests the LLSL-HX increased COP and Q_{vol} by about (8 to 10) %.

The lower performance of R-450A and R-515B can be mostly related to their lower Q_{vol}, 13.3 % and 26.2 %, respectively, in relation to HFC-134a. The COP lines for R-450A and R-515B (Figure 3.3-4) reflect the trends in compressor isentropic efficiency (Figure 3.3-6). The lower Q_{vol}, and sometimes lower compressor volumetric efficiency (Figure 3.3-7), required higher compressor speeds for R-450A and R-515B (Figure 3.3-8). The associated increase in frictional losses caused the compressor isentropic efficiency to be low. The MBHP measurements also showed a larger pressure drop for these two blends compared to the other fluids tested, especially in the evaporator. Note these data do not constitute the absolute potential for R-450A and R-515B since the MBHP hardware was not optimized for these fluids. The approach used in the limited scope simulation study[1] gave a more fair comparison of fluid performance potential, since all fluids were evaluated with the same compressor isentropic efficiency and the heat exchanger circuitry was optimized for each fluid.

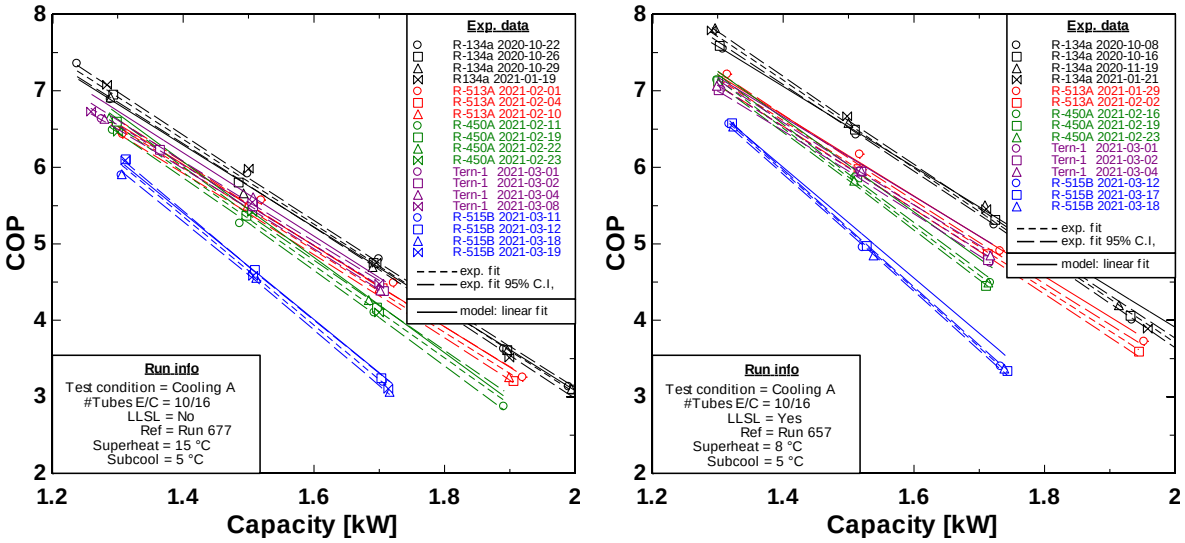

Figure 3.3-4. Cooling COP for HFC-134a and the replacement candidates (a) without LLSL-HX and (b) with LLSL-HX.

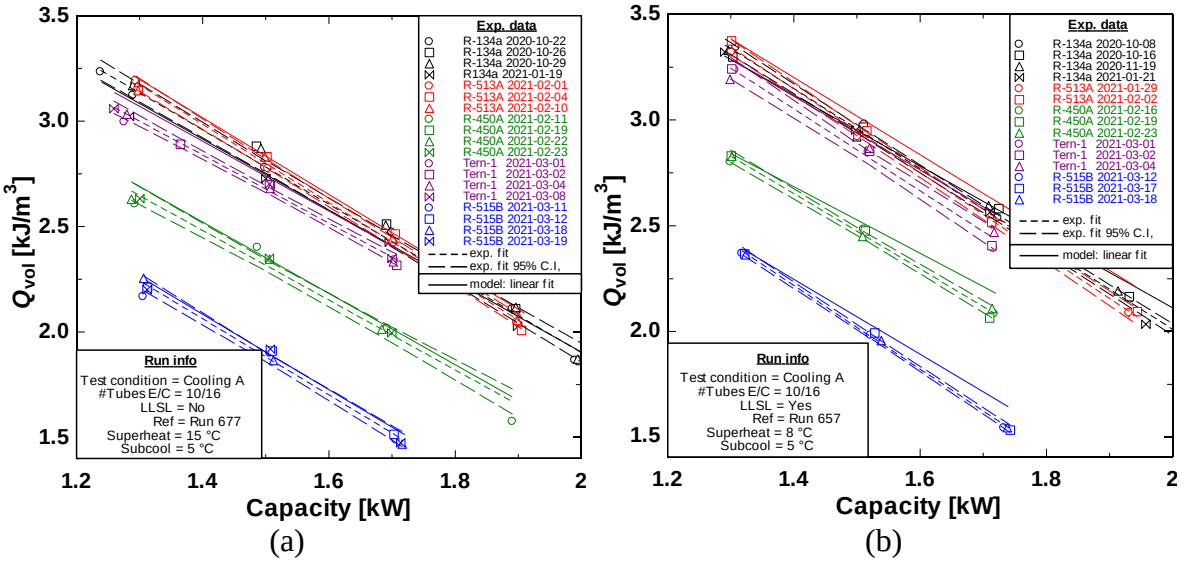

Figure 3.3-5. Cooling volumetric capacity for HFC-134a and the replacement candidates (a) without LLSL-HX and (b) with LLSL-HX.

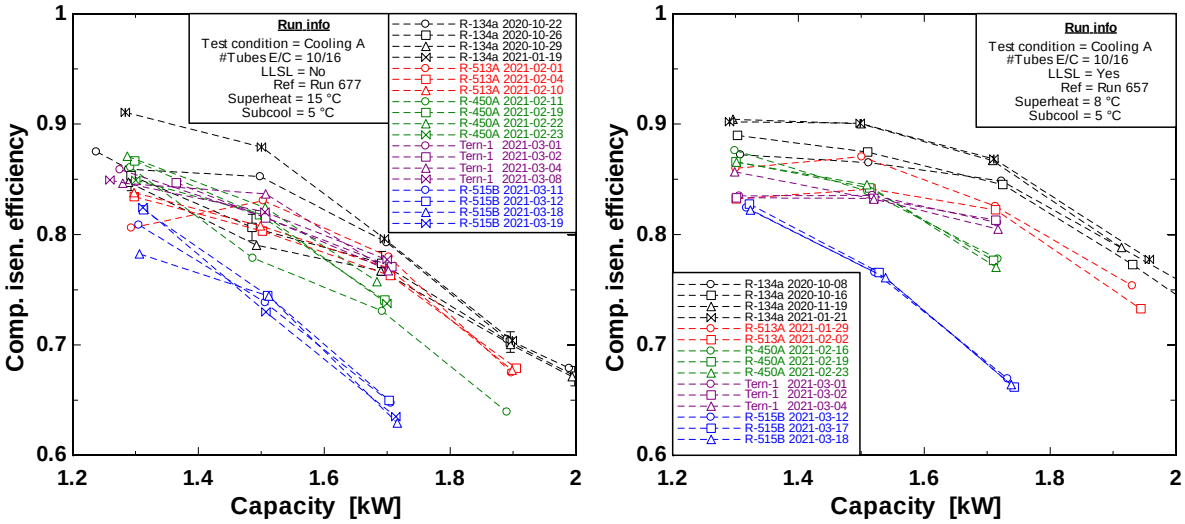

Figure 3.3-6. Compressor isentropic efficiency (a) without LLSL-HX and (b) with LLSL-HX.

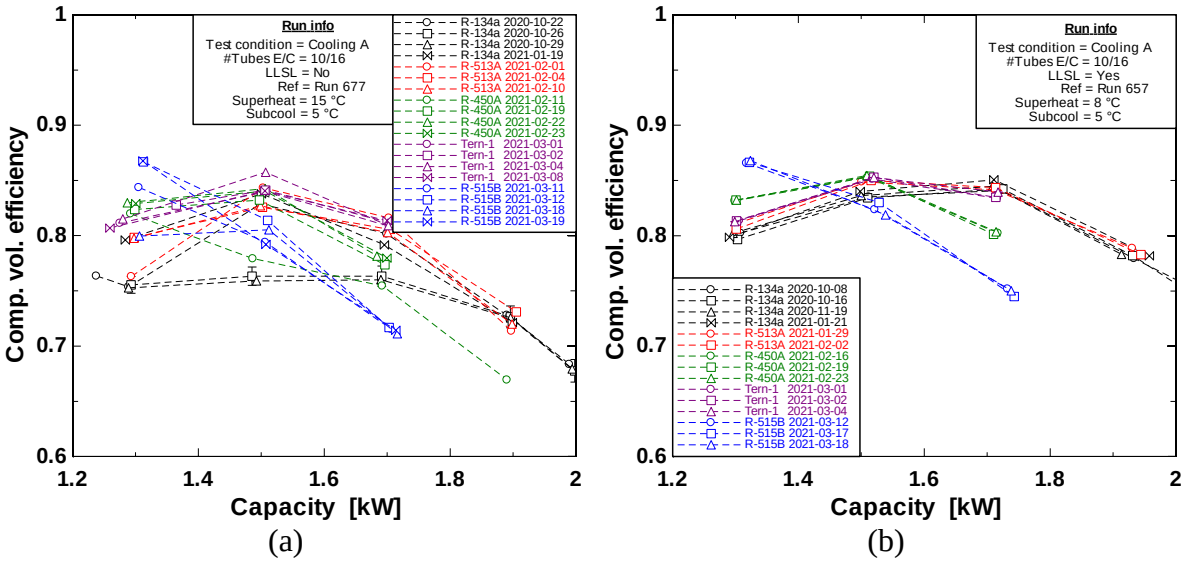

Figure 3.3-7. Compressor volumetric efficiency (a) without LLSL-HX and (b) with LLSL-HX.

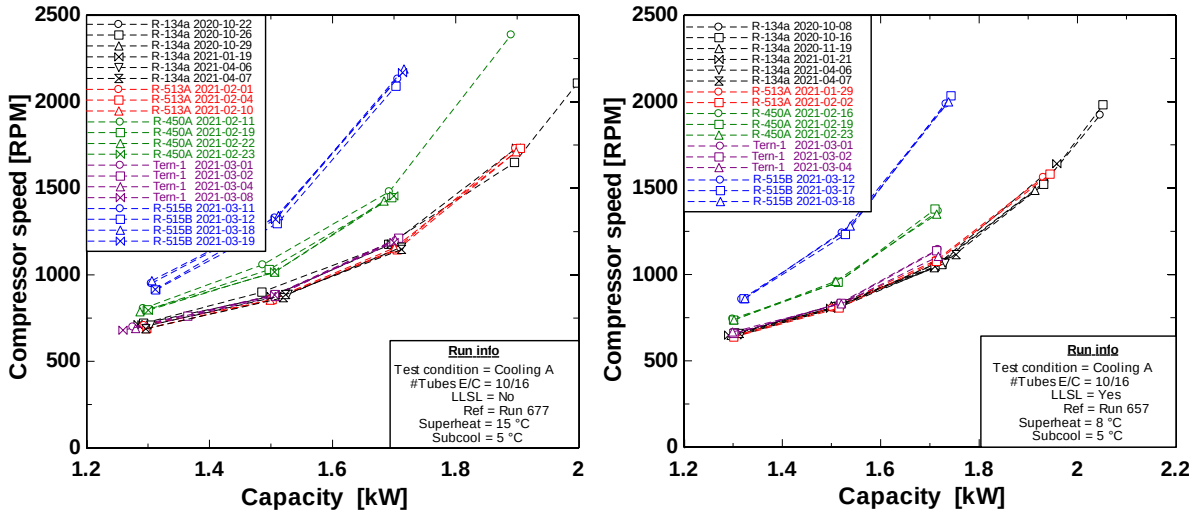

Figure 3.3-8. Compressor speed (a) without LLSL-HX and (b) with LLSL-HX.

Model Validation. The CYCLE_D-HX simulation COP and Q_{vol} predictions were also correlated to capacity using linear regression (solid lines on Figure 3.3-4 and Figure 3.3-5). For the tests without the LLSL-HX, the model-predicted values were within the confidence intervals of the experimental results, within about ±1.5 % of the curve fit. The predictions for Tern-1 were an exception, where the model overpredicted the experimental data by about 3 %. For the tests with the LLSL-HX, the CYCLE_D-HX predicted the COP and Q_{vol} within the confidence intervals at 1.3 kW capacity. At 1.5 kW, the COP and Q_{vol} were overpredicted by (0 to 3) %, and at 1.7 kW the COP and Q_{vol} were overpredicted by (1 to 5) %.

Differences between the test data and the CYCLE_D-HX prediction are primarily attributed to the refrigerant heat transfer and pressure drop in the condenser and evaporator, since the thermodynamic property data for the tested fluids are well established and the other hardware performance parameters are input to the model based on each experimental test (including compressor efficiency, LLSL-HX effectiveness, suction & discharge line pressure drop, HTF temperatures, see Section 3.3.3). Using the R-450A tests without the LLSL-HX as an example, the pressure drop in the condenser and evaporator were predicted within about ±5 % (Figure 3.3-8(a1)), the condenser saturation and outlet temperatures were underpredicted by about 0.3 °C (Figure 3.3.-8(b1)), and the evaporator saturation and outlet temperatures were overpredicted by about 0.6 °C (Figure 3.3-8(c1)). Overpredicted evaporator temperatures indicate an underestimation of overall heat transfer resistance between the HTF and the refrigerant. The error is not likely in the thermal resistances of the tube wall conduction and HTF convection, since the heat exchanger size and flow were fixed and empirically determined from the baseline tests and included in the model 'reference case' data. So, we infer the culprit was an underpredicted refrigerant flow-boiling heat transfer resistance. The overpredicted condenser saturation temperature was attributed to an underprediction of refrigerant condensation heat transfer resistance, for similar reasons given for the evaporator. Some of the condenser saturation temperature difference is related to the difference in measured and predicted COP (which determines the amount of heat rejected in

the condenser), though this effect appears to be small since for R-450A the underpredicted condenser saturation temperature persists despite the nearly exact prediction of COP at 1.5 kW (Figure 3.3-4(a)).

The R-450A tests with the LLSL-HX highlight the effects of an underprediction in evaporator pressure drop. The evaporator pressure drop is predicted within ±1 % at (1.3 and 1.5) kW (Figure 3.3-5(a2)), and the evaporator saturation temperature was overpredicted by 0.6 °C (Figure 3.3-5(b2)). In contrast, at 1.7 kW capacity the pressure drop was underpredicted by 10 %, and the evaporator saturation temperature was overpredicted by 1.2 °C. Pressure drop in the evaporator causes a reduction in saturation temperature that is unfavorable to countercurrent heat exchange, requiring a lower saturation temperature to drive the heat transfer. So underpredicting pressure drop results in overpredicted saturation temperature and a subsequent overprediction of COP (Figure 3.3-4(b)) as expected from the Carnot efficiency of a heat pump operating with a underpredicted temperature lift. This overprediction of COP occurred despite an overprediction of condenser pressure drop of (0 to 15) %, indicating the evaporator pressure drop is more important for determining the cycle COP.

In summary, the CYCLE_D-HX model predicted the same relative COP and Q_{vol} ranking as the experimental data, giving confidence to the HFC-134a replacement candidate screening performed in the limited-scope project. All four low-GWP candidates are acceptable for testing in the ECU as none had significant deviations from modeled performance, excessive discharge temperatures, or other hardware-related problems.

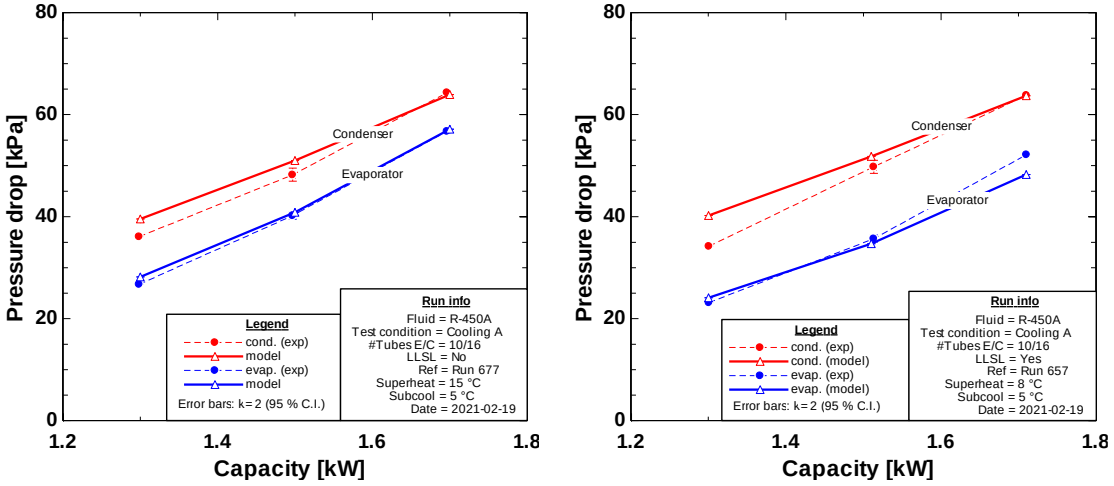

(a1) - without LLSL-HX (a2) - with LLSL-HX

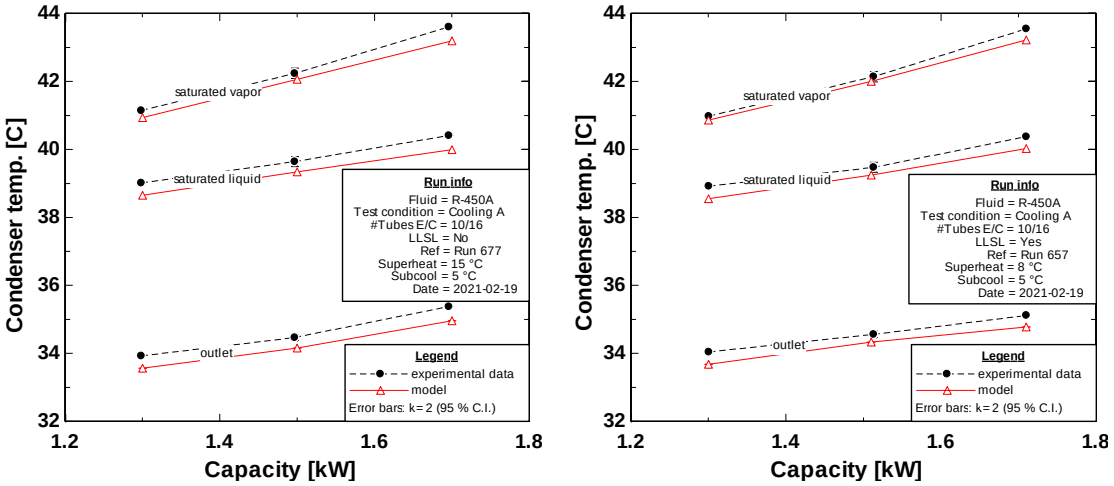

(b1) - without LLSL-HX (b2) - with LLSL-HX

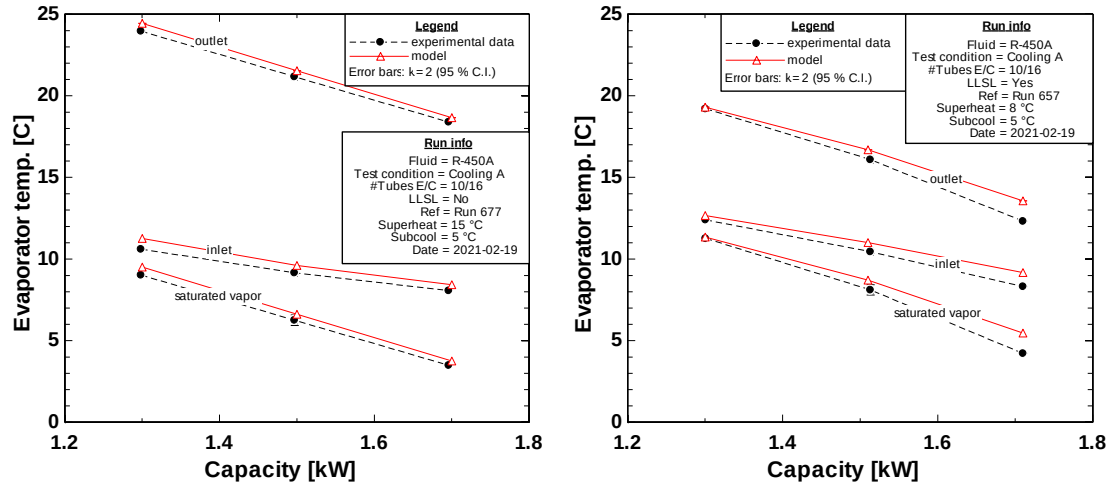

(c1) - without LLSL-HX (c2) - with LLSL-HX

Figure 3.3-9. R-450A measurement and model prediction of: (a) evaporator and condenser pressure drop, (b) evaporator temperatures, and (c) condenser temperatures.

3.4. Task 4: Refrigerant Forced-Convection Heat-Transfer Testing

Measured refrigerant flow boiling heat-transfer coefficients within a micro-fin tube are presented in this section for three low-GWP HFC/HFO refrigerant blends, R-513A, R-450A, and R-515B. A new correlation of the flow boiling heat-transfer coefficient, including data for previously measured HFC-134a[57], is presented. The micro-fin tube is a good choice for experimentation because this type of enhancement is ubiquitous in unitary equipment. Measurements were made to validate and improve the existing NIST evaporation correlation to include HFC/HFO blends for application in heat exchanger and air-conditioning system simulation tools.

3.4.1. Test Apparatus

Figure 3.4-1shows a sketch of the experimental apparatus used to establish and measure convective boiling heat transfer coefficients. The experimental test facility consisted of two main systems: the refrigerant loop and the water loop. The refrigerant flow rate, pressure, and quality were fixed at the inlet to the test section. The water flow rate and the inlet temperature were fixed to establish the overall refrigerant quality change in the test section. The water temperature drop, the tube wall temperature, the refrigerant temperatures, pressures, and pressure drops were measured at several axial locations along the test section. These measurements were used to calculate the local heat-transfer coefficient for the micro-fin tube.

The test section consisted of a pair of 3.34 m long, horizontal tubes connected by a U-bend. A fixed test pressure was maintained by balancing the refrigerant duty between the subcooler, the test section, the preheater and the condensers. A magnetically coupled gear pump delivered the test refrigerant to the entrance of the test section as saturated, near zero quality liquid. Another magnetically coupled gear pump supplied a steady flow of water to the annulus of the test section. The inlet temperature of the water loop was held constant for each test with a water-chilled heat exchanger and variable electric heaters. The refrigerant and water flow rates were controlled by varying the pump speeds using frequency inverters. Redundant flow rate measurements were made with Coriolis flowmeters and with turbine flowmeters for both the refrigerant and water sides.

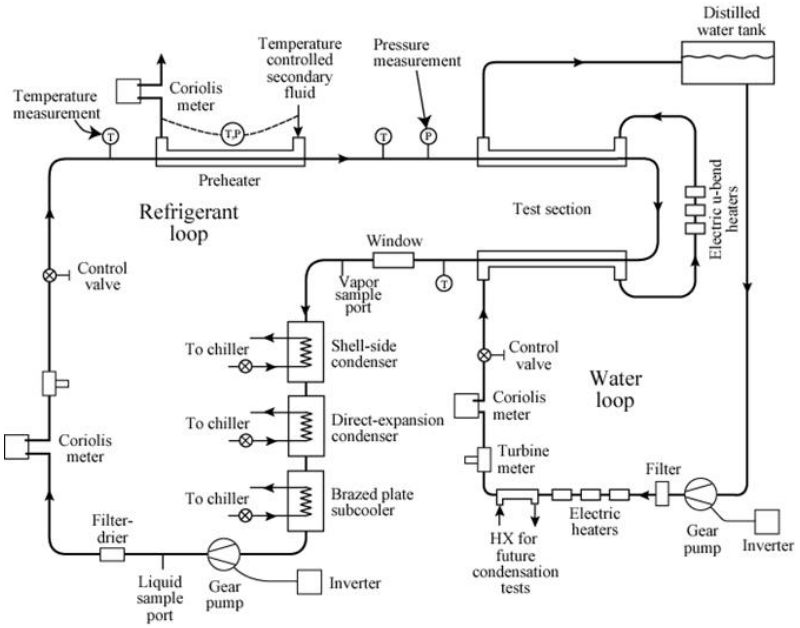

Figure 3.4-1. Schematic of flow boiling test apparatus.

Figure 3.4-2. shows a cross section of the test section with a detail of the micro-fin tube geometry. The test refrigerant flowed inside a micro-fin tube, while distilled water flowed either in parallel flow or counterflow to the refrigerant in the annulus that surrounded the micro-fin tube. Conducting some tests in parallel flow and others in counterflow (as shown in Figure 3.4-3.) produced a broad range of heat fluxes at both low and high flow qualities. The annulus gap was 2.2 mm, and the micro-fin tube wall thickness was 0.3 mm. The micro-fin tube had 60, 0.2 mm high fins that rifled down the axis of the tube at a helix angle (α) of 18° with respect to the tube axis. For this geometry, the cross-sectional flow area was 60.8 mm^2, giving an equivalent smooth diameter (D_e) of 8.8 mm. The root diameter of the micro-fin tube was 8.91 mm. The inside-surface area per unit length of the tube was estimated to be 44.6 mm. The hydraulic diameter (D_h) was measured with a polar planimeter from a scaled drawing of the tube cross section and determined to be approximately 5.45 mm. The ratio of the inner surface area of the micro-fin tube to the surface area of a smooth tube of the same D_e was 1.6.

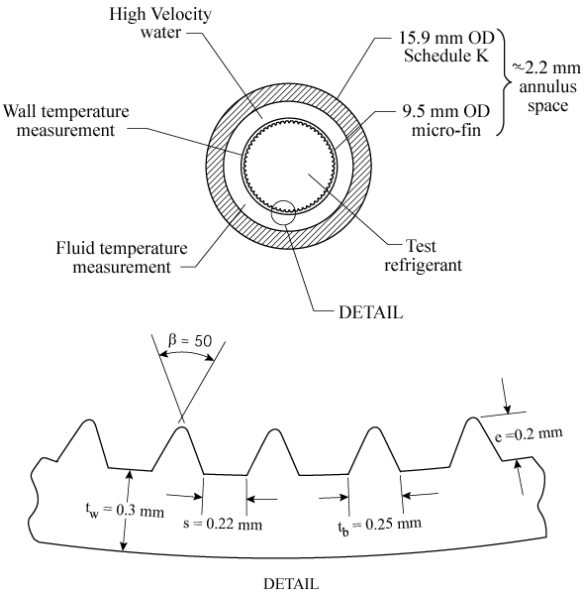

Figure 3.4-2. Cross section of flow-boiling test section.

Figure 3.4-3. provides a detailed schematic of the test section. The annulus was constructed by connecting a series of tubes with 14 pairs of stainless-steel flanges. This construction permitted the measurement of both the outer micro-fin wall temperature and the water temperature drop as discussed in the following two paragraphs. The design also avoided abrupt discontinuities such as unheated portions of the test section and tube-wall "fins" between thermopile ends.

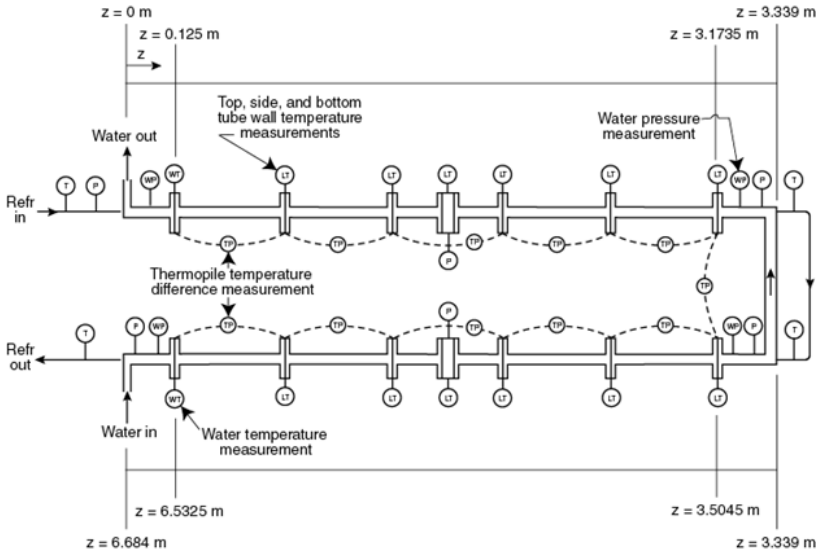

Figure 3.4-3. Detailed schematic of test section (counterflow)

Figure 3.4-3. shows that thermocouple wires pass between 12 of the gasketed flange pairs to measure the refrigerant-tube wall temperature at ten locations on the top, side, and bottom of the tube wall. These locations were separated by 0.6 m on average, and they were located near the intersection of the shell flanges. In addition to these, thermocouples were also

mounted next to the pressure taps near the middle of each test section length. The thermocouple junction was soldered to the outside surface and was sanded to a thickness of approximately 0.5 mm. The leads were strapped to a thin non-electrically-conducting epoxy layer on the wall for a distance of 14.3 mm before they passed between a pair of the shell flanges. The wall temperature was corrected for a heat flux dependent fin effect. The correction was typically 0.05 K. Figure 3.4-3. also shows that a chain of thermopiles was used to measure the water temperature drop between each flange location. Each thermopile consisted of ten thermocouples in series, with the ten junctions at each end evenly spaced around the circumference of the annulus. Because the upstream junctions of one thermopile and the downstream junctions of another enter the annulus at the same axial location (except at the water inlet and outlet), the junctions of the adjacent piles were alternated around the circumference. A series of Teflon half-rings attached to the inner refrigerant tube centered the tube in the annulus. The half-rings were circumferentially baffled to mix the water flow. Mixing was further ensured by a turbulent water Reynolds number[58].

As shown in Figure 3.4-3., six refrigerant pressure taps along the test section allowed the measurement of the upstream absolute pressure and five pressure drops along the test section. Two sets of two water pressure taps were used to measure the water pressure drop along each tube. Also, a sheathed thermocouple measured the refrigerant temperature at each end of the two refrigerant tubes, with the junction of each centered radially. Only the thermocouple at the inlet of the first tube was used in the calculations. The entire test section was wrapped with 5 cm of foam insulation to minimize heat transfer between the water and the ambient.

3.4.2. Data Analysis and Correlation Development

The convective boiling heat-transfer coefficient based on the actual inner surface area ($h_{2\phi}$) was calculated as:

$$h_{2\phi} = \frac{q''}{T_w - T_s} \tag{3.4-1}$$

where the measured wall temperatures (T_w) were fitted to their axial position (distance along the test section) to reduce the uncertainty in the measurement.

The average estimated expanded uncertainty of the wall temperature fit for all the measurements at the 95 % confidence level, was approximately 0.42 K and 0.36 K, for the counterflow and the parallel flow data, respectively. The median of the uncertainty in T_w was approximately 0.4 K.

The water temperature (T_f) was determined from the measured temperature change obtained from each thermopile and the inlet water temperature measurement. The water temperature gradient (dT_f/dz) was calculated with second-order finite difference equations using the measured water temperatures and their locations along the tube length z. The water temperature gradients were then fitted with respect to the tube length. The measured water temperatures typically agreed with the integrated fit of the water temperature gradient to within 0.2 K.

The fitted, local, axial water temperature gradient (dT_f/dz), the measured water mass flow rate ($\dot{m}$), and the properties of the water were used to calculate the local heat flux (q'') to the micro-fin tube based on the actual inner surface area:

$$q'' = \frac{\dot{m}_f}{p}\left(c_{p_f} \frac{dT_f}{dz} + v_f \frac{dP_f}{dz} \right) \tag{3.4-2}$$

where p is the wetted perimeter of the inside of the micro-fin tube. The specific heat (c_{pf}) and the specific volume (v_f) of the water were calculated locally as a function of the water temperature. The water pressure gradient (dP_f/dz) was linearly interpolated between the pressure taps to the location of the wall thermocouples. The pressure gradient term was typically less than 3 % of the temperature gradient term. The heat flux obtained by Eq. (3.4-2) was reduced by the amount of heat lost to the surroundings. The heat loss to the surroundings was obtained by calibration of single-phase heat-transfer tests, and it was based on the temperature difference between the room and the test fluid. Typically, the heat loss correction was less than a 0.1 % of that obtained from Eq. (3.4-2). The relative uncertainty of the heat flux measurement was less than 40 % of the measured value, while the average uncertainty for the counterflow and the parallel flow data was approximately 7 % and 20 % of the measured value, respectively.

The local Nusselt number (Nu) was calculated using the hydraulic diameter and the heat-transfer coefficient based on the actual inner surface area of the tube as:

$$\mathrm{Nu} = \frac{h_{2\phi} D_h}{k_l} \tag{3.4-3}$$

The uncertainty of Nu was between roughly 10 % and 40 %. Measurements of Nu with uncertainties greater than 30 % were discarded. Reduction in the uncertainty can be achieved with repeat measurements for the same operating conditions. However, repeat measurements are difficult to obtain due to the chaotic nature of two-phase flow and the many fixed parameters that need to be matched between measurements.

The 432 measured local convective boiling Nusselt numbers (Nu) for R-515B, R-450A, R-513A, and HFC-134a were compared to the pure-refrigerant (single component) version of the Hamilton et al. correlation[59]:

$$\mathrm{Nu_p} = 482.18\,\mathrm{Re}^{0.3}\,\mathrm{Pr}^{C_1}\left(\frac{P_s}{P_c}\right)^{C_2}\mathrm{Bo}^{C_3}\left(-\log_{10}\frac{P_s}{P_c}\right)^{C_4} M_w{}^{C_5} \tag{3.4-4}$$

where

$$C_1 = 0.51 x_q$$
$$C_2 = 5.57 x_q - 5.21 x_q^2$$
$$C_3 = 0.54 - 1.56 x_q + 1.42 x_q^2$$
$$C_4 = -0.81 + 12.56 x_q - 11.00 x_q^2$$
$$C_5 = 0.25 - 0.035 x_q^2$$

Here, the all-liquid Reynolds number (Re), the Boiling number (Bo), the liquid Prandtl number (Pr), the reduced pressure (P_s/P_c), and the quality (x_q) are all evaluated locally at the saturation temperature. The all-liquid Reynolds number and the Nusselt number are based on the hydraulic diameter (D_h). The Nusselt number is also based on the actual inner surface area of the tube.

Figure 3.4-4 plots the present measurements versus predicted values of the Nusselt number for R-515B, R-450A, and R-513A. Previously made measurements for R-450A[60] , R-513A[57] and HFC-134a[57] are also included in the comparison. The Hamilton et al. correlation[59] predicts approximately 43 % measurements to within ± 20 %.

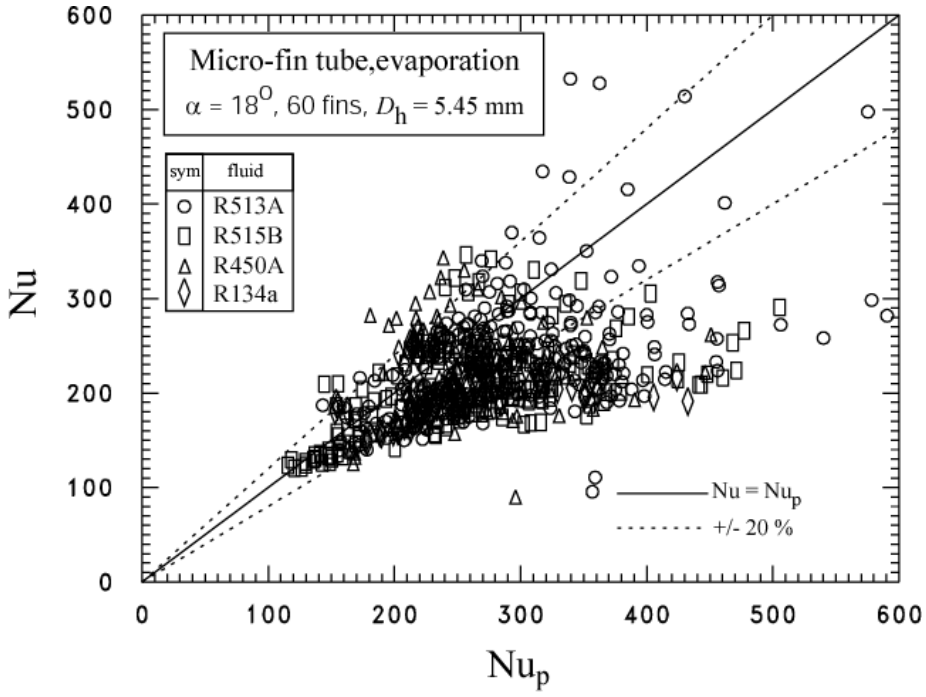

Figure 3.4-4. Comparison between measured Nusselt numbers and those predicted by the Hamilton et al. correlation[59].

A new correlation was developed to more accurately represent the current flow-boiling heat-transfer measurements:

$$\mathrm{Nu_p} = 242.5\,\mathrm{Re}^{0.26(1-x_q)}\,\mathrm{Bo}^{0.28}\,\mathrm{B_{nd}}^{-0.61x_q} \tag{3.4-5}$$

The new correlation (Eq. 3.4-5) predicts approximately 71 % of the measured convective boiling Nusselt numbers for R-515B, R-450A, R-513A, and HFC-134a to within approximately ± 20 % (Figure 3.4-5.). B_{nd} is the dimensionless Bond number[61], which includes fin geometry parameters and the surface tension as defined in the Nomenclature. The correlation is valid for Re between 1000 and 14000, Bo between 0.000002 and 0.001, and B_{nd} between 0.002 and 0.05. Equation (3.4-4) was developed with data where the refrigerant reduced temperature ranged between approximately 0.71 and 0.94.

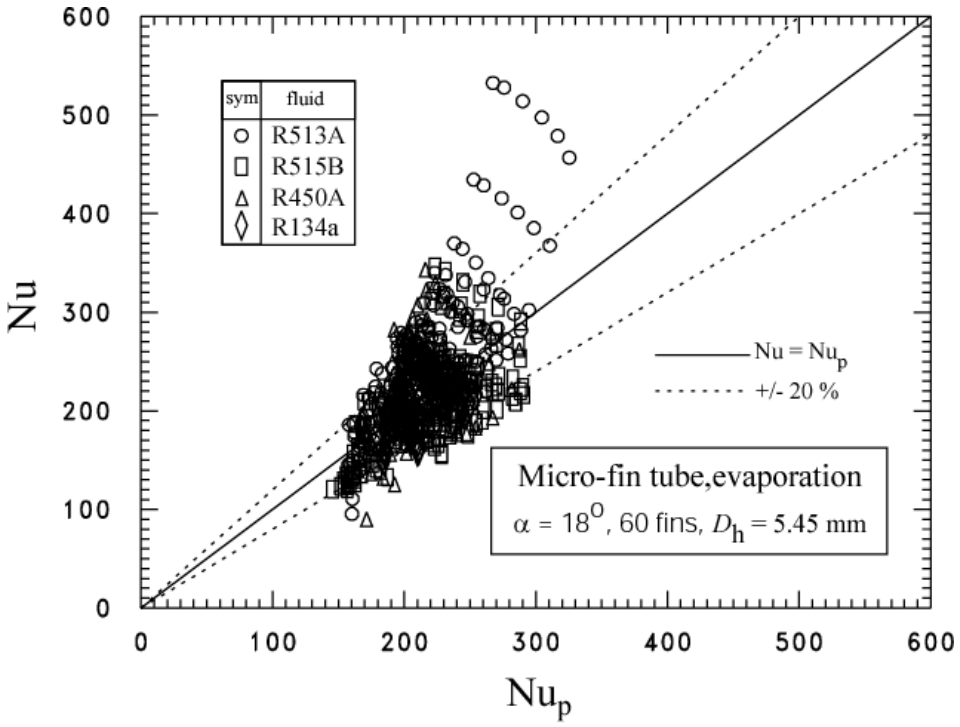

Figure 3.4-5. Comparison between measured Nusselt numbers and those predicted by the new correlation given by Eq. (3.4-5).

3.5. Task 5: Selection of Final Blends for Testing in Military ECU

3.5.1. Evaluation of "New" Fluids

The project plan calls for experimental evaluation of four blends in the MBHP (discussed earlier) to inform the selection of three 'best' blends for testing in the ECU. While cycle simulation results from the limited-scope project gave us a good basis for selecting 'best' blends, we continually monitored technical developments in low-GWP fluids to make sure that we did not overlook any promising new fluids.

A review of ASHRAE Standard 34 shows three new single-compound refrigerants that were classified since the completion of the analysis for the limited-scope project in 2017:

- HFO-1336mzz(E) ($CF_3CH=CHCF_3$), safety classification A1, NBP = 7.4 °C
- HFO-1132a ($CF_2=CH_2$), safety classification A2, NBP = –83 °C
- R-13I1 (CF_3I), safety classification A1, NBP = –21.9 °C

As indicated by its relatively high NBP, HFO-1336mzz(E) is a low-pressure refrigerant and not suitable for application in medium-pressure AC equipment, even as a blend component. The very low NBP of HFO-1132a, on the other hand, makes it unsuitable at the other extreme; in a blend it would result in high pressures and a significant temperature glide. HFO-1132a is also flammable.

Consideration of CF_3I. The NBP of CF_3I, on the other hand, is close to that of HFC-134a (–26.1 °C), which makes CF_3I, thermodynamically at least, a fluid warranting consideration. Its GWP is also very low; a relatively old study characterized its GWP as "likely to be very small, less than 5."[62] The appeal of CF_3I is further increased by its flame-suppression characteristics. A drawback of CF_3I is its reactivity, which would require the application of proprietary chemical stabilizers not available on the open market.

We spent a considerable analytical effort to formulate, within the constraints of publicly available data, a state-of-the-art representation of thermodynamic properties of both the pure fluid and blends containing CF_3I. This effort was summarized by Bell and McLinden.[63] We also added CF_3I to the screening developed under the limited-scope project in a search for the best performing CF_3I-based blends. Although the COP and volumetric capacity of the pure CF_3I was poor compared to HFC-134a, these simulations identified some blends of CF_3I with HFC-152a and HFC-32 as having potentially favorable performance. The high-performing blends, however, contained a low fraction of CF_3I. Specifically, for R-152a/CF_3I blends a mole fraction of HFC-152a of 0.80 (mass fraction of 0.57) yielded the same COP as HFC-134a. For blends with HFC-32, the corresponding mole fraction was 0.75 (mass fraction of 0.32). This led us to question whether such blends were still nonflammable.

The flame inhibition characteristics of CF_3I have been studied. We could find no information on the specific mixture of HFC-152a/CF_3I, but Yang et al.[64] report that CF_3I is substantially more effective than HFC-125 in inhibiting the flammability of HFC-32 (a minimum concentration of 0.0536 $kg \cdot m^{-3}$ for CF_3I versus 0.0984 $kg \cdot m^{-3}$ for HFC-125). We can use information on the blend R-410A (the blend of HFC-32 and HFC-125 at a mass composition of (50.0/50.0) and the blend R-466A (the blend of HFC-32, HFC-125, and CF_3I at a mass

composition of (49.0/11.5/39.5)) to formulate an informed guess on the flammability of HFC-152a/CF_3I) with the following reasoning. Both R-410A and R-466A are classified as A1 (i.e., nonflammable) and contain about 50 % of the flammable HFC-32 with a with a 50 % content of flame suppressing agents (i.e., HFC-125 and/or CF_3I). In the detailed report of flammability testing contained in the application to the Standard 34 committee[65] it is seen that R-466A exhibits a flame angle as large as 40˚ in the ASTM E681 test protocol under some conditions. This is "not flammable" under the E681 protocol (which defines "flammable" as a flame angle of 90˚ or larger), but it does indicate that R-466A was formulated close to the border of flammability. Given that HFC-152a is more flammable than HFC-32, a CF_3I fraction greater than 50 % would likely be required to suppress flammability, i.e., compositions that showed lower performance in the simulations.

There are also stability and toxicity concerns around CF_3I. Although having a safety classification of A1, CF_3I has a relatively low "refrigerant concentration limit" (RCL) of 2 000 ppm (i.e., a concentration in air of 0.2 % by volume).[66] This compares to an RCL of 50 000 ppm for HFC-134a.[12] The RCL considers a range of hazards and is "intended to reduce the risks of acute toxicity, asphyxiation, and flammability hazards in normally occupied, enclosed spaces."[12] The RCL impacts the maximum charge allowed in a particular system. We also note that in a review of the toxicity of CF_3I, the National Research Council recommended that it be used (as a fire suppressant) only in unoccupied spaces.[67] The chemical stability of the CF_3I molecule is substantially lower than typical HFC refrigerants, and it would require stabilizers for use in a refrigeration system. Such stabilizers have been developed, but they are proprietary. NIST engaged with a refrigerant manufacturer that was pursuing the development of CF_3I-containing refrigerant blends, such as R-466A, in an attempt to obtain samples of CF_3I and the necessary stabilizers. These negotiations were not successful.

Finally, a recent "roundtable discussion" published in *ASHRAE Journal* [68] illustrates that industry disagreed about the future of CF_3I and CF_3I blends. One company stated that "An emerging nonflammable (ASHRAE class A1) <750 GWP candidate, R-466A, is under heavy consideration by a number of manufacturers." And that "R-466A would be an ideal interim solution … until further innovation could lead to even lower GWP nonflammable alternatives." In contrast, a second company stated that R-466A was "in our opinion, questionable for stability and for compatibility with materials as a result of potential acid formation. This can lead to reliability, durability and performance problems over time." And "No major North American equipment or compressor manufacturers have announced or shared that they are developing equipment and component parts around this refrigerant. This suggests it is not presently viewed as a viable candidate."

Taking all of the above in its totality, we conclude that it is not feasible to include CF_3I at this point in time. The ultimate utility of CF_3I as a refrigerant remains an open research question.

Consideration of HFO-1132(E). In addition to the fluids noted above that were added to the ASHRAE standard another isomer of difluoroethene is currently being studied for use as a refrigerant:

- HFO-1132(E) (*trans*-1,2-difluoroethene), safety classification not assigned, NBP = –53 °C

The –53 ˚C boiling point of HFO-1132(E) is similar to that of R-410A (–51.5 ˚C), making it of high commercial interest. Limited data on this fluid are now becoming available.[69 70] HFO-1132(E) was one of the fluids identified in the comprehensive screening of McLinden et al.[71] that was in the category of "novel molecules" for which "few data could be found." The analysis of McLinden et al. was based on a predicted critical temperature of 370.5 K, which resulted in a low volumetric capacity relative to R-410A (which was the baseline for that study); this contrasts the recently measured critical temperature of 348.8 K,[70] which is similar to R-410A. Much of the research on HFO-1132(E) remains proprietary, making detailed simulations of its performance impossible at this time. Furthermore, it is flammable (likely ASHRAE classification of "2") and not commercially available. For these reasons, HFO-1132(E) was dropped from further consideration in this project.

3.5.2. Selection of Four Blends for Testing in Mini-Breadboard Heat Pump

The cycle simulation results from the limited-scope project were the primary basis for selecting 'best' blends for testing (Table 3.5-1). As noted in the previous section, no new fluids were identified that could be considered as viable blend components.

The criteria for blend selection consisted of the following parameters: (1) non-flammability ($\overline{\Pi} < 0$); (2) minimum GWP; (3) maximum coefficient of performance (COP); and (4) the volumetric capacity (Q_{vol}) matching that of the baseline HFC-134a. We also considered market availability as a practical parameter influencing our decision. Table 3.5-1 shows that the selection parameters of the competing blends are very close to each other. The following four blends, based on HFC-134a, HFO-1234yf, HFO-1234ze(E) and HFC-227ea, were selected for tests in the mini-breadboard heat pump:

- R-513A: [R-134a/1234yf (44/56*)], GWP = 573. R-513A was identified in our limited-scope study (blend # 2). Its ASHRAE safety classification is A1.
- R-450A: [R-134a/1234ze(E) (42/58*)], GWP = 547. R-450A was not specifically identified in the limited-scope study; however, its make-up and performance are similar to those for blend # 9. Its ASHRAE A1 safety classification and market availability provided a practical argument for its selection.
- Tern-1: [R-134a/1234yf/1234ze(E) (49.2/33.9/16.9*)], GWP = 640. This blend was identified in our limited-scope study (blend #4). It was formulated using the laboratory facilities at NIST-Boulder. We adopted the Tern-1 name here for convenience.
- R-515B: [R-1234ze(E)/227ea (91.1/8.9*)], GWP = 344. R-515B was not identified in the limited-scope study. We opted to include this blend because of its significantly lower GWP than those of other fluids. Considering that the preference for low-GWP fluids is expected to increase following the Montreal Protocol timetable for GWP reduction, it will be of interest to explore the performance potential of this somewhat lower-pressure blend than HFC-134a. According to our detailed cycle simulations, the COP of R-515B is within 2.6 % of HFC-134a. The volumetric capacity is 27 % lower, which can be mitigated by a compressor with a larger displacement.

* Composition stated in mass percent

Table 3.5-13.5-2. Selected "best" blends from the limited-scope project (sorted by GWP) [3]

	Components	Composition (molar)	GWP	$\bar{\Pi}$ *	COP/ $COP_{R\text{-}134a}$	Q_{vol}/ $Q_{vol,\ R\text{-}134a}$
	Class 1 nonflammable (predicted)					
1	R-134a/1234yf	0.44/0.56	537	-0.1	0.987	1.025
2	R-134a/1234yf**	0.468/0.532	573	-0.4	0.988	1.027
3	R-134a/1234yf/134	0.48/0.48/0.04	633	-1.1	0.987	0.975
4	R-134a/1234yf/1234ze(E)#	0.52/0.32/0.16	640	-1.2	0.987	0.989
5	R-134a/1234yf	0.52/0.48	640	-1.2	0.989	1.029
6	R-134a/1234yf/134	0.4/0.44/0.16	665	-1.3	0.986	0.958
7	R-134a/125/1234yf	0.44/0.04/0.52	676	-1.5	0.985	1.049
8	R-134a/227ea/1234yf	0.40/0.04/0.56	681	-1.5	0.984	1.007
9	R-134a/1234ze(E)	0.60/0.40	745	-2.4	0.988	0.908
10	R-134a/1234yf	0.60/0.40	745	-2.4	0.990	1.031
11	R-134a/1234ze(E)/1243zf	0.60/0.36/0.04	750	-1.5	0.990	0.966
12	R-134a/1234yf/1234ze(E)	0.64/0.2/0.16	799	-3.0	0.990	0.986
13	R-134a/152a/1234yf	0.64/0.04/0.32	817	-1.8	0.993	1.023
14	R-134a/1234yf/134	0.52/0.32/0.16	824	-3.2	0.990	0.966
15	R-134a/1234ze(E)	0.68/0.32	852	-3.7	0.991	0.929
16	R-134a/1234yf/1243zf	0.68/0.2/0.12	870	-1.1	0.994	1.020
	Class 2L flammable (predicted)					
17	R-152a/1234yf	0.08/0.92	8	7.7	0.98	0.957
18	R-134a/1234yf	0.20/0.80	238	2.8	0.98	0.996
19	R-134a/152a/1234yf	0.20/0.16/0.64	270	8.7	0.987	0.984
20	R-152a/1234yf/134	0.16/0.48/0.36	417	7.5	0.984	0.900
21	R-134a/1234yf	0.36/0.64	436	1.0	0.985	1.018
22	R-134a/1234yf/1243zf	0.36/0.44/0.20	451	5.2	0.988	1.004
23	R-134a/152a/1234yf	0.36/0.20/0.44	496	8.3	0.994	0.994

* Normalized flammability index [3,72]
** Designated by ASHRAE Std. 34 as R-513A; safety classification: A1.
\# Referred to as Tern-1

3.5.3. Selection of Three Blends for Testing in ECU

The tests conducted in the mini-breadboard heat pump on HFC-134a and the four blends validated the prediction capability of the CYCLE_D-HX model used in the limited-scope project thus confirming the relative merits of blends established earlier. Blends R-513A, R-440A, and R-515B have the ASHRAE safety designation A1 (low toxicity, no flame propagation). While Tern-1 does not have ASHRAE classification, it can also be considered an A1 blend, since its 'non-flammability' was confirmed by the ASTM E861 test prescribed in ASHRAE Standard 34, and its three components are classified as 'low-toxicity' fluids by this standard. It is uncertain at this time whether the ASTM E861 test is stringent enough for military requirements; since this issue has not been determined yet, we decided to use the ASHRAE flammability criteria in this study.

The following are the three blends we have selected for testing in the ECU in environmental chambers.

1. R-513A: [R-134a/1234yf (44/56)*], GWP = 573
   $COP/COP_{R\text{-}134a} = 0.988$; $Q_{vol}/Q_{vol,\ R\text{-}134a} = 1.027$
   This blend possesses a very good combination of three important attributes: its GWP is second to the lowest on our list; its COP is 1.2 % below $COP_{R\text{-}134a}$, which makes it the second top COP of blends with GWP < 750; and its volumetric capacity is the highest on our list, 2.7 % better than that of HFC-134a. In addition, this blend is an azeotrope and is commercially available.

2. Tern-1: [R-134a/1234yf/1234ze(E) (49.2/33.9/16.9)*], GWP = 640
   $COP/COP_{R\text{-}134a} = 0.987$; $Q_{vol}/Q_{vol,\ R\text{-}134a} = 0.989$
   Compared to R-513A, Tern-1 comprises 5.2 % more of HFC-134a and includes 16.9 % HFO-1234ze(E), which is less flammable (lower burning velocity) than HFO-1234yf. As a result, Turn-1 is expected to be farther away from the flammability boundary than R-513A (see Section 3.2.4) and is a more conservative choice should military criteria with respect to flammability become more rigorous (see Section 3.2.5). The simulated COP of Tern-1 is 1.3 % below $COP_{R\text{-}134a}$. The 1.1 % lower volumetric capacity than that for HFC-134a is a trivial difference.

3. R-515B: [R-1234ze(E)/227ea (91.1/8.9)*], GWP = 344
   $COP/COP_{R\text{-}134a} = 0.973$; $Q_{vol}/Q_{vol,\ R\text{-}134a} = 0.738$
   The main motivation to select this blend for further testing is its significantly lower GWP than those of other blends chosen. The data presented in Section 3.2.4 indicate that R-515B is closer to the flammability boundary than the other blends. Per CYCLE_D-HX simulations with optimized heat exchangers, the COP of this blends is lower than $COP_{R\text{-}134a}$ by 2.6 %, and the volumetric capacity is lower than $Q_{vol,\ R\text{-}134a}$ by 26.2 %, which would have to be mitigated by a larger compressor and some efficiency enhancing features. Despite these shortfalls, it is of interest to explore the performance potential of this low-pressure blend in case lower-GWP fluids become strongly preferred in the future. R-515B is an azeotrope and is commercially available.

By the above selection of three blends we propose to drop R-450A from further testing. The volumetric capacity of R-450A is 13.3 % lower than $Q_{vol,\ R\text{-}134a}$, so it is about half the way between $Q_{vol,\ R\text{-}134a}$ and $Q_{vol,\ R\text{-}515B}$. We are convinced that testing R-515B instead of R-450A will provide more useful data (performance of a low-pressure fluid), in particular that the measurements taken on the ECU with the selected blends will provide a broad spectrum of data for validating a detail ECU simulation model. The model then can be used for predicting performance of other fluids that were not included in the ECU tests.

*Composition stated in mass percent

4. Conclusions to Date

Task 1. We have carried out measurements on the thermophysical properties of refrigerant blends identified in the limited-scope project. For three blends (at two compositions each) we have completed comprehensive measurements comprising vapor-liquid equilibria (VLE), density (P, ρ, T, x), speed of sound, and thermal conductivity; these measurements covered a combined temperature range of 230 to 400 K, with pressures up to 50 MPa. For three additional blends (also at two compositions each) we have carried out only VLE measurements. The measurements were selected to provide an optimal data set for the purposes of fitting mixture property models, and these data have allowed us to improve the refrigerant mixture models needed for conducting the MBHP tests (Task 3), refrigerant two-phase heat-transfer tests (Task 4), and ECU tests (Task 7). While the improved property models will be important for these tasks, no major deficiencies were identified in the models used in the limited-scope project; in other words, the selection of "best blends" made in the limited-scope project remain valid. In the second phase of the project these data, along with literature data, will be used to develop a mixture model optimized for blends of low-GWP fluids, especially blends containing HFOs; this optimized model will be used in the detailed simulations of Task 7.

Task 2.
Specific interim conclusions are:

1. Three blends Tern-1, R-513A, and R-450A are of similar flammability, with R-450A slightly better. While R-515B is non-flammable by the E681 test, it is close to the border of flammability. If a Class 1 flammability rating via ASHRAE Standard 34 (i.e., based on the ASTM E681 test) is acceptable, then R-515B may be the best refrigerant, since it has lowest GWP. But this depends upon how the live-fire test compares to the E681 test.
2. The calculated overall reaction rate predicts that for the candidate blends, the effect of humidity in the air will be small for an increase from 0 to 50 % r.h., but large for 50 % r.h. to 100 % r.h. Thus, levels of humidity above 0.014 moles H_2O/mole air (50 % r.h. at 23 °C) may have large effects on the flammability of the blends.
3. HFC-134a should be tested at high ambient temperature and high humidity as a benchmark.
4. We suggest live-fire tests of HFC-134a with increasing amounts of added HFO-1234yf to enable correlation to the small-scale experimental and numerical results.

Task 3. The Mini-Breadboard Heat Pump (MBHP) was used to experimentally evaluate HFC-134a and four candidate low-GWP blends: R-513A, R-450A, R-515B, and Tern-1. The purpose of these tests was to: (1) validate the CYCLE_D-HX simulation model[52, 53] used in the limited-scope project[1], and (2) qualify the three 'best' blends for testing in a military ECU (Task 7). Cycle performance of each fluid was measured over a range of capacity including (1.3, 1.5, and 1.7) kW, where 1.5 kW was the rating point. The varying capacity provided measurements to verify the model's prediction ability over a range of mass and heat flux. Each capacity point was tested both without and with a LLSL-HX. The test-to-test variation, largely driven by compressor efficiency, yielded representative average COP and Q_{vol} values with (0.5 to 1.0) % confidence intervals. No tests had excessive discharge temperatures or other hardware-related problems.

All 121 experimental tests were then simulated using CYCLE_D-HX. For R-513A, R-450A, and R-515B in the basic cycle (tests without the LLSL-HX), the model-predicted values were within the confidence intervals of the experimental results, within about ±1.5 % of the curve fit. For Tern-1, the model overpredicted the experimental data by about 3 %. For the tests with the LLSL-HX, at 1.5 kW, the COP and Q_{vol} were overpredicted by (0 to 3) %. Importantly, the model provided the same relative COP and Q_{vol} ranking as the experimental data, giving confidence to the screening study performed in the limited-scope project.

Task 4. An experimental apparatus was used to establish and measure 432 convective-boiling heat-transfer coefficients for R-515B, R-450A, R-513A, and HFC-134a in a micro-fin tube. The heat-transfer coefficients were local (a function of thermodynamic quality) and were obtained with a fluid-heating boundary condition. It has been shown that data taken with an electrically-heated boundary condition can differ significantly in its behavior with respect to quality as compared to the fluid-heating boundary condition. These measurements were used to develop an improved correlation for the local Nusselt number for the micro-fin tube. The new correlation predicted 71 % of the measured convective boiling Nusselt numbers for R-515B, R-450A, R-513A, and HFC-134a to within ± 20 %. The correlation is valid for Reynolds numbers (Re) between 1000 and 14000, Boiling numbers (Bo) between 0.000002 and 0.001, and Bond numbers (B_{nd}) between 0.002 and 0.05. The correlation was developed with data where the refrigerant reduced temperature ranged between approximately 0.71 and 0.94. The data taken and the new correlation was tailored for use in Task 7 of the project for simulations of the ECU system with optimized heat exchangers.

Task 5. We selected R-513A [R-134a/1234yf (44/56)*], Tern-1 [R-134a/1234yf/1234ze(E) (49.2/33.9/16.9)*], and R-515B [R-1234ze(E)/227ea (91.1/8.9)*] for ECU testing in the NIST environmental chambers. Each of these blends has the potential of being a fluid of choice depending on the weights applied to the selection criteria (GWP, COP, Q_{vol}, flammability characteristics, see Section 3.5.3).

In addition, the ECU measurements with these fluids will provide a diverse database for validating a detailed ECU system model, which can be used later to simulate performance of other blends of possible interest.

In the above blend selection, we adopted the ASTM E681 test method as stipulated by ASHRAE Standard 34 for qualifying 'non-flammability' of refrigerants. Based on the present interim results, it will likely be possible to replace HFC-134a with a blend having at least 50 % lower GWP than that of HFC-134a. If military requirements for 'non-flammability' are more stringent than the E681 standard, a smaller reduction of GWP will be possible with qualifying blends.

Future Tasks. The remaining work (Task 7) includes experimental and simulation components. In the experimental effort, NIST will procure, install, and instrument a 3-ton military ECU in the NIST environmental chambers and will conduct performance tests according to the AHRI Standard 210/240[54] using HFC-134a, R-513A, Tern-1, and R-515B. The tests will be conducted at three standard test conditions consisting of the indoor 26.7 °C

* Compositions stated as mass percent

dry bulb and 15.8 °C dew point and three outdoor temperatures of 27.8 °C, 35.0 °C, and 46.1°C. These tests will include "soft optimization" of the ECU, which will entail a modification of the expansion device and optimization of the refrigerant charge but the same heat exchangers and compressor will be used for all fluids.

Within the simulation effort, NIST will apply two NIST 'first-principles-based' simulation models: EVAP-COND[73] and ACSIM. EVAP-COND is a software package for predicting performance of finned-tube evaporators and condensers. It is equipped with a computational-intelligence-based module to optimize the refrigerant circuitry. ACSIM is an in-house system model, which utilizes EVAP-COND components for simulating evaporators and condensers.

NIST will update ACSIM and EVAP-COND with improved blend thermophysical properties routines (from Task 1) and two-phase heat-transfer routines (from Task 4), and will 'tune' the EVAP-COND and ACSIM models to predict ECU laboratory results. The EVAP-COND's optimization module will be used to arrive at the optimum refrigerant circuitry for each studied blend. These optimized refrigerant circuit architectures will be used by ACSIM to predict the performance potential of competing blends in completely optimized ECU systems. The analysis will include the performance of carbon dioxide as a refrigerant.

The preparation of the final report will conclude this project. The report will document research results from all tasks. In the final part, it will provide a complete performance characterization of HFC-134a and three selected low-GWP blends in a soft-optimized ECU and in an ECU with optimized heat exchangers, based on detailed ECU simulations.

5. Literature Cited

1. Domanski, P. A.; McLinden, M. O.; Bell, I. H.; Linteris, G. T. *Low-GWP Alternative Refrigerant Blends for HFC-134a*; NIST Technical Note 2014; National Institute of Standards and Technology: Gaithersburg, MD, 2018.
2. McLinden, M. O.; Brown, J. S.; Brignoli, R.; Kazakov, A. F.; Domanski, P. A., Limited options for low-global-warming-potential refrigerants. *Nat Commun* **2017,** *8*.
3. Bell, I. H.; Domanski, P. A.; McLinden, M. O.; Linteris, G. T., The hunt for nonflammable refrigerant blends to replace R-134a. *Int J Refrig* **2019,** *104*, 484-495.
4. Wagner, W.; Kleinrahm, R., Densimeters for very accurate density measurements of fluids over large ranges of temperature, pressure, and density. *Metrologia* **2004,** *41*, S24-S39.
5. McLinden, M. O.; Lösch-Will, C., Apparatus for wide-ranging, high-accuracy fluid (p, ρ, T) measurements based on a compact two-sinker densimeter. *J. Chem. Thermodyn.* **2007,** *39*, 507-530.
6. Healy, J.; DeGroot, J. J.; Kestin, J., The theory of the transient hot-wire method for measuring the thermal conductivity. *Physica* **1976,** *C82*, 392-408.
7. Bell, I. H.; Lemmon, E. W., Automatic Fitting of Binary Interaction Parameters for Multi-fluid Helmholtz-Energy-Explicit Mixture Models. *J. Chem. Eng. Data* **2016,** *61* (11), 3752–3760-3752–3760.
8. Kunz, O.; Wagner, W., The GERG-2008 wide-range equation of state for natural gases and other mixtures: An expansion of GERG-2004. *J. Chem. Engr. Data* **2012,** *57*, 3032-3091.
9. Lemmon, E. W.; Jacobsen, R. T., Equations of state for mixtures of R-32, R-125, R-134a, R-143a, and R-152a. *Journal of Physical and Chemical Reference Data* **2004,** *33*, 593-620.
10. Williams, F. A., A unified view of fire suppression. *J. Fire Flamma.* **1974,** *5*, 54-63.
11. Davis, S. G.; Pagliaro, J. L.; Debold, T. F.; van Wingerden, M.; van Wingerden, K., Flammability and explosion characteristics of mildly flammable refrigerants. *Journal of Loss Prevention in the Process Industries* **2017,** *49*, 662-674.
12. ASHRAE, *ANSI/ASHRAE Standard 34-2019, Designation and Safety Classification of Refrigerants*. American Society of Heating, Refrigerating and Air-Conditioning Engineers: Atlanta, GA, 2019.
13. Papas, P.; Verma, P.; Lord, R.; Burns, L., Turbulent deflagrations of mildly flammable refrigerant-air mixtures. *Journal of Loss Prevention in the Process Industries* **2019,** *61*, 255-261.
14. Linteris, G.; Bell, I.; McLinden, M., An Empirical Model for Refrigerant Flammability Based on Molecular Structure and Thermodynamics. *International Journal of Refrigeration* **2019,** *104*, 144-150.
15. Linteris, G. T.; Babushok, V. I.; Pagliaro, J. L.; Burgess, J. D. R.; Manion, J. A.; Takahashi, F.; Katta, V. R.; Baker, P. T., Understanding overpressure in the FAA aerosol can test by $C_3H_2F_3Br$ (2-BTP). *Combust. Flame* **2016,** *167*, 452-462.
16. Linteris, G.; Pagliaro, J. L.; Sunderland, P. B. *Test Results Prepared for Honeywell: Igniter Material Effects in the Japanese High Pressure Gas Law Test*; NIST Technical Note 1902; National Institute of Standards and Technology: Gaithersburg, MD, 2016; p 52.
17. ASHRAE *ANSI/ASHRAE Standard 34-2019, Designation and Safety Classification of Refrigerants*; American Society of Heating,, Refrigerating and Air-Conditioning Engineers,: Atlanta, GA, 2019.
18. ISO *International Organization for Standarization (ISO-817): Refrigerants—Designation and safety classification.* ; Geneva, Switzerland, 2017.
19. ASTM, ASTM E681-09: Standard test method for concentration limits of flammability of chemicals (vapors and gases). In *ASTM Fire Standards*, Sixth ed.; American Society of Testing and Materials: West Conshohocken, PA, 2015.

20. Richard, R. G., *Personal Communication*. 2011.
21. Richard, R. G.; Kannoy, D.; Kusmierz, A. *Binary Refrigerant Flame Boundary Concentrations (ASHRAE Research Project 1507-RP Final Report)*; ASHRAE,: Atlanta, GA, 2017; p 59.
22. Kim, D. K.; Klieger, A. E.; Lomax, P. Q.; McCoy, C. G.; Reymann, J. Y.; Sunderland, P. B., An improved test method for refrigerant flammability limits in a 12 L vessel. *Sci. Technol. Built Environ.* **2018,** *24* (8), 861-866.
23. Richard, R. G. *Refrigerant flammability testing in large volume vessels*; DOE/CE/23810-87; Allied Signal Buffalo Research Laboratories: Buffalo, NY, March 1998, 1998; p 11 p.
24. Kelley, A. P.; Jomaas, G.; Law, C. K., Critical radius for sustained propagation of spark-ignited spherical flames. *Combust. Flame* **2009,** *156* (5), 1006-1013.
25. Berger, L.; Hesse, R.; Kleinheinz, K.; Hegetschweiler, M. J.; Attili, A.; Beeckmann, J.; Linteris, G. T.; Pitsch, H., A DNS study of the impact of gravity on spherically expanding laminar premixed flames. *Combust. Flame* **2020,** *216*, 412-425.
26. Pagliaro, J. L. *Inhibition of laminar premixed flames by Halon 1301 alternatives*; Ph.D. Thesis; University of Maryland: College Park, MD, 2015, 2015.
27. Pagliaro, J. L.; Linteris, G. T.; Sunderland, P. B.; Baker, P. T., Combustion inhibition and enhancement of premixed methane-air flames by halon replacements. *Combust. Flame* **2015,** *162* (1), 41-49.
28. Linteris, G. T.; Pagliaro, J. L. *Burning Velocity Measurements and Simulations for Understanding the Performance of Fire Suppressants in Aircraft*; NIST TN 1904; National Institute or Standards and Technology: Gaithersburg, MD, 2016, 2016; pp 1-49.
29. Linteris, G. T.; Pagliaro, J. L. *Test results prepared for Honeywell: Flammability of refrigerants in the Japanese high pressure gas law test*; NISTIR 7178; Gaithersburg MD, 10/05/2011, 2011; p 48 p.
30. Chen, Z.; Burke, M. P.; Ju, Y., On the critical flame radius and minimum ignition energy for spherical flame initiation. *Proc. Combust. Inst.* **2011,** *33* (1), 1219-1226.
31. Goodwin, D. G.; Moffat, H. K.; Speth, R. L. *Cantera: An object-oriented software toolkit for chemical kinetics, thermodynamics, and transport processes. http:/www.cantera.org, Version 2.1.1*; California Institute of Technology: Pasedena, CA, 2016.
32. Peters, N., *Turbulent Combustion*. Cambridge University Press: Cambridge, 2000.
33. Hansen, O. R.; Hinze, P.; Engel, D.; Davis, S., Using computational fluid dynamics (CFD) for blast wave predictions. *Journal of Loss Prevention in the Process Industries* **2010,** *23* (6), 885-906.
34. Hisken, H.; Enstad, G.; Middha, P.; van Wingerden, K., Investigation of concentration effects on the flame acceleration in vented channels. *Journal of Loss Prevention in the Process Industries* **2015,** *36*, 447-459.
35. Linteris, G. T.; Burgess, D. R.; Babushok, V.; Zachariah, M.; Tsang, W.; Westmoreland, P., Inhibition of premixed methane-air flames by fluoroethanes and fluoropropanes. *Combust. Flame* **1998,** *113* (1-2), 164-180.
36. Linteris, G. T.; Truett, L., Inhibition of premixed methane-air flames by fluoromethanes. *Combust. Flame* **1996,** *105* (1-2), 15-27.
37. Katta, V. R.; Takahashi, F.; Linteris, G. T., Fire-suppression characteristics of CF_3H in a cup burner. *Combust. Flame* **2006,** *144* (4), 645-661.
38. Babushok, V. I.; Linteris, G. T.; Meier, O., Combustion properties of halogenated fire suppressants. *Combust Flame* **2012,** *159*, 3569-3575.
39. Linteris, G. T.; Burgess, D. R.; Takahashi, F.; Katta, V. R.; Chelliah, H. K.; Meier, O., Stirred reactor calculations to understand unwanted combustion enhancement by potential halon replacements. *Combust. Flame* **2012,** *159* (3), 1016-1025.
40. Pagliaro, J. L.; Bouvet, N.; Linteris, G. T., Premixed flame inhibition by CF_3Br and $C_3H_2F_3Br$ (2-BTP). *Combust. Flame* **2016,** *169*, 272-286.

41. Takahashi, F.; Katta, V. R.; Linteris, G. T.; Babushok, V. I., Combustion inhibition and enhancement of cup-burner flames by CF_3Br, C_2HF_5, $C_2HF_3Cl_2$, and $C_3H_2F_3Br$. *Proc. Combust. Inst.* **2015,** *35*, 2741-2748.
42. Takahashi, F.; Katta, V. R.; Linteris, G. T.; Meier, O. C., Cup-burner flame structure and extinguishment by CF3Br and C2HF5 in microgravity. *Proc. Combust. Inst.* **2013,** *34*, 2707-2717.
43. Linteris, G. T.; Babushok, V. I.; Sunderland, P. B.; Takahashi, F.; Katta, V. R.; Meier, O., Unwanted combustion enhancement by C6F12O fire suppressant. *Proc. Combust. Inst.* **2013,** *34*, 2683-2690.
44. Burgess Jr, D. R.; Zachariah, M. R.; Tsang, W.; Westmoreland, P. R. *Thermochemical and Chemical Kinetic Data for Fluorinated Hydrocarbons*; NIST Technical Note 1412; National Institute of Standards and Technology: Gaithersburg, MD, 1995.
45. Burgess, D. R.; Babushok, V. I.; Linteris, G. T.; Manion, J. A., A Chemical Kinetic Mechanism for 2-Bromo-3,3,3-trifluoropropene (2-BTP) Flame Inhibition. *Int. J. Chem. Kinet.* **2015,** *47* (9), 533-563.
46. Babushok, V. I.; Burgess, D. R.; Kim, D. K.; Hegetschweiler, M. J.; Linteris, G. T. *Kinetic Model for Refrigerant-Air Flames*; NIST Technical Note xxxx; National Institute of Standards and Technology: Gaithersburg, MD, 2021, 2021; p to be submitted.
47. Linteris, G. T.; Babushok, V. I., Laminar burning velocity predictions for C_1 and C_2 hydrofluorocarbon refrigerants with air. *J Fluorine Chem* **2020,** *230*.
48. Babushok, V. I.; Burgess, D. R.; Hegetschweiler, M. J.; Linteris, G. T., Flame propagation in the mixtures of O2/N2 oxidizer with fluorinated propene refrigerants (CH2CFCF3, CHFCHCF3, CH2CHCF3). *Combust. Sci. Technol.* **2020**, 1-24.
49. Hegetschweiler, M. J.; Linteris, G. T. *Data Reduction Tool for Spherical Constant Volume Flame Experiments*; NIST Technical Note in preparation; National Institute of Standards and Technology: Gaithersburg, MD, 2021; p 999.
50. Kim, D. K.; Babushok, V. I.; Burgess, D. R.; Hegetschweiler, M. J.; Linteris, G. T., Burning Velocity of Blends of R-152a with R-134a or R-1234yf and air. *Combust. Sci. Technol.* **2020**, to be submitted.
51. Barat, R. B., Correlating laminar burning velocities using perfectly stirred reactor theory. *Chem. Eng. Sci.* **2001,** *56*, 2761-2766.
52. Brown, J. S., Brignoli, R., Domanski, P.A., Yoon, Y.J. *CYCLE_D-HX: NIST Vapor Compression Cycle Model Accounting for Refrigerant Thermodynamic and Transport Properties; Version 2.0*, National Institute of Standards and Technology: Gaithersburg, MD, 2021.
53. Brignoli, R.; Brown, J. S.; Skye, H. M.; Domanski, P. A., Refrigerant performance evaluation including effects of transport properties and optimized heat exchangers. *Int J Refrig* **2017,** *80*, 52-65.
54. AHRI, 210/240-2017 Standard for Performance Rating of Unitary A/C and Air Source Heat Pump Equipment. Arlington, VA, 2017.
55. Skye, H. M. *Heat Pump Test Apparatus for the Evaluation of Low Global Warming Potential Refrigerants*; NIST Technical Note 1895, National Institute of Standards and Technology: Gaithersburg, MD, 2015.
56. McLinden, M. O.; Radermacher, R., Methods for comparing the performance of pure and mixed refrigerants in the vapour compression cycle. *International Journal of Refrigeration* **1987,** *10* (6), 318-325.
57. Kedzierski, M. A.; Park, K. J., Horizontal Convective Boiling of R134a, R1234yf/R134a, and R1234ze(E) within a Micro-Fin Tube. *J Enhanc Heat Transf* **2013,** *20* (4), 333-346.
58. Kattan, N.; Thome, J. R.; Favrat, D., R-502 and two near-azeotropic alternatives. Part 1: In-tube flow-boiling tests. *ASHRAE Transactions* **1995,** *101* (1), 491-508.
59. Hamilton, L.; Kedzierski, M.; Kaul, M., Horizontal convective boiling of pure and mixed refrigerants within a micro-fin tube. *J Enhanc Heat Transf* **2008,** *15* (3).
60. Kedzierski, M. A.; Kang, D., Horizontal convective boiling of R1234yf, R134a, and R450A within a micro-fin tube. *Int J Refrig* **2018,** *88*, 538-551.

61. Kedzierski, M. A.; Lin, L.; Kang, D., Pool Boiling of Low-Global Warming Potential Replacements for R134a on a Reentrant Cavity Surface. *J Heat Trans-T Asme* **2018,** *140* (12).
62. Solomon, S.; Burkholder, J. B.; Ravishankara, A. R.; Garcia, R. R., Ozone depletion and global warming potentials of CF_3I. *J. Geo. Res. Atmospheres* **1994,** *99*, 20929-20935.
63. Bell, I. H.; McLinden, M. O., The status of thermodynamic data and models for CF_3I and its mixtures. *Int. J. Thermopysics* **2020,** *41*, 134.
64. Yang, Z.; Liu, H.; Wu, X., Theoretical and experimental study of the inhibition and inert effect of HFC125, HFC227ea and HFC13I1 on the flammability of HFC32. *Process Safety and Environmental Protection* **2012,** *90*, 311–316.
65. Yana Motta, S. F. *Submission to ASHRAE SSPC 34 Committee. Request for Refrigerant Designation and Safety Classification For R-32/R-125/CF_3I (49.0/11.5/39.5 % by mass) Zeotropic Refrigerant Blend*; Honeywell International, Inc., Buffalo, NY: 2018.
66. ASHRAE, Addendum t to Standard 34-2019, Designation and Safety Classification of Refrigerants. American Society of Heating, Refrigerating and Air-Conditioning Engineers: 2019.
67. National Research Council, *Iodotrifluoromethane: Toxicity Review (2004)*. Washington, DC: The National Academies Press.
68. Allgood, C.; Johnston, P.; Kim, S.; Kujak, S.; Yana Motta, S., Roundtable: A conversation on refrigerants. *ASHRAE J.* **2021,** *March 2021*, 30-37.
69. Akasaka, R.; Fukuda, S.; Sakoda, N.; Higashi, Y. In *pvT Property measurement and development of an equation of state for new refrigerant HFO1132(E)*, Proceedings of the 2020 JSRAE Annual Conference, Tsu-city, September 8-11, 2020; Tsu-city, 2020.
70. Perera, U. A.; Miyazaki, T.; Sakoda, N.; Higashi, Y. In *Determination of saturation pressure and critical pressure for new refrigerant HFO1132(E)*, Proceedings of the 2020 JSRAE Annual Conference, Tsu-city, September 8-11, 2020; Tsu-city, 2020.
71. McLinden, M. O.; Brown, J. S.; Brignoli, R.; Kazakov, A. F.; Domanski, P. A., Limited options for low-global-warming-potential refrigerants. *Nat. Comm.* **2017,** *8*, 14476.
72. Linteris, G. T.; Bell, I. H.; McLinden, M. O., An empirical model for refrigerant flammability based on molecular structure and thermodynamics. *International Journal of Refrigeration* **2019,** *104*, 144-150.
73. Domanski, P. A.; Yashar, D. A.; Wojtusiak, J. *EVAP-COND, Version 5.0; Simulation Models for Finned-Tube Heat Exchangers with Circuitry Optimization*, National Institute of Standards and Technology, Gaithersburg, MD: 2021.
74. Outcalt, S. L.; Lemmon, E. W., Bubble point measurements of eight binary mixtures for organic rankine cycle applications. *J. Chem. Engr. Data* **2013,** *58*, 1853-1860.
75. Hust, J. G.; Filla, J.; Smith, D. R., A modified digital PID temperature controller for thermal property measurements. *Journal of Thermal Insulation* **1987,** *11* (10), 102-107.
76. McLinden, M. O.; Kleinrahm, R.; Wagner, W., Force transmission errors in magnetic suspension densimeters. *Int. J. Thermophys.* **2007,** *28*, 429-448.
77. McLinden, M. O.; Richter, M., Application of a two-sinker densimeter for phase-equilibrium measurements: A new technique for the detection of dew points and measurements on the (methane + propane) System. *J. Chem. Thermodyn.* **2016,** *99*, 105-115.
78. McLinden, M. O.; Splett, J. D., A liquid density standard over wide ranges of temperature and pressure based on toluene. *J. Res. Natl. Inst. Stand. Technol.* **2008,** *113*, 29-67.
79. McLinden, M. O., Thermodynamic properties of propane. I. p-ρ-T behavior from 265 K to 500 K with pressures to 36 MPa. *J. Chem. Eng. Data* **2009,** *54*, 3181-3191.
80. Lemmon, E. W.; McLinden, M. O.; Wagner, W., Thermodynamic properties of propane. III. A Reference Equation of State for Temperatures from the Melting Line to 650 K and Pressures up to 1000 MPa. *Journal of Chemical and Engineering Data* **2009,** *54*, 3141-3180.

81. Meier, K.; Kabelac, S., Thermodynamic Properties of Propane. IV. Speed of Sound in the Liquid and Supercritical Regions. *J. Chem. Engr. Data* **2012,** *57*, 3391-3398.
82. Roder, H. M., A transient hot wire thermal conductivity apparatus for fluids. *J Res Natl Bur Stand* **1981,** *86* (5), 457-493.
83. Healy, J. J.; de Groot, J. J.; Kestin, J., The theory of the transient hot-wire method for measuring thermal conductivity. *Physica* **1976,** *82*, 392-408.
84. Harris, G. L.; Torres, J. A. *Selected laboratory and measurement practices and procedures, to support basic mass calibrations*; NISTIR 6969; National Institute of Standards and Technology: 2003.
85. Richter, M.; McLinden, M. O., Vapor-phase (p, ρ, T, x) behavior and virial coefficients for the (methane + propane) system. *J. Chem. Eng. Data* **2014,** *59*, 4151-4164.
86. Rosenfeld, Y., Relation between the transport coefficients and the internal entropy of simple systems. *Phys. Rev. A* **1977,** *15*, 2545–2549-2545–2549.
87. Bell, I. H.; Messerly, R.; Thol, M.; Costigliola, L.; Dyre, J., Modified Entropy Scaling of the Transport Properties of the Lennard-Jones Fluid. *J. Phys. Chem. B* **2019,** *123* (29), 6345–6363-6345–6363.
88. Bell, I. H., Entropy Scaling of Viscosity – I: A Case Study of Propane. *J. Chem. Eng. Data* **2020**, 3203–3215-3203–3215.
89. Bell, I. H., Entropy Scaling of Viscosity—II: Predictive Scheme for Normal Alkanes. *J. Chem. Eng. Data* **2020,** *65* (11), 5606–5616-5606–5616.
90. Yang, X.; Xiao, X.; May, E. F.; Bell, I. H., Entropy Scaling of Viscosity—III: Application to Refrigerants and Their Mixtures. *J. Chem. Eng. Data* **2021**.
91. Liu, H.; Yang, F.; Yang, Z.; Duan, Y., Modeling the viscosity of hydrofluorocarbons, hydrofluoroolefins and their binary mixtures using residual entropy scaling and cubic-plus-association equation of state. *J. Mol. Liq.* **2020,** *308*, 113027-113027.
92. Lötgering-Lin, O.; Gross, J., Group Contribution Method for Viscosities Based on Entropy Scaling Using the Perturbed-Chain Polar Statistical Associating Fluid Theory. *Ind. Eng. Chem. Res.* **2015,** *54* (32), 7942–7952-7942–7952.
93. Lötgering-Lin, O.; Fischer, M.; Hopp, M.; Gross, J., Pure Substance and Mixture Viscosities Based on Entropy Scaling and an Analytic Equation of State. *Ind. Eng. Chem. Res.* **2018,** *57* (11), 4095–4114-4095–4114.
94. Fouad, W. A.; Alasiri, H., Molecular dynamic simulation and SAFT modeling of the viscosity and self-diffusion coefficient of low global warming potential refrigerants. *J. Mol. Liq.* **2020,** *317*, 113998-113998.
95. Bell, I. H.; Dyre, J. C.; Ingebrigtsen, T. S., Excess-entropy scaling in supercooled binary mixtures. *Nature Communications* **2020,** *11* (1).
96. Kondo, S.; Takizawa, K.; Takahashi, A.; Tokuhashi, K.; Sekiya, A., Flammability limits of five selected compounds each mixed with HFC-125. *Fire Saf. J.* **2009,** *44* (2), 192-197.
97. Shebeko, Y. N.; Azatyan, V. V.; Bolodian, I. A.; Navzenya, V. Y.; Kopyov, S. N.; Shebeko, D. Y.; Zamishevski, E. D., The influence of fluorinated hydrocarbons on the combustion of gaseous mixtures in a closed vessel. *Combust. Flame* **2000,** *121* (3), 542-547.
98. Pagliaro, J. L.; Linteris, G. T.; Babushok, V. I., Premixed flame inhibition by $C_2HF_3Cl_2$ and C_2HF_5. *Combust. Flame* **2016,** *163*, 54-65.
99. Shephard, J. E.; Krok, J. C.; Lee, J. J. *Spark Ignition Energy Measurements in Jet A*; Calif. Inst. Tech: 1999.
100. Metghalchi, M.; Keck, J. C., Laminar burning velocity of propane-air mixtures at high temperature and pressure. *Combust. Flame* **1980,** *38*, 143-154.
101. Metghalchi, M.; Keck, J. C., Burning velocities of mixtures of air with methanol, isooctane, and indolene at high pressure and temperature. *Combust. Flame* **1982,** *48*, 191-210.

102. Hill, P. G.; Hung, J., Laminar Burning Velocities of Stoichiometric Mixtures of Methane with Propane and Ethane Additives. *Combustion Science and Technology* **1988,** *60*, 7-30.
103. Takizawa, K.; Takahashi, A.; Tokuhashi, K.; Kondo, S.; Sekiya, A., Burning velocity measurement of fluorinated compounds by the spherical-vessel method. *Combust Flame* **2005,** *141* (3), 298-307.
104. Lewis, B.; von Elbe, G., *Combustion, Flames, and Explosions of Gases*. 1961.
105. Saeed, K.; Stone, C. R., Measurements of the laminar burning velocity for mixtures of methanol and air from a constant-volume vessel using a multizone model. *Combustion and Flame* **2004,** *139* (1-2), 152-166.
106. Eisazadeh-Far, K.; Moghaddas, A.; Al-Mulki, J.; Metghalchi, H., Laminar burning speeds of ethanol/air/diluent mixtures. *Proc. Combust. Inst.* **2011,** *33* (1), 1021-1027.
107. Williams, F. A. In *A review of some theoretical considerations of turbulent flame structure*, AGARD Conference Proceeding, 1975.
108. Takizawa, K.; Takahashi, A.; Tokuhashi, K.; Kondo, S.; Sekiya, A., Burning velocity measurement of HFC-41, HFC-152a, and HFC-161 by the spherical-vessel method. *J Fluorine Chem* **2006,** *127* (12), 1547-1553.
109. Marshall, S. P.; Taylor, S.; Stone, C. R.; Davies, T. J.; Cracknell, R. F., Laminar burning velocity measurements of liquid fuels at elevated pressures and temperatures with combustion residuals. *Combustion and Flame* **2011,** *158* (10), 1920-1932.
110. Babushok, V. I.; Burgess Jr, D. R.; Kim, D. K.; Hegetschweiler, M. J.; Linteris, G. T. *Modeling of Combustion of Fluorine-Containing Refrigerants*; NIST Technical Note in preparation; National Institute of Standards and Technology: Gaithersburg, MD, 2021; p 999.

Appendix A: Details of Experiments and Modeling

A.1. Task 1 - Details of Thermophysical Properties Measurements and Modeling

A.1.1. Vapor-Liquid Equilibria

A schematic of the instrument used to make the measurements is shown in Figure A.1-1; it is an updated version of the instrument described by Outcalt and Lemmon.[74] The heart of the instrument was a cylindrical stainless steel measuring cell with a sapphire window on each end so that the liquid level in the cell was visible. The cell had an internal volume of approximately 30 mL. The operating range of the apparatus was 270 K to 360 K, with pressures to 7 MPa.

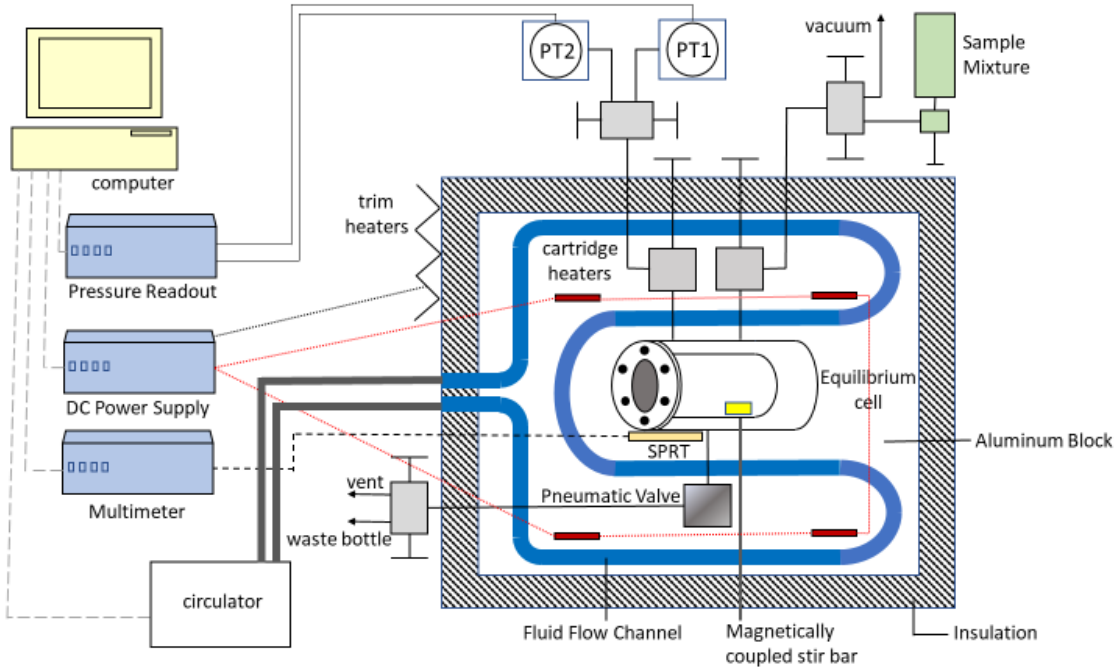

Figure A.1-1. Schematic of instrument for vapor liquid equilibria measurements.

Main components of the instrument include a stainless steel equilibrium cell housed in a thermostated aluminum block, standard platinum resistance thermometer (SPRT), and two oscillating quartz crystal pressure transducers (PT1 and PT2) with maximum pressure ranges of 0.7 MPa and 7 MPa.

The cell was fitted inside a temperature-controlled, insulated aluminum block. The valves for filling the system were installed in the aluminum block to limit the sample volume outside the temperature-controlled zone. Cooling fluid from an external refrigerated circulator flowed through channels drilled into the aluminum block. Cartridge heaters installed in the aluminum block provided heat for operation above ambient temperature. Thin-film type heaters were adhered to the outside of the block for fine control of the temperature. Temperature control was automated with the modified PID algorithm of Hust et al.[75]

Temperature was measured with a standard platinum resistance thermometer (SPRT) installed in a thermowell adjacent to the measuring cell. The pressure was measured with one of two oscillating-quartz-crystal pressure transducers connected to the system through one of the ports at the top of the cell. These transducers had full-scale ranges of 0.7 MPa and 7.0 MPa; the low-range transducer had the higher sensitivity, and it was used whenever possible. The transducers were thermostatted in separate thermostats maintained at 313 K.

For loading, the sample bottle was connected to the system in an inverted position so that the liquid phase was loaded into the cell. Prior to loading a sample into the system, the system was evacuated and cooled to approximately 270 K, and the pressure reading under vacuum was recorded. The sample was then quickly loaded into the system until only a small vapor space remained in the equilibrium cell. Stirring of the sample was effected by a stir bar inside the cell that was magnetically coupled to an external motor.

By loading the sample from the liquid phase of the sample bottle and filling the measuring cell nearly full, the liquid-phase composition in the cell was nearly that of the bulk composition of the sample bottle. Small corrections to the composition were made using the mixture model in REFPROP and assuming equilibrium between the liquid and vapor phases in both the sample bottle and measuring cell.

Measurements commenced at 270 K. After temperature and pressure equilibrium were obtained, the conditions were recorded. The temperature was then increased by an increment of 10 K. As the temperature was increased, the liquid expanded, eventually filling the cell with compressed liquid. As a result, it was necessary to periodically release a small amount of liquid from the bottom of the cell to maintain a vapor space; this was done by opening a pneumatically actuated valve. Repeat measurements were conducted at a minimum of two temperatures. These repeats established the repeatability of the measurements and also helped to determine whether the loss of small amounts of the liquid phase affected the sample composition to the extent that duplicate measurements at a given temperature yielded different bubble-point pressures. In almost all instances this was not the case.

The principal sources of uncertainty in these measurements arose from the measurement of temperature, pressure, and sample composition as well as repeatability of the measurements. The SPRT was calibrated with fixed-point cells, and the standard (k = 1) uncertainty in temperature, including calibration, repeatability and possible temperature gradients was estimated to be 20 mK. The pressure transducers were calibrated with a piston gage, and the zero of the transducers was regularly checked. The uncertainty in the pressure was 0.005 % of the full-scale pressure (i.e., 0.035 kPa or 0.35 kPa for the two transducers). As described in section A.1-5, the uncertainty in the composition due to the weighings was less than 0.0001 mole fraction. Because of the two-phase nature of the liquid-phase samples and because the weighings could determine only the overall (bulk) composition of the sample, it was necessary to estimate the change in composition caused by the liquid/vapor fractionation inside the cylinder. This change was less than 0.0005 mole fraction, and its standard uncertainty was estimated to be less than 0.0001 mole fraction. Thus, the combined, expanded uncertainty in composition of the liquid-phase samples was estimated to be less than 0.00028 mole fraction. In addition to these uncertainties, the standard deviation in repeat

measurements were added in quadrature to arrive at the overall uncertainty, which is stated in the tables of VLE data presented below.

Table A.1-1. Measured vapor-liquid equilibria (VLE) data for the system R-1234yf/134a at a molar composition of (0.320/0.680).

Listed are temperature T, bubble-point pressure P_{bub}, expanded (k = 2) state point uncertainty in the bubble-point pressure U_c, and relative deviation from the mixture EOS. The standard uncertainty in temperature is 20 mK, and the standard uncertainty in composition is 0.00028 mole fraction. Two replicate measurements are given for most temperatures.

T/K	P_{bub}/kPa	U_c/%	Δ_{Pbub}/%
269.99	282.7	0.835	0.111
279.99	399.3	0.614	0.031
279.99	399.6	0.613	0.106
289.99	549.3	0.466	-0.057
289.99	549.6	0.466	-0.002
299.99	739.7	0.362	0.033
299.99	739.8	0.362	0.046
309.99	975.1	0.286	0.022
309.99	974.5	0.286	-0.039
319.99	1262.0	0.234	-0.043
319.99	1261.8	0.234	-0.059
329.99	1609.3	0.190	-0.024
329.99	1608.6	0.190	-0.068
339.99	2024.3	0.157	-0.010
339.99	2023.2	0.157	-0.064
349.99	2516.9	0.132	0.011
349.99	2515.1	0.132	-0.061
359.99	3098.6	0.112	-0.007
359.99	3095.7	0.112	-0.101

Table A.1-2. Measured vapor-liquid equilibria (VLE) data for the system R-1234yf/134a at a molar composition of (0.647/0.353).

Listed are temperature T, bubble-point pressure P_{bub}, expanded (k = 2) state point uncertainty in the bubble-point pressure U_c, and relative deviation from the mixture EOS. The standard uncertainty in temperature is 20 mK, and the standard uncertainty in composition is 0.00028 mole fraction. Two replicate measurements are given for most temperatures. Two replicate measurements are given for most temperatures.

T/K	P_{bub}/kPa	U_c/%	Δ_{Pbub}/%
269.99	289.9	0.793	0.121
269.99	290.0	0.793	0.155
279.99	406.9	0.587	0.068
279.99	407.0	0.587	0.093
289.99	557.8	0.443	0.223
289.99	556.5	0.444	-0.010
289.99	556.5	0.444	-0.010
299.99	745.2	0.348	0.052
299.99	745.2	0.348	0.052
309.99	977.0	0.274	-0.024
309.99	976.8	0.274	-0.044
319.99	1259.8	0.225	-0.024
319.99	1259.3	0.226	-0.063
329.99	1610.4	0.183	0.630
329.99	1599.0	0.184	-0.082
339.99	2005.3	0.153	-0.017
339.99	2003.8	0.153	-0.092
349.99	2482.2	0.128	-0.126
349.99	2482.9	0.128	-0.098
359.99	3047.8	0.109	-0.141

Table A.1-3. Measured vapor-liquid equilibria (VLE) data for the system R-134a/1234ze(E) at a molar composition of (0.334/0.666).

Listed are temperature T, bubble-point pressure P_{bub}, expanded (k = 2) state point uncertainty in the bubble-point pressure U_c, and relative deviation from the mixture EOS. The standard uncertainty in temperature is 20 mK, and the standard uncertainty in composition is 0.00028 mole fraction.

T/K	P_{bub}/kPa	U_c/%	Δ_{Pbub}/%
269.99	222.3	1.170	-0.173
279.99	318.1	0.846	-0.133
289.99	442.8	0.628	-0.094
299.99	601.4	0.477	-0.074
299.99	601.1	0.477	-0.114
309.99	799.6	0.383	-0.027
319.99	1043.7	0.308	0.051
319.99	1043.0	0.308	-0.018
329.99	1339.6	0.249	0.116
339.99	1694.3	0.204	0.179
349.99	2115.3	0.170	0.218
359.99	2614.9	0.145	0.363
359.99	2609.0	0.145	0.137

Table A.1-4. Measured vapor-liquid equilibria (VLE) data for the system R-134a/1234ze(E) at a molar composition of (0.663/0.337).

Listed are temperature T, bubble-point pressure P_{bub}, expanded (k = 2) state point uncertainty in the bubble-point pressure U_c, and relative deviation from the mixture EOS. The standard uncertainty in temperature is 20 mK, and the standard uncertainty in composition is 0.00028 mole fraction.

T/K	P_{bub}/kPa	U_c/%	Δ_{Pbub}/%
269.99	244.0	0.951	-0.222
279.99	348.6	0.694	-0.209
289.99	484.6	0.520	-0.195
299.99	657.0	0.399	-0.246
309.99	872.8	0.315	-0.200
319.99	1138.3	0.256	-0.122
329.99	1460.0	0.207	-0.058
339.99	1846.1	0.170	0.025
349.99	2304.5	0.142	0.077
359.99	2843.2	0.120	0.022
289.99	484.3	0.520	-0.265

Table A.1-5. Measured vapor-liquid equilibria (VLE) data for the system R-1234yf/1234ze(E) at a molar composition of (0.324/0.676).

Listed are temperature T, bubble-point pressure P_{bub}, expanded (k = 2) state point uncertainty in the bubble-point pressure U_c, and relative deviation from the mixture EOS. The standard uncertainty in temperature is 20 mK, and the standard uncertainty in composition is 0.00028 mole fraction. Two replicate measurements are given for most temperatures. Two replicate measurements are given for most temperatures.

T/K	P_{bub}/kPa	U_c/%	Δ_{Pbub}/%
270.00	229.5	0.924	-0.110
270.00	229.5	0.924	-0.110
280.00	325.4	0.676	-0.044
280.00	325.5	0.676	-0.013
290.00	449.1	0.510	-0.023
290.00	449.2	0.510	-0.001
300.00	605.7	0.393	0.020
300.00	605.4	0.393	-0.029
310.00	799.6	0.313	-0.029
310.00	799.1	0.313	-0.091
320.00	1038.6	0.255	0.107
320.00	1037.1	0.256	-0.038
330.00	1325.4	0.207	0.065
330.00	1324.7	0.208	0.012
340.00	1669.5	0.171	0.117
340.00	1667.8	0.171	0.015
340.00	1668.5	0.171	0.057
350.00	2077.0	0.143	0.149
350.00	2076.2	0.143	0.110
360.00	2556.7	0.121	0.157
360.00	2557.1	0.121	0.173

Table A.1-6. Measured vapor-liquid equilibria (VLE) data for the system R-1234yf/1234ze(E) at a molar composition of (0.638/0.362).

Listed are temperature T, bubble-point pressure P_{bub}, expanded (k = 2) state point uncertainty in the bubble-point pressure U_c, and relative deviation from the mixture EOS. The standard uncertainty in temperature is 20 mK, and the standard uncertainty in composition is 0.00028 mole fraction. Two replicate measurements are given for most temperatures. Two replicate measurements are given for most temperatures.

T/K	P_{bub}/kPa	U_c/%	Δ_{Pbub}/%
270.00	258.9	0.769	0.332
270.00	258.0	0.771	-0.017
280.00	363.5	0.567	0.198
280.00	362.9	0.568	0.033
280.00	362.8	0.568	0.005
290.00	497.8	0.430	0.144
290.00	497.1	0.430	0.004
290.00	497.0	0.431	-0.016
300.00	666.3	0.333	0.060
300.00	665.7	0.333	-0.030
300.00	665.6	0.334	-0.045
310.00	874.6	0.266	0.008
310.00	873.8	0.267	-0.084
310.00	873.7	0.267	-0.095
320.00	1128.8	0.219	0.013
320.00	1127.8	0.219	-0.076
320.00	1127.7	0.219	-0.085
330.00	1435.4	0.179	0.065
330.00	1434.0	0.179	-0.033
330.00	1434.0	0.179	-0.033
340.00	1800.0	0.148	0.064
340.00	1798.8	0.148	-0.003
340.00	1799.1	0.148	0.014
350.00	2229.1	0.125	-0.029
350.00	2231.3	0.124	0.070
360.00	2734.0	0.106	-0.117
360.00	2738.9	0.106	0.062

Table A.1-7. Measured vapor-liquid equilibria (VLE) data for the system R125/1234yf at a molar composition of (0.349/0.651).

Listed are temperature T, bubble-point pressure P_{bub}, expanded (k = 2) state point uncertainty in the bubble-point pressure U_c, and relative deviation from the mixture EOS. The standard uncertainty in temperature is 20 mK, and the standard uncertainty in composition is 0.00028 mole fraction.

T/K	P_{bub}/kPa	U_c/%	Δ_{Pbub}/%
270.00	393.4	0.536	-0.148
270.00	393.8	0.536	-0.046
280.00	542.2	0.404	-0.084
290.00	729.5	0.317	-0.032
300.00	959.9	0.251	-0.108
300.00	960.4	0.251	-0.056
310.00	1240.8	0.202	-0.122
315.00	1401.0	0.186	-0.201
315.00	1401.8	0.186	-0.144
320.00	1577.9	0.169	-0.154
325.00	1770.1	0.154	-0.150
330.00	1979.7	0.140	-0.116
330.00	1980.8	0.140	-0.060
335.00	2206.6	0.129	-0.112

Table A.1-8. Measured vapor-liquid equilibria (VLE) data for the system R-125/1234yf at a molar composition of (0.664/0.336).

Listed are temperature T, bubble-point pressure P_{bub}, expanded (k = 2) state point uncertainty in the bubble-point pressure U_c, and relative deviation from the mixture EOS.

T/K	P_{bub}/kPa	U_c/%	Δ_{Pbub}/%
270.00	494.0	0.455	-0.234
270.00	494.6	0.455	-0.113
280.00	677.4	0.344	-0.081
290.00	905.9	0.270	-0.099
290.00	907.0	0.270	0.022
300.00	1186.1	0.215	-0.195
310.00	1525.9	0.174	-0.265
310.00	1527.6	0.174	-0.154
315.00	1721.4	0.161	-0.241
320.00	1935.0	0.146	-0.211
325.00	2167.5	0.133	-0.192
330.00	2421.0	0.122	-0.142
330.00	2423.6	0.122	-0.035
335.00	2695.5	0.112	-0.121

A.1.2. Density (*P, ρ, T, x*) Measurements

Instrument description. The present measurements utilized a two-sinker densimeter with a magnetic suspension coupling. This type of instrument applies the Archimedes (buoyancy) principle to provide an absolute determination of the density. This general type of instrument is described by Wagner and Kleinrahm,[4] and our instrument is described in detail by McLinden and Lösch-Will.[5] Briefly, two sinkers of nearly the same mass (~60 g) and same surface area (~41.5 cm^2), but very different volumes, were each weighed with a high-precision balance while they were immersed in the sample of unknown density. The basic form of the working equation for this type of instrument gives the fluid density ρ as:

$$r = \frac{(m_1 - m_2) - (W_1 - W_2)}{(V_1 - V_2)}, \qquad \text{(A.1-2)}$$

where m and V are the mass and volume of the sinkers, W are the balance readings, and the subscripts refer to the two sinkers. One sinker was made of tantalum (m = 60.094 633 g, V = 3.60 872 cm^3) and the other of titanium (m = 60.075 386 g, V = 13.315 284 cm^3). A magnetic suspension coupling transmitted the gravity and buoyancy forces on the sinkers to the balance, thus isolating the fluid sample from the balance. With the two-sinker method, systematic errors in the weighing and from other sources approximately cancel. Figure A.1-2 shows the entire instrument and Figure A.1-3 shows the two sinkers inside the cell.

Figure A.1-2. Two-sinker densimeter.

The main part of the instrument is to the right of center with the vacuum thermostat below and balance above; the instruments are on the left side; a vacuum system for both evacuating

the measuring cell and maintaining the vacuum thermostat is on the right. A separate system for calibrating sinker volumes sits to the right of the instrument rack.

Figure A.1-3. Sinkers in the two-sinker densimeter (shown removed from the measuring cell).

The titanium sinker is on the bottom, with the tantalum sinker above. The magnetic suspension coupling is at the top of the image; this comprises the electromagnet, which hangs from the balance; and the permanent magnet, which picks up the sinkers via "lifting forks;" the top of the measuring cell passes between the electromagnet and permanent magnet. In this photo, the titanium sinker is suspended off of its rest and is being weighed.

In addition to the sinkers, two calibration masses (designated m_{cal} and m_{tare}) were also weighed by placing them directly on the balance pan. This provided a calibration of the balance and also the information needed to correct for magnetic effects as described by McLinden et al.[76] The four weighings (two sinkers and two calibration masses) yield a set of four equations that were solved to yield a balance calibration factor α and a parameter ϕ characterizing the efficiency of the magnetic suspension coupling. With these additional terms, the fluid density is:

$$\rho_{fluid} = \left\{ \left[\left(m_1 - m_2 \right) - \frac{\left(W_1 - W_2 \right)}{\alpha f} \right] \Big/ \left(V_1 - V_2 \right) \right\} - \rho_0 \quad \text{(A.1-3)}$$

,

where ρ_0 is the indicated density when the sinkers are weighed in vacuum. In other words, ρ_0 is an "apparatus zero." The density given by Eq. (A.1-3) compensates for the magnetic effects of both the apparatus and the fluid being measured. The difference of the value of ϕ from 1 indicates the magnitude of the force transmission error.[7]

The densimeter was thermostated by means of a multi-layer, vacuum-insulated thermostat. A copper shield with heaters at the top and side surrounded the measuring cell. An additional isothermal shield with heaters at the top and sides and a fluid cooling channel at the top surrounded the "inner shield"; it was maintained at a temperature approximately 1 K below the measuring-cell temperature. A chiller that circulated ethanol was used at temperatures below room temperature.

The temperature was measured with a 25 Ω standard platinum resistance thermometer (SPRT) and an AC resistance bridge referenced to a thermostated standard resistor. The temperature inside the measuring cell was constant within 5 mK. Pressures were measured with one of three vibrating-quartz-crystal type pressure transducers having full-scale pressure ranges of 2.8 MPa, 13.8 MPa, or 69 MPa. The transducers and pressure manifold were thermostated at T = 313.15 K to minimize the effects of variations in laboratory temperature.

Density measurement sequence—liquid and supercritical states. A combination of measurements along isochores and along isotherms was carried out. The evacuated measuring cell was cooled and then the gas-phase sample from the sample bottle was condensed into the measuring cell; higher pressures were obtained by closing the valve to the sample bottle and then increasing the cell temperature in steps along a pseudoisochore. Once a new setpoint temperature and pressure was reached an additional equilibration time of 30–60 minutes was allowed; four replicate density determinations were then carried out. When the maximum desired pressure along a pseudoisochore was reached, a portion of the sample was vented into a waste bottle to decrease the pressure; measurements were made in this manner along an isotherm to a minimum pressure of approximately 1 MPa or slightly above the bubble-point pressure, whichever was higher. Measurements then resumed at increasing temperatures along the next, lower-density pseudoisochore. This procedure did not require any pump and thus avoided any chance for sample contamination that a pump or compressor might introduce; it also minimized the number of manual sample-handling steps.

Between each of the measured blend compositions and also before and after all of the testing, the densimeter cell was evacuated for a minimum of 36 h. This was done to clear the previously measured sample and to check the zero of the pressure transducers and the ρ_0 of the apparatus (Eq. A.1-3). The ρ_0 varied by less than 0.0011 kg·m^{-3}.

Vapor-phase (P, ρ, T, x) and dew point. The density in the vapor phase was measured along isotherms at temperatures from 253.15 K to 293.15 K. Each isotherm started at a low pressure (40 to 100 kPa); the pressure was increased in steps by cycling two pneumatic valves piped in series to introduce additional gaseous sample. The dew point was determined by continuing the vapor-phase isotherms into the two-phase region. As the pressure reached the dew point the value of the coupling parameter ϕ in Eq. (A.1-3) increased dramatically because of adsorption and condensation onto the sinkers; the intersection of lines fitted to the single-phase and two-phase data yielded the dew point. This effect and its exploitation for the

measurement of dew points is discussed by McLinden and Richter,[77] and the dew points measured here will be analyzed in the second phase of the project. With this technique the filling/pressure line was completely vapor filled up to the dew-point pressure, minimizing uncertainties in the hydrostatic head correction. An additional advantage is that a dew-point measurement is much less sensitive to the presence of a non-condensable impurity (such as air) compared to a bubble-point measurement. Each isotherm started with a fresh sample.

(*P, ρ, T, x*) *measurement uncertainties.* The measurement uncertainty of the experimental density data measured with the two-sinker densimeter has been evaluated in previous works.[5 78 79] Only a brief description of the main uncertainty sources is given here. The main sources of the uncertainty in density, in order of significance, arose from the sinker volumes (V_1, V_2), the weighings of the sinkers and calibration masses (W_1, W_2, W_{cal}, W_{tare}) and their masses (m_1, m_2, m_{cal}, m_{tare}), and the apparatus zero ρ_0. The variance in the replicate balance readings was also included. The standard uncertainty in the density measurement is given by

$$u\left(r\right)/\mathrm{kg\cdot m^{-3}} = \left[\left\{28\right\}^2 + \left\{0.20\left(T/\mathrm{K} - 293\right)\right\}^2 + \left\{0.63p/\mathrm{MPa}\right\}^2\right]^{1/2} \cdot 10^{-6}\, r/\mathrm{kg\cdot m^{-3}} + 0.0010 \qquad \text{(A.1-4)}$$

where the term in brackets is from the uncertainty in the sinker volumes, and the final, constant term includes all other uncertainties.

The SPRT used to measure the temperature of the mixture was calibrated in our laboratory on ITS-90 from 83 K to 505 K by use of fixed-point cells. The standard uncertainty of the temperature, including the uncertainty in the fixed-point cells, drift in the SPRT and in the standard resistor, and any temperature gradients, is 3 mK. The pressure transducers were calibrated with one of two gas-operated piston gages. We estimated the standard uncertainty in pressure to be ($20\times10^{-6}\cdot p$ + 0.03 kPa) for the vapor-phase measurements and ($26\times10^{-6}\cdot p$ + 1.0 kPa) for the liquid-phase measurements. To the above uncertainty estimates we added the standard deviations actually observed in the multiple temperature, pressure, and balance readings made over the 12 minutes necessary to complete a single density determination.

For mixtures a considerable fraction of the overall density uncertainty is due to uncertainty in the composition. This arises from the gravimetric preparation of the gas mixture used to charge the densimeter, but a larger contribution arose from possible adsorption of sample onto the inner walls of the sample cylinder, filling lines, measuring cell, etc. In other words, the composition in the measuring cell was not necessarily a simple ratio of the component masses loaded into the sample cylinder.

For purposes of comparing (P, ρ, T, x) measurements to a model, it is customary to assume that the temperature, pressure, and composition are known exactly, and to lump all uncertainties into a single value for the density, a so-called state-point uncertainty. This value is tabulated in the data tables for each measured point.

Table A.1-9. Measured (P, ρ, T, x) data for the system R-1234yf/134a at a molar composition of (0.33634/0.66366).

Listed are temperature T, pressure P, density ρ, standard uncertainty in pressure $u(P)$, relative combined, expanded (k = 2) state-point uncertainty in the density U_c, and relative deviation from the mixture EOS Δ_ρ. The standard uncertainty in temperature is 3 mK. Data are presented in the sequence measured. Average values for the replicate measurements at each (T, P) state point are given.

T/K	P/MPa	ρ/ kg·m^{-3}	$u(P)$/kPa	U_c/%	Δ_ρ/%
Vapor-phase					
293.154	0.0645	2.847	0.030	0.139	-0.001
293.156	0.1202	5.369	0.030	0.078	-0.026
293.156	0.1813	8.215	0.030	0.054	-0.032
293.156	0.2435	11.203	0.030	0.037	-0.038
293.156	0.3038	14.196	0.030	0.031	-0.047
293.154	0.3601	17.079	0.030	0.027	-0.058
293.157	0.4207	20.292	0.030	0.024	-0.067
293.157	0.4801	23.564	0.030	0.021	-0.081
293.157	0.5407	27.045	0.030	0.020	-0.100
293.154	0.5781	29.102	0.530	0.172	-0.697
283.158	0.0616	2.819	0.030	0.154	-0.015
283.158	0.1024	4.733	0.030	0.086	-0.024
283.156	0.1513	7.084	0.030	0.057	-0.030
283.155	0.1844	8.710	0.030	0.047	-0.040
283.156	0.2242	10.712	0.030	0.039	-0.043
283.159	0.2682	12.975	0.030	0.036	-0.051
283.159	0.3068	15.018	0.030	0.031	-0.059
283.158	0.3406	16.850	0.030	0.027	-0.070
283.157	0.3810	19.100	0.030	0.025	-0.081
283.158	0.4105	20.780	0.030	0.024	-0.092
273.156	0.0591	2.806	0.030	0.145	-0.026
273.157	0.0854	4.087	0.030	0.099	-0.041
273.158	0.1103	5.314	0.030	0.079	-0.034
273.157	0.1557	7.609	0.030	0.055	-0.045
273.156	0.1557	7.609	0.030	0.055	-0.040
273.157	0.1864	9.198	0.030	0.052	-0.047
273.158	0.2055	10.205	0.030	0.042	-0.051
273.158	0.2323	11.640	0.030	0.038	-0.058
273.156	0.2569	12.982	0.030	0.034	-0.067

Table A.1-9. (continued)

T/K	P/MPa	ρ/ kg·m^{-3}	$u(P)$/kPa	U_c/%	Δ_ρ/%
273.155	0.2866	14.639	0.030	0.031	-0.078
273.157	0.3006	15.435	0.030	0.030	-0.084
273.156	0.3038	15.614	0.030	0.029	-0.089
273.154	0.3099	15.790	0.570	0.364	-1.181
263.157	0.0460	2.260	0.030	0.197	-0.047
263.158	0.0604	2.986	0.030	0.136	-0.041
263.157	0.0803	3.993	0.030	0.103	-0.039
263.160	0.1010	5.060	0.030	0.083	-0.041
263.157	0.1207	6.089	0.030	0.072	-0.046
263.159	0.1410	7.166	0.030	0.061	-0.048
263.159	0.1603	8.206	0.030	0.057	-0.055
263.157	0.1800	9.285	0.030	0.047	-0.061
263.155	0.2014	10.472	0.030	0.042	-0.074
263.155	0.2082	10.855	0.030	0.040	-0.075
263.154	0.2231	11.427	0.590	0.577	-99.106
253.155	0.0439	2.247	0.030	0.188	-0.056
253.157	0.0615	3.169	0.030	0.140	-0.053
253.156	0.0764	3.964	0.030	0.104	-0.055
253.155	0.0908	4.738	0.030	0.089	-0.055
253.157	0.1064	5.585	0.030	0.083	-0.055
253.157	0.1214	6.410	0.030	0.105	-0.082
253.158	0.1310	6.949	0.030	0.065	-0.070
Compressed-liquid and supercritical states					
230.018	1.0576	1377.826	1.150	0.015	-0.127
240.013	4.0960	1357.442	1.880	0.020	-0.123
240.015	2.5156	1353.415	1.770	0.019	-0.121
240.017	1.4521	1350.630	2.110	0.021	-0.121
249.999	10.5097	1346.407	1.720	0.018	-0.122
250.005	8.7756	1341.986	1.630	0.018	-0.121
250.005	7.1237	1337.663	1.670	0.018	-0.120
250.007	5.5507	1333.409	1.340	0.016	-0.119
250.008	4.0542	1329.242	1.490	0.017	-0.118
250.007	1.5142	1321.869	1.600	0.018	-0.116
260.006	9.9755	1318.072	1.880	0.019	-0.116
260.007	9.9631	1318.033	1.310	0.015	-0.116
260.009	8.4079	1313.584	1.720	0.018	-0.115
260.006	5.5221	1304.933	1.650	0.018	-0.114
260.008	4.1796	1300.704	1.540	0.017	-0.113

Table A.1-9. (continued)

T/K	P/MPa	ρ/ kg·m^{-3}	$u(P)$/kPa	U_c/%	Δ_ρ/%
260.007	1.6895	1292.499	1.400	0.016	-0.111
269.996	9.5068	1288.959	1.360	0.015	-0.113
269.999	8.1305	1284.487	1.300	0.015	-0.113
269.998	5.5605	1275.750	1.470	0.016	-0.112
270.000	4.3640	1271.459	1.240	0.015	-0.111
269.999	2.1260	1263.066	1.520	0.016	-0.109
280.001	9.3445	1259.774	1.450	0.016	-0.110
280.002	8.1204	1255.273	1.530	0.016	-0.109
280.004	6.9504	1250.820	1.560	0.017	-0.109
280.002	4.7596	1242.075	1.530	0.016	-0.108
280.002	3.7348	1237.760	1.380	0.015	-0.107
280.002	1.8254	1229.313	1.400	0.016	-0.105
295.002	11.6641	1224.821	1.700	0.017	-0.104
295.004	9.4725	1215.562	1.440	0.016	-0.104
295.002	7.4648	1206.491	1.390	0.015	-0.102
295.005	5.6265	1197.556	1.450	0.016	-0.102
295.003	3.9356	1188.754	1.270	0.015	-0.100
295.006	2.3904	1180.086	1.230	0.015	-0.098
309.994	10.9362	1175.984	1.560	0.016	-0.096
309.995	10.0282	1171.275	1.390	0.015	-0.096
309.994	8.3387	1162.044	1.430	0.016	-0.095
309.994	6.0523	1148.363	1.380	0.015	-0.092
309.994	4.0423	1134.895	1.320	0.015	-0.089
309.994	3.4279	1130.444	1.180	0.014	-0.088
325.000	10.8843	1126.954	1.300	0.015	-0.086
325.003	8.7589	1112.710	1.350	0.015	-0.083
325.000	6.3017	1093.916	1.220	0.015	-0.077
325.000	4.2422	1075.416	1.350	0.016	-0.071
325.002	2.5328	1057.236	1.170	0.015	-0.067
339.995	8.5374	1054.188	1.260	0.015	-0.063
339.995	6.7027	1035.338	1.250	0.015	-0.054
339.996	5.1479	1016.459	1.150	0.015	-0.045
339.998	4.1584	1002.423	1.100	0.015	-0.039
339.995	2.5732	974.714	1.190	0.015	-0.037
344.995	4.1226	973.807	1.120	0.015	-0.023
349.993	5.6823	972.933	1.130	0.015	-0.019
354.997	7.2507	972.074	1.120	0.015	-0.021
359.997	8.8219	971.227	1.160	0.015	-0.027
359.997	7.5859	952.038	1.090	0.015	-0.010

Table A.1-9. (continued)

T/K	P/MPa	ρ/ kg·m^{-3}	$u(P)$/kPa	U_c/%	Δ_ρ/%
359.998	6.1084	923.683	1.100	0.015	0.017
360.000	4.8366	890.821	1.110	0.015	0.045
359.998	3.5802	839.396	1.050	0.015	0.087
364.997	4.5968	838.736	1.050	0.016	0.090
369.997	5.6301	838.098	1.050	0.016	0.082
375.000	6.6755	837.453	1.080	0.016	0.076
379.995	7.7284	836.812	1.060	0.016	0.060
379.996	6.8786	805.893	1.100	0.016	0.095
379.996	6.2346	774.666	1.050	0.016	0.132
379.997	5.1658	681.598	1.050	0.017	0.324
384.996	5.8202	681.229	1.040	0.017	0.259
389.995	6.4842	680.854	1.050	0.017	0.209
394.995	7.1547	680.450	1.050	0.017	0.179
400.001	7.8310	680.027	1.050	0.017	0.154
400.000	7.0690	616.988	1.060	0.018	0.207
399.998	5.9665	460.146	1.050	0.021	0.240
400.000	5.0347	305.067	1.070	0.028	0.072
400.000	3.8496	183.201	1.090	0.043	-0.047
400.000	2.9176	121.603	1.100	0.043	-0.080

Table A.1-10. Measured (*P, ρ, T, x*) data for the system R-1234yf/134a at a molar composition of (0.64709/0.35291).

Listed are temperature *T*, pressure *P*, density *ρ*, standard uncertainty in pressure u(*P*), relative combined, expanded (k = 2) state-point uncertainty in the density Uc, and relative deviation from the mixture EOS. The standard uncertainty in temperature is 3 mK. Data are presented in the sequence measured. Average values for the replicate measurements at each (*T*, *P*) state point are given.

T/K	*P*/MPa	*ρ*/ kg·m^{-3}	*u*(*P*)/kPa	U_c/%	Δ_ρ/%
Vapor-phase					
293.156	0.0660	3.024	0.030	0.126	0.159
293.155	0.1241	5.762	0.030	0.074	0.175
293.154	0.1874	8.833	0.030	0.047	0.179
293.155	0.2418	11.555	0.030	0.037	0.178
293.157	0.3059	14.865	0.030	0.030	0.175
293.155	0.3654	18.045	0.030	0.026	0.169
293.155	0.4237	21.280	0.030	0.023	0.157
293.155	0.4801	24.530	0.030	0.021	0.147
283.154	0.0625	2.968	0.030	0.134	0.175
283.155	0.1042	4.999	0.030	0.081	0.187
283.156	0.1422	6.894	0.030	0.060	0.183
283.158	0.1879	9.226	0.030	0.045	0.181
283.157	0.2286	11.356	0.030	0.037	0.175
283.157	0.2648	13.299	0.030	0.033	0.169
283.156	0.3048	15.499	0.030	0.029	0.162
283.155	0.3462	17.841	0.030	0.026	0.153
283.155	0.3815	19.892	0.030	0.024	0.143
283.155	0.4209	22.247	0.030	0.022	0.130
273.153	0.0674	3.327	0.030	0.121	0.157
273.152	0.0932	4.638	0.030	0.088	0.174
273.153	0.1291	6.498	0.030	0.063	0.169
273.152	0.1513	7.670	0.030	0.055	0.169
273.151	0.1823	9.331	0.030	0.046	0.165
273.152	0.2106	10.885	0.030	0.040	0.157
273.151	0.2449	12.804	0.030	0.035	0.149
273.151	0.2755	14.567	0.030	0.031	0.144
273.152	0.2965	15.794	0.030	0.029	0.137
263.156	0.0442	2.252	0.030	0.182	0.137
263.156	0.0696	3.581	0.030	0.114	0.155
263.156	0.0818	4.224	0.030	0.097	0.159
263.156	0.1050	5.469	0.030	0.076	0.161
263.155	0.1269	6.663	0.030	0.063	0.156

Table A.1-10. (continued)

T/K	P/MPa	ρ/kg·m^{-3}	$u(P)$/kPa	U_c/%	Δ_ρ/%
263.155	0.1476	7.807	0.030	0.054	0.154
263.156	0.1671	8.903	0.030	0.049	0.151
263.154	0.1854	9.953	0.030	0.044	0.144
253.154	0.0413	2.189	0.030	0.191	0.131
253.153	0.0569	3.040	0.030	0.137	0.134
253.155	0.0718	3.859	0.030	0.108	0.141
253.153	0.0861	4.650	0.030	0.090	0.143
253.154	0.1014	5.514	0.030	0.076	0.138
253.154	0.1161	6.352	0.030	0.066	0.139
253.153	0.1302	7.164	0.030	0.060	0.138
Compressed-liquid and supercritical states					
230.002	0.9128	1336.222	2.220	0.023	-0.296
239.998	1.0653	1309.005	1.270	0.016	-0.293
239.998	1.0651	1309.002	1.190	0.016	-0.293
249.997	5.6266	1294.295	1.880	0.020	-0.290
249.998	4.1645	1290.030	1.930	0.020	-0.290
249.999	1.6129	1282.245	1.770	0.019	-0.290
259.997	9.4759	1278.562	1.630	0.018	-0.284
259.999	7.9770	1274.037	1.500	0.017	-0.285
259.997	5.2635	1265.460	1.300	0.016	-0.285
260.000	3.9996	1261.256	1.280	0.015	-0.286
259.999	1.6694	1253.139	1.430	0.017	-0.286
269.994	8.9006	1249.632	1.880	0.019	-0.278
269.997	7.5847	1245.109	1.420	0.016	-0.279
269.997	6.3403	1240.695	1.540	0.017	-0.279
269.998	4.0550	1232.170	1.490	0.017	-0.281
269.998	1.9836	1223.903	1.440	0.016	-0.282
280.001	8.6323	1220.574	1.520	0.017	-0.270
280.001	7.4700	1216.029	1.430	0.016	-0.271
280.001	5.3396	1207.255	1.400	0.016	-0.273
280.003	3.4024	1198.696	1.270	0.015	-0.275
280.003	1.6537	1190.428	1.490	0.016	-0.277
295.003	10.5573	1185.253	1.400	0.016	-0.251
295.004	9.5150	1180.602	1.420	0.016	-0.253
295.003	7.5910	1171.564	1.330	0.015	-0.255
295.006	5.8284	1162.653	1.370	0.015	-0.257
295.003	4.2089	1153.864	1.550	0.017	-0.260
295.003	2.0563	1141.048	1.290	0.015	-0.264

Table A.1-10. (continued)

T/K	P/MPa	ρ/kg·m^{-3}	$u(P)$/kPa	U_c/%	Δ_ρ/%
309.994	9.9069	1137.041	1.290	0.015	-0.229
309.999	8.2737	1127.710	1.360	0.015	-0.231
309.996	6.0974	1114.100	1.390	0.016	-0.235
309.997	4.1899	1100.709	1.350	0.015	-0.239
309.995	2.0299	1083.314	1.550	0.017	-0.248
325.002	8.6630	1079.822	1.250	0.015	-0.204
325.003	8.0388	1075.113	1.260	0.015	-0.204
325.001	5.8320	1056.789	1.300	0.015	-0.209
325.002	3.9881	1038.780	1.290	0.015	-0.216
325.002	2.1196	1016.673	1.290	0.016	-0.237
339.997	7.5364	1013.684	1.220	0.015	-0.173
339.997	5.9387	995.131	1.110	0.015	-0.176
339.997	4.0328	967.738	1.170	0.015	-0.185
339.996	2.6131	940.709	1.120	0.015	-0.211
344.995	4.0305	939.822	1.080	0.015	-0.169
349.994	5.4565	938.943	1.130	0.015	-0.145
354.994	6.8882	938.074	1.110	0.015	-0.132
359.998	8.3244	937.210	1.130	0.015	-0.128
359.998	6.4863	904.331	1.140	0.015	-0.110
359.998	5.0076	867.437	1.070	0.015	-0.086
359.999	3.5874	807.728	1.050	0.016	-0.030
364.998	4.5146	807.093	1.040	0.016	-0.018
369.998	5.4569	806.464	1.050	0.016	-0.016
374.998	6.4088	805.823	1.060	0.016	-0.019
379.998	7.3671	805.162	1.060	0.016	-0.028
379.997	6.5403	772.196	1.070	0.016	0.024
379.998	5.5548	711.581	1.050	0.017	0.162
384.998	5.2432	595.068	1.040	0.018	0.665
389.997	5.7522	594.705	1.040	0.018	0.549
394.997	6.2656	594.329	1.050	0.018	0.485
399.999	6.7830	593.964	1.050	0.018	0.438
400.002	5.8987	475.041	1.050	0.021	0.718
400.001	4.9852	322.447	1.070	0.027	0.759
400.001	3.9472	203.238	1.090	0.040	0.598
400.001	2.7048	115.490	1.100	0.040	0.344
400.003	1.7401	66.680	1.110	0.117	0.139

Table A.1-11. Measured (P, ρ, T, x) data for the system R-134a/1234ze(E) at a molar composition of (0.33250/0.66750).

Listed are temperature T, pressure P, density ρ, standard uncertainty in pressure $u(P)$, relative combined, expanded (k = 2) state-point uncertainty in the density U_c, and relative deviation from the mixture EOS Δ_ρ. The standard uncertainty in temperature is 3 mK. Data are presented in the sequence measured. Average values for the replicate measurements at each (T, P) state point are given.

T/K	P/MPa	ρ/kg·m^{-3}	$u(P)$/kPa	U_c/%	Δ_ρ/%
Vapor-phase					
293.156	0.0577	2.640	0.030	0.160	-0.028
293.156	0.0577	2.640	0.030	0.136	-0.028
293.157	0.1025	4.739	0.030	0.086	-0.040
293.159	0.1415	6.606	0.030	0.057	-0.048
293.159	0.1817	8.574	0.030	0.045	-0.056
293.157	0.2212	10.545	0.030	0.038	-0.071
293.158	0.2624	12.649	0.030	0.033	-0.077
293.157	0.3013	14.681	0.030	0.028	-0.090
293.157	0.3417	16.848	0.030	0.027	-0.102
293.159	0.3807	18.993	0.030	0.024	-0.110
283.155	0.0603	2.864	0.030	0.129	-0.024
283.156	0.0947	4.540	0.030	0.082	-0.038
283.157	0.1255	6.070	0.030	0.062	-0.043
283.155	0.1532	7.466	0.030	0.051	-0.047
283.155	0.1838	9.042	0.030	0.043	-0.055
283.157	0.2107	10.449	0.030	0.038	-0.062
283.158	0.2430	12.172	0.030	0.034	-0.067
283.157	0.2700	13.645	0.030	0.031	-0.072
283.156	0.3015	15.394	0.030	0.029	-0.079
283.157	0.3218	16.544	0.030	0.027	-0.085
283.157	0.3241	16.674	0.030	0.027	-0.085
273.158	0.0496	2.438	0.030	0.154	-0.047
273.155	0.0751	3.720	0.030	0.108	-0.052
273.155	0.1059	5.298	0.030	0.072	-0.051
273.154	0.1269	6.393	0.030	0.060	-0.049
273.155	0.1524	7.744	0.030	0.056	-0.048
273.155	0.1754	8.986	0.030	0.044	-0.050
273.158	0.2011	10.397	0.030	0.040	-0.052
273.160	0.2238	11.666	0.030	0.039	-0.055
263.161	0.0376	1.917	0.030	0.235	-0.057
263.161	0.0628	3.225	0.030	0.122	-0.046
263.158	0.0860	4.454	0.030	0.086	-0.038

Table A.1-11. (continued)

T/K	P/MPa	ρ/kg·m^{-3}	$u(P)$/kPa	U_c/%	Δ_ρ/%
263.156	0.1004	5.231	0.030	0.082	-0.042
263.156	0.1206	6.333	0.030	0.062	-0.042
263.158	0.1452	7.697	0.030	0.052	-0.036
263.160	0.1565	8.337	0.030	0.054	-0.032
253.167	0.0361	1.913	0.030	0.202	-0.084
253.163	0.0455	2.419	0.030	0.159	-0.070
253.163	0.0606	3.244	0.030	0.125	-0.037
253.163	0.0760	4.094	0.030	0.102	-0.045
253.164	0.0905	4.906	0.030	0.081	-0.030
Compressed-liquid and supercritical states					
230.011	0.9398	1379.400	2.120	0.021	0.062
230.011	0.9410	1379.400	2.100	0.021	0.062
230.010	0.9419	1379.406	1.660	0.018	0.062
245.008	14.0799	1368.702	1.800	0.018	0.058
245.008	14.0811	1368.706	1.760	0.018	0.059
245.013	11.8531	1364.114	1.630	0.017	0.066
245.011	7.7630	1355.310	1.920	0.019	0.079
245.012	4.0499	1346.804	1.780	0.018	0.092
245.015	1.3039	1340.152	1.630	0.017	0.103
259.998	15.4284	1335.162	1.960	0.019	0.083
260.001	13.4515	1330.555	1.460	0.016	0.089
260.000	11.5563	1326.008	1.680	0.017	0.095
260.000	8.0156	1317.092	1.350	0.015	0.107
260.001	3.2734	1304.149	1.750	0.018	0.125
260.002	1.8344	1299.957	1.250	0.015	0.131
279.999	18.6289	1294.065	1.580	0.016	0.099
280.001	15.1498	1284.619	1.560	0.016	0.109
280.002	11.9530	1275.346	1.400	0.015	0.119
280.002	7.6361	1261.735	1.470	0.016	0.135
280.002	3.8418	1248.486	1.550	0.016	0.150
280.004	1.5807	1239.867	1.480	0.016	0.161
304.997	19.1999	1233.418	1.480	0.015	0.116
304.998	16.3852	1223.766	1.640	0.016	0.124
304.998	12.5771	1209.525	1.390	0.015	0.135
304.997	8.1740	1190.906	1.500	0.016	0.151
304.997	4.4491	1172.670	1.630	0.016	0.169
304.997	1.3206	1154.826	1.480	0.016	0.187
309.996	4.0730	1153.572	1.410	0.015	0.176

Table A.1-11. (continued)

T/K	P/MPa	ρ/kg·m^{-3}	$u(P)$/kPa	U_c/%	Δ_ρ/%
319.988	9.5781	1151.337	1.380	0.015	0.156
329.988	15.0585	1149.270	1.260	0.015	0.141
339.994	20.5178	1147.397	1.500	0.016	0.130
339.994	15.6051	1122.887	1.480	0.016	0.146
339.994	12.3123	1103.560	1.400	0.015	0.161
339.994	8.2775	1074.984	1.430	0.016	0.188
339.997	4.2837	1037.485	1.120	0.015	0.235
339.994	2.4419	1014.334	1.200	0.015	0.268
349.993	6.0374	1012.627	1.140	0.015	0.240
359.995	9.6560	1011.043	1.100	0.015	0.206
369.995	13.2786	1009.529	1.130	0.015	0.179
379.994	16.8942	1008.053	1.160	0.016	0.159
379.994	13.7847	978.472	1.200	0.016	0.178
379.994	10.9640	944.282	1.170	0.016	0.207
379.996	8.1076	895.878	1.090	0.016	0.266
379.996	5.0537	795.139	1.090	0.016	0.455
384.994	5.9657	794.626	1.060	0.016	0.381
389.994	6.8886	794.099	1.060	0.016	0.317
394.993	7.8191	793.564	1.060	0.016	0.270
399.997	8.7563	793.013	1.070	0.017	0.237
399.998	7.2821	727.654	1.080	0.017	0.252
399.998	6.1369	629.406	1.080	0.018	0.148
399.998	5.0684	399.697	1.100	0.022	-1.144
399.998	3.8715	206.293	1.120	0.037	-0.785
399.998	2.5928	110.897	1.130	0.037	-0.431

Table A.1-12. Measured (P, ρ, T, x) data for the system R-134a/1234ze(E) at a molar composition of (0.66356/0.33644).

Listed are temperature T, pressure P, density ρ, standard uncertainty in pressure $u(P)$, relative combined, expanded (k = 2) state-point uncertainty in the density U_c, and relative deviation from the mixture EOS Δ_ρ. The standard uncertainty in temperature is 3 mK. Data are presented in the sequence measured. Average values for the replicate measurements at each (T, P) state point are given.

T/K	P/MPa	ρ/kg·m^{-3}	$u(P)$/kPa	U_c/%	Δ_ρ/%
Vapor-phase					
293.154	0.0537	2.364	0.030	0.152	-0.057
293.157	0.1002	4.458	0.030	0.083	-0.062
293.158	0.1512	6.808	0.030	0.059	-0.063
293.160	0.2037	9.290	0.030	0.042	-0.076
293.159	0.2550	11.783	0.030	0.034	-0.092
293.159	0.3029	14.175	0.030	0.030	-0.106
293.158	0.3501	16.597	0.030	0.026	-0.121
293.157	0.4017	19.330	0.030	0.024	-0.139
293.159	0.4503	21.986	0.030	0.023	-0.159
293.158	0.4808	23.697	0.030	0.021	-0.174
283.154	0.0511	2.329	0.030	0.175	-0.064
283.155	0.1060	4.903	0.030	0.078	-0.065
283.157	0.1536	7.203	0.030	0.054	-0.072
283.157	0.2028	9.644	0.030	0.041	-0.081
283.158	0.2510	12.108	0.030	0.034	-0.093
283.158	0.3013	14.762	0.030	0.029	-0.109
283.158	0.3528	17.573	0.030	0.026	-0.135
273.158	0.0489	2.313	0.030	0.168	-0.083
273.156	0.0815	3.895	0.030	0.101	-0.060
273.156	0.1208	5.844	0.030	0.067	-0.062
273.155	0.1640	8.046	0.030	0.048	-0.073
273.157	0.2017	10.021	0.030	0.048	-0.079
273.158	0.2410	12.141	0.030	0.035	-0.095
263.158	0.0468	2.302	0.030	0.168	-0.073
263.157	0.0780	3.880	0.030	0.105	-0.067
263.156	0.1066	5.359	0.030	0.073	-0.066
263.154	0.1329	6.745	0.030	0.058	-0.069
263.154	0.1571	8.047	0.030	0.055	-0.073
263.154	0.1722	8.874	0.030	0.046	-0.075
253.162	0.0449	2.301	0.030	0.205	-0.092
253.159	0.0651	3.361	0.030	0.129	-0.076
253.158	0.0933	4.875	0.030	0.091	-0.068

Table A.1-12. (continued)

T/K	P/MPa	ρ/kg·m^{-3}	$u(P)$/kPa	U_c/%	Δ_ρ/%
Compressed-liquid and supercritical states					
230.010	0.9663	1402.623	4.570	0.037	0.095
230.008	0.9667	1402.628	5.590	0.044	0.095
230.009	0.9687	1402.626	4.200	0.034	0.095
245.011	12.0546	1386.704	1.590	0.017	0.094
245.011	12.0502	1386.694	1.780	0.018	0.094
245.015	9.9508	1382.143	1.490	0.016	0.100
245.013	7.9659	1377.720	1.510	0.017	0.107
245.012	4.2868	1369.139	1.610	0.017	0.120
245.015	1.4248	1362.070	1.840	0.018	0.132
260.002	15.7691	1356.809	1.700	0.017	0.108
260.003	14.0267	1352.679	1.400	0.016	0.113
260.005	12.1367	1348.071	1.710	0.017	0.119
260.003	8.6023	1339.042	1.840	0.018	0.131
260.004	3.8613	1325.928	1.660	0.017	0.150
260.007	1.3603	1318.456	1.170	0.015	0.162
280.000	18.3310	1312.269	1.910	0.018	0.121
280.001	14.9348	1302.734	1.580	0.016	0.130
280.003	11.8171	1293.387	1.540	0.016	0.141
280.002	7.6042	1279.684	1.550	0.016	0.158
280.003	3.8966	1266.338	1.450	0.016	0.177
280.008	1.6837	1257.638	1.280	0.015	0.190
304.999	19.5685	1250.996	1.420	0.015	0.129
304.999	15.4975	1236.449	1.530	0.016	0.141
304.999	11.8883	1222.160	1.320	0.015	0.156
304.999	7.7059	1203.446	1.400	0.015	0.177
304.999	4.1635	1185.110	1.320	0.015	0.203
304.999	1.8789	1171.601	1.170	0.014	0.225
314.993	7.4883	1169.120	1.190	0.014	0.187
339.999	21.4741	1164.055	1.370	0.015	0.127
339.996	15.6947	1134.447	1.480	0.016	0.150
339.996	11.8006	1110.170	1.280	0.015	0.176
339.998	8.0476	1081.430	1.190	0.015	0.217
339.998	3.9440	1038.952	1.150	0.015	0.301
339.997	2.3054	1015.611	1.160	0.015	0.360
349.993	5.8381	1013.890	1.090	0.015	0.295
359.998	9.4056	1012.324	1.090	0.015	0.238
369.995	12.9837	1010.853	1.180	0.015	0.193
379.996	16.5642	1009.426	1.140	0.016	0.159

Table A.1-12. (continued)

T/K	P/MPa	ρ/kg·m^{-3}	$u(P)$/kPa	U_c/%	Δ_ρ/%
379.997	14.1225	984.560	1.210	0.016	0.186
379.997	11.0710	945.135	1.110	0.016	0.238
379.998	7.9933	886.503	1.080	0.016	0.339
379.998	5.1088	765.284	1.070	0.016	0.608
384.995	5.9414	764.838	1.050	0.016	0.491
389.995	6.7865	764.397	1.060	0.016	0.408
394.995	7.6408	763.955	1.060	0.017	0.346
399.999	8.5025	763.500	1.070	0.017	0.301
399.998	6.0366	536.798	1.780	0.026	-0.164
400.003	3.7066	175.446	1.120	0.042	-0.615
400.001	1.5024	54.037	1.140	0.131	-0.361

Table A.1-13. Measured (P, ρ, T, x) data for the system R-1234yf/1234ze(E) at a molar composition of (0.33584/0.66416).

Listed are temperature T, pressure P, density ρ, standard uncertainty in pressure $u(P)$, relative combined, expanded (k = 2) state-point uncertainty in the density U_c, and relative deviation from the mixture EOS Δ_ρ. The standard uncertainty in temperature is 3 mK. Data are presented in the sequence measured. Average values for the replicate measurements at each (T, P) state point are given.

T/K	P/MPa	ρ/kg·m^{-3}	$u(P)$/kPa	U_c/%	Δ_ρ/%
Vapor-phase					
293.153	0.1061	5.092	0.030	0.075	-0.050
293.154	0.1509	7.323	0.030	0.060	-0.051
293.158	0.2004	9.856	0.030	0.042	-0.056
293.159	0.2535	12.651	0.030	0.035	-0.062
293.158	0.3023	15.303	0.030	0.029	-0.072
293.156	0.3517	18.067	0.030	0.026	-0.076
293.156	0.3755	19.431	0.030	0.025	-0.079
293.156	0.4052	21.172	0.030	0.023	-0.082
293.158	0.4144	21.715	0.030	0.023	-0.081
293.159	0.4193	22.010	0.030	0.023	-0.079
283.150	0.0765	3.784	0.030	0.104	-0.054
283.150	0.1235	6.190	0.030	0.064	-0.047
283.150	0.1635	8.289	0.030	0.049	-0.049
283.150	0.2026	10.400	0.030	0.040	-0.048
283.150	0.2436	12.667	0.030	0.034	-0.053
283.150	0.2626	13.743	0.030	0.032	-0.052
283.152	0.2826	14.887	0.030	0.031	-0.049
283.153	0.3025	16.048	0.030	0.028	-0.050
283.153	0.3172	16.913	0.030	0.027	-0.048
283.154	0.3319	17.791	0.030	0.026	-0.046
273.157	0.0565	2.884	0.030	0.143	-0.095
273.156	0.0813	4.182	0.030	0.098	-0.070
273.156	0.1041	5.396	0.030	0.076	-0.057
273.158	0.1251	6.533	0.030	0.068	-0.048
273.157	0.1506	7.934	0.030	0.055	-0.047
273.157	0.1789	9.520	0.030	0.045	-0.040
273.158	0.2038	10.942	0.030	0.041	-0.037
273.159	0.2259	12.228	0.030	0.036	-0.030
263.155	0.0592	3.149	0.030	0.129	-0.067
263.153	0.0824	4.421	0.030	0.093	-0.056
263.154	0.1038	5.616	0.030	0.077	-0.046
263.155	0.1236	6.739	0.030	0.063	-0.036

Table A.1-13. (continued)

T/K	P/MPa	ρ/kg·m^{-3}	$u(P)$/kPa	U_c/%	Δ_ρ/%
263.156	0.1420	7.797	0.030	0.054	-0.027
253.155	0.0395	2.173	0.030	0.191	-0.082
253.152	0.0631	3.506	0.030	0.119	-0.060
253.153	0.0849	4.760	0.030	0.091	-0.031
253.153	0.1050	5.942	0.030	0.071	-0.024
Compressed-liquid and supercritical states					
230.007	0.8784	1338.848	1.230	0.016	0.046
230.004	0.8783	1338.855	1.250	0.016	0.046
240.002	6.0634	1325.128	2.100	0.022	0.054
240.004	4.2970	1321.033	1.400	0.017	0.057
240.008	2.6142	1317.007	1.460	0.017	0.060
240.003	1.2209	1313.598	1.480	0.017	0.062
240.001	1.2191	1313.601	1.610	0.018	0.062
250.000	10.2447	1310.027	1.480	0.017	0.060
250.002	8.6454	1306.194	1.480	0.017	0.063
250.001	5.2840	1297.786	2.080	0.021	0.069
250.001	2.2462	1289.697	1.780	0.019	0.074
250.001	1.2160	1286.830	1.750	0.019	0.075
259.997	9.4609	1283.176	1.740	0.018	0.073
259.999	7.8656	1278.858	1.380	0.016	0.075
259.999	6.3383	1274.596	1.540	0.017	0.077
259.997	3.4945	1266.270	1.650	0.018	0.081
259.999	1.2243	1259.202	1.740	0.019	0.085
269.995	8.9145	1255.977	1.660	0.017	0.082
269.996	7.4945	1251.634	1.300	0.015	0.084
269.999	6.1360	1247.333	1.480	0.016	0.086
269.995	3.5968	1238.910	1.520	0.017	0.089
269.998	1.3080	1230.781	1.450	0.016	0.091
280.000	8.3907	1227.760	1.350	0.015	0.091
280.003	7.1400	1223.389	1.350	0.015	0.092
280.002	4.7940	1214.791	1.480	0.016	0.094
280.004	2.6525	1206.367	1.240	0.015	0.096
280.004	1.6537	1202.235	1.430	0.016	0.096
295.003	11.4293	1198.217	1.320	0.015	0.100
295.003	9.1249	1189.218	1.320	0.015	0.101
295.005	6.0230	1175.988	1.240	0.015	0.102
295.006	4.1645	1167.315	1.200	0.014	0.102
295.005	1.6701	1154.569	1.250	0.015	0.100

Table A.1-13. (continued)

T/K	P/MPa	ρ/kg·m^{-3}	$u(P)$/kPa	U_c/%	Δ_ρ/%
310.001	10.1305	1150.870	1.280	0.015	0.114
310.003	8.2970	1141.824	1.120	0.014	0.114
310.002	5.8188	1128.430	1.210	0.015	0.112
310.005	4.3376	1119.616	1.200	0.015	0.110
310.000	1.7391	1102.274	1.250	0.015	0.102
314.997	4.1433	1101.096	1.160	0.014	0.113
319.994	6.5521	1100.014	1.100	0.014	0.122
324.992	8.9552	1098.971	1.160	0.014	0.131
324.993	6.8863	1085.356	1.130	0.014	0.129
324.994	5.0663	1071.889	1.170	0.014	0.126
324.994	3.4730	1058.570	1.170	0.015	0.120
324.995	1.6643	1041.020	1.090	0.014	0.106
329.991	3.6505	1040.015	1.120	0.014	0.127
334.990	5.6441	1039.089	1.140	0.015	0.142
339.997	7.6437	1038.200	1.150	0.015	0.151
339.998	6.1682	1024.498	1.100	0.014	0.151
339.999	4.8763	1010.886	1.110	0.014	0.149
340.000	3.4110	992.892	1.100	0.015	0.143
339.999	1.9412	970.611	1.150	0.015	0.124
349.995	5.1155	968.963	1.090	0.015	0.172
359.999	8.3222	967.480	1.080	0.015	0.178
360.000	7.2697	953.571	1.110	0.015	0.184
360.001	6.0691	935.147	1.080	0.015	0.193
360.002	5.0693	916.771	1.070	0.015	0.204
360.001	4.0665	893.911	1.080	0.015	0.223
370.001	6.5744	892.621	1.060	0.015	0.204
379.996	9.1111	891.418	1.070	0.015	0.173
379.997	7.5159	858.682	1.100	0.016	0.191
380.000	6.0718	816.850	1.070	0.016	0.227
379.998	5.0507	770.576	1.070	0.016	0.192
380.000	4.0343	659.766	1.070	0.017	0.172
384.996	4.6155	659.407	1.050	0.017	0.117
389.997	5.2102	659.054	1.050	0.017	0.090
394.994	5.8136	658.681	1.050	0.017	0.203
400.001	6.4252	658.305	1.080	0.018	0.185
400.001	5.4776	532.489	1.060	0.019	-0.032
400.002	4.1094	250.120	1.090	0.033	-0.514
399.997	2.7673	127.701	1.100	0.033	-0.284
400.005	1.6855	67.553	1.110	0.115	-0.309
400.002	0.9735	36.215	1.520	0.405	-0.408

Table A.1-14. Measured (P, ρ, T, x) data for the system R-1234yf/1234ze(E) at a molar composition of (0.66660/0.33340).

Listed are temperature T, pressure P, density ρ, standard uncertainty in pressure $u(P)$, relative combined, expanded (k = 2) state-point uncertainty in the density U_c, and relative deviation from the mixture EOS Δ_ρ. The standard uncertainty in temperature is 3 mK. Data are presented in the sequence measured. Average values for the replicate measurements at each (T, P) state point are given.

T/K	P/MPa	ρ/kg·m^{-3}	$u(P)$/kPa	U_c/%	Δ_ρ/%
Vapor-phase					
293.149	0.0630	2.989	0.030	0.129	-0.033
293.149	0.1234	5.943	0.030	0.066	-0.037
293.150	0.1856	9.084	0.030	0.051	-0.050
293.150	0.2442	12.136	0.030	0.035	-0.061
293.151	0.3014	15.222	0.030	0.031	-0.078
293.153	0.3596	18.472	0.030	0.025	-0.094
293.153	0.4200	21.977	0.030	0.025	-0.110
281.157	0.0508	2.512	0.030	0.194	-0.040
281.157	0.1027	5.151	0.030	0.089	-0.044
281.157	0.1533	7.806	0.030	0.052	-0.055
281.156	0.2005	10.359	0.030	0.040	-0.065
281.158	0.2515	13.204	0.030	0.038	-0.075
281.161	0.3025	16.160	0.030	0.032	-0.086
281.160	0.3251	17.506	0.030	0.027	-0.087
281.160	0.3451	18.717	0.030	0.025	-0.089
273.156	0.0564	2.879	0.030	0.173	-0.055
273.155	0.0900	4.640	0.030	0.088	-0.053
273.156	0.1201	6.254	0.030	0.069	-0.052
273.156	0.1595	8.420	0.030	0.050	-0.061
273.155	0.1933	10.320	0.030	0.048	-0.067
273.158	0.2131	11.461	0.030	0.039	-0.068
273.153	0.2310	12.503	0.030	0.038	-0.075
273.154	0.2511	13.692	0.030	0.033	-0.073
263.154	0.0523	2.775	0.030	0.149	-0.068
263.155	0.0770	4.120	0.030	0.099	-0.054
263.155	0.1069	5.786	0.030	0.077	-0.055
263.154	0.1207	6.567	0.030	0.063	-0.056
263.152	0.1401	7.678	0.030	0.055	-0.056
263.152	0.1637	9.054	0.030	0.049	-0.064
263.151	0.1799	10.015	0.030	0.043	-0.062
253.155	0.0368	2.019	0.030	0.212	-0.077
253.152	0.0614	3.408	0.030	0.126	-0.062

Table A.1-14. (continued)

T/K	P/MPa	ρ/kg·m^{-3}	$u(P)$/kPa	U_c/%	Δ_ρ/%
253.152	0.0842	4.714	0.030	0.095	-0.059
253.152	0.1051	5.941	0.030	0.071	-0.058
253.154	0.1102	6.246	0.030	0.074	-0.060
253.157	0.1202	6.842	0.030	0.063	-0.057
Compressed-liquid and supercritical states					
230.014	0.9578	1320.352	1.630	0.019	0.070
230.012	0.9575	1320.359	1.500	0.018	0.070
230.010	0.9583	1320.366	1.670	0.019	0.070
240.008	5.5444	1305.661	1.480	0.017	0.070
240.011	5.5463	1305.663	1.340	0.016	0.071
240.013	3.9585	1301.686	2.170	0.023	0.074
240.011	2.4590	1297.830	1.400	0.017	0.077
240.010	1.2698	1294.682	4.020	0.038	0.080
250.004	9.6755	1290.781	1.790	0.019	0.072
250.006	8.0610	1286.603	1.340	0.016	0.074
250.004	5.0435	1278.444	1.660	0.018	0.080
250.007	2.3030	1270.555	1.400	0.017	0.085
250.007	1.2491	1267.385	2.250	0.023	0.087
260.000	9.0427	1263.765	1.520	0.017	0.081
260.001	7.6043	1259.563	1.210	0.015	0.083
260.004	6.2283	1255.416	1.370	0.016	0.085
260.002	2.4583	1243.330	1.860	0.019	0.092
260.003	1.3290	1239.466	1.250	0.015	0.094
269.998	8.5423	1236.120	1.580	0.017	0.090
269.999	7.2638	1231.889	1.380	0.016	0.092
270.001	6.0400	1227.696	1.540	0.017	0.094
269.997	3.7481	1219.475	1.490	0.017	0.097
270.002	1.6598	1211.443	1.280	0.015	0.100
279.999	8.3244	1208.371	1.500	0.016	0.100
280.003	7.1923	1204.103	1.220	0.015	0.101
280.001	5.0620	1195.688	1.300	0.015	0.104
280.004	3.1089	1187.411	1.250	0.015	0.106
280.001	1.3268	1179.339	1.580	0.017	0.108
295.004	10.4177	1175.186	1.340	0.015	0.117
295.003	8.3964	1166.449	1.410	0.016	0.119
295.004	7.4455	1162.109	1.230	0.015	0.120
295.004	5.6599	1153.532	1.250	0.015	0.122
295.005	3.2518	1140.885	1.250	0.015	0.123

Table A.1-14. (continued)

T/K	P/MPa	ρ/kg·m^{-3}	$u(P)$/kPa	U_c/%	Δ_ρ/%
295.004	2.5156	1136.726	1.220	0.015	0.123
309.998	10.5000	1132.914	1.340	0.015	0.142
310.002	8.8111	1124.052	1.320	0.015	0.144
310.000	6.5191	1110.918	1.360	0.016	0.146
310.001	4.4981	1097.962	1.230	0.015	0.147
310.004	3.2886	1089.421	1.170	0.015	0.146
310.000	1.6602	1076.765	1.490	0.017	0.142
314.996	3.8770	1075.564	1.360	0.016	0.155
319.993	6.0927	1074.429	1.220	0.015	0.166
324.992	8.3118	1073.367	1.260	0.015	0.174
324.994	7.0981	1064.512	1.350	0.016	0.176
324.994	4.9574	1046.987	1.300	0.015	0.177
324.996	3.5777	1033.973	1.220	0.015	0.175
324.994	1.6530	1012.488	1.450	0.017	0.159
329.990	3.4644	1011.475	1.160	0.015	0.184
334.990	5.2816	1010.507	1.160	0.015	0.200
339.996	7.1043	1009.576	1.100	0.014	0.208
339.998	5.8662	996.239	1.100	0.015	0.212
340.000	5.1260	987.381	1.190	0.015	0.213
339.999	3.5439	965.403	1.210	0.015	0.211
339.999	2.0871	939.259	1.150	0.015	0.200
349.997	4.9567	937.639	1.130	0.015	0.247
360.000	7.8541	936.080	1.140	0.015	0.242
360.002	7.2613	927.025	1.130	0.015	0.249
360.001	5.9880	904.517	1.170	0.016	0.269
360.001	4.9740	882.133	1.090	0.015	0.295
360.001	4.0423	855.376	1.060	0.015	0.338
364.999	5.1397	854.591	1.050	0.015	0.315
369.997	6.2494	853.933	1.080	0.016	0.289
374.999	7.3667	853.266	1.060	0.016	0.259
379.996	8.4858	852.569	1.130	0.016	0.231
379.998	7.5529	829.783	1.090	0.016	0.254
380.001	7.0689	815.792	1.050	0.016	0.270
380.000	6.0517	778.564	1.060	0.016	0.326
379.999	5.0385	718.365	1.050	0.017	0.431
384.997	4.7731	602.491	1.050	0.018	0.548
389.997	5.2796	602.119	1.050	0.018	0.451
394.994	5.7916	601.753	1.050	0.018	0.400
399.998	6.3086	601.368	1.050	0.018	0.370

Table A.1-14. (continued)

T/K	P/MPa	ρ/kg·m^{-3}	$u(P)$/kPa	U_c/%	Δ_ρ/%
400.002	5.5254	486.233	1.060	0.020	0.153
400.003	5.0718	394.718	1.070	0.023	-0.169
400.002	4.3633	273.239	1.080	0.031	-0.186
400.004	3.8560	213.394	1.090	0.038	-0.099
400.002	3.1672	153.911	1.100	0.039	-0.092
400.005	2.7375	124.515	1.100	0.039	-0.138
400.004	2.2406	95.385	1.110	0.039	-0.193
400.005	1.6796	67.018	1.110	0.115	-0.230

A.1.3. Liquid-Phase Speed of Sound

Speed of sound instrument description. The speed of sound was measured over wide ranges of temperature and pressure in a dual-path, pulse-echo-type instrument. In this technique, a piezoelectric transducer is located within a sample volume of the test fluid. It is excited with a sinusoidal burst, near the crystal resonance frequency, thus emitting ultrasonic pulses from each face of the crystal, which travel through the fluid sample, reflect off planar surfaces at each end of the sample volume, and return to the transducer, which also serves as the detector. The difference in the arrival times of the echo signals give the speed of sound by

$$w = \frac{2(L_2 - L_1)}{\Delta t} \tag{A.1-5}$$

where w is the speed of sound, L_1 and L_2 are the path lengths, and Δt is the time difference. The differential nature of this technique cancels end effects and improves the accuracy.

A quartz crystal with a diameter of 24 mm, thickness of 0.36 mm, and resonant frequency of 8.000 MHz served as the ultrasonic transducer. The quartz crystal is “X-cut,” which means that its thickness expands and contracts when a voltage is applied to electrodes on opposite faces of the crystal. It was excited with a 10-cycle sinusoidal burst from an arbitrary function generator. The fluid path lengths on the opposite faces of the crystal were 30 mm and 12 mm (ratio of 2.5:1); these separations of the crystal and the reflectors were provided by tubular spacers fabricated of a machinable ceramic. A high-speed switch connected the crystal to the function generator during the input sinusoidal burst and then, after a delay of 6 μs, switched the crystal to the input of a three-stage amplifier (5× per stage for a total of 125×), which then fed into a digital storage oscilloscope. The echo signals were recorded for off-line analysis.

Figure A.1-4. Dual-path, pulse-echo, speed of sound instrument.

The figure shows the thermostat (left of center, which contains the measuring cell) and the fluid manifold and pressure transducer, and a vacuum system for evacuating the measuring cell (to the left of the thermostat).

The measuring cell holding the crystal and fluid sample was contained in a pressure vessel rated to 93 MPa. This, in turn, was held in a thermostated liquid bath operating from –45 ˚C to 150 ˚C. A photo of the bath and associated fluid-handling manifold is shown as Figure A.1-4. A photo of the instruments (which are located in the adjacent room) is shown as Figure A.1-5. A schematic of the measuring cell is shown as Figure A.1-6.

The temperature of the fluid bath was measured with a long-stem 25-ohm standard platinum resistance thermometer (SPRT); the temperature-sensing portion of the SPRT was located immediately adjacent to the pressure vessel, as indicated in Figure A.1-6. The resistance of the SPRT was ratioed to a standard resistor with an AC resistance bridge. The pressure was measured with a vibrating-quartz-crystal pressure transducer with a maximum pressure of 138 MPa. The transducer was held at room temperature.

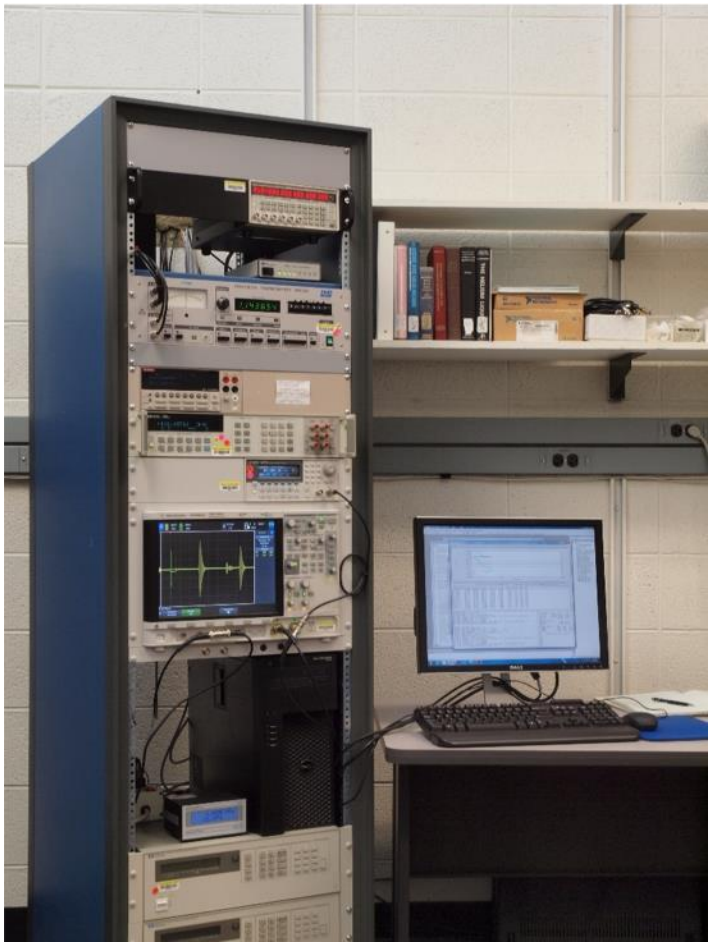

Figure A.1-5. Instrument rack for the pulse-echo speed of sound instrument.

Speed of sound measurement sequence. The entire experiment was controlled by a PC running a custom control program. At each (*T*, *P*) state point multiple echo signals were recorded and analyzed. The pressure of the fluid sample and the temperature of the thermostat bath were scanned every 30 s. The approach to equilibrium conditions was determined by monitoring three quantities: (1) the difference of the average temperature computed over the previous eight scans compared to the set-point temperature; (2) the standard deviation of the previous eight temperature scans; (3) the rate of change of pressure with time, computed with a linear fit of the previous eight pressure readings. When all three of these were within preset tolerances a "converged" flag was set in the control program, and measurements commenced following an additional equilibration time of 20 minutes.

A single measurement set comprised recording three echo signals and the four temperature and pressure readings made at the start and end of the set and between the recording of the echoes. Four such sets, spaced 10 minutes apart, were recorded before moving to the next (*T*, *P*) state point. These raw data were analyzed with a separate program to generate the (*T*, *P*, *w*) data points.

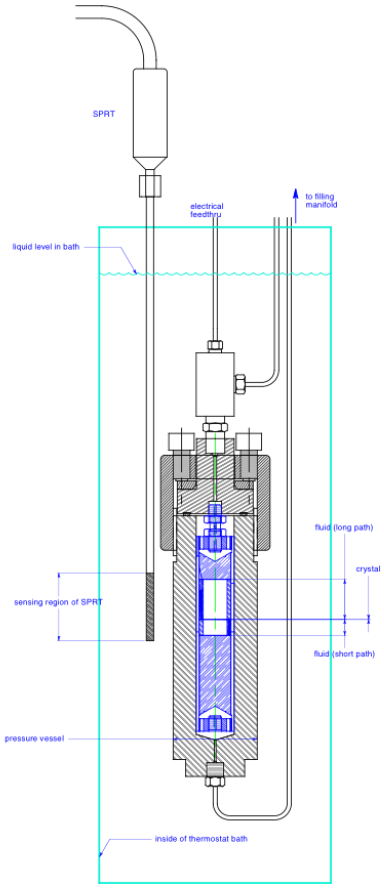

Figure A.1-6. Schematic diagram of the measuring cell inside the pressure vessel.

When measurements at the first temperature were completed, the temperature was increased by an increment of 5 K or 10 K; since the cell was completely filled with liquid, the increase in temperature also increased the pressure. Measurements continued along this pseudoisochore (line of nearly constant density) until either the desired maximum temperature or maximum pressure was reached. The bath was then cooled to the starting temperature of the next isochore, and a portion of the sample in the measuring cell was vented to a waste bottle to achieve a starting pressure for the next isochore of 1 MPa or the saturation pressure (whichever was greater). The next isochore then commenced. This process was repeated to cover the liquid surface.

Speed of sound calibrations and measurement uncertainties. The difference of the path lengths in the measuring cell, i.e., $(L_2 - L_1)$ in Eq. (A.1-4), was calibrated as a function of temperature and pressure with measurements on propane over the temperature range of 260 K to 420 K, with pressures to 56 MPa. The propane speed of sound, as calculated with the equation of state (EOS) of Lemmon et al.[80], was taken as the known quantity in the calibration. The EOS, in turn, represents the high-accuracy propane measurements of Meier and Kabelac [81] with an average absolute deviation of 0.012 %. The RMS deviation of the calibration equation from the measurements was 0.010 %. Combining, in quadrature, the deviation of the EOS from the data of Meier and Kabelac [81] with the deviation of the path-

length calibration equation from the present measurements yields an estimated combined standard uncertainty of 0.016 % in our speed of sound measurements.

The SPRT, standard resistor, and resistance bridge were calibrated as a system over the range of 234.316 K to 429.749 K (–38.834 ˚C to 156.599 ˚C) with fixed-point cells (mercury triple point, water triple point, and indium freezing point). The standard uncertainty in the SPRT/resistor/bridge system was estimated as 3 mK. The short-term (minute-to-minute) variations in the fluid-bath temperature were 2 mK or less. No long-term (hour-to-hour) variation was observed. The temperature gradients in the bath were less than 2.5 mK over the region of the pressure vessel. The combined standard (k = 1) uncertainty in the temperature measurement, including the effects of the SPRT, standard resistor, resistance bridge, calibration standards, stability of the fluid bath, and temperature gradients in the bath was 4 mK.

The pressure transducer was calibrated by the manufacturer with piston gages; this calibration included a temperature-compensation term. The zero of the transducer was checked regularly (while the system was evacuated between samples) and readings were corrected for any drift in the zero. The standard uncertainty in pressure was 0.007 MPa.

When reporting the uncertainties in experimental data it is customary to combine the effects of the state-point uncertainty (i.e., the effects of the uncertainties in temperature, pressure, and composition) with those in the uncertainty of the primary measurand (i.e., the speed of sound):

$$U_c(w) = 2 \times 100 \times \left\{ u^2(w) + \left[\frac{\partial w}{\partial T}\right]^2 u^2(T) + \left[\frac{\partial w}{\partial p}\right]^2 u^2(P) \right\} / w \ , \qquad \text{(A.1-6)}$$

where the $u(x)$ are the standard (k = 1) uncertainties in the different measurands (temperature, pressure, and speed of sound), the derivatives of the speed of sound with temperature and pressure are computed with an equation of state. The coverage factor of 2 corresponds to a 95 % confidence interval, and the factor of 100 converts the relative deviation to a percentage deviation. The $U_c(w)$ is the relative, combined, expanded (k = 2) uncertainty in the speed of sound; it averaged 0.07 % for the present measurements.

Speed of sound results. The measurements carried out are depicted in Figure 3.1-2. The measured data, as well as the relative, combined, expanded (k = 2) uncertainty in the speed of sound for each point, are reported in Tables A.1-15 through A.1-20. As indicated above, the data in these tables are the averages of four sets of three replicates each.

Table A.1-15. Measured speed of sound data for the system R-1234yf/134a at a molar composition of (0.33634/0.66366).

Listed are temperature *T*, pressure *P*, speed of sound *w*, relative combined, expanded ($k = 2$) state point uncertainty in the speed of sound U_c, and relative deviation from the mixture EOS. Average values for the replicate measurements at each (*T*, *P*) state point are given. The different isochores are separated by blank lines.

T/K	*P*/MPa	*w*/m·s^{-1}	U_c/%	Δ_w/%
230.013	0.353	790.84	0.041	0.126
235.007	0.658	769.59	0.041	0.164
240.004	0.678	746.67	0.042	0.192
245.004	0.690	723.74	0.044	0.209
250.005	0.704	700.89	0.046	0.217
254.995	1.231	682.11	0.047	0.227
259.987	5.247	689.09	0.045	0.131
264.996	9.178	695.40	0.044	0.055
254.993	0.651	677.79	0.048	0.240
259.986	4.420	683.24	0.046	0.150
264.996	8.392	690.07	0.045	0.067
269.993	12.399	697.15	0.043	-0.002
259.986	1.278	659.86	0.049	0.226
264.995	5.122	666.92	0.047	0.130
269.993	9.068	674.67	0.046	0.049
274.996	12.964	681.96	0.044	-0.012
264.994	1.260	637.06	0.052	0.224
269.991	4.977	644.66	0.050	0.128
274.995	8.710	652.21	0.048	0.049
279.999	12.442	659.66	0.046	-0.014
269.991	1.167	613.65	0.055	0.223
274.995	4.716	621.41	0.053	0.131
280.000	8.276	629.11	0.050	0.054
285.001	11.853	636.78	0.048	-0.011
274.993	1.193	591.14	0.059	0.215
279.999	4.586	599.13	0.056	0.129
285.000	7.981	606.95	0.053	0.056
290.003	11.378	614.61	0.051	-0.003

Table A.1-15. (continued)

T/K	P/MPa	w/m·s^{-1}	U_c/%	Δ_w/%
279.998	0.890	565.36	0.064	0.212
285.000	4.124	573.74	0.060	0.131
290.003	7.359	581.87	0.057	0.066
294.998	10.590	589.77	0.054	0.012
284.998	1.183	545.28	0.068	0.198
290.001	4.259	553.65	0.064	0.126
294.997	7.347	561.90	0.060	0.068
299.998	10.440	569.91	0.057	0.019
290.000	1.199	522.32	0.074	0.186
294.997	4.134	531.05	0.069	0.126
299.999	7.087	539.59	0.065	0.077
304.998	10.041	547.87	0.061	0.035
294.996	1.213	499.13	0.081	0.170
299.998	4.004	508.17	0.075	0.134
304.998	6.801	516.85	0.070	0.095
310.000	9.603	525.24	0.066	0.059
299.997	1.313	476.73	0.089	0.158
304.996	3.957	485.96	0.082	0.136
309.999	6.613	494.84	0.076	0.110
314.995	9.266	503.35	0.071	0.084
304.995	1.397	453.89	0.099	0.136
309.998	3.908	463.47	0.091	0.134
314.995	6.420	472.55	0.084	0.123
320.004	8.941	481.25	0.078	0.106
309.997	1.503	431.03	0.111	0.103
314.994	3.859	440.71	0.101	0.128
320.004	6.236	450.01	0.092	0.136
325.009	8.608	458.78	0.085	0.131
314.992	1.733	409.82	0.124	0.062
320.002	3.960	419.66	0.112	0.109
325.008	6.201	429.07	0.102	0.136
330.000	8.441	437.99	0.094	0.148

Table A.1-15. (continued)

T/K	P/MPa	w/m·s^{-1}	U_c/%	Δ_w/%
320.002	1.827	386.04	0.142	-0.020
325.008	3.924	396.35	0.127	0.078
330.000	6.023	405.99	0.115	0.136
335.004	8.112	414.85	0.105	0.170
325.006	2.025	363.70	0.164	-0.098
329.999	3.980	374.21	0.145	0.055
335.002	5.935	383.73	0.130	0.136
340.007	7.905	392.88	0.118	0.188
329.998	2.229	341.01	0.191	-0.240
335.002	4.041	351.53	0.167	-0.017
340.007	5.877	361.47	0.148	0.113
345.013	7.718	370.79	0.134	0.203
335.001	2.392	317.01	0.230	-0.333
340.006	4.087	328.15	0.198	-0.056
345.013	5.792	338.36	0.173	0.121
340.006	2.607	293.45	0.282	-0.412
345.012	4.167	304.49	0.237	-0.194
345.012	2.910	271.59	0.345	-0.484

Table A.1-16. Measured speed of sound data for the system R-1234yf/134a at a molar composition of (0.64709/0.35291).

Listed are temperature *T*, pressure *P*, speed of sound *w*, relative combined, expanded ($k = 2$) state point uncertainty in the speed of sound U_c, and relative deviation from the mixture EOS. Average values for the replicate measurements at each (*T*, *P*) state point are given. The different isochores are separated by blank lines.

T/K	*P*/MPa	*w*/m·s^{-1}	U_c/%	Δ_w/%
235.007	0.663	746.03	0.043	-0.064
240.002	0.672	723.28	0.044	-0.042
245.003	0.694	700.73	0.046	-0.030
250.004	0.708	678.16	0.048	-0.037
254.995	0.720	655.72	0.050	-0.050
259.987	2.996	651.70	0.050	-0.095
264.997	6.626	658.38	0.048	-0.177
269.993	10.288	665.31	0.046	-0.244
260.001	0.801	633.95	0.053	-0.054
264.995	4.338	640.85	0.051	-0.142
269.993	7.925	648.05	0.049	-0.215
274.995	11.487	654.98	0.047	-0.273
264.994	1.250	615.38	0.055	-0.093
269.992	4.705	622.85	0.053	-0.174
274.995	8.164	630.22	0.050	-0.237
280.000	11.622	637.48	0.049	-0.286
269.990	1.132	591.90	0.059	-0.145
274.995	4.413	599.48	0.056	-0.205
279.999	7.714	607.04	0.053	-0.258
285.001	11.008	614.44	0.051	-0.297
274.994	1.218	570.34	0.062	-0.178
279.999	4.366	578.19	0.059	-0.232
285.001	7.517	585.89	0.056	-0.273
290.002	10.656	593.38	0.054	-0.296
279.998	1.243	548.15	0.067	-0.220
284.999	4.239	556.18	0.063	-0.254
290.003	7.244	564.05	0.060	-0.279
294.998	10.251	571.77	0.057	-0.298

Table A.1-16. (continued)

T/K	P/MPa	w/m·s^{-1}	U_c/%	Δ_w/%
284.998	1.205	525.15	0.073	-0.271
290.002	4.071	533.56	0.068	-0.283
294.998	6.933	541.67	0.064	-0.293
299.998	9.802	549.61	0.061	-0.298
290.000	1.169	501.82	0.080	-0.348
294.997	3.881	510.45	0.074	-0.328
299.999	6.601	518.81	0.070	-0.309
304.997	9.317	526.84	0.066	-0.297
294.995	1.281	480.27	0.087	-0.381
299.998	3.860	489.10	0.081	-0.338
304.998	6.446	497.61	0.075	-0.309
309.999	9.038	505.86	0.071	-0.287

Table A.1-17. Measured speed of sound data for the system R-134a/1234ze(E) at a molar composition of (0.32916/0.67084).

Listed are temperature *T*, pressure *P*, speed of sound *w*, relative combined, expanded ($k = 2$) state point uncertainty in the speed of sound U_c, and relative deviation from the mixture EOS. Average values for the replicate measurements at each (*T*, *P*) state point are given.

T/K	*P*/MPa	*w*/m·s^{-1}	U_c/%	Δ_w/%
235.008	0.525	812.57	0.039	1.043
240.003	0.537	789.62	0.040	1.009
245.004	0.541	766.62	0.041	0.966
250.004	0.549	743.64	0.042	0.915
254.994	0.553	720.81	0.044	0.875
259.987	0.559	698.02	0.046	0.838
269.992	1.140	657.06	0.050	0.783
274.995	4.782	663.40	0.048	0.710
280.000	8.458	669.98	0.046	0.634
285.001	12.144	676.62	0.045	0.561
290.003	15.823	683.20	0.044	0.493
294.998	19.487	689.68	0.043	0.430
299.999	23.144	696.07	0.042	0.373
304.997	26.739	702.09	0.041	0.324
310.000	30.316	707.98	0.040	0.278
314.994	33.894	713.91	0.040	0.238
320.004	37.460	719.74	0.039	0.203
325.010	41.009	725.47	0.038	0.171
330.000	44.515	731.03	0.038	0.144
335.004	47.984	736.38	0.038	0.119
340.009	51.440	741.68	0.037	0.098
274.989	1.010	633.32	0.052	0.749
279.995	4.674	641.29	0.050	0.663
284.997	8.321	649.02	0.048	0.584
290.000	11.947	656.43	0.047	0.506
294.995	15.574	663.80	0.045	0.436
299.996	19.173	670.85	0.044	0.374
304.995	22.769	677.82	0.043	0.317
309.998	26.350	684.61	0.042	0.268
314.993	29.899	691.17	0.041	0.224
320.005	33.452	697.64	0.040	0.183
325.008	36.980	703.96	0.040	0.148
329.999	40.468	710.07	0.039	0.119

Table A.1-17. (continued)

T/K	P/MPa	w/m·s^{-1}	U_c/%	Δ_w/%
335.004	43.903	715.84	0.039	0.092
340.008	47.327	721.56	0.038	0.071
345.014	50.738	727.19	0.038	0.052
279.994	0.983	610.28	0.056	0.712
284.996	4.446	618.17	0.053	0.622
289.998	7.896	625.79	0.051	0.536
294.994	11.388	633.58	0.049	0.451
299.996	14.861	641.10	0.047	0.380
304.995	18.318	648.38	0.046	0.316
309.997	21.756	655.44	0.045	0.261
314.993	25.181	662.33	0.043	0.211
320.003	28.593	669.03	0.043	0.169
325.009	31.978	675.51	0.042	0.130
330.000	35.346	681.89	0.041	0.098
335.003	38.647	687.82	0.040	0.070
340.008	41.950	693.72	0.040	0.043
345.012	45.243	699.54	0.039	0.020
284.995	1.030	587.84	0.060	0.670
289.997	4.364	596.15	0.056	0.572
294.994	7.702	604.29	0.054	0.484
299.996	11.081	612.50	0.052	0.398
304.995	14.423	620.29	0.050	0.330
309.997	17.750	627.78	0.048	0.265
314.992	21.047	634.96	0.046	0.212
320.001	24.301	641.73	0.045	0.169
325.008	27.528	648.23	0.044	0.124
329.999	30.759	654.73	0.043	0.086
335.003	33.970	661.02	0.042	0.051
340.008	37.171	667.20	0.041	0.021
345.013	40.356	673.25	0.041	-0.004
289.996	1.161	566.13	0.064	0.612
294.992	4.345	574.65	0.060	0.515
299.994	7.543	583.01	0.057	0.428
304.994	10.731	591.05	0.054	0.351
309.996	13.911	598.82	0.052	0.282
314.992	17.077	606.34	0.050	0.222

Table A.1-17. (continued)

T/K	P/MPa	w/m·s^{-1}	U_c/%	Δ_w/%
320.003	20.248	613.69	0.049	0.168
325.008	23.442	621.11	0.047	0.122
329.999	26.574	628.01	0.046	0.080
335.003	29.665	634.47	0.045	0.036
340.006	32.755	640.89	0.044	0.000
345.014	35.827	647.15	0.043	-0.026
294.991	0.899	540.26	0.070	0.549
299.994	3.918	549.04	0.065	0.460
304.993	6.942	557.56	0.062	0.380
309.996	9.974	565.85	0.059	0.306
314.991	12.986	573.78	0.056	0.244
320.001	15.983	581.33	0.054	0.188
325.007	18.972	588.66	0.052	0.135
329.999	21.942	595.75	0.050	0.086
335.003	24.877	602.46	0.048	0.044
340.007	27.825	609.15	0.047	0.004
345.013	30.764	615.69	0.046	-0.031
299.991	0.756	515.11	0.077	0.473
304.993	3.626	524.27	0.072	0.399
309.995	6.506	533.14	0.067	0.331
314.991	9.373	541.58	0.063	0.270
320.001	12.244	549.72	0.060	0.211
325.007	15.100	557.52	0.057	0.159
329.998	17.941	565.04	0.055	0.108
335.002	20.767	572.22	0.053	0.059
340.008	23.590	579.25	0.051	0.014
345.013	26.400	586.06	0.049	-0.027
304.991	1.377	498.72	0.081	0.388
309.994	4.125	507.93	0.076	0.335
314.990	6.876	516.79	0.071	0.285
320.001	9.632	525.29	0.067	0.233
325.007	12.380	533.43	0.063	0.181
329.998	15.115	541.25	0.060	0.131
335.003	17.824	548.60	0.057	0.079
340.008	20.519	555.69	0.055	0.034
345.013	23.229	562.73	0.053	-0.014

Table A.1-17. (continued)

T/K	p/MPa	w/m·s^{-1}	U_c/%	Δ_w/%
309.993	1.253	473.32	0.091	0.296
314.989	3.848	482.89	0.084	0.278
320.000	6.456	492.03	0.078	0.249
325.006	9.061	500.75	0.073	0.210
329.997	11.654	509.07	0.069	0.166
335.002	14.232	516.91	0.065	0.118
340.007	16.806	524.47	0.062	0.068
345.012	19.379	531.84	0.059	0.018
314.990	1.546	453.04	0.100	0.206
319.999	4.024	462.90	0.092	0.223
325.005	6.490	472.10	0.085	0.222
329.997	8.953	480.84	0.079	0.197
335.002	11.402	489.00	0.074	0.153
340.008	13.858	496.96	0.070	0.106
345.013	16.312	504.64	0.066	0.055
319.999	1.756	431.60	0.111	0.132
325.005	4.078	441.42	0.101	0.196
329.997	6.412	450.80	0.093	0.209
335.001	8.742	459.60	0.087	0.191
340.007	11.076	468.04	0.081	0.155
345.013	13.404	476.10	0.076	0.108
325.005	1.948	409.78	0.125	0.079
329.997	4.146	419.95	0.113	0.176
335.001	6.350	429.46	0.104	0.206
340.007	8.553	438.42	0.095	0.199
345.012	10.760	446.98	0.089	0.163
329.998	2.044	386.06	0.144	0.020
335.002	4.096	396.26	0.129	0.145
340.006	6.157	405.92	0.117	0.205
345.013	8.225	415.07	0.107	0.205
335.000	2.385	366.39	0.163	0.003
340.006	4.329	377.01	0.145	0.176
345.013	6.278	386.87	0.130	0.244
340.005	2.348	338.90	0.199	-0.022
345.013	4.140	349.93	0.174	0.211
345.010	2.550	315.54	0.238	0.004

Table A.1-18. Measured speed of sound data for the system R-134a/1234ze(E) at a molar composition of (0.63688/36312).

Listed are temperature *T*, pressure *P*, speed of sound *w*, relative combined, expanded ($k = 2$) state point uncertainty in the speed of sound U_c, and relative deviation from the mixture EOS. Average values for the replicate measurements at each (*T*, *P*) state point are given. The different isochores are separated by blank lines.

T/K	*P*/MPa	*w*/m·s^{-1}	U_c/%	Δ_w/%
229.997	0.131	829.10	0.039	1.135
235.007	0.589	808.34	0.039	1.121
240.004	0.609	785.19	0.040	1.098
245.006	0.605	761.97	0.041	1.077
250.005	0.609	738.83	0.043	1.048
254.994	0.618	715.85	0.044	1.025
259.988	0.611	692.86	0.046	1.017
269.993	5.812	685.99	0.045	0.853
274.995	9.842	693.24	0.044	0.748
280.000	13.884	700.47	0.043	0.653
285.001	17.913	707.56	0.042	0.568
290.003	21.919	714.46	0.041	0.492
294.998	25.905	721.19	0.040	0.423
299.999	29.876	727.77	0.039	0.361
304.998	33.823	734.20	0.039	0.306
310.000	37.736	740.43	0.038	0.257
314.995	41.622	746.51	0.038	0.211
320.004	45.494	752.47	0.037	0.169
269.993	3.174	666.80	0.048	0.924
274.995	7.130	674.44	0.046	0.803
280.000	11.085	681.95	0.045	0.695
285.001	15.028	689.29	0.043	0.600
290.003	18.959	696.46	0.042	0.514
294.999	22.863	703.42	0.041	0.440
299.999	26.745	710.16	0.040	0.372
304.998	30.611	716.76	0.040	0.311
310.000	34.457	723.21	0.039	0.257
314.993	38.265	729.45	0.039	0.210
320.004	42.025	735.38	0.038	0.167
325.008	45.773	741.24	0.038	0.125

Table A.1-18. (continued)

T/K	P/MPa	w/m·s^{-1}	U_c/%	Δ_w/%
269.987	1.099	650.78	0.050	0.987
274.991	4.970	658.61	0.048	0.854
279.996	8.848	666.34	0.046	0.736
284.998	12.716	673.89	0.045	0.632
290.001	16.573	681.26	0.044	0.540
294.996	20.399	688.35	0.043	0.458
299.998	24.212	695.26	0.042	0.386
304.997	28.005	702.00	0.041	0.321
309.999	31.782	708.59	0.040	0.263
314.996	35.538	715.02	0.039	0.211
320.004	39.328	721.55	0.039	0.164
325.009	43.044	727.69	0.038	0.123
330.000	46.700	733.54	0.038	0.086
335.004	50.316	739.13	0.037	0.050
274.990	1.038	627.36	0.053	0.977
279.995	4.733	635.34	0.051	0.836
284.997	8.434	643.22	0.049	0.713
290.000	12.131	650.91	0.047	0.604
294.995	15.817	658.41	0.046	0.507
299.997	19.484	665.63	0.044	0.423
304.995	23.137	672.69	0.043	0.349
309.998	26.772	679.54	0.042	0.283
314.994	30.385	686.21	0.041	0.225
320.004	33.986	692.71	0.040	0.173
325.009	37.562	699.04	0.040	0.126
330.000	41.101	705.15	0.039	0.083
335.003	44.595	710.97	0.039	0.044
340.007	48.088	716.76	0.038	0.008
279.994	1.100	604.88	0.057	0.958
284.996	4.633	613.08	0.054	0.813
289.999	8.175	621.14	0.051	0.686
294.995	11.707	628.97	0.049	0.575
299.996	15.229	636.54	0.048	0.477
304.996	18.740	643.90	0.046	0.391
309.997	22.215	650.90	0.045	0.317
314.994	25.689	657.82	0.044	0.250

Table A.1-18. (continued)

T/K	P/MPa	w/m·s^{-1}	U_c/%	Δ_w/%
320.003	29.154	664.55	0.043	0.190
325.009	32.599	671.10	0.042	0.137
330.000	36.014	677.47	0.041	0.090
335.004	39.380	683.47	0.040	0.046
340.008	42.752	689.47	0.040	0.007
345.013	46.114	695.38	0.039	-0.028
284.995	1.402	584.62	0.060	0.928
289.997	4.794	593.04	0.057	0.781
294.995	8.187	601.25	0.054	0.654
299.996	11.580	609.23	0.052	0.541
304.994	14.949	616.85	0.050	0.444
309.997	18.320	624.30	0.048	0.358
314.992	21.683	631.61	0.046	0.283
320.002	25.028	638.61	0.045	0.216
325.009	28.354	645.41	0.044	0.157
330.000	31.643	651.94	0.043	0.104
335.003	34.896	658.15	0.042	0.056
340.009	38.152	664.32	0.041	0.012
345.013	41.393	670.37	0.041	-0.027
289.996	1.173	559.27	0.065	0.917
294.993	4.392	567.96	0.061	0.768
299.994	7.623	576.43	0.058	0.638
304.994	10.850	584.61	0.055	0.525
309.996	14.070	592.50	0.053	0.426
314.993	17.273	600.08	0.051	0.339
320.002	20.478	607.48	0.049	0.262
325.008	23.661	614.60	0.047	0.194
330.000	26.822	621.49	0.046	0.133
335.002	29.939	627.95	0.045	0.077
340.007	33.106	634.64	0.044	0.025
345.012	36.236	641.04	0.043	-0.019
294.991	1.056	534.63	0.071	0.893
299.994	4.110	543.54	0.066	0.750
304.993	7.173	552.18	0.063	0.621
309.996	10.239	560.54	0.059	0.510
314.991	13.297	568.59	0.056	0.412

Table A.1-18. (continued)

T/K	P/MPa	w/m·s^{-1}	U_c/%	Δ_w/%
320.003	16.348	576.32	0.054	0.327
325.008	19.388	583.79	0.052	0.249
329.997	22.381	590.80	0.050	0.178
335.002	25.368	597.59	0.048	0.114
340.009	28.359	604.32	0.047	0.058
345.012	31.341	610.89	0.046	0.006
299.992	1.274	513.38	0.077	0.855
304.992	4.193	522.57	0.071	0.718
309.995	7.123	531.46	0.067	0.596
314.992	10.048	539.99	0.063	0.491
320.001	12.974	548.17	0.060	0.394
325.007	15.890	556.02	0.057	0.307
329.999	18.784	563.55	0.055	0.231
335.002	21.654	570.67	0.052	0.159
340.007	24.524	577.65	0.051	0.095
345.013	27.388	584.46	0.049	0.037
304.992	1.802	495.84	0.082	0.803
309.995	4.602	505.21	0.076	0.679
314.990	7.403	514.17	0.071	0.567
320.001	10.211	522.77	0.067	0.466
325.007	13.007	530.95	0.063	0.375
329.998	15.788	538.80	0.060	0.291
335.002	18.543	546.15	0.057	0.210
340.008	21.304	553.38	0.055	0.139
345.013	24.059	560.42	0.053	0.074
309.994	1.809	472.09	0.091	0.764
314.990	4.450	481.66	0.084	0.658
320.002	7.105	490.82	0.078	0.560
325.006	9.758	499.55	0.073	0.463
329.999	12.400	507.86	0.068	0.375
335.003	15.021	515.63	0.065	0.287
340.007	17.643	523.20	0.061	0.206
345.013	20.252	530.47	0.059	0.139

Table A.1-18. (continued)

T/K	P/MPa	w/m·s^{-1}	U_c/%	Δ_w/%
314.990	1.964	449.98	0.101	0.715
319.999	4.471	459.83	0.092	0.637
325.006	6.981	469.12	0.085	0.552
329.998	9.484	477.92	0.079	0.464
335.003	11.973	486.12	0.074	0.371
340.007	14.470	494.12	0.070	0.285
345.013	16.965	501.84	0.066	0.206
319.999	2.064	426.84	0.114	0.678
325.006	4.432	436.97	0.103	0.621
329.997	6.793	446.45	0.094	0.551
335.002	9.139	455.13	0.087	0.464
340.007	11.502	463.64	0.081	0.379
345.013	13.861	471.75	0.076	0.295
325.004	1.764	396.62	0.136	0.618
329.997	3.937	406.94	0.122	0.606
335.002	6.104	416.39	0.111	0.563
340.007	8.292	425.54	0.101	0.492
345.013	10.485	434.26	0.093	0.412
329.996	2.021	374.75	0.155	0.545
335.001	4.057	385.21	0.138	0.582
340.007	6.114	395.14	0.124	0.551
345.013	8.179	404.50	0.113	0.492
335.001	2.355	354.21	0.177	0.499
340.007	4.283	365.13	0.155	0.554
345.013	6.220	375.25	0.139	0.542
340.007	2.528	330.08	0.211	0.419
345.012	4.316	341.30	0.182	0.514
345.013	2.760	306.71	0.253	0.343

Table A.1-19. Measured speed of sound data for the system R-1234yf/1234ze(E) at a molar composition of (0.33584/0.66416).

Listed are temperature *T*, pressure *P*, speed of sound *w*, relative combined, expanded ($k = 2$) state point uncertainty in the speed of sound U_c, and relative deviation from the mixture EOS. Average values for the replicate measurements at each (*T*, *P*) state point are given.

T/K	*P*/MPa	*w*/m·s^{-1}	U_c/%	Δ_w/%
230.014	0.267	806.10	0.039	0.224
240.003	0.542	761.96	0.041	0.170
245.003	0.534	739.27	0.043	0.147
250.004	0.543	716.62	0.044	0.099
229.999	0.263	806.07	0.039	0.214
235.008	0.521	784.77	0.040	0.216
254.995	0.542	694.03	0.046	0.049
259.987	0.551	671.60	0.048	0.000
264.995	0.547	649.01	0.051	-0.053
269.992	2.854	645.90	0.050	-0.054
269.991	2.931	646.50	0.050	-0.057
274.995	6.403	652.94	0.049	-0.073
279.999	9.895	659.50	0.047	-0.098
269.991	1.097	631.33	0.053	-0.081
274.994	4.515	638.06	0.051	-0.095
279.999	7.939	644.80	0.049	-0.118
285.000	11.337	651.32	0.047	-0.144
274.993	1.131	609.30	0.056	-0.147
279.998	4.419	616.37	0.054	-0.160
285.000	7.667	623.04	0.052	-0.182
290.002	10.969	630.08	0.050	-0.208
279.997	1.194	587.52	0.059	-0.220
285.000	4.323	594.65	0.057	-0.232
290.002	7.458	601.75	0.054	-0.250
294.998	10.584	608.69	0.052	-0.268
284.999	1.104	564.22	0.064	-0.308
290.001	4.108	571.77	0.061	-0.312
294.997	7.105	579.14	0.058	-0.321
299.999	10.097	586.32	0.055	-0.331

Table A.1-19. (continued)

T/K	P/MPa	w/m·s^{-1}	U_c/%	Δ_w/%
290.000	1.075	541.34	0.069	-0.407
294.997	3.934	549.11	0.065	-0.398
299.999	6.792	556.67	0.062	-0.393
304.997	9.651	564.09	0.059	-0.392
294.995	1.063	518.44	0.075	-0.525
299.998	3.801	526.62	0.071	-0.489
304.996	6.527	534.46	0.067	-0.465
309.999	9.236	541.90	0.063	-0.446
299.996	1.352	498.92	0.081	-0.631
304.996	3.965	507.27	0.076	-0.570
309.999	6.596	515.51	0.071	-0.525
314.994	9.206	523.32	0.067	-0.488
304.994	1.235	474.32	0.090	-0.781
309.998	3.713	483.04	0.084	-0.674
314.994	6.188	491.40	0.078	-0.594
320.003	8.666	499.42	0.074	-0.536
309.997	1.379	452.78	0.100	-0.909
314.993	3.723	461.69	0.092	-0.755
320.004	6.073	470.18	0.086	-0.643
325.009	8.419	478.31	0.080	-0.564
314.992	1.642	432.89	0.110	-1.014
320.002	3.877	442.08	0.101	-0.813
325.008	6.112	450.77	0.093	-0.671
329.999	8.337	459.02	0.087	-0.573
320.001	1.562	407.47	0.127	-1.183
325.007	3.651	416.91	0.115	-0.905
329.999	5.740	425.83	0.106	-0.717
335.003	7.817	434.09	0.098	-0.590
325.006	1.684	384.70	0.145	-1.319
329.998	3.647	394.49	0.131	-0.968
335.003	5.598	403.39	0.120	-0.732

Table A.1-19. (continued)

T/K	P/MPa	w/m·s^{-1}	U_c/%	Δ_w/%
340.007	7.566	412.01	0.110	-0.584
329.998	1.945	364.29	0.165	-1.375
335.002	3.785	374.11	0.148	-0.973
340.007	5.635	383.35	0.134	-0.715
345.013	7.491	392.12	0.123	-0.550
335.001	2.049	340.38	0.197	-1.462
340.006	3.780	350.84	0.174	-0.979
345.012	5.516	360.52	0.155	-0.682
340.006	2.260	318.25	0.235	-1.445
345.012	3.869	328.91	0.204	-0.920
345.012	2.476	295.80	0.286	-1.345

Table A.1-20. Measured speed of sound data for the system R-1234yf/1234ze(E) at a molar composition of (0.66660/0.33340).

Listed are temperature *T*, pressure *P*, speed of sound *w*, relative combined, expanded ($k = 2$) state point uncertainty in the speed of sound U_c, and relative deviation from the mixture EOS. Average values for the replicate measurements at each (*T*, *P*) state point are given. The different isochores are separated by blank lines.

T/K	*P*/MPa	w/m·s^{-1}	U_c/%	Δ_w/%
229.998	0.450	777.99	0.041	0.128
235.008	0.591	756.13	0.042	0.161
240.004	0.607	733.50	0.043	0.156
245.003	0.616	710.97	0.045	0.143
250.005	0.624	688.51	0.047	0.119
254.994	0.792	667.55	0.049	0.100
259.987	4.524	674.41	0.047	0.041
269.993	11.961	687.78	0.045	-0.081
259.986	1.160	648.25	0.051	0.053
269.990	8.269	661.67	0.047	-0.066
274.995	11.836	668.41	0.046	-0.121
265.003	4.628	654.24	0.049	-0.006
264.994	1.127	625.75	0.054	-0.002
269.991	4.572	633.05	0.052	-0.061
274.995	8.070	640.62	0.049	-0.119
280.000	11.531	647.83	0.048	-0.167
269.991	1.128	603.60	0.057	-0.066
274.994	4.428	611.11	0.054	-0.119
280.000	7.740	618.59	0.052	-0.168
285.001	11.049	625.95	0.050	-0.211
274.993	1.123	581.33	0.061	-0.139
279.999	4.282	589.10	0.058	-0.181
285.000	7.446	596.77	0.055	-0.220
290.002	10.608	604.28	0.053	-0.253
279.997	1.130	559.12	0.065	-0.222
285.000	4.140	567.06	0.061	-0.249
290.003	7.161	574.92	0.058	-0.274
294.997	10.166	582.50	0.056	-0.294

Table A.1-20. (continued)

T/K	P/MPa	w/m·s^{-1}	U_c/%	Δ_w/%
284.999	1.148	536.92	0.070	-0.314
290.001	4.005	545.01	0.066	-0.315
294.998	6.873	552.95	0.062	-0.324
299.999	9.747	560.75	0.059	-0.330
290.000	1.030	513.07	0.077	-0.415
294.997	3.758	521.57	0.072	-0.393
299.998	6.487	529.78	0.068	-0.377
304.998	9.212	537.70	0.064	-0.366
294.995	1.070	490.76	0.084	-0.524
299.998	3.690	499.76	0.078	-0.475
304.997	6.300	508.33	0.073	-0.432
309.998	8.904	516.52	0.069	-0.401
299.996	1.030	467.14	0.093	-0.651
304.996	3.494	476.27	0.086	-0.555
310.000	5.961	485.01	0.080	-0.483
314.993	8.401	493.16	0.075	-0.424
304.995	1.196	446.00	0.103	-0.765
309.998	3.530	455.33	0.095	-0.624
314.994	5.869	464.26	0.088	-0.522
320.004	8.211	472.78	0.082	-0.446
309.997	0.984	418.91	0.119	-0.946
314.993	3.165	428.60	0.108	-0.738
320.005	5.351	437.71	0.100	-0.587
325.008	7.532	446.32	0.092	-0.482
314.991	1.535	403.52	0.129	-1.006
320.002	3.623	413.31	0.116	-0.768
325.008	5.715	422.57	0.107	-0.595
329.999	7.793	431.19	0.098	-0.473
320.002	1.614	380.30	0.148	-1.169
325.008	3.572	390.39	0.133	-0.859
329.999	5.527	399.80	0.121	-0.639
335.004	7.472	408.44	0.111	-0.487

A.1.4. Liquid-phase Thermal Conductivity

The transient hot wire (THW) apparatus is an absolute technique used to measure the thermal conductivity. The apparatus described in this study[82] can operate at temperatures ranging from 60 to 340 K and pressures up to 70 MPa. The basis of the THW apparatus are two platinum wires of differing lengths, which function as both heating elements and thermometers. The principle of the THW technique is to observe the temperature rise of the wire during a step power pulse through the wire over a short duration. The following equation,

$$\Delta T_{id} = \Delta T - \sum \delta T_i = \frac{q}{4\pi\lambda} \ln\left(\frac{4K}{a^2 C} t\right) \quad \text{(A.1-7)}$$

relates the measured temperature rise ΔT to the ideal temperature rise ΔT_{id} of an infinite line source where q is the applied power, λ is the thermal conductivity, K is the thermal diffusivity, a is the radius of the wire, C is the exponential of Euler's constant, and t is the time. The equation for the infinite line source is an ideal scenario assuming a wire of near-zero diameter and infinite length with zero heat capacity and the term $\Sigma\delta T_i$ is the sum of corrections that are applied to the measured temperature rise. A more in-depth explanation of each correction required is described in the work of Healy et al.[83]

The apparatus consists of a measuring cell containing the hot wires situated in one arm of a Wheatstone bridge to measure the difference between the long-wire and short-wire resistances increases during heating; a beryllium copper pressure vessel rated to 70 MPa and a cryostat to maintain the temperature complete the basic apparatus. Figure A.1-7 shows the arrangement of the long and short hot wires on the Wheatstone bridge. The two-wire arrangement used in this THW apparatus allows for the elimination of end effects. During measurements, an in-situ calibration is performed to correlate the wire resistances to their temperature. The heating of the platinum wires is done using a 1000 Hz alternating current power source to avoid polarization errors that may occur with ionic impurities in the refrigerants studied with bare hot wires.

Measurements are performed over a 1 s time period to minimize convective heat transfer and at five temperature rises to rule out any power level dependency. The data are measured isothermally from 200 to 340 K in 20 K increments. Increasing the system temperature causes the resistance of the long and short wires to increase. Therefore, prior to starting any measurements the Wheatstone bridge is balanced using decade resistors so that the voltage measured across the bridge reads zero. Saturated binary liquid refrigerant mixture samples of HFO-1234yf, HFC-134a. and HFO-1234ze(E) prepared in 300 mL transfer vessels were used to load the hot-wire system. The mixtures were prepared in such a manner that it minimized the vapor space in the transfer vessel. When loading the sample the transfer vessel was inverted to load from the liquid phase. Given the two-phase nature of the sample, flash calculations using REFPROP were performed to correct for modest changes in the bulk sample composition as the sample was withdrawn. The liquid phase composition changes were found to be between 0.0002 and 0.0005 mole fraction of the bulk sample composition. For each fluid measurements at nine pressures were performed along an isotherm starting from roughly 0.5 MPa above the bubble point pressure to 50 MPa. For mixtures containing HFO-1234yf the pressure was limited to 12 MPa because this component has the potential to

polymerize at high pressures. The combined expanded uncertainty of the thermal conductivity measurement for the liquid mixtures measured here is less than 1%. Figure A.1-8 shows the relationship between the thermal conductivity and density for each binary mixture.

Representative measured data are presented in Tables A.1-21 through A.1-26. For the sake of brevity, the tables present a single measured point at each nominal pressure, rather than the five distinct temperature rises actually measured. All of the measured data will be presented in a forthcoming journal paper.

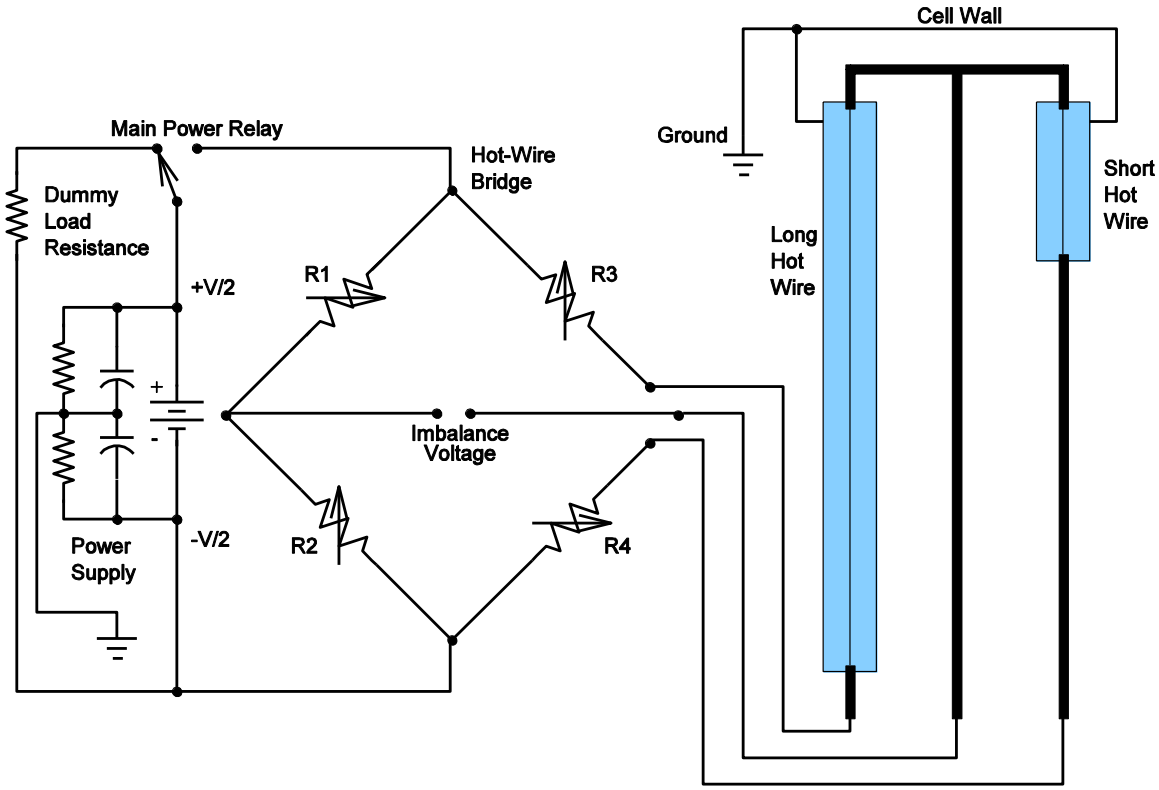

Figure A.1-7. Circuit diagram of the Wheatstone bridge and long and short hot wire arrangement.

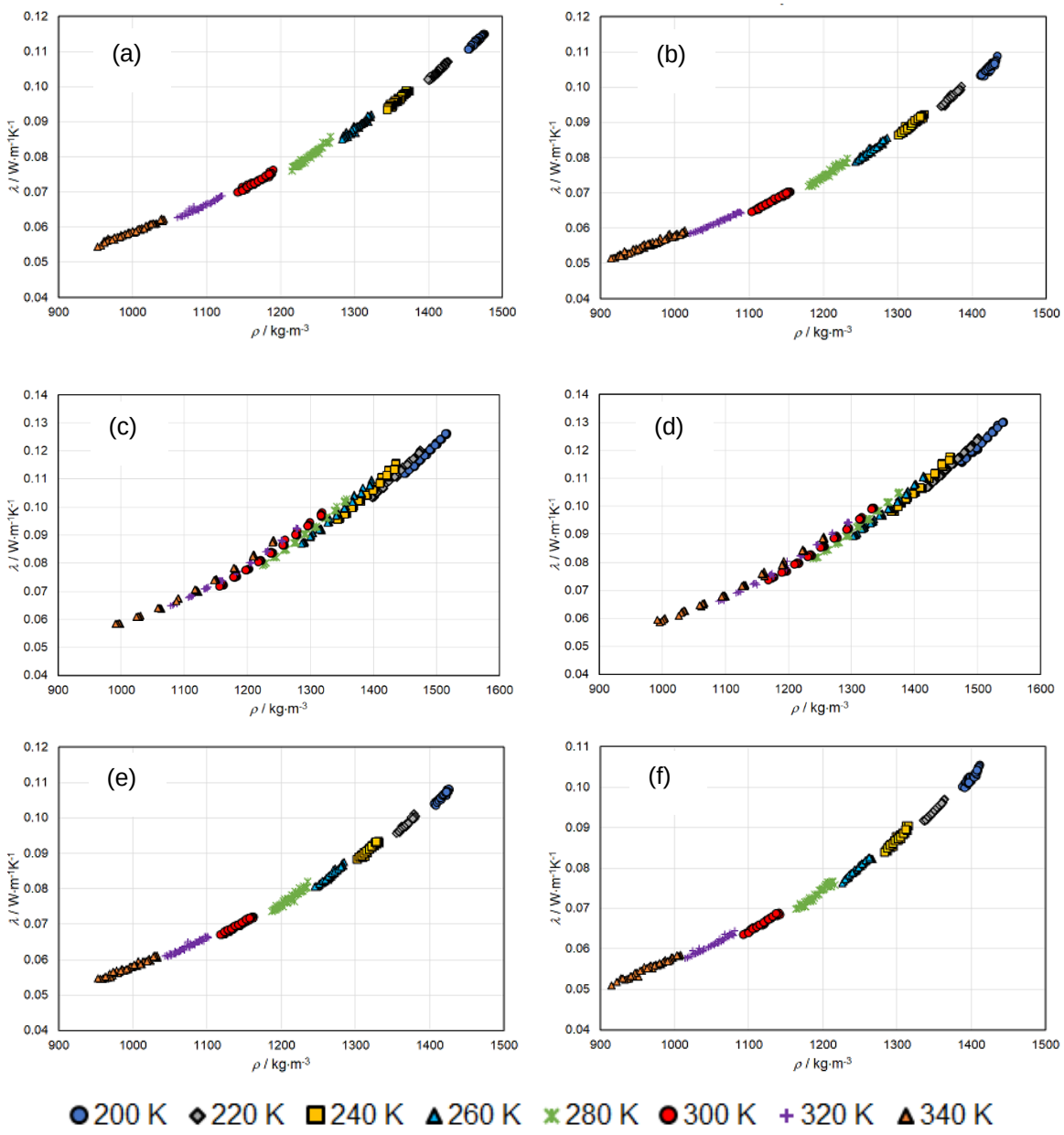

Figure A.1-8. Effect of density on the thermal conductivity for binary mixtures of R-1234yf, R-134a, and R-1234ze(E) at temperatures ranging from 200 K to 340 K.

The mixtures are: (a) R-1234yf/134a (0.320/0.680 molar); (b) R-1234yf/134a (0.647/0.353 molar); (c) R-134a/1234ze(E) (0.334/0.666 molar); (d) R-134a/1234ze(E) (0.663/0.337 molar); (e) R-1234yf/1234ze(E) (0.323/0.677 molar); (f) R-1234yf/1234ze(E) (0.642/0.358 molar).

Table A.1-21. Representative thermal conductivity data measured for the system R-1234yf/134a at a molar composition of (0.320/0.680).

T / K	P/ MPa	λ / W·m^{-1}K^{-1}	T / K	P / MPa	λ / W·m^{-1}K^{-1}
201.920	2.155	0.11140	282.240	2.300	0.07806
201.919	2.152	0.11161	282.224	1.078	0.07749
201.893	3.573	0.11198	282.175	2.126	0.07834
201.891	3.573	0.11179	282.356	1.050	0.07758
201.557	8.921	0.11391	282.361	2.070	0.07789
202.247	11.885	0.11494	282.260	3.289	0.07888
202.271	10.415	0.11427	282.264	4.704	0.07995
202.347	7.678	0.11310	282.182	6.006	0.08076
202.344	5.055	0.11286	282.197	7.420	0.08166
202.353	0.950	0.11111	282.118	8.924	0.08273
222.435	12.026	0.10695	282.039	11.634	0.08412
222.516	10.314	0.10628	302.260	1.157	0.07035
222.472	9.034	0.10560	302.271	2.011	0.07119
222.504	7.633	0.10502	302.270	2.888	0.07171
222.514	6.297	0.10455	302.273	3.599	0.07206
222.560	4.869	0.10364	302.264	4.346	0.07273
222.573	3.656	0.10321	302.241	5.327	0.07347
222.559	2.334	0.10277	302.230	6.113	0.07382
222.593	1.040	0.10199	302.218	7.070	0.07485
242.683	11.940	0.09869	302.198	7.905	0.07525
242.739	10.479	0.09787	322.071	1.909	0.06311
242.757	8.972	0.09692	321.974	2.440	0.06397
242.764	6.293	0.09659	322.022	3.119	0.06467
242.741	7.673	0.09629	322.015	3.843	0.06512
242.782	5.024	0.09540	321.927	4.558	0.06579
242.799	3.483	0.09499	321.915	5.342	0.06625
242.801	2.154	0.09437	321.921	6.093	0.06671
242.826	0.969	0.09325	321.921	7.042	0.06820
262.143	11.959	0.09162	321.900	7.920	0.06890
262.172	10.621	0.09055	342.135	2.579	0.05605
262.188	8.969	0.08970	342.208	2.979	0.05646
262.159	7.513	0.08927	342.181	3.464	0.05722
262.192	6.185	0.08881	342.175	4.056	0.05812
262.226	4.808	0.08875	342.031	4.670	0.05902
262.208	4.829	0.08812	342.399	5.405	0.05956
262.233	3.524	0.08651	342.420	6.237	0.06018
262.240	2.081	0.08620	342.382	6.964	0.06089
262.218	0.990	0.08561	342.340	7.878	0.06236

Table A.1-22. Representative thermal conductivity data measured for the system R-1234yf/134a at a molar composition of (0.647/0.353).

T / K	P / MPa	λ / W·m^{-1}K^{-1}	T / K	P / MPa	λ / W·m^{-1}K^{-1}
202.029	1.154	0.10308	281.872	3.306	0.07380
202.036	2.153	0.10403	281.818	4.506	0.07453
201.465	3.573	0.10469	281.905	6.008	0.07547
201.725	3.572	0.10469	281.875	7.681	0.07612
201.472	4.962	0.10517	281.809	7.700	0.07615
202.101	4.975	0.10469	281.128	8.935	0.07827
202.049	6.238	0.10480	282.007	10.353	0.07781
202.034	7.559	0.10495	282.028	11.999	0.07857
202.039	9.049	0.10585	302.464	1.299	0.06506
202.015	10.412	0.10713	302.105	1.997	0.06605
202.060	11.793	0.10701	302.248	2.737	0.06654
222.284	1.181	0.09488	302.133	3.483	0.06698
222.303	2.158	0.09514	301.907	4.298	0.06796
222.305	3.461	0.09616	301.874	5.131	0.06844
222.292	4.773	0.09669	302.199	6.288	0.06891
222.272	6.329	0.09752	302.105	7.096	0.06981
222.275	7.767	0.09758	302.176	8.035	0.07007
222.262	9.136	0.09832	322.289	1.638	0.05874
222.251	10.532	0.09885	322.225	2.316	0.05941
222.244	11.818	0.09926	322.172	2.976	0.06032
242.508	1.033	0.08689	322.219	3.707	0.06100
242.486	2.304	0.08751	322.121	4.434	0.06180
242.532	3.531	0.08780	322.001	5.249	0.06241
242.530	4.935	0.08832	322.139	6.155	0.06322
242.540	6.142	0.08895	322.083	7.072	0.06397
242.523	7.541	0.08974	322.045	8.031	0.06449
242.500	8.973	0.09024	342.621	2.401	0.05164
242.495	10.579	0.09077	342.534	2.847	0.05208
242.472	11.946	0.09184	342.736	3.460	0.05328
262.259	1.077	0.07923	342.613	3.980	0.05413
262.294	2.162	0.08018	342.476	3.966	0.05440
262.254	3.386	0.08084	342.501	4.729	0.05572
262.200	4.727	0.08119	342.640	4.770	0.05548
262.261	6.172	0.08160	342.474	5.410	0.05584
262.225	7.558	0.08285	342.357	6.220	0.05716
262.176	9.057	0.08327	342.474	7.052	0.05765
262.127	10.486	0.08422	341.938	7.035	0.05796
262.088	11.886	0.08514	342.045	7.968	0.05841
281.922	1.103	0.07236	341.993	7.955	0.05900
281.860	2.032	0.07294	342.226	2.698	0.05245

Table A.1-23. Representative thermal conductivity data measured for the system R-134a/1234ze(E)) at a molar composition of (0.334/0.666).

T / K	P / MPa	λ / W·m^{-1}K^{-1}	T / K	P / MPa	λ / W·m^{-1}K^{-1}
202.306	1.006	0.11192	282.586	1.027	0.07981
202.356	6.092	0.11376	282.497	5.018	0.08243
202.339	11.496	0.11505	282.413	9.586	0.08472
202.328	17.141	0.11665	282.314	14.660	0.08730
202.325	23.189	0.11893	282.249	20.585	0.09057
202.319	29.514	0.12054	282.287	27.011	0.09311
202.317	36.292	0.12279	282.114	34.280	0.09661
202.210	42.843	0.12437	282.010	41.528	0.09871
202.207	50.101	0.12622	282.115	50.057	0.10198
222.169	1.056	0.10367	302.384	0.961	0.07264
222.565	5.931	0.10541	302.252	4.796	0.07501
222.552	11.136	0.10792	302.093	8.766	0.07760
222.536	16.705	0.10965	302.017	13.756	0.08079
222.523	22.545	0.11217	302.041	19.225	0.08340
222.502	29.147	0.11436	301.872	25.374	0.08657
222.490	35.966	0.11594	301.831	32.621	0.09001
222.477	42.648	0.11734	301.760	40.836	0.09354
222.474	50.056	0.12027	301.735	50.102	0.09730
242.282	1.066	0.09586	322.937	1.401	0.06497
242.262	5.686	0.09794	322.899	4.685	0.06805
242.240	10.677	0.09960	322.696	8.283	0.07091
242.230	16.211	0.10246	322.692	12.567	0.07383
242.205	22.160	0.10487	322.674	17.834	0.07684
242.183	28.493	0.10626	322.579	23.979	0.08026
242.162	35.235	0.10873	322.458	31.757	0.08405
242.135	42.241	0.11054	321.971	40.469	0.08811
242.117	50.302	0.11354	321.578	49.979	0.09222
262.459	1.107	0.08759	342.146	2.213	0.05862
262.412	5.364	0.08999	341.996	4.487	0.06087
262.317	10.428	0.09243	341.895	7.685	0.06391
262.270	15.664	0.09503	342.268	7.683	0.06405
262.217	21.652	0.09751	341.838	11.489	0.06754
262.170	27.658	0.09965	341.916	16.350	0.07034
262.124	34.362	0.10199	341.899	22.524	0.07403
262.079	42.081	0.10489	342.360	22.522	0.07416
262.023	50.155	0.10792	341.766	30.150	0.07793
			341.625	39.113	0.08293
			341.507	50.178	0.08820

Table A.1-24. Representative thermal conductivity data measured for the system R-134a/1234ze(E)) at a molar composition of (0.663/0.337).

T / K	P / MPa	λ / W·m^{-1}K^{-1}	T / K	P / MPa	λ / W·m^{-1}K^{-1}
202.414	0.987	0.11549	282.675	0.976	0.08186
202.412	6.060	0.11748	282.606	5.044	0.08448
202.410	11.549	0.11964	282.552	9.791	0.08700
202.411	17.236	0.12010	282.475	14.660	0.08946
202.418	23.225	0.12327	282.413	20.690	0.09308
202.342	29.496	0.12454	282.382	26.559	0.09525
202.352	35.981	0.12704	282.328	33.614	0.09844
202.367	42.732	0.12895	282.272	41.127	0.10155
202.367	49.945	0.12998	282.249	49.838	0.10511
222.064	1.065	0.10711	302.774	1.302	0.07414
222.214	5.868	0.10911	302.671	4.832	0.07664
222.257	11.181	0.11148	302.597	8.887	0.07975
222.241	16.618	0.11292	302.619	13.716	0.08232
222.216	22.787	0.11515	302.479	19.229	0.08542
222.202	28.987	0.11771	302.335	25.600	0.08900
222.192	35.725	0.11943	302.237	32.919	0.09191
222.017	42.464	0.12160	302.301	40.862	0.09563
221.978	50.005	0.12412	302.176	49.796	0.09927
242.597	1.100	0.09880	322.776	1.570	0.06657
242.565	5.653	0.10123	322.781	4.653	0.06924
242.536	10.781	0.10295	322.086	8.416	0.07251
242.521	16.107	0.10506	321.956	13.014	0.07611
242.498	22.116	0.10631	321.887	17.630	0.07869
242.473	28.225	0.10981	322.338	24.025	0.08251
242.456	34.938	0.11133	321.852	39.832	0.09054
242.437	42.219	0.11428	322.164	50.069	0.09430
242.419	50.130	0.11722	342.332	2.379	0.05897
262.970	1.072	0.08986	342.189	4.494	0.06231
262.931	5.384	0.09218	342.127	7.289	0.06531
262.887	10.105	0.09439	342.046	11.277	0.06809
262.853	15.441	0.09723	341.971	16.146	0.07184
262.800	21.204	0.09959	341.882	22.092	0.07578
262.758	27.697	0.10202	341.772	29.594	0.07943
262.703	34.550	0.10423	341.695	38.837	0.08415
262.666	41.737	0.10805	341.629	50.136	0.08911
262.612	49.833	0.11047			

Table A.1-25. Representative thermal conductivity data measured for the system R-1234yf/1234ze(E) at a molar composition of (0.323/0.677).

T / K	P / MPa	λ / W·m^{-1}K^{-1}	T / K	P / MPa	λ / W·m^{-1}K^{-1}
202.374	1.088	0.10437	282.065	1.039	0.07407
202.342	2.401	0.10476	282.045	2.153	0.07456
202.348	3.644	0.10480	282.055	3.428	0.07570
202.400	4.960	0.10560	281.981	4.771	0.07657
202.395	6.309	0.10606	281.991	6.062	0.07716
202.587	8.086	0.10660	281.947	7.336	0.07787
202.579	9.299	0.10688	282.026	8.962	0.07881
202.570	10.592	0.10694	281.959	10.640	0.07939
202.566	11.912	0.10731	282.001	12.325	0.08024
222.322	1.028	0.09612	302.454	1.118	0.06715
222.311	2.300	0.09663	302.396	1.865	0.06788
222.299	3.552	0.09710	302.422	2.697	0.06870
222.277	4.896	0.09752	302.393	3.469	0.06919
222.271	6.165	0.09839	302.370	4.307	0.06956
222.256	7.719	0.09877	302.562	5.164	0.07011
222.234	9.091	0.09904	302.512	6.104	0.07065
222.226	10.750	0.10019	302.479	7.129	0.07158
222.057	12.065	0.09975	302.441	8.075	0.07193
242.560	1.127	0.08892	322.230	1.463	0.06079
242.557	2.313	0.08932	322.256	2.145	0.06158
242.543	3.553	0.08959	322.219	2.828	0.06223
242.512	4.916	0.09007	322.138	3.480	0.06300
242.490	6.300	0.09110	322.182	4.418	0.06493
242.465	7.672	0.09171	322.150	5.293	0.06421
242.436	8.979	0.09241	322.123	6.224	0.06504
242.498	10.373	0.09297	322.113	7.045	0.06538
242.482	11.940	0.09308	322.105	8.047	0.06607
262.821	1.020	0.08055	342.054	2.207	0.05453
262.331	2.316	0.08159	341.934	2.733	0.05601
262.401	3.564	0.08212	341.986	3.349	0.05687
262.302	4.849	0.08288	341.960	4.033	0.05685
262.301	6.199	0.08343	341.881	4.655	0.05804
262.222	7.587	0.08538	341.812	5.465	0.05821
262.133	8.944	0.08527	342.373	6.254	0.05875
262.098	10.612	0.08587	341.873	7.094	0.06015
262.180	11.997	0.08652	341.901	8.002	0.06093

Table A.1-26. Representative thermal conductivity data measured for the system R-1234yf/1234ze(E) at a molar composition of (0.642/0.358).

T / K	P / MPa	λ / W·m^{-1}K^{-1}	T / K	P / MPa	λ / W·m^{-1}K^{-1}
202.210	1.019	0.10063	282.395	0.916	0.07010
202.133	2.678	0.10049	282.367	2.179	0.07087
202.191	3.759	0.10202	282.313	3.392	0.07173
202.197	5.086	0.10246	282.261	4.656	0.07257
202.226	6.239	0.10248	282.139	6.225	0.07349
202.196	7.850	0.10265	282.141	7.739	0.07467
202.180	9.424	0.10287	282.038	9.183	0.07596
201.797	10.729	0.10362	282.083	10.489	0.07641
201.801	12.035	0.10472	282.106	11.877	0.07667
222.731	1.046	0.09173	302.587	1.090	0.06385
222.719	2.361	0.09268	302.518	1.939	0.06494
222.702	3.690	0.09303	302.442	2.694	0.06512
222.688	4.991	0.09363	302.357	3.521	0.06579
222.672	6.293	0.09420	302.380	4.214	0.06629
222.659	7.651	0.09471	302.283	5.050	0.06706
222.506	9.142	0.09493	302.314	6.072	0.06753
222.479	10.635	0.09549	302.290	7.078	0.06838
222.458	12.078	0.09613	302.250	7.996	0.06877
242.358	1.133	0.08430	322.788	1.475	0.05775
242.363	2.377	0.08508	322.756	2.215	0.05866
242.389	3.632	0.08568	322.753	2.789	0.05912
242.259	4.942	0.08661	322.657	3.256	0.05958
242.286	6.294	0.08717	322.645	4.395	0.06051
242.307	7.642	0.08788	322.641	5.290	0.06141
242.242	8.910	0.08816	322.514	6.137	0.06193
242.208	10.456	0.08835	322.532	7.099	0.06279
242.189	12.002	0.08916	322.436	7.960	0.06353
262.665	6.173	0.07972	343.282	2.172	0.05105
262.630	1.147	0.07707	343.167	2.801	0.05272
262.645	2.253	0.07758	343.087	3.351	0.05326
262.596	3.544	0.07877	342.997	4.040	0.05464
262.543	4.833	0.07958	343.920	4.956	0.05526
262.556	7.515	0.08049	343.259	5.456	0.05596
262.513	9.047	0.08141	342.640	6.125	0.05670
262.471	10.549	0.08238	342.593	7.006	0.05736
262.415	11.983	0.08226	342.450	7.928	0.05830

A.1.5. Mixture Preparation

All of the property measurements rely on preparation of the sample mixtures and accurate determination of their composition. The (P, ρ, T, x) and speed-of-sound measurements utilized gas-phase mixtures, while the VLE and thermal conductivity measurements utilized liquid-phase mixtures. The mixtures were prepared gravimetrically (by weighing) to achieve low uncertainties in the composition.

The pure-fluid refrigerants used to prepare the mixtures were used as received except that we degassed them (prior to preparing the mixtures) by freezing the pure components in liquid nitrogen, evacuating the vapor space, and thawing; this sequence was repeated until the residual pressure over the frozen sample was less than 0.01 Pa. We analyzed the pure-fluid refrigerants in-house using gas chromatography with mass spectrometry (GC-MS) and found no significant impurities.

The gas-phase blends were prepared in aluminum gas cylinders of approximately 6, 10 or 13 L internal volume depending on the pressure of the blend. The sample mass was determined by a double substitution weighing design as described by Harris andTorres,[84] with a nearly identical "tare" or reference cylinder serving as the main substitution mass. Further details are provided by Richter and McLinden.[85] The uncertainty of the measured gas-phase mixture compositions, arising from the weighings, was 0.0001 mole fraction. The sample cylinders were loaded to pressures corresponding to the dew-point pressure at T = 293.15 K. There may have been a small amount of liquid in the sample cylinders after filling, but they were heated continuously to T > 313 K for the duration of the testing to ensure that only single-phase vapor was present. Due to sorption effects, the composition of the sample in the measuring cell could be different from that calculated from the sample masses loaded into the sample cylinder, and this contributed an additional uncertainty of 0.0002 mole fraction. The combined, expanded uncertainty was estimated to be 0.00022 mole fraction.

The liquid-phase mixtures were prepared in 300 mL stainless steel cylinders. The fluid with the higher boiling point was added first, then the second component. The vapor space above the mixture samples was degassed by freezing the sample with liquid nitrogen and opening the cylinder to vacuum. After evacuation, the sample was then heated to drive volatile impurities (such as air) into the vapor space. The entire cycle (freezing, evacuation, and heating) was repeated a minimum of three times for each sample. Mixtures were prepared with the goal of filling the sample cylinder with about 280 mL of liquid at ambient temperature. Thus, in each completed mixture cylinder there was a vapor space above the liquid phase.

A balance with a precision of 0.1 mg was used in the preparation of the liquid-phase mixtures. Utilizing the double-substitution weighing design of Harris and Torres,[84] measurement of the mass of each component consisted of weighing four masses: (1) a reference cylinder of approximately the same mass and volume as the empty sample cylinder, (2) the sample cylinder, (3) the sample cylinder plus a 20 g sensitivity weight, and (4) the reference cylinder plus the 20 g sensitivity weight. This weighing sequence was repeated four times for each mass determination. The density of ambient air was calculated based on measurements of temperature, pressure, and relative humidity, and the weighings were

corrected for the effects of air buoyancy. The standard deviation of the repeat weighings was at most 1.5 mg. The uncertainty in the composition due to the weighings was less than 0.0001 mole fraction. Because of the two-phase nature of the liquid-phase samples and because the weighings could determine only the overall (bulk) composition of the sample it was necessary to estimate the change in composition caused by the liquid/vapor fractionation inside the cylinder. This change was less than 0.0005 mole fraction, and its standard uncertainty was estimated to be less than 0.0001 mole fraction. Thus, the combined, expanded uncertainty in composition of the liquid-phase samples was estimated to be less than 0.00028 mole fraction.

A.1-6. Mixture Modeling

The multi-fluid modeling used in NIST REFPROP yields the most accurate mixture models available today. This approach combines the most accurate pure fluid equations of state with reducing and departure functions to correct for the changes to thermodynamics caused by mixture interactions. This model forms the basis of the GERG-2008 model, used for custody transfer of natural gas mixtures, amongst many other uses. The refrigeration industry has been using the multi-fluid modeling approach for many years and will likely do so for many years to come.

Pure fluid equations of state. In this framework, the equation of state for a pure component is given in terms of the Helmholtz energy, in terms of the Massieu potential, given by $\alpha = a/(RT)$. Thermodynamic properties are obtained from combinations of the Helmholtz energy and its derivatives. For instance, the pressure is obtained from $p = -\partial a/\partial v$. The total α is given as the sum of ideal-gas (non-interacting) and residual (interacting) contributions. The ideal-gas portion can in principle be obtained from theory for the given molecular species, and the residual contribution is entirely empirical, fit to experimental data as well and constrained to have the desired behavior at extremes in temperature and pressure. For most pure fluids, the residual Helmholtz energy can be expressed generically as

$$\alpha^{\mathrm{r}} = \sum_i n_i \delta^{d_i} \tau^{t_i} \exp(-c_i \delta^{l_i} - \eta_i(\delta - \varepsilon_i)^2 - \beta_i(\tau - \gamma_i)^2) \qquad \text{(A.1-8)}$$

where $\tau = T_{\mathrm{red}}/T$ and $\delta = \rho/\rho_{\mathrm{red}}$ with T_{red} and ρ_{red} being the reducing temperature and reducing density, respectively. All remaining variables are empirical coefficients particular to the given fluid.

Mixture equation of state. The same thermodynamic identities hold for mixtures as for pure fluids. The Helmholtz energy for a mixture is commonly obtained as the sum of a corresponding states contribution and a departure term.

$$\alpha^r = \alpha^r_{CS}(\tau, \delta, \bar{x}) + \alpha^r_{dep}(\tau, \delta, \bar{x}) \qquad \text{(A.1-9)}$$

in which

$$\alpha^r = \sum_{i=1}^{N} x_i \alpha^r_{o,i}(\tau, \delta) + \sum_{i=1}^{N} \sum_{j=i+1}^{N} F_{ij} x_i x_j \alpha^r_{ij}(\tau, \delta), \qquad \text{(A.1-10)}$$

and for mixtures $\tau = T_{red}(\bar{x})/T$ and $\delta = \rho/\rho_{\mathrm{red}}(\bar{x})$. The reducing functions are given by

$$T_{\mathrm{r}}(\bar{x}) = \sum_{i=1}^{N}\sum_{j=1}^{N} x_i x_j \beta_{T,ij}\gamma_{T,ij}\frac{x_i+x_j}{\beta_{T,ij}^2 x_i+x_j}\left(T_{\mathrm{c},i}\cdot T_{\mathrm{c},j}\right)^{0.5} \quad \text{(A.1-11)}$$

$$\frac{1}{\rho_{\mathrm{r}}(\bar{x})} = \sum_{i=1}^{N}\sum_{j=1}^{N} x_i x_j \beta_{v,ij}\gamma_{v,ij}\frac{x_i+x_j}{\beta_{v,ij}^2 x_i+x_j}\frac{1}{8}\left(\frac{1}{\rho_{\mathrm{c},i}^{1/3}}+\frac{1}{\rho_{\mathrm{c},j}^{1/3}}\right)^3. \quad \text{(A.1-12)}$$

Thus the reducing functions have four adjustable parameters per *ij* binary pair.

The phase equilibrium pressure is the result of an iterative calculation to equate pressure, temperature, chemical potentials of all species in all phases and amount of substances.

Parameter Optimization. We used the parameter optimization approach described in [7]. The parameters $\beta_{T,ij}$ and $\gamma_{T,ij}$ were obtained for each binary pair individually, leaving the other interaction parameters set to their default values. The experimental data were added to the database of experimental data used in the fitting tool. Then the python script was launched which carried out the optimization, doing a stochastic global optimization over the two interaction parameters with the DEAP software package. The approach used is a classical evolutionary optimization methodology with crossover/mutation, etc. The open-source fitting routines are at https://github.com/ianhbell/binfit. This mixture behavior is ideal enough that simpler optimization approaches could have been used, but this implementation has proven to be reliable for fitting interaction parameters, particularly for fitting interaction parameters to outputs of iterative routines that can fail for a variety of different reasons. Failures of iterative routines are handled by adding a large contribution to the cost function. Derivatives are not used in the optimization approach, so the cost function to be minimized need not be differentiable.

Mixture thermal conductivity model. In recent years it has become increasingly clear that the transport properties are strongly connected with the residual entropy (i.e., the entropy of a fluid minus the contribution of the ideal-gas, or zero-density limit). This result was first proposed by Rosenfeld in 1977 [86] based on the limited molecular dynamics simulations available at that time. The advent of modern computational resources has meant that Rosenfeld's suggestion has been investigated in greater detail in recent years. The Lennard-Jones 12-6 fluid, one of the most popular molecular model fluids because it includes physically reasonable attraction and repulsion contributions, has recently been shown to follow entropy scaling for viscosity, thermal conductivity, and self-diffusion. [87] Additional studies have demonstrated that the general framework of modified residual entropy scaling allows for an excellent collapse of the experimental transport data for other systems, including the viscosity of propane[88], normal alkanes[89], and refrigerants.[90]

Other researchers [91-94] have applied an older variant of entropy scaling to refrigerant mixtures, but their overall approach of reducing by the dilute-gas viscosity does not follow the correct theoretical constraints in the liquid phase, which is particularly problematic for small molecules like methane and argon.

The approach of modified residual entropy scaling meets the required theoretical limits in the liquid phase, does not diverge at zero density like the original Rosenfeld scaling approach,

and also allows for a formulation consistent with highly accurate dilute-gas measurements and modeling.

In this work we follow the modified residual entropy scaling approach. To begin, the residual entropy is defined by

$$s^{\mathrm{r}} \equiv s(T,\rho) - s^{\mathrm{ig}}(T,\rho) \tag{A.1-13}$$

where s is the entropy per particle and s^{ig} is the ideal-gas entropy per particle, so the value of the reduced scaled residual entropy is given by $s^{+} \equiv -s^{\mathrm{r}}/k_B$ if s^{r} is on a per-particle basis. The residual entropy s^{r} is a measure of the structure of the fluid phase. Intermolecular interactions have the impact of reducing the possible microstates, so s^{r} is generally negative, and therefore s^{+} is positive.

The Rosenfeld-scaled (or macroscopically scaled) thermal conductivity is defined based on non-dimensionalizing the thermal conductivity by the appropriate length, time, and energy scales for the liquid phase. This yields the definition

$$\tilde{\lambda} = \frac{\lambda}{k_B \rho_N^{2/3} \sqrt{k_B T/m}} \tag{A.1-14}$$

As the number density $\rho_N = \rho N_A$ goes to zero at constant temperature, the value of $\tilde{\lambda}$ diverges, but this divergence can be repaired by taking advantage of the result noted by Rosenfeld for inverse-power-law (IPL) fluids of very low but finite density that scaled transport properties are proportional to $(s^{+})^{-2/3}$, which allows for the definition of a term that breaks the zero-density divergence:

$$\lambda^{+} = \tilde{\lambda} \times (s^{+})^{2/3} \tag{A.1-15}$$

In the case of mixtures, a mixing rule must be defined for the effective mass of one particle m. In other works, the mass of the heaviest particle has been used [95]. Mass-fraction weighting of the molecular masses of the components has proven to be the most successful scaling approach in this case, slightly better than mole-fraction weighting of the molecular masses. Otherwise, the quantities ρ_N and s^{+} are obtained from an empirical equation of state. In this case, we have used the updated interaction parameters fitted in this work.

A.2. Task 2 - Flammability Experiments and Test Data

First, the experimental data for the ASHRAE Standard 34 E681 test are presented. Following that, the modified Japanese High-Pressure Gas Law test is described and the experimental results in that device are presented. The next section presents the experimental approach for the laminar burning velocity measurements in the 2-L chamber, and the experimental results for that test are provided.

A.2.1. ASHRAE Standard 34 E681 Test Data

Table A.2-1. E681 test results for R-513A, NIST-ternary blend, R-450A, R-515B, and blends of R-1234yf/134a at a molar composition of (0.26/0.74), (0.28/0.72), and (0.30/0.70).

Volume Fraction (%)	Pressure (mmHg)	Air R.H. (%)	Flame Angles (degrees)	Result (Go/ NoGo)	Comment
R-1234yf/134a/1234ze(E) (32.0/52.0/16.0 by vol%) flammability at 60 °C					
6	760	49.3	No angle	No Go	Just spark, no flame
7	760	50.2	No angle	No Go	Little flame bubble around the spark, disappears within 1”
8	760	49.4	No angle	No Go	Little flame bubble around the spark, disappears within 1”
9	760	49.7	No angle	No Go	Little flame bubble around the spark, disappears within 1”
10	760	51.8	No angle	No Go	Little flame bubble around the spark, disappears within 1”
11	760	51.8	No angle	No Go	Little flame bubble around the spark, disappears within 1”
12	760	52.0	No angle	No Go	Little flame bubble around the spark, disappears within 1”
13	760	51.5	No angle	No Go	Little flame bubble around the spark, disappears within 1”
R-1234yf/134a (74.0/26.0 by vol%) flammability at 60 °C					
6	760	51.1	No angle	No Go	Candle flame
7	760	51.1	No angle	No Go	Flame didn’t reach the top
7	760	51.3	No angle	No Go	Flame didn’t reach the top
8	760	52	86	No Go	
8	760	50.3	95	Go	
8	760	49.9	100	Go	
9	760	51.6	92	Go	
9	760	51.2	85	No Go	
9	760	51.2	90	No Go	

10	760	51.7	88	No Go	
10	760	51.5	91	Go	
10	760	51.2	98	Go	
11	760	51.8	100	Go	
11	760	51.5	81	No Go	
11	760	50.6	82	No Go	
12	760	51.7	88	No Go	
12	760	50.7	88	No Go	
13	760	50.6	No angle	No Go	

R-1234yf/134a (72.0/28.0 by vol%) flammability at 60 °C

6	760	50.4	No angle	No Go	
7	760	50.3	No angle	No Go	Flame didn’t reach the top
8	760	51.9	90	No Go	
8	760	48.9	95	Go	
8	760	49.8	88	Go	
9	760	52.0	91	Go	
9	760	50.5	91	Go	
9	760	49.9	95	Go	
10	760	51.9	100	Go	
10	760	48.9	90	No Go	
10	760	50.2	92	Go	
11	760	48.9	95	Go	
11	760	51.9	97	Go	
11	760	51.3	95	Go	
12	760	51.4	No angle	No Go	Flame fell apart
13	760	51.8	No angle	No Go	Flame fell apart at the top of the flask

R-1234yf/134a (70.0/30.0 by vol%) flammability at 60 °C

6.1	760	49.7	No angle	No Go	Spark only
7.0	760	50.4	No angle	No Go	Flame didn’t reach the top
8.0	760	52.0	55	No Go	Practically no angle, flame didn’t reach the top, it was around 55 deg wide before it disappeared
8.0	760	50.6	80	No Go	
8.0	760	49.7	80	No Go	
8.9	760	50.8	91	Go	

8.9	760	50.1	76	No Go	
8.9	760	50.4	85	No Go	
10.0	760	50.0	90	No Go	
10.0	760	50.2	73	No Go	
10.0	760	49.2	80	No Go	
11.1	760	51.0	90	No Go	
11.1	760	49.5	80	No Go	
11.1	760	49.4	90	No Go	
12.0	760	51.5	45	No Go	Practically no angle, flame didn't reach the top, it was around 45 deg wide before it disappeared
12.0	760	49.5	No angle	No Go	Fell apart before reaching the top of the flask
13.0	760	50.1	No angle	No Go	Didn't reach the top

R-1234yf/134a/227ea (56.0/40.0/4.0 by vol%) flammability at 60 °C

6.1	760	51.8	No angle	No Go	Spark only
7.0	760	51.4	No angle	No Go	Small candle like flame, doesn't reach the top
8.0	760	50.9	No angle	No Go	Small candle like flame, doesn't reach the top
8.9	760	50.6	No angle	No Go	Small candle like flame, doesn't reach the top
8.9	760	51.7	No angle	No Go	Small candle like flame, doesn't reach the top
10.0	760	52.8	No angle	No Go	Small candle like flame, doesn't reach the top
11.1	760	50.7	No angle	No Go	Small candle like flame, doesn't reach the top
12.0	760	52.0	No angle	No Go	Small candle like flame, doesn't reach the top
13.0	760	52.4	No angle	No Go	Small candle like flame, doesn't reach the top

A.2.2. Japanese High-Pressure Gas Law Test

JHPGL Experiment Description. The constant-volume combustion device [29] is based on the Japanese High Pressure Gas Law (JHPGL), and is similar to the design of Takizawa [96], Shebeko [97], and others. The experimental 2-L apparatus is shown in Figure A.2-1 while the plumbing schematic is shown in Figure A.2-1. The chamber consists of a stainless steel (316) sphere with an inner diameter of 15.24 cm, a volume of 1.85 L, and wall thickness of 2.54 cm; the vessel has nine tapped openings for gas inlet and outlet ports, and various transducers. Gases are introduced via the partial pressure mixing technique, and ignition is provided by a fused platinum wire (Alfa Aesar 43014-BY). Rather than basing flammability on a thermocouple temperature rise as specified in the JHPGL, a dynamic pressure transducer was added, allowing a pressure-based criterion.

Figure A.2-1. Spherical 2-L chamber for JHPGL tests and constant volume method laminar burning velocity measurements.

Component partial pressures are determined with an absolute pressure transducer (Omega PX811-030AV, 0 to 206.8 kPa range) with a claimed accuracy of ±0.1%, coupled to a digital strain gage readout (Omega* DP80). These are periodically calibrated against a Baratron 627D (claimed accuracy of 0.12%) and a Wallace & Tiernan 1500 (claimed accuracy of 0.066%) pressure gage. Uncertainty in the pressure reading is estimated to be 2 % of the reading. The refrigerants were HFC-134a , HFO-1234yf , R-513A , HFO-1234ze(E) , and R-515B.

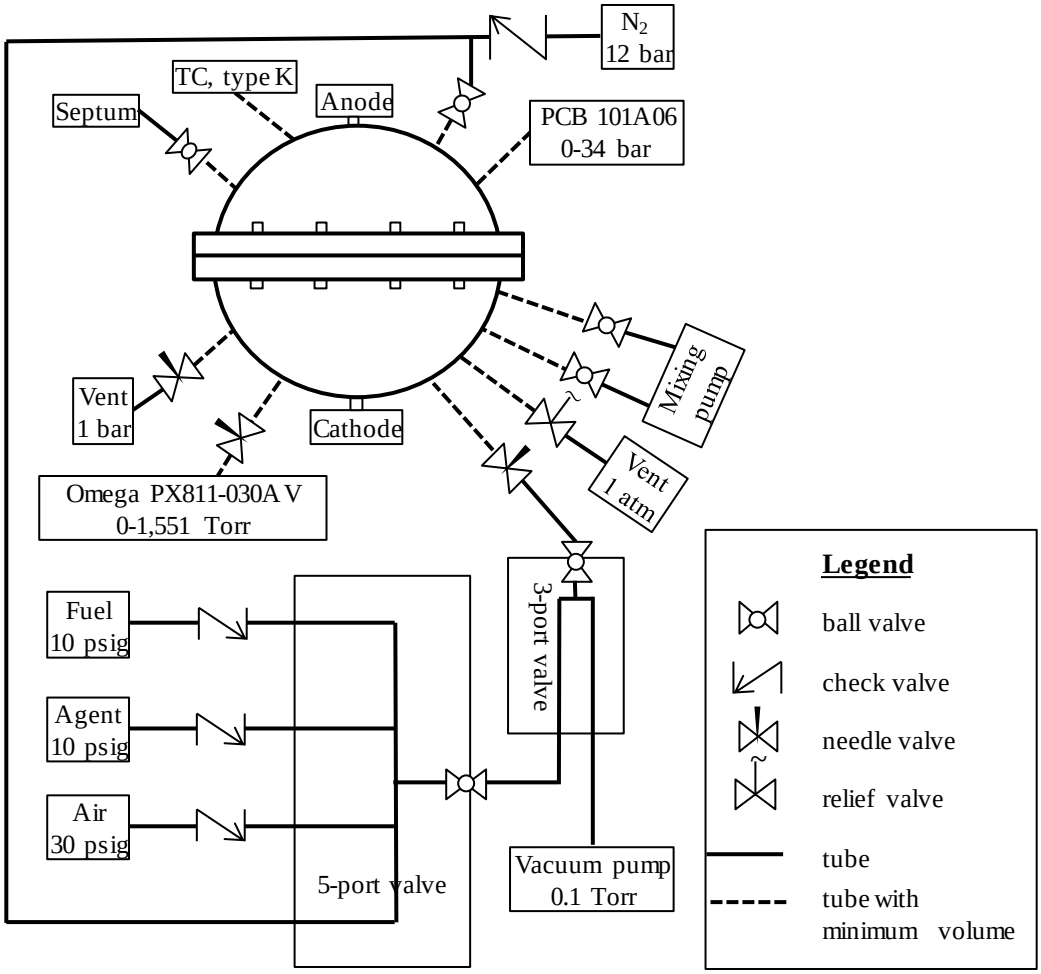

Figure A.2-2. Plumbing schematic diagram for 2-L chamber.

The air was house compressed air (filtered and dried) which is additionally cleaned by passing it through an 0.01 μm filter, a carbon filter, and a desiccant bed to remove small aerosols, organic vapors, and water vapor. The relative humidity of the dry shop air was measured in previous work to be less than 2 % at 22°C. When desired, water was added as a reactant using a 50 μL syringe (Millipore Sigma, Model # 22269-U) through a septum (subsequently closed-off via a ball valve) and allowed to vaporize. After all gases were added they were mixed by a stainless-steel bellows pump in an external loop (evacuated between tests) and allowed to settle for 5 minutes before ignition. The initial temperature of the vessel, measured by a fine type-K thermocouple on the chamber exterior wall, was typically (26.2 ± 0.6) °C .

The igniter configuration was modified slightly from that recommended in the JHPGL. Rather than the igniter leads entering the chamber from two locations at right angles to each other, two parallel copper leads (57 mm long, 1 mm diameter) were used separated by 4 mm and with Teflon insulation around the copper wires in select locations. Crimp-on connections (Digi-Key A2161-ND and A34501-ND) were used between the copper and platinum wires instead of welds. Hence, the igniter could be inserted through a single 6.35 mm inner

diameter orifice, with easily replaceable fusible wire. A variable transformer AC power supply (Powerstat, model 30N116C) provided 100 VAC to the igniter, and its manual switch-controlled ignition. An isolation transformer (Hammond Manufacturing, model 171G, 1000 VA) was used to separate the ignition system from the house electrical supply. This provided a more consistent energy to the igniter and prevented blowing the 10 A fuse in the variable transformer. The platinum wire (20 mm long, 0.3 mm diameter) melted and ruptured violently during each ignition and was replaced.

A data acquisition system (DAS, National Instruments models NI USB-6259 and NI SCC-68, with LabVIEW VI) connected to a personal computer (Dell OptiPlex 7060) recorded the dynamic pressure during each experiment. A dynamic pressure sensor (PCB Piezotronics, model 101A06) with a rise time of 1.5 µsec, a range of 3450 kPa, and reported accuracy of 0.07 kPa, measured the pressure rise in the chamber. The DAS collected data for 60 s at 100 Hz.

Product gases were removed from the chamber at the end of each test to prevent contamination for the subsequent test. Gaseous nitrogen was introduced to the chamber soon after the ignition: 1.) to quickly purge the corrosive acid gases present for some experiments, and 2.) to reduce the temperature of the product gases (to protect components). After ignition, followed by a 10 s delay, gaseous nitrogen at 11 bar pressurized the chamber for 5 s after which the exhaust valve was opened, and N_2 flowed continuously for 10 sec. Following the nitrogen purge, clean and dried shop air flushed the chamber for ten minutes, the chamber was evacuated and maintained for 2 minutes, followed by dry air purge for 2 minutes (with these last two steps repeated).

Japanese High-Pressure Gas Law Test Data

Table A.2-2. Japanese High-Pressure Gas Law test results obtained at NIST for: R-513A, NIST-ternary blend, R-450A, R-515B, and blends of R-1234yf/134a, all with dry or 50 % r.h. air as listed.

Volume Fraction %	Nominal Humidity	Run No.	Run Date	Partial Pressure, torr					P_{tot}	P	Pressure Rise, bar
				p_1	p_2	p_3	p_{air}	p_w			
R-513A (R134a/1234yf) (0.469/0.531, mole fraction)											
7.0	Dry	16	2020-10-22	26.2	29.7	N/A	742.4	N/A	798.2	759.8	0.003
8.0		17	2020-10-22	29.9	33.9		734.5		798.3	759.9	0.097
9.3		1	2020-10-20	34.6	39.3		724.4		798.2	760.0	0.080
10.0		2	2020-10-20	37.4	42.4		718.6		798.3	759.9	0.202
10.5		3	2020-10-20	39.3	44.5		714.5		798.2	759.7	0.178
11.0		4	2020-10-20	41.2	46.7		710.5		798.3	760.0	0.191
11.0		18	2020-10-22	41.1	46.7		710.5		798.2	759.8	0.214
11.3		10	2020-10-21	42.1	47.7		708.7		798.4	760.3	0.253
11.5		11	2020-10-21	43.0	48.8		706.6		798.4	760.0	0.242
12.0		12	2020-10-21	44.9	50.9		702.8		798.4	760.0	0.255
12.5		7	2020-10-21	46.7	53.0		698.7		798.4	760.1	0.178
13.0		8	2020-10-21	48.6	55.1		694.6		798.3	760.1	0.209
14.0		9	2020-10-21	52.4	59.4		686.7		798.3	760.1	0.239
15.0		13	2020-10-22	56.1	63.6		678.7		798.4	759.7	0.165
16.0		15	2020-10-22	59.9	67.9		670.5		798.2	760.0	0.164
17.0		14	2020-10-22	63.6	72.1		662.8		798.4	760.3	0.004
11.5		5	2020-10-20	43.0	48.8		706.6		798.4	760.0	0.094
12.0		6	2020-10-21	44.9	50.9		702.7		798.5	760.1	0.004
5.0	42	10	2020-11-12	18.7	21.2	N/A	747.7	11.0	798.3	759.8	0.027
6.0	52	9	2020-11-12	22.4	25.4		739.7	10.9	798.3	759.2	0.061
7.0	46	8	2020-11-12	26.2	29.7		732.1	10.4	798.2	759.4	0.077
8.0	55	7	2020-11-12	29.9	33.9		724.4	10.3	798.3	759.5	0.096
10.0	50	1	2020-11-10	37.4	42.4		707.8	10.9	798.3	759.5	0.306
11.0	58	5	2020-11-10	41.1	46.7		700.1	10.8	798.4	759.8	0.446
12.0	58	2	2020-11-10	44.9	50.9		692.0	10.7	798.3	759.3	0.474
13.0	55	6	2020-11-12	48.6	55.1		683.5	11.2	798.1	759.2	0.330
14.0	45	3	2020-11-10	52.3	59.4		676.3	10.4	798.2	759.4	0.173
16.0	53	4	2020-11-10	59.8	67.9		660.1	11.0	798.5	759.7	0.095
18.0	53	11	2020-11-12	67.3	76.3		644.4	10.5	798.3	759.4	0.035
19.0	58	12	2020-11-12	71.1	80.6		636.3	10.6	798.4	759.7	0.002
R-450A (R134a/1234ze(E)) (0.447/0.553, mole fraction)											
4.0	Dry	13	2020-11-25	14.3	17.7	N/A	766.7	N/A	798.2	759.9	0.044
6.0		10	2020-11-25	21.4	26.4		750.8		798.2	760.1	0.027
8.0		6	2020-11-24	28.6	35.3		734.7		798.2	759.6	0.046
10.0		1	2020-11-24	35.7	44.2		718.8		798.4	760.2	0.141
10.9		11	2020-11-25	39.2	48.5		715.6		803.0	760.3	0.061
12.0		3	2020-11-24	42.8	53.0		702.9		798.2	760.2	0.258
13.0		4	2020-11-24	46.4	57.4		695.0		798.3	760.0	0.147
15.0		7	2020-11-24	53.5	66.2		679.0		798.2	759.9	0.164
16.0		12	2020-11-25	57.1	70.6		671.0		798.2	759.9	0.137
18.0		8	2020-11-25	64.2	79.4		655.0		798.2	759.6	0.030
20.0		9	2020-11-25	71.4	88.3		639.0		798.2	760.0	0.028

22.0		14	2020-11-25	78.5	97.1		623.3		798.4	759.9	0.014
11.0		2	2020-11-24	39.3	48.6		710.8		798.2	760.1	0.004
11.0		5	2020-11-24	39.2	48.5		710.7		798.1	759.4	0.003
5.0	53	14	2020-11-23	17.8	22.1	N/A	747.7	11.1	798.3	759.5	0.012
6.0	53	5	2020-11-20	21.3	26.4		739.6	11.1	798.2	760.2	0.066
7.0	56	6	2020-11-20	25.0	30.9		731.2	11.6	798.4	760.1	0.095
8.0	42	1	2020-11-19	28.5	35.4		726.2	8.5	798.3	759.7	0.128
9.0	56	7	2020-11-20	32.1	39.8		715.6	11.2	798.3	760.0	0.186
10.0	53	2	2020-11-19	35.6	44.2		708.4	10.5	798.4	759.6	0.262
11.0	55	8	2020-11-20	39.2	48.6		700.3	10.8	798.4	759.8	0.124
12.5	58	13	2020-11-23	44.6	55.1		687.7	11.2	798.3	759.3	0.185
13.0	57	9	2020-11-20	46.4	57.3		683.9	10.9	798.2	759.7	0.161
14.0	56	3	2020-11-19	50.0	61.8		676.1	10.7	798.3	759.5	0.205
15.0	58	10	2020-11-20	53.5	66.2		668.0	10.8	798.2	759.8	0.156
16.0	57	4	2020-11-19	57.1	70.6		660.4	10.7	798.3	759.5	0.019
17.0	59	15	2020-11-23	60.9	74.9		652.1	10.9	798.4	759.4	0.083
19.0	60	16	2020-11-23	67.8	83.9		636.2	10.8	798.3	759.6	0.060
11.0	50	11	2020-11-20	39.2	48.6		700.9	9.9	798.3	759.9	0.083
13.0	55	12	2020-11-23	46.3	57.6		684.2	10.5	798.3	759.7	0.141

NIST Ternary Blend (R134a/1234yf/1234ze(E) (0.52/0.32/0.16, mole fraction)

10.5	Dry	7	2020-11-04	311.9	192.1	96.0	714.5	N/A	798.4	760.2	0.003
11.0		5	2020-11-04	312.0	192.0	96.2	710.6		798.5	760.0	0.003
11.3		8	2020-11-04	312.0	192.1	95.9	708.5		798.3	760.2	0.210
11.4		1	2020-11-03	311.8	192.1	95.9	711.4		803.2	764.8	0.211
12.0		6	2020-11-04	312.0	192.1	95.9	702.6		798.4	759.9	0.203
12.5		2	2020-11-03	312.0	191.9	96.0	698.4		798.3	760.0	0.123
13.5		3	2020-11-03	312.0	192.0	95.9	690.5		798.4	760.0	0.000
14.0		4	2020-11-04	312.0	191.9	96.0	686.6		798.4	760.1	0.001
8.0	54	5	2020-11-06	33.2	20.5	10.2	723.6	11.0	798.3	759.3	0.002
9.0	53	4	2020-11-06	37.3	23.0	11.5	716.0	10.7	798.3	759.7	0.138
10.0	55	7	2020-11-09	41.5	25.5	12.7	707.9	11.0	798.4	758.7	0.192
11.0	52	1	2020-11-06	45.3	28.2	14.0	700.9	10.3	798.4	759.8	0.406
12.0	50	9	2020-11-09	49.8	30.6	15.3	691.9	10.9	798.3	759.6	0.451
13.0	50	2	2020-11-06	53.9	33.2	16.6	685.2	9.6	798.3	759.8	0.234
15.0	57	3	2020-11-06	62.2	38.3	19.1	668.2	10.7	798.3	759.4	0.131
16.0	63	6	2020-11-06	66.4	40.9	20.5	659.2	11.6	798.3	759.6	0.120
17.0	57	10	2020-11-09	70.5	43.5	21.7	652.5	10.5	798.3	759.8	0.083
18.0	60	11	2020-11-09	74.7	46.0	22.9	644.0	10.9	798.4	759.8	0.048
12.0	57	8	2020-11-09	49.8	30.6	15.4	691.8	11.0	798.4	760.2	0.023

R-515B (R1234ze(E)/R227ea) (0.939/0.061, mole fraction)

4.0	Dry	15	2020-11-16	2.0	30.0	N/A	766.6	N/A	798.1	759.7	0.005
5.0		14	2020-11-16	2.5	37.5		758.8		798.4	759.9	0.072
6.0		13	2020-11-16	2.9	45.0		750.7		798.3	759.8	0.101
7.0		7	2020-11-13	3.4	52.5		742.7		798.3	759.0	0.053
8.0		6	2020-11-13	3.9	60.0		734.7		798.3	759.6	0.415
9.0		9	2020-11-13	4.4	67.5		726.7		798.3	759.6	0.507
9.6		1	2020-11-13	4.7	72.0		721.6		798.1	759.7	1.031
9.6		17	2020-11-18	4.7	71.9		722.2		798.4	760.3	1.564
10.0		8	2020-11-13	4.9	74.9		718.7		798.2	759.8	1.221
10.0		16	2020-11-18	4.9	74.9		718.9		798.3	760.4	0.852
11.0		2	2020-11-13	5.4	82.4		710.8		798.4	760.0	0.400

12.0		3	2020-11-13	5.9	89.9		702.8		798.3	759.7	0.329
13.0		4	2020-11-13	6.4	97.4		694.7		798.2	759.7	0.241
14.0		10	2020-11-16	6.9	104.9		686.9		798.3	759.6	0.227
16.0		11	2020-11-16	7.9	119.9		671.0		798.4	760.0	0.058
17.0		12	2020-11-16	8.3	127.3		663.0		798.3	759.8	0.004
9.0		5	2020-11-13	4.4	67.5		726.6		798.2	759.7	0.169
9.3		18	2020-11-18	4.6	69.7		724.4		798.2	759.6	0.213
4.0	50	13	2020-11-18	2.0	29.9	N/A	756.2	10.7	798.4	760.1	0.018
5.0	53	11	2020-11-18	2.5	37.4		747.6	11.2	798.3	759.6	0.053
6.0	53	10	2020-11-18	2.9	44.9		740.1	10.9	798.5	760.2	0.002
8.0	45	9	2020-11-18	3.9	59.9		725.4	9.1	798.2	759.8	0.150
9.0	55	8	2020-11-17	4.4	67.4		715.9	11.0	798.5	759.8	1.269
10.0	52	2	2020-11-16	4.9	74.9		708.2	10.4	798.1	759.2	1.658
11.0	55	4	2020-11-17	5.4	82.3		700.2	10.8	798.3	759.6	0.974
12.0	53	12	2020-11-18	5.9	89.9		691.6	11.3	798.3	760.1	0.210
13.0	50	5	2020-11-17	6.4	97.3		685.1	9.6	798.2	758.6	0.186
15.0	58	6	2020-11-17	7.4	112.3		668.1	10.8	798.3	758.6	0.086
17.0	58	7	2020-11-17	8.3	127.3		652.2	10.7	798.2	759.8	0.013
9.0	42	1	2020-11-16	4.4	67.4		718.2	8.5	798.2	759.1	0.134
11.0	46	3	2020-11-17	5.4	82.4		701.6	9.0	798.1	758.8	0.036

R134a/1234yf (0/1.0, mole fraction)

7.0	Dry	1	2020-12-14	56.0	N/A	N/A	743.9	N/A	799.1	760.5	0.060
8.0		2	2020-12-14	64.0			735.2		798.4	759.4	1.462
8.5		8	2020-12-15	67.8			731.2		798.3	760.1	2.666
9.0		3	2020-12-14	72.0			727.2		798.4	760.0	3.667
10.0		4	2020-12-14	79.8			719.3		798.3	759.7	1.981
11.0		5	2020-12-14	87.8			713.0		800.0	760.4	0.815
12.0		6	2020-12-14	95.8			703.5		798.4	759.6	0.006
13.0		7	2020-12-14	103.8			695.3		798.3	759.7	0.183
8.0	44	4	2021-01-12	63.8	N/A	N/A	727.0	9.0	798.5	759.6	2.81
9.0	45	3	2021-01-12	71.8			718.5	9.1	798.2	759.5	4.61
10.0	45	5	2021-01-12	79.7			711.4	9.1	798.8	759.9	1.87
9.0	47	1	2021-01-12	71.8			718.2	9.5	798.2	759.9	2.55
8.9	46	2	2021-01-12	71.8			723.0	9.4	802.9	760.2	2.57

R134a/1234yf (0.2/0.8, mole fraction)

7.0	Dry	8	2020-12-22	11.2	44.7	N/A	743.2	N/A	798.2	759.9	0.089
8.0		1	2020-12-15	12.9	50.9		735.3		798.3	759.9	0.494
9.0		9	2020-12-22	14.4	57.6		727.3		798.4	760.0	1.540
10.0		11	2020-12-22	16.1	63.8		719.4		798.2	759.7	0.466
11.0		5	2020-12-18	17.5	70.4		711.2		798.4	759.9	0.678
12.0		6	2020-12-18	19.2	76.6		703.3		798.3	759.8	0.006
9.0		7	2020-12-18	14.4	57.4		727.3		798.3	760.2	0.239
9.0		2	2020-12-15	14.4	57.5		727.2		798.3	759.6	0.013
10.0		3	2020-12-15	16.0	63.8		719.4		798.4	760.1	0.990
11.0		4	2020-12-15	17.6	70.2		711.5		798.4	760.1	0.223
10.0		10	2020-12-22	16.0	63.8		719.5		798.3	760.0	0.071
8.0	47	3	2021-01-06	12.7	51.2	N/A	726.1	9.5	798.3	759.4	1.271
9.0	47	1	2021-01-05	14.3	57.4		718.3	9.4	798.2	759.2	1.987
10.0	46	2	2021-01-06	15.9	63.9		710.4	9.2	798.3	759.7	0.795

R134a/1234yf (0.3/0.7, mole fraction)

8.0	Dry	5	2021-01-08	19.2	44.7	N/A	735.8	N/A	798.4	759.9	0.087
9.0		3	2021-01-08	21.6	50.3		730.9		801.4	760.1	0.787
10.0		4	2021-01-08	24.0	55.8		719.8		798.3	760.0	0.780
11.0		2	2021-01-08	26.4	61.5		711.9		798.4	759.9	0.203
10.0		1	2021-01-08	24.0	55.8		719.9		798.4	760.2	0.524
9.0	46	5	2021-01-06	21.5	50.3	N/A	718.4	9.3	798.3	759.5	0.003
10.0	51	4	2021-01-05	23.9	55.9		709.7	10.1	798.3	759.5	1.271
11.0	53	3	2021-01-05	26.2	61.7		701.0	10.5	798.2	759.2	1.047
12.0	43	1	2021-01-05	28.6	67.1		695.3	8.4	798.2	759.3	0.592
11.0	47	2	2021-01-05	26.2	61.5		702.5	9.3	798.2	759.5	0.310

R134a/1234yf (0.4/0.6, mole fraction)

9.0	Dry	5	2021-01-11	28.8	43.2	N/A	727.6	N/A	798.3	760.1	0.090
10.0		2	2021-01-11	31.9	48.0		719.8		798.4	760.2	0.239
11.0		4	2021-01-11	35.2	52.6		711.8		798.4	760.2	0.119
11.0		3	2021-01-11	35.2	52.7		711.9		798.4	760.2	0.067
11.0		1	2021-01-11	35.2	52.7		711.9		798.5	760.4	0.024
10.0	51	2	2021-01-06	31.9	47.9	N/A	709.5	10.2	798.2	758.5	0.865
11.0	53	1	2021-01-06	35.1	52.7		701.4	10.4	798.4	759.5	0.936
12.0	51	3	2021-01-06	38.4	57.4		693.7	10.0	798.2	759.5	0.783

R134a/1234yf (0.5/0.5, mole fraction)

7.0	Dry	13	2020-12-23	28.0	27.9	N/A	743.4	N/A	798.4	760.1	0.067
8.0		10	2020-12-07	32.0	31.9		735.1		798.3	759.4	0.114
10.0		6	2020-12-04	40.0	40.0		719.2		798.7	760.1	0.152
11.0		1	2020-11-30	44.0	43.9		710.9		798.2	759.2	0.205
11.5		3	2020-12-01	45.9	45.9		707.2		798.5	759.7	0.261
12.0		4	2020-12-03	47.9	47.8		703.0		798.3	759.7	0.315
13.0		7	2020-12-07	51.9	52.2		694.8		798.3	759.6	0.227
15.0		8	2020-12-07	59.9	59.9		679.1		798.3	759.3	0.146
17.0		9	2020-12-07	67.9	67.9		663.3		798.3	759.3	0.117
18.0		11	2020-12-23	71.9	71.8		655.6		798.4	760.4	0.104
20.0		12	2020-12-23	79.9	79.7		639.8		798.4	760.3	0.032
10.0		5	2020-12-04	40.0	39.8		719.1		798.3	759.6	0.026
11.5		2	2020-11-30	45.9	45.9		707.1		798.4	759.5	0.059

R134a/1234yf (0.55/0.45, mole fraction)

9.0	46	6	2021-01-22	39.6	32.5	N/A	718.6	9.2	798.3	758.9	0.065
10.0	53	5	2021-01-22	44.0	35.9		709.3	10.5	798.3	759.7	0.121
11.0	50	4	2021-01-22	48.3	39.5		702.2	9.8	798.4	759.7	0.227
12.0	58	3	2021-01-22	52.7	43.1		692.9	11.3	798.4	759.7	0.271
13.0	58	11	2021-01-25	57.1	46.6		685.2	11.1	798.4	759.8	0.147
14.0	59	12	2021-01-25	61.5	50.3		677.1	11.2	798.4	759.6	0.041
15.0	59	7	2021-01-22	65.9	53.8		669.1	11.2	798.4	759.7	0.172
16.0	66	8	2021-01-25	70.3	57.4		659.9	12.2	798.3	759.5	0.131
17.0	63	10	2021-01-25	74.7	61.0		652.8	11.5	798.4	759.6	0.102
18.0	59	9	2021-01-25	79.0	64.6		645.8	10.6	798.4	760.0	0.008
13.0	58	1	2021-01-21	57.1	46.7		684.6	11.3	798.2	758.5	0.078
13.4	59	2	2021-01-22	58.7	48.1		681.5	11.3	798.3	759.3	0.007

R134a/1234yf (0.7/0.3, mole fraction)

7.0	Dry	9	2020-12-09	39.2	16.7	N/A	743.1	N/A	798.3	759.2	0.006
8.0		5	2020-12-08	44.8	19.1		735.1		798.3	759.7	0.071
10.0		4	2020-12-08	55.9	23.9		719.2		798.3	759.7	0.072
11.0		6	2020-12-08	61.5	26.4		711.2		798.4	759.0	0.171
12.0		1	2020-12-08	67.1	28.7		703.1		798.3	759.9	0.176
13.0		7	2020-12-08	72.7	31.1		695.4		798.4	759.0	0.154
14.0		2	2020-12-08	78.3	33.5		687.1		798.3	759.9	0.160
15.0		8	2020-12-09	83.8	35.9		679.2		798.3	759.8	0.149
16.0		3	2020-12-08	89.4	38.2		671.2		798.2	759.5	0.005
17.0		10	2020-12-11	95.0	40.7		663.4		798.2	759.6	0.049
18.0		11	2020-12-23	100.6	43.1		655.7		798.3	760.2	0.015

R134a/1234yf (0.8/0.2, mole fraction)

11.0	Dry	4	2020-12-09	70.3	17.5	N/A	711.2	N/A	798.3	759.5	0.004
12.0		5	2020-12-09	76.7	19.1		703.2		798.3	759.6	0.006
13.0		1	2020-12-09	83.0	20.7		695.3		798.4	759.8	0.082
14.0		2	2020-12-09	89.4	22.4		687.3		798.3	759.8	0.124
15.1		3	2020-12-09	95.8	25.2		678.0		798.2	759.9	0.107
16.0		6	2020-12-09	102.2	25.6		671.4		798.5	760.0	0.034
17.0		7	2020-12-10	108.5	27.2		663.0		798.3	759.9	0.070
18.0		8	2020-12-11	115.0	28.7		655.4		798.4	759.9	0.101
19.0		9	2020-12-11	121.3	30.3		647.3		798.2	760.1	0.110
20.0		10	2020-12-11	127.8	31.9		639.5		798.3	759.8	0.033

R134a/1234yf (0.9/0.1, mole fraction)

13.0	Dry	4	2020-12-10	93.4	10.4	N/A	695.1	N/A	798.3	759.8	0.023
14.0		1	2020-12-10	100.6	11.1		687.2		798.3	759.8	0.155
15.0		2	2020-12-10	107.8	12.1		679.1		798.3	760.1	0.070
16.0		3	2020-12-10	115.0	12.8		671.2		798.2	759.9	0.034
17.0		5	2020-12-10	122.1	13.5		663.4		798.2	760.0	0.113
18.0		6	2020-12-11	129.3	14.4		655.4		798.4	760.1	0.132
19.0		7	2020-12-11	136.6	15.0		647.4		798.4	759.8	0.016

R134a/1234yf (1.0/0, mole fraction)

13.0	57	11	2021-01-21	103.8	N/A	N/A	685.2	10.9	798.3	759.2	0.023
14.0	55	2	2021-01-15	111.7			677.6	10.4	798.2	759.1	0.087
15.0	44	1	2021-01-15	119.6			671.8	8.3	798.3	759.5	0.102
16.0	58	3	2021-01-15	127.7			661.2	10.8	798.4	759.3	0.103
17.0	60	4	2021-01-19	135.7			652.8	11.0	798.2	759.7	0.030
17.9	62	5	2021-01-19	143.6			647.2	11.3	800.6	759.8	0.033
19.0	60	6	2021-01-19	151.7			637.3	10.8	798.2	759.7	0.096
20.0	61	7	2021-01-19	159.7			629.3	10.8	798.4	759.7	0.095
20.9	68	8	2021-01-19	167.5			620.2	11.9	798.3	759.6	0.068
22.0	65	9	2021-01-21	175.6			612.9	11.2	798.3	759.2	0.053
22.9	65	10	2021-01-21	183.5			605.2	11.1	798.3	759.3	0.053

A.2.3. Constant Volume (2 L) Laminar Burning Velocity Measurements

Experiment Description. The experimental approach for measuring the laminar burning velocity LBV in the 2-L chamber from the pressure rise has been described in previous work [26, 27, 40, 98], and this description is an updated version of that in Pagliaro et al. [27]. The experiment uses the same 2-L chamber and gas preparation system as described above for the modified JHPGL test. Instead of the hot-wire ignition, the LBV measurement uses an electrical spark from a capacitive discharge ignition system (based on the work of Shepherd et al. [99]). A 1 kV to 15 kV power supply and custom-made capacitor banks (1 nF to 50 nF) provide variable ignition energies, with an estimated operating range of 0.05 mJ to 500 mJ. Two tungsten electrodes form a gap in the center of the chamber. Thin electrodes (0.4 mm diameter) minimize heat loss from the flame, and the spark gap is adjustable (2 mm, typical).

Gases and mixture preparation are the same as in the JHPGL test, with the additional refrigerant HFC-152a (Honeywell). Ignition is attempted several times, while gradually increasing the capacitor charging voltage, until ignition occurs. This ensures the ignition energy is within an order of magnitude of the minimum value. The explosion pressure is recorded at 4000 Hz with the dynamic pressure sensor, and the product gases are immediately purged, as described above. Laminar burning velocity is determined from the pressure trace using a thermodynamic model, developed by Metghalchi and Keck [100, 101] and further refined by others [102, 103]. A brief overview of the method follows; however, the current work uses an updated software package that allows for inclusion of radiation heat losses, burned gas dissociation, and accounts for extrapolation errors due to the range of selected pressure-rise data [49]. Nonetheless, the present data were reduced assuming adiabatic conditions and using a 2-zone model as described below.

Burning Velocity from the Pressure Trace. The content of the chamber is divided into burned and unburned zones separated by a reaction sheet, assumed to be infinitely thin, spherical, and smooth (no instabilities). Initially, the unburned gas is considered perfectly mixed and at rest. As the unburned gases react, a spatially uniform increase in pressure occurs. The burned gas is in chemical equilibrium and both the burned and unburned gases are considered as ideal, semi-perfect gases. Both zones are adiabatic, and the unburned gas is isentropically compressed as the mixture reacts in the flame sheet.

With these assumptions, the instantaneous flame radius and burning velocity can be expressed in terms of the chamber pressure by applying conservation of mass. The results are given in Eq. A.2-1 and Eq. A.2-2 (detailed formulation of the equations can be found in refs. [100, 102]),

$$r_f = R\left[1 - (1 - x_b)(P_0/P)^{1/\gamma_u}\right]^{1/3} \quad \text{(A.2-1)}$$

$$S_L = R/3(R/r_f)^2(P_0/P)^{1/\gamma_u}(dx_b/dt) \quad \text{(A.2-2)}$$

in which r_f is the flame radius, S_u is the laminar burning velocity, R is the chamber radius, x_b is the mass fraction of burned gas, P is the instantaneous pressure, P_0 is the initial pressure, and γ_u is the unburned gas specific heat ratio. To determine burning velocity, the

mass fraction of burned gas x_b must be related to the chamber pressure (for simplification, early studies applied a linear relationship [104]). Alternatively, a thermodynamic closed system analysis on the contents within the chamber can be performed. A two-zone approach is used in the present work. The burned gas zone also can be modeled using incremental shell volumes [105, 106], allowing burned gas density and temperature gradients; nonetheless, since previous studies have shown that (for adiabatic flames) inclusion of the gradients has negligible effect on the burning velocity [101, 102], we retain the two-zone model. The fraction of mass burned x_b is found from simultaneous solution of the conservation of mass and energy equations given in Eq. A.2-3 and Eq. A.2-4, applied for the two zones,

$$\frac{V}{M} = \int_0^{x_b} v_b dx + \int_{x_b}^1 v_u dx \tag{A.2-3}$$

$$\frac{E}{M} = \int_0^{x_b} e_b dx + \int_{x_b}^1 e_u dx \tag{A.2-4}$$

where V is the volume of the chamber, E is the total internal energy of the gases in the chamber, M is the mass of the gas in the chamber, e and v are the internal energy and specific volume of the gas, and the subscripts b and u refer to the burned and unburned gas.

Thermodynamic data for the unburned and burned gases are required for model implementation. Data for all of the species are taken from the recent detailed kinetic model of Babushok et al. [46].

The unburned gas properties are related to the chamber pressure through isentropic compression:

$$T_u = T_{u0}\left(\frac{P}{P_0}\right)^{(\gamma_u - 1)/\gamma_u} \tag{A.2-5}$$

in which T_{u0} is the initial unburned temperature. Since γ_u is a function of the unburned gas temperature T_u and the initial mixture composition, T_u and γ_u are solved iteratively at each pressure increment. The properties of the unburned gas mixture, v_u and e_u, are determined from the mixture composition and temperature.

The remaining unknowns in the conservation equations (v_b, e_b, and x_b) are found through iteration of T_b (v_b and e_b are functions of temperature) and x_b at each pressure increment, until the proper values of T_b and x_b are obtained. Burned gas species concentrations, required for the determination of v_b and e_b, are estimated for each value of T and P using a constant volume equilibrium calculation performed via the open-source Cantera software package [31]. Once $x_b(P)$ is known, the burning velocity $S_u(P, T_u)$ is calculated over the experimental range of pressure and temperature using Eq. A.2-2.

Data Reduction. Figure A.2-3 shows a typical pressure trace (solid line) from an experiment (CH_4-air, ϕ=1.0), along with T_b, T_u, and r_f, which are outputs of the two-zone model calculation. Only a portion of the pressure data is used for obtaining burning velocity, as denoted by the thick line on the pressure trace. For small r_f, the flame behavior is affected by

flame stretch and the ignition process, and for large r_f, by heat losses to the walls and cellular instabilities; hence, typically only the central 75 % of the pressure data are used. The present data reduction was performed using a new NIST-developed tool, CVDART (Constant Volume Data Reduction Tool) [49] which allows for detailed examination of the effects of different data ranges. The data range selected for each test was manually selected to minimize the effects of ignition and flame instabilities due to cellular flame formation at the larger radii.

Spherically propagating flames are subject to stretch rates inversely proportional to the flame radius [107],

$$\kappa = \frac{2}{r_f}\frac{dr_f}{dt} \tag{A.2-6}$$

where κ is the stretch rate and dr_f/dt is the flame front velocity. Figure A.2-3 also shows the stretch rate for this experiment.

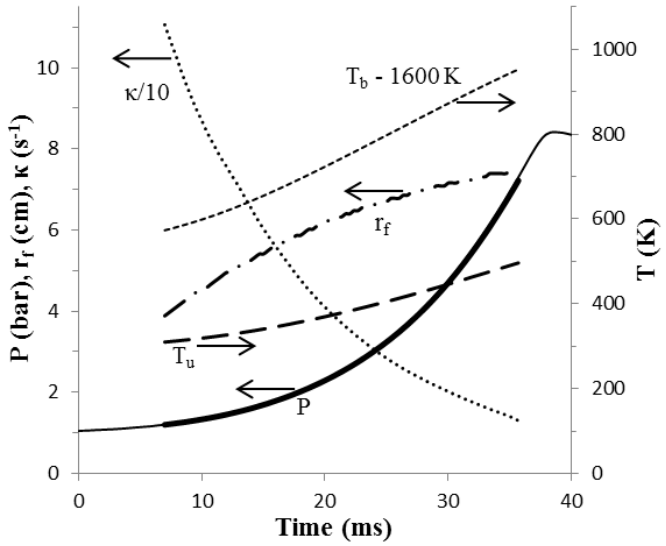

Figure A.2-3. Experimental pressure trace P, flame radius rf, flame stretch rate κ, and gas temperature (unburned Tu and burned Tb) as a function of time.

A single experiment provides burning velocity data for a range of pressure and temperature of the unburned gas, and these data are fit to the equation [33]:

$$S_L = S_{L,0}\left(\frac{T}{T_0}\right)^{\alpha}\left(\frac{P}{P_0}\right)^{\beta} \tag{A.2-7}$$

in which S_L is the laminar burning velocity, P_0 is the initial pressure, T_0 is the initial temperature, $S_{L,0}$ is the laminar burning velocity at the initial conditions; α, β, and $S_{L,0}$ are

the fitting parameters. In the experiments performed, T_0 is 299 ±2 K, and P_0 is 0.868 bar, 1 bar, and 1.13 bar, (to provide more data for the curve fit). As described in Takizawa et al. [108], S_u^0, α, and β depend upon ϕ and can be fit to the following equations (2–4):

$$S_{L0} = S_{L0,max} + s_1(f - f_{max})^2 + s_2(f - f_{max})^3 \quad \text{(A.2-8)}$$

$$a = a_1 + a_2(f - 1) \quad \text{(A.2-9)}$$

$$b = b_1 + b_2(f - 1) \quad \text{(A.2-10)}$$

Thus, a_1, a_2, b_1, b_2, s_1, s_2, $S_{L0,max}$, and f_{max} are fitting parameters to the data, with $S_{L0,max}$ the maximum laminar burning velocity over all ϕ, and ϕ_{max}, the value of ϕ at which it occurs.

Figure A.2-4 shows the burning velocity of stoichiometric methane-air as a function of unburned gas temperature and chamber pressure. The light grey surface is the fit following Eq. A.2-7, and the darker grey data points (and lines through them) are the S_L values at each combination of unburned gas pressure and temperature for a specific run, to which Eq. A.2-7 is fit.

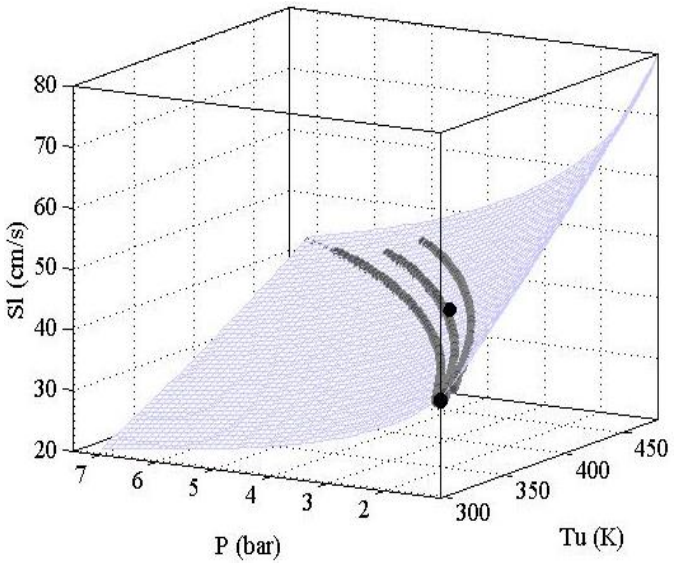

Figure A.2-4. Three-dimensional plot of burning velocity as a function of pressure P and unburned gas temperature Tu.

The dark grey dots represent the data from three experiments, one at each initial pressure. The light grey surface represents the fitted results using Eq. A.2-7 and the black dots are the reported S_L at ambient (T_0=298 K, P_0=1 bar) and compressed (T_0=400 K, P_0=3 bar) conditions.

In the present method, spherical flame propagation is a critical condition for accurate determination of S_L from the pressure trace. Buoyancy can distort the shape of the flame, especially for slow burning mixtures (which are of particular interest in the present work).

Takizawa et al. [103] estimated the minimum burning velocity measurable without error associated with buoyancy. Results showed that burning velocities as low as 6 cm/s could be measured with the constant-volume method. In the present work, cellular instabilities, which also invalidate the spherical flame assumption, are monitored through inspection of the S_L data of individual test runs. The onset of cellular instabilities is typically detected via a distinct increase in S_L [105, 109], and these data (if occurring) are omitted during the experimental data fitting.

Uncertainties. Uncertainties in the measured parameters presented as expanded uncertainties ku_c from a combined standard uncertainty (estimated standard deviation) u_c, and a coverage factor k=2 (level of confidence approximately 95%). Relative uncertainties ku_c/X are reported, with X being the measured value of the parameter under consideration. Uncertainties in initial temperature and pressure, dynamic pressure rise, agent volume fraction, equivalence ratio, and burning velocity calculation and fitting to Eq. A.2-7 are considered. The expanded relative uncertainties related to reactant mixture preparation are 1.0% for the equivalence ratio, 0.3% for the volume fraction of air, and 0.8% for the volume fraction of fuel. Uncertainty in the volume fraction of refrigerant ranged from 4% at low concentrations (volume fraction of 0.01) to <1% at higher concentrations (volume fraction of 0.05). Relative uncertainties for the dynamic pressure rise, initial pressure, and initial temperature are 1.3%, 0.7%, and 0.4 %. Thus, the maximum expanded relative uncertainty (ku_c/X) for the reported experimental burning velocities is 12%. This does not consider the uncertainty due to the selected data range for the extrapolation, which are discussed in detail for the present data in Kim et al.[110].

Experimental Burning Velocity Test Data. Table A.2.3 lists the fitting parameters (Eq. A.2-8, to A.2.10) for the burning velocity as a function of with ϕ , T_u and P for pure HFC-152a and its mixtures with HFC-134a and HFO-1234yf. The corresponding raw experimental data are given in Table A.2.4.

Table A.2-3. Fitting parameters for the variation of S_L with ϕ , T_u and P for experimental burning velocity data obtained in 2-L experiment from pressure rise data for R-152a/134a and R-152a/1234yf mixtures. Data presented for 298 K, 101 kPa initial conditions, and dry air (<2% r.h.) of wet air (50 % r.h.) as noted.

Composition (mole frac)	Humidity	S_{u0} (cm/s)				α		β	
		$S_{u0,max}$	s1	ϕ_{max}	s2	a1	a2	b1	b2
R-152a									
(1.0)	Dry	22.92	-85.94	1.10	-13.80	1.25	-0.56	-0.06	0.20
R-152a/134a									
(0.8/0.2)		18.05	-75.78	1.09	-6.23	2.26	-2.01	-0.71	-0.33
R-152a/134a									
(0.5/0.5)		9.99	-35.48	1.04	20.44	1.96	0.21	-0.19	-0.17
R-152a/1234yf									
(0.5/0.5)		13.40	-39.50	1.04	3.51	1.86	-1.49	-0.15	0.35
(0.4/0.6)		9.38	-50.71	0.99	61.30	2.48	-3.06	-0.21	0.75
(0.4/0.6)	Wet	11.61	-13.87	0.88	-11.07	2.36	-2.54	-0.27	0.69
(0.3/0.7)	Dry	5.74	-44.45	1.00	77.11	1.12	2.99	0.19	-0.51

Table A.2-4. Experimental burning velocity data obtained in 2-L experiment from pressure rise data for R-152a/134a and R-152a/1234yf mixtures. Data presented for 298K, 101 kPa initial conditions, dry air (<2% r.h.) and wet air (50 % r.h.) as noted. Blend compositions given in mole fraction.

Equivalence Ratio (ϕ)	Nominal Humidity	Run #	Run Date	Partial Pressure, torr				P_{tot}	P_{final}	Capacitance [nF]	Voltage [kV]	Nominal Spark Energy [mJ]
				p_1	p_2	p_{air}	p_w					
R-152a												
0.8	Dry	2	2019-12-05	43.6	N/A	647.9	N/A	692.2	659.7	10	10	2.5
		1	2019-12-05	50.3		747.4		798.3	760.1	10	10	2.5
		3	2019-12-09	57.0		846.6		904.3	860.2	10	10	2.5
0.9		4	2019-12-11	48.7		642.9		692.2	660.0	10	10	2.5
		5	2019-12-11	56.1		741.5		798.3	760.2	10	10	2.5
		6	2019-12-11	63.6		840.0		904.3	860.0	10	10	2.5
1		19	2019-12-16	53.7		637.8		692.2	659.9	10	10	2.5
		20	2019-12-16	62.0		735.7		798.3	760.2	10	10	2.5
		21	2019-12-16	70.1		833.5		904.3	860.2	10	10	2.5
1.1		7	2019-12-11	58.6		632.9		692.2	659.9	10	10	2.5
		8	2019-12-11	67.6		730.1		798.3	759.9	10	10	2.5
		9	2019-12-11	76.6		827.0		904.2	860.0	10	10	2.5
1.2		10	2019-12-11	63.5		628.1		692.1	659.7	10	10	2.5
		11	2019-12-11	73.2		724.5		798.3	760.1	10	10	2.5
		12	2019-12-11	82.9		820.7		904.3	859.8	10	10	2.5
1.3		13	2019-12-12	68.2		623.3		692.2	660.8	10	10	2.5
		14	2019-12-12	78.7		719.0		798.4	760.4	10	10	2.5
		15	2019-12-12	89.1		814.6		904.3	860.3	10	10	2.5
1.4		16	2019-12-12	72.9		618.7		692.2	660.0	10	10	2.5
		17	2019-12-12	84.1		713.6		798.3	760.5	10	10	2.5
		18	2019-12-12	95.3		808.5		904.3	859.9	10	10	2.5
R-152a/134a (0.8/0.2)												
0.8	Dry	21	2019-01-02	37.8	9.4	644.4	N/A	692.2	659.7	50	10	12.5
		2	2019-12-20	43.5	10.9	743.3		798.3	760.5	50	10	12.5
		9	2019-12-23	49.3	12.3	842.0		904.3	860.4	50	10	12.5
0.9		20	2019-01-02	42.1	10.5	638.9		692.2	659.7	50	10	12.5
		3	2019-12-20	48.6	12.1	737.0		798.3	760.4	50	10	12.5
		10	2019-12-23	55.0	13.7	834.9		904.3	860.1	50	10	12.5

1		16	2019-01-02	45.7	12.3	633.6		692.2	659.8	50	10	12.5
		4	2019-12-20	53.5	13.4	730.8		798.3	760.3	50	10	12.5
		11	2019-12-23	60.6	15.1	827.9		904.3	860.3	50	10	12.5
1.1		1	2019-01-02	50.6	12.6	628.3		692.2	660.1	50	10	12.5
		5	2019-12-20	58.4	14.6	724.7		798.3	760.3	50	10	12.5
		12	2019-12-23	66.1	16.5	821.1		904.3	860.0	50	10	12.5
1.2		17	2019-01-02	54.7	13.7	623.1		692.2	659.9	50	10	12.5
		6	2019-12-20	63.1	15.8	718.8		798.3	760.1	50	10	12.5
		13	2019-12-23	69.5	19.9	814.2		904.3	859.9	50	10	12.5
1.3		18	2019-01-02	58.8	14.7	618.0		692.2	659.8	50	10	12.5
		7	2019-12-20	67.8	17.0	712.9		798.3	760.0	50	10	12.5
		14	2019-12-23	76.8	19.2	807.6		904.3	859.8	50	10	12.5
1.4		19	2019-01-02	62.9	15.7	613.0		692.2	660.4	50	10	12.5
		8	2019-12-20	72.5	18.1	707.0		798.3	760.3	50	10	12.5
		15	2019-12-23	82.1	20.5	801.1		904.3	859.9	50	10	12.5
R-152a/134a (0.5/0.5)												
0.8	Dry	12	2019-11-08	26.9	26.8	637.8	N/A	692.2	659.7	100	15	56.3
		3	2019-11-01	31.0	31.0	736.3		799.0	760.5	100	15	56.3
		4	2019-11-01	31.0	30.9	736.3		798.9	760.8	100	15	56.3
		18	2019-11-12	35.1	35.0	833.3		904.1	859.7	100	15	56.3
0.85		25	2019-11-13	28.4	28.4	634.7		692.1	659.7	100	15	56.3
		5	2019-11-01	32.8	32.7	732.8		799.0	760.9	100	15	56.3
		24	2019-11-13	37.1	37.1	829.2		904.1	859.5	100	15	56.3
0.9		11	2019-11-08	30.0	29.9	631.7		692.2	659.9	100	15	56.3
		2	2019-11-01	34.6	34.5	729.2		799.0	760.9	100	15	56.3
		19	2019-11-12	39.1	39.0	825.4		904.1	859.7	100	15	56.3
1		10	2019-11-08	33.0	32.9	625.7		692.2	659.9	100	15	56.3
		1	2019-11-01	38.0	38.0	722.3		799.0	760.5	100	15	56.3
		17	2019-11-12	43.0	42.9	816.8		903.4	859.3	100	15	56.3
1.1		13	2019-11-08	35.9	35.8	619.9		692.1	659.7	100	15	56.3
		6	2019-11-01	41.4	41.4	715.4		798.9	760.4	100	15	56.3
		20	2019-11-12	46.9	46.8	809.8		904.0	859.6	100	15	56.3
1.2		14	2019-11-08	38.8	38.7	614.0		692.2	659.8	100	15	56.3
		7	2019-11-01	44.8	44.7	708.8		799.0	760.8	100	15	56.3
		23	2019-11-13	50.7	50.6	802.2		904.1	859.8	100	15	56.3
1.3		15	2019-11-12	41.6	41.6	608.4		692.2	659.7	100	15	56.3
		8	2019-11-01	48.1	48.0	702.2		799.0	760.6	100	15	56.3
		21	2019-11-13	54.3	54.3	794.9		904.1	859.7	100	15	56.3
1.4		16	2019-11-12	44.4	44.3	602.8		692.2	660.3	100	15	56.3
		9	2019-11-04	51.2	51.2	695.8		799.0	760.8	100	15	56.3
		22	2019-11-13	58.0	57.9	787.5		904.1	859.8	100	15	56.3

R-152a/1234yf (0.5/0.5)

0.7	Dry	8	2020-02-12	22.3	22.2	753.2	N/A	798.3	759.9	100	15	56.3
0.8	Dry	9	2020-02-12	21.9	21.7	647.8		692.1	659.5	100	15	56.3
		2	2020-02-11	25.2	25.1	747.2		798.3	759.7	100	15	56.3
		16	2020-02-13	28.6	28.5	846.5		904.2	859.6	100	15	56.3
0.9		10	2020-02-12	24.4	24.3	642.7		692.1	659.5	100	15	56.3
		3	2020-02-12	28.1	28.1	741.4		798.3	760.1	100	15	56.3
		17	2020-02-13	31.8	31.8	839.9		904.2	859.5	100	15	56.3
1		11	2020-02-13	26.9	26.8	637.8		692.2	659.5	100	15	56.3
		1	2020-02-11	31.0	30.9	735.7		798.3	759.8	100	15	56.3
		18	2020-02-14	35.1	35.0	833.4		904.2	859.7	100	15	56.3
1.1		12	2020-02-13	29.3	29.3	632.8		692.2	659.5	100	15	56.3
		4	2020-02-12	33.8	33.8	730.0		798.3	760.2	100	15	56.3
		19	2020-02-14	38.3	38.2	827.1		904.3	860.0	100	15	56.3
1.2		13	2020-02-13	31.7	31.7	628.0		692.1	660.0	100	15	56.3
		5	2020-02-12	36.6	36.6	724.5		798.3	760.1	100	15	56.3
		20	2020-02-14	41.5	41.3	820.7		904.2	860.0	100	15	56.3
1.3		14	2020-02-13	34.1	34.1	623.2		692.1	660.0	100	15	56.3
		6	2020-02-12	39.5	39.3	718.8		798.3	759.9	100	15	56.3
		21	2020-02-14	44.5	44.5	814.5		904.3	859.8	100	15	56.3
1.4		15	2020-02-13	36.5	36.4	618.7		692.4	659.7	100	15	56.3
		7	2020-02-12	42.1	42.0	713.6		798.3	759.8	100	15	56.3
		22	2020-02-14	47.6	47.6	808.3		904.3	859.7	100	15	56.3

R-152a/1234yf (0.4/0.6)

0.8	Dry	1	2020-02-20	17.5	26.1	647.8	N/A	692.2	660.0	100	15	56.3
0.9	Dry	2	2020-02-20	19.5	29.2	647.8		692.2	659.9	100	15	56.3
		8	2020-02-21	22.5	33.7	642.8		798.3	760.4	100	15	56.3
		14	2020-02-21	25.5	38.2	741.4		904.3	860.1	100	15	56.3
1		3	2020-02-20	21.5	32.2	839.9		692.2	659.9	100	15	56.3
		9	2020-02-21	24.8	37.1	637.8		798.3	760.0	100	15	56.3
		15	2020-02-24	28.1	42.0	735.6		904.3	860.0	100	15	56.3
1.1		4	2020-02-20	23.5	35.1	833.4		692.2	659.8	100	15	56.3
		10	2020-02-21	27.1	40.5	633.0		798.3	759.9	100	15	56.3
		16	2020-02-24	30.7	45.9	730.0		904.3	859.8	100	15	56.3
1.2		5	2020-02-20	25.4	38.0	826.9		692.2	659.7	100	15	56.3
		11	2020-02-21	29.3	43.8	628.1		798.3	760.2	100	15	56.3
		17	2020-02-24	33.2	49.7	724.4		904.3	859.8	100	15	56.3
1.3		6	2020-02-20	27.3	40.9	820.6		692.2	659.7	100	15	56.3
		12	2020-02-21	31.5	47.1	623.2		798.2	760.1	100	15	56.3
		18	2020-02-24	35.7	53.4	718.8		904.3	859.8	100	15	56.3
1.4		7	2020-02-20	29.2	43.7	814.4		692.1	659.6	100	15	56.3
		13	2020-02-21	33.7	50.4	618.6		798.2	760.0	100	15	56.3

		19	2020-02-24	38.1	57.1	713.4		904.3	859.7	100	15	56.3
0.9	46.1	16	Feb-9-2020	19.2	28.8	636.2	8.2	692.2	659.8	100	15	56.3
	41.7	18	Feb-9-2020	22.1	33.3	734.7	8.6	798.4	759.8	100	15	56.3
	39.0	17	Feb-9-2020	25.0	37.7	832.7	9.1	904.3	859.8	100	15	56.3
1	47.6	3	Feb-1-2020	21.2	31.9	630.6	8.4	692.1	659.7	100	15	56.3
	45.0	1	Feb-1-2020	24.3	36.7	728.0	9.2	798.3	759.5	100	15	56.3
	40.2	2	Feb-1-2020	27.7	41.4	825.6	9.3	904.2	859.5	100	15	56.3
1.1	51.8	6	Feb-2-2020	23.2	34.7	625.1	9.1	692.1	659.1	100	15	56.3
	44.6	4	Feb-2-2021	26.7	40.1	722.3	9.1	798.4	759.1	100	15	56.3
	39.6	5	Feb-2-2022	30.3	45.3	819.4	9.1	904.2	859.7	100	15	56.3
1.2	49.8	7	Feb-2-2020	24.9	37.5	620.9	8.7	692.2	659.9	100	15	56.3
	42.2	9	Feb-3-2020	28.8	43.3	716.9	9.0	798.3	759.9	100	15	56.3
	38.3	8	Feb-3-2020	32.7	49.0	812.8	9.6	904.3	859.7	100	15	56.3
1.3	49.2	11	Feb-4-2020	26.9	40.4	616.2	8.5	692.1	659.4	100	15	56.3
	44.6	10	Feb-4-2020	31.2	46.4	711.6	8.9	798.3	758.9	100	15	56.3
	41.8	12	Feb-4-2020	35.2	52.7	806.8	9.5	904.3	859.4	100	15	56.3
1.4	50.2	14	Feb-4-2020	28.8	43.2	611.5	8.6	692.1	659.3	100	15	56.3
	45.2	13	Feb-4-2020	33.2	49.8	706.1	9.0	798.3	759.3	100	15	56.3
	41.3	15	Feb-5-2020	37.5	56.5	800.9	9.3	904.3	859.7	100	15	56.3

R-152a/R234yf (0.3/0.7)

0.9	Dry	1	2020-02-17	16.9	39.2	742.7	N/A	798.4	760.8	100	15	56.3
1		7	2020-02-17	16.2	37.5	639.1		692.1	659.8	100	15	56.3
		2	2020-02-17	18.6	43.3	737.0		798.4	760.6	100	15	56.3
		12	2020-02-19	21.2	48.9	834.8		904.2	859.9	100	15	56.3
1.1		8	2020-02-17	17.7	40.9	634.2		692.2	659.9	100	15	56.3
		3	2020-02-17	20.4	47.2	731.4		798.4	760.5	100	15	56.3
		13	2020-02-19	23.0	53.6	828.2		904.2	859.9	100	15	56.3
1.2		9	2020-02-19	19.0	44.4	629.2		692.2	660.0	100	15	56.3
		4	2020-02-17	22.1	51.0	725.7		798.2	760.2	100	15	56.3
		14	2020-02-19	25.0	57.8	822.0		904.2	859.9	100	15	56.3
1.3		10	2020-02-19	20.5	47.8	624.6		692.3	660.0	100	15	56.3
		5	2020-02-17	23.7	55.0	720.3		798.3	760.2	100	15	56.3
		15	2020-02-19	26.8	62.3	815.8		904.2	859.7	100	15	56.3
1.4		11	2020-02-19	22.0	51.0	619.9		692.3	660.6	100	15	56.3
		6	2020-02-17	25.3	58.9	714.8		798.4	759.9	100	15	56.3
		16	2020-02-19	29.5	65.7	809.7		904.2	859.6	100	15	56.3

A.3 Task 4 - Tabulated Flow-Boiling Heat-Transfer Measurements

Table A.3-1. Measured flow-boiling heat-transfer data for R-515B, R-450A, R-513A, and HFC-134a.

Listed are Nusselt number Nu, thermodynamic quality x_q, reduced pressure p, Boiling number Bo, Bond number B_{nd}, Reynolds number Re, and the relative combined, expanded (k = 2) uncertainty in the Nusselt number U_c. Data are presented in the sequence measured. The last column provides the test refrigerant.

Nu	x_q	P_r	Bo	B_{nd}	Re	U_c/%	fluid
207.5	0.15	0.11	0.000128	0.0224	5853.3	27.0	R-513A
532.5	0.29	0.11	0.000424	0.0225	5836.2	21.0	R-513A
527.8	0.40	0.11	0.000463	0.0225	5831.9	20.0	R-513A
514.0	0.61	0.10	0.000529	0.0225	5820.7	20.0	R-513A
497.5	0.83	0.10	0.000590	0.0223	5805.9	21.0	R-513A
478.7	0.99	0.10	0.000653	0.0223	5787.9	22.0	R-513A
456.7	0.99	0.10	0.000723	0.0223	5766.5	24.0	R-513A
172.8	0.12	0.11	0.000108	0.0225	5818.1	27.0	R-513A
434.5	0.24	0.10	0.000352	0.0225	5803.0	21.0	R-513A
428.6	0.33	0.10	0.000384	0.0225	5798.8	20.0	R-513A
415.6	0.51	0.10	0.000438	0.0222	5788.0	20.0	R-513A
401.2	0.69	0.10	0.000489	0.0223	5773.4	20.0	R-513A
385.3	0.91	0.10	0.000541	0.0223	5753.8	21.0	R-513A
367.6	0.99	0.10	0.000598	0.0221	5729.9	23.0	R-513A
161.5	0.10	0.10	0.000084	0.0223	6801.2	27.0	R-513A
369.9	0.19	0.10	0.000254	0.0223	6782.9	21.0	R-513A
364.3	0.26	0.10	0.000277	0.0223	6779.1	20.0	R-513A
350.2	0.38	0.10	0.000317	0.0223	6766.7	19.0	R-513A
334.6	0.52	0.10	0.000354	0.0221	6748.3	19.0	R-513A
317.4	0.67	0.10	0.000391	0.0221	6722.1	20.0	R-513A
298.3	0.86	0.10	0.000432	0.0219	6684.8	22.0	R-513A
139.6	0.08	0.10	0.000062	0.0225	7943.2	27.0	R-513A
323.5	0.15	0.10	0.000191	0.0222	7918.7	20.0	R-513A
318.3	0.20	0.10	0.000208	0.0223	7914.5	19.0	R-513A
305.9	0.29	0.10	0.000237	0.0223	7900.0	19.0	R-513A
291.4	0.39	0.10	0.000265	0.0223	7878.1	19.0	R-513A
275.2	0.51	0.10	0.000293	0.0221	7846.7	19.0	R-513A
257.5	0.65	0.10	0.000324	0.0221	7801.7	21.0	R-513A
140.0	0.13	0.11	0.000113	0.0225	3867.1	28.0	R-513A
281.2	0.23	0.11	0.000281	0.0225	3860.8	23.0	R-513A
283.5	0.30	0.11	0.000306	0.0225	3859.0	23.0	R-513A
285.1	0.44	0.10	0.000350	0.0225	3854.4	23.0	R-513A
285.4	0.59	0.10	0.000390	0.0225	3848.5	24.0	R-513A

Table A.3-1. (continued)

Nu	x_q	P_r	Bo	B_{nd}	Re	U_c/%	fluid
284.1	0.76	0.10	0.000432	0.0223	3840.6	26.0	R-513A
281.8	0.97	0.10	0.000478	0.0223	3829.8	29.0	R-513A
340.0	0.24	0.10	0.000293	0.0223	3969.0	25.0	R-513A
337.8	0.32	0.10	0.000320	0.0223	3967.4	24.0	R-513A
330.9	0.46	0.10	0.000366	0.0223	3963.0	23.0	R-513A
323.1	0.62	0.10	0.000408	0.0223	3957.0	23.0	R-513A
313.6	0.79	0.10	0.000452	0.0223	3948.7	24.0	R-513A
302.3	0.99	0.10	0.000499	0.0221	3937.4	26.0	R-513A
309.4	0.21	0.10	0.000252	0.0223	4170.2	25.0	R-513A
306.9	0.27	0.10	0.000275	0.0223	4168.7	24.0	R-513A
300.2	0.40	0.10	0.000314	0.0223	4164.2	23.0	R-513A
292.1	0.53	0.10	0.000351	0.0223	4158.1	23.0	R-513A
282.7	0.68	0.10	0.000388	0.0223	4149.9	24.0	R-513A
272.2	0.87	0.10	0.000429	0.0221	4138.4	26.0	R-513A
201.8	0.05	0.11	0.000190	0.0225	5732.2	22.0	R-513A
201.3	0.13	0.11	0.000161	0.0225	5728.1	21.0	R-513A
198.2	0.19	0.10	0.000135	0.0225	5723.5	20.0	R-513A
191.8	0.24	0.10	0.000111	0.0225	5718.7	21.0	R-513A
177.4	0.28	0.10	0.000083	0.0225	5712.3	29.0	R-513A
208.2	0.20	0.10	0.000200	0.0223	2673.0	29.0	R-513A
207.4	0.25	0.10	0.000218	0.0223	2672.3	27.0	R-513A
204.8	0.35	0.10	0.000249	0.0223	2670.5	25.0	R-513A
201.6	0.45	0.10	0.000278	0.0223	2668.2	25.0	R-513A
197.6	0.58	0.10	0.000308	0.0223	2665.2	25.0	R-513A
192.8	0.72	0.10	0.000341	0.0221	2661.0	27.0	R-513A
168.4	0.04	0.10	0.000211	0.0225	6109.5	18.0	R-513A
172.4	0.13	0.10	0.000180	0.0222	6104.1	17.0	R-513A
174.9	0.20	0.10	0.000151	0.0222	6097.9	16.0	R-513A
174.7	0.25	0.10	0.000124	0.0223	6091.1	17.0	R-513A
169.4	0.30	0.10	0.000093	0.0223	6082.3	24.0	R-513A
183.7	0.28	0.10	0.000194	0.0222	2675.8	30.0	R-513A
184.0	0.28	0.10	0.000194	0.0222	2675.1	30.0	R-513A
182.4	0.28	0.10	0.000196	0.0223	2647.4	30.0	R-513A
219.1	0.33	0.10	0.000231	0.0223	2653.5	30.0	R-513A
205.2	0.31	0.10	0.000217	0.0223	2656.5	30.0	R-513A
148.3	0.08	0.11	0.000077	0.0225	6063.3	30.0	R-513A
145.1	0.10	0.11	0.000086	0.0225	6062.2	26.0	R-513A
315.8	0.18	0.10	0.000248	0.0225	6046.8	20.0	R-513A
309.9	0.25	0.10	0.000271	0.0225	6043.5	19.0	R-513A

Table A.3-1. (continued)

Nu	x_q	P_r	Bo	B_{nd}	Re	U_c/%	fluid
298.3	0.37	0.10	0.000309	0.0222	6033.5	18.0	R-513A
285.9	0.50	0.10	0.000345	0.0223	6019.1	18.0	R-513A
272.7	0.66	0.10	0.000382	0.0223	5998.8	19.0	R-513A
258.1	0.84	0.10	0.000422	0.0221	5970.2	20.0	R-513A
162.7	0.04	0.11	0.000160	0.0224	7327.9	19.0	R-513A
164.6	0.10	0.11	0.000135	0.0225	7320.8	18.0	R-513A
164.2	0.16	0.11	0.000113	0.0225	7312.8	17.0	R-513A
161.1	0.20	0.10	0.000092	0.0225	7304.0	18.0	R-513A
151.2	0.23	0.10	0.000068	0.0225	7292.5	25.0	R-513A
204.6	0.07	0.11	0.000248	0.0224	4385.6	23.0	R-513A
202.8	0.17	0.11	0.000210	0.0224	4382.8	22.0	R-513A
198.5	0.25	0.11	0.000175	0.0225	4379.7	21.0	R-513A
190.6	0.31	0.11	0.000143	0.0225	4376.5	22.0	R-513A
174.7	0.37	0.11	0.000105	0.0225	4372.4	30.0	R-513A
235.9	0.08	0.11	0.000285	0.0225	4308.2	23.0	R-513A
234.9	0.20	0.11	0.000243	0.0225	4305.5	22.0	R-513A
231.5	0.29	0.11	0.000203	0.0225	4302.4	21.0	R-513A
224.7	0.36	0.10	0.000167	0.0225	4299.3	22.0	R-513A
209.4	0.43	0.10	0.000125	0.0225	4295.3	30.0	R-513A
250.7	0.12	0.11	0.000456	0.0225	4247.8	18.0	R-513A
251.4	0.31	0.11	0.000389	0.0225	4242.7	17.0	R-513A
249.3	0.46	0.10	0.000326	0.0225	4237.1	16.0	R-513A
244.3	0.58	0.10	0.000268	0.0225	4231.2	17.0	R-513A
231.5	0.68	0.10	0.000201	0.0223	4223.6	23.0	R-513A
194.6	0.05	0.10	0.000232	0.0225	7621.9	16.0	R-513A
199.1	0.15	0.10	0.000197	0.0225	7611.6	15.0	R-513A
201.1	0.23	0.10	0.000165	0.0222	7599.5	14.0	R-513A
199.9	0.29	0.10	0.000135	0.0222	7586.0	15.0	R-513A
192.2	0.34	0.10	0.000100	0.0223	7567.9	21.0	R-513A
230.7	0.13	0.11	0.000496	0.0224	2301.6	26.0	R-513A
230.6	0.34	0.11	0.000426	0.0225	2300.0	24.0	R-513A
228.8	0.51	0.11	0.000362	0.0225	2298.5	23.0	R-513A
225.3	0.63	0.11	0.000303	0.0225	2297.1	25.0	R-513A
219.5	0.08	0.11	0.000327	0.0225	7652.6	16.0	R-513A
225.9	0.22	0.10	0.000279	0.0225	7637.3	14.0	R-513A
230.7	0.33	0.10	0.000235	0.0222	7619.0	13.0	R-513A
232.3	0.41	0.10	0.000194	0.0223	7598.4	14.0	R-513A
227.9	0.49	0.10	0.000147	0.0223	7570.3	19.0	R-513A
220.8	0.52	0.10	0.000121	0.0221	7552.8	28.0	R-513A

Table A.3-1. (continued)

Nu	x_q	P_r	Bo	B_{nd}	Re	U_c/%	fluid
190.1	0.58	0.10	0.000108	0.0218	7386.0	28.0	R-513A
219.8	0.61	0.09	0.000108	0.0216	7363.3	30.0	R-513A
136.0	0.08	0.08	0.000084	0.0197	4810.7	28.0	R-450A
135.8	0.11	0.08	0.000094	0.0197	4810.5	24.0	R-450A
261.5	0.19	0.08	0.000235	0.0195	4798.4	19.0	R-450A
259.7	0.25	0.08	0.000257	0.0195	4797.9	18.0	R-450A
253.4	0.37	0.08	0.000294	0.0195	4793.3	18.0	R-450A
245.1	0.49	0.08	0.000328	0.0195	4785.0	18.0	R-450A
235.2	0.64	0.08	0.000363	0.0193	4772.1	19.0	R-450A
223.8	0.81	0.08	0.000402	0.0194	4752.6	21.0	R-450A
129.3	0.06	0.08	0.000051	0.0195	7087.3	28.0	R-450A
127.2	0.07	0.08	0.000057	0.0195	7085.8	24.0	R-450A
264.0	0.13	0.08	0.000162	0.0196	7056.5	18.0	R-450A
259.4	0.17	0.08	0.000177	0.0196	7054.0	17.0	R-450A
247.2	0.25	0.08	0.000202	0.0194	7040.9	16.0	R-450A
233.0	0.34	0.08	0.000225	0.0194	7018.5	16.0	R-450A
217.5	0.44	0.08	0.000250	0.0192	6984.5	17.0	R-450A
200.9	0.56	0.07	0.000276	0.0191	6934.2	17.0	R-450A
139.3	0.11	0.08	0.000098	0.0195	3818.6	28.0	R-450A
253.9	0.19	0.08	0.000227	0.0195	3811.8	23.0	R-450A
255.1	0.25	0.08	0.000247	0.0195	3812.0	23.0	R-450A
253.0	0.37	0.08	0.000283	0.0195	3810.3	23.0	R-450A
248.4	0.49	0.08	0.000316	0.0195	3806.2	24.0	R-450A
241.5	0.62	0.08	0.000350	0.0194	3799.4	26.0	R-450A
232.6	0.79	0.08	0.000388	0.0194	3788.9	28.0	R-450A
191.7	0.21	0.08	0.000209	0.0195	2137.3	29.0	R-450A
196.4	0.27	0.08	0.000228	0.0195	2137.6	28.0	R-450A
202.4	0.37	0.08	0.000261	0.0195	2138.1	29.0	R-450A
209.1	0.78	0.08	0.000382	0.0192	4845.5	19.0	R-450A
123.1	0.06	0.08	0.000049	0.0195	7014.5	29.0	R-450A
120.9	0.07	0.08	0.000055	0.0195	7012.9	25.0	R-450A
245.5	0.12	0.08	0.000153	0.0196	6982.2	19.0	R-450A
241.0	0.16	0.08	0.000167	0.0196	6979.1	18.0	R-450A
229.6	0.24	0.08	0.000191	0.0194	6965.6	17.0	R-450A
216.7	0.32	0.08	0.000213	0.0194	6943.3	17.0	R-450A
202.8	0.42	0.08	0.000235	0.0192	6910.3	17.0	R-450A
187.8	0.53	0.07	0.000260	0.0191	6861.9	18.0	R-450A
132.8	0.11	0.08	0.000097	0.0195	3856.4	27.0	R-450A
239.5	0.19	0.08	0.000226	0.0195	3849.3	21.0	R-450A

Table A.3-1. (continued)

Nu	x_q	P_r	Bo	B_{nd}	Re	U_c/%	fluid
238.6	0.25	0.08	0.000247	0.0195	3849.4	20.0	R-450A
234.8	0.36	0.08	0.000282	0.0195	3847.6	20.0	R-450A
229.2	0.48	0.08	0.000315	0.0195	3843.7	20.0	R-450A
222.4	0.62	0.08	0.000350	0.0194	3837.2	21.0	R-450A
214.3	0.79	0.08	0.000387	0.0194	3827.4	23.0	R-450A
134.3	0.09	0.08	0.000089	0.0195	3861.3	30.0	R-450A
133.9	0.11	0.08	0.000100	0.0195	3861.6	27.0	R-450A
246.5	0.20	0.08	0.000236	0.0195	3855.9	21.0	R-450A
245.5	0.26	0.08	0.000257	0.0195	3856.2	20.0	R-450A
241.6	0.38	0.08	0.000294	0.0195	3854.9	19.0	R-450A
235.6	0.50	0.08	0.000329	0.0195	3851.1	20.0	R-450A
228.5	0.65	0.08	0.000364	0.0195	3844.8	21.0	R-450A
219.8	0.82	0.08	0.000404	0.0193	3834.8	23.0	R-450A
130.7	0.09	0.08	0.000089	0.0195	3969.6	29.0	R-450A
130.6	0.11	0.08	0.000100	0.0195	3969.9	26.0	R-450A
242.4	0.20	0.08	0.000240	0.0195	3961.2	20.0	R-450A
241.4	0.26	0.08	0.000262	0.0195	3961.1	19.0	R-450A
237.0	0.38	0.08	0.000299	0.0195	3959.0	19.0	R-450A
231.4	0.51	0.08	0.000335	0.0195	3954.6	19.0	R-450A
224.3	0.66	0.08	0.000371	0.0194	3947.7	21.0	R-450A
216.0	0.83	0.08	0.000410	0.0194	3937.0	22.0	R-450A
171.4	0.18	0.08	0.000177	0.0195	2141.7	30.0	R-450A
177.0	0.22	0.08	0.000193	0.0195	2142.0	29.0	R-450A
184.0	0.31	0.08	0.000221	0.0195	2142.3	30.0	R-450A
175.2	0.09	0.08	0.000315	0.0195	4915.4	16.0	R-450A
182.2	0.22	0.08	0.000273	0.0195	4912.2	15.0	R-450A
188.2	0.33	0.08	0.000234	0.0195	4905.5	14.0	R-450A
192.6	0.41	0.08	0.000198	0.0195	4895.9	15.0	R-450A
195.2	0.49	0.08	0.000157	0.0194	4880.9	19.0	R-450A
194.0	0.53	0.08	0.000134	0.0194	4870.6	26.0	R-450A
168.4	0.60	0.07	0.000124	0.0190	4760.3	26.0	R-450A
192.9	0.63	0.07	0.000124	0.0190	4746.4	29.0	R-450A
155.4	0.07	0.08	0.000250	0.0195	5792.4	15.0	R-450A
163.7	0.17	0.08	0.000217	0.0195	5786.7	14.0	R-450A
171.5	0.26	0.08	0.000186	0.0195	5776.6	14.0	R-450A
178.1	0.33	0.08	0.000158	0.0195	5763.0	15.0	R-450A
183.4	0.39	0.08	0.000126	0.0194	5742.3	20.0	R-450A
184.1	0.42	0.08	0.000108	0.0194	5728.4	26.0	R-450A
174.1	0.49	0.07	0.000115	0.0190	5577.4	25.0	R-450A

Table A.3-1. (continued)

Nu	x_q	P_r	Bo	B_{nd}	Re	U_c/%	fluid
196.0	0.52	0.07	0.000115	0.0190	5557.3	27.0	R-450A
192.3	0.11	0.08	0.000402	0.0195	3779.3	17.0	R-450A
196.6	0.28	0.08	0.000348	0.0195	3779.5	16.0	R-450A
200.4	0.41	0.08	0.000298	0.0195	3777.4	15.0	R-450A
203.0	0.52	0.08	0.000252	0.0195	3773.6	15.0	R-450A
204.4	0.62	0.08	0.000198	0.0194	3766.7	20.0	R-450A
203.9	0.66	0.08	0.000168	0.0194	3761.8	28.0	R-450A
181.1	0.10	0.08	0.000371	0.0195	2443.5	23.0	R-450A
183.0	0.26	0.08	0.000320	0.0195	2445.5	21.0	R-450A
183.7	0.38	0.08	0.000273	0.0195	2446.6	21.0	R-450A
182.6	0.48	0.08	0.000230	0.0195	2446.9	22.0	R-450A
178.5	0.57	0.08	0.000179	0.0195	2446.4	28.0	R-450A
157.0	0.06	0.08	0.000226	0.0197	6589.4	15.0	R-450A
167.0	0.16	0.08	0.000196	0.0197	6582.2	15.0	R-450A
176.2	0.23	0.08	0.000168	0.0197	6570.1	14.0	R-450A
184.7	0.30	0.08	0.000143	0.0197	6554.3	16.0	R-450A
192.6	0.35	0.08	0.000114	0.0195	6530.5	20.0	R-450A
195.0	0.38	0.08	0.000097	0.0195	6514.6	26.0	R-450A
187.4	0.44	0.07	0.000111	0.0191	6331.6	25.0	R-450A
209.3	0.47	0.07	0.000110	0.0190	6307.1	27.0	R-450A
185.5	0.09	0.08	0.000336	0.0195	4754.0	17.0	R-450A
192.5	0.24	0.08	0.000291	0.0195	4751.2	15.0	R-450A
198.2	0.35	0.08	0.000250	0.0195	4744.9	14.0	R-450A
202.6	0.44	0.08	0.000211	0.0195	4735.9	15.0	R-450A
204.9	0.52	0.08	0.000166	0.0194	4721.6	20.0	R-450A
203.7	0.56	0.08	0.000141	0.0194	4712.0	28.0	R-450A
169.1	0.64	0.07	0.000125	0.0190	4607.5	27.0	R-450A
195.2	0.67	0.07	0.000125	0.0190	4594.3	29.0	R-450A
124.1	0.08	0.08	0.000057	0.0196	6739.5	26.0	R-450A
252.4	0.14	0.08	0.000163	0.0194	6713.0	19.0	R-450A
246.2	0.18	0.08	0.000178	0.0194	6711.1	18.0	R-450A
232.9	0.26	0.08	0.000204	0.0194	6699.6	17.0	R-450A
219.2	0.35	0.08	0.000227	0.0194	6679.4	17.0	R-450A
205.2	0.45	0.08	0.000252	0.0192	6648.7	17.0	R-450A
190.1	0.57	0.07	0.000278	0.0191	6602.9	18.0	R-450A
129.5	0.09	0.08	0.000075	0.0196	4900.2	30.0	R-450A
126.7	0.11	0.08	0.000084	0.0196	4900.0	26.0	R-450A
250.1	0.19	0.08	0.000222	0.0194	4885.5	19.0	R-450A
246.2	0.24	0.08	0.000242	0.0194	4884.4	18.0	R-450A

Table A.3-1. (continued)

Nu	x_q	P_r	Bo	B_{nd}	Re	U_c/%	fluid
237.7	0.36	0.08	0.000276	0.0194	4878.8	18.0	R-450A
228.9	0.47	0.08	0.000309	0.0194	4869.5	18.0	R-450A
219.3	0.61	0.08	0.000342	0.0192	4855.6	19.0	R-450A
208.8	0.78	0.08	0.000378	0.0192	4835.1	21.0	R-450A
133.9	0.11	0.08	0.000091	0.0196	3827.2	29.0	R-450A
231.4	0.18	0.08	0.000205	0.0194	3821.3	22.0	R-450A
229.3	0.23	0.08	0.000224	0.0194	3821.5	21.0	R-450A
224.1	0.34	0.08	0.000256	0.0194	3819.7	20.0	R-450A
217.5	0.44	0.08	0.000285	0.0194	3815.2	21.0	R-450A
209.9	0.57	0.08	0.000316	0.0194	3807.8	22.0	R-450A
201.3	0.72	0.08	0.000350	0.0192	3796.3	23.0	R-450A
178.5	0.09	0.08	0.000275	0.0197	5855.7	17.0	R-450A
187.8	0.21	0.08	0.000238	0.0197	5850.3	15.0	R-450A
196.4	0.30	0.08	0.000204	0.0195	5840.1	15.0	R-450A
203.6	0.37	0.08	0.000173	0.0195	5826.2	16.0	R-450A
209.1	0.44	0.08	0.000136	0.0194	5804.6	21.0	R-450A
209.5	0.48	0.08	0.000116	0.0194	5790.2	28.0	R-450A
191.2	0.54	0.07	0.000123	0.0190	5632.9	25.0	R-450A
216.0	0.58	0.07	0.000122	0.0190	5612.2	28.0	R-450A
132.7	0.04	0.08	0.000110	0.0194	6649.7	23.0	R-450A
139.7	0.09	0.08	0.000097	0.0194	6645.6	21.0	R-450A
146.1	0.13	0.08	0.000085	0.0194	6638.9	19.0	R-450A
151.7	0.16	0.08	0.000074	0.0194	6630.2	20.0	R-450A
156.7	0.19	0.08	0.000061	0.0194	6617.2	27.0	R-450A
158.5	0.11	0.08	0.000086	0.0197	5053.7	28.0	R-450A
311.8	0.19	0.08	0.000229	0.0197	5041.0	21.0	R-450A
306.4	0.25	0.08	0.000250	0.0197	5040.5	20.0	R-450A
294.8	0.37	0.08	0.000286	0.0195	5035.7	19.0	R-450A
282.2	0.49	0.08	0.000319	0.0195	5026.7	19.0	R-450A
268.5	0.63	0.08	0.000354	0.0195	5012.6	20.0	R-450A
253.3	0.80	0.08	0.000392	0.0194	4991.4	21.0	R-450A
154.4	0.11	0.09	0.000082	0.0199	5310.3	28.0	R-450A
321.6	0.19	0.09	0.000229	0.0200	5296.8	21.0	R-450A
317.6	0.25	0.09	0.000250	0.0199	5296.9	20.0	R-450A
306.8	0.36	0.09	0.000286	0.0199	5292.8	19.0	R-450A
294.6	0.49	0.08	0.000320	0.0198	5284.3	19.0	R-450A
281.0	0.63	0.08	0.000354	0.0198	5270.4	19.0	R-450A
265.9	0.80	0.08	0.000392	0.0196	5249.0	20.0	R-450A
163.6	0.12	0.09	0.000084	0.0204	5148.1	29.0	R-450A

Table A.3-1. (continued)

Nu	x_q	P_r	Bo	B_{nd}	Re	U_c/%	fluid
346.1	0.20	0.09	0.000239	0.0202	5139.1	22.0	R-450A
341.6	0.26	0.09	0.000260	0.0202	5139.8	21.0	R-450A
330.5	0.38	0.09	0.000298	0.0202	5137.7	20.0	R-450A
318.7	0.51	0.09	0.000333	0.0202	5132.0	20.0	R-450A
305.3	0.66	0.09	0.000369	0.0202	5122.1	20.0	R-450A
290.5	0.83	0.09	0.000409	0.0200	5106.7	22.0	R-450A
186.3	0.13	0.08	0.000109	0.0196	4838.3	30.0	R-450A
253.1	0.21	0.08	0.000194	0.0194	4817.5	19.0	R-450A
252.8	0.26	0.08	0.000212	0.0194	4814.8	18.0	R-450A
248.1	0.35	0.08	0.000242	0.0194	4806.3	17.0	R-450A
240.6	0.46	0.08	0.000271	0.0192	4794.4	17.0	R-450A
231.1	0.58	0.08	0.000300	0.0192	4777.6	18.0	R-450A
219.4	0.72	0.07	0.000332	0.0191	4753.8	18.0	R-450A
242.7	0.17	0.10	0.000075	0.0221	8878.1	28.0	R-513A
237.9	0.19	0.10	0.000081	0.0221	8873.5	26.0	R-513A
225.8	0.23	0.10	0.000093	0.0221	8859.2	24.0	R-513A
212.7	0.27	0.10	0.000104	0.0221	8838.4	23.0	R-513A
198.7	0.32	0.10	0.000115	0.0219	8809.2	22.0	R-513A
184.0	0.37	0.10	0.000127	0.0219	8768.0	23.0	R-513A
216.1	0.12	0.10	0.000051	0.0219	10756.5	29.0	R-513A
213.2	0.13	0.10	0.000056	0.0219	10751.5	28.0	R-513A
204.0	0.16	0.10	0.000064	0.0219	10735.6	26.0	R-513A
193.3	0.19	0.10	0.000071	0.0217	10712.3	25.0	R-513A
181.2	0.22	0.10	0.000079	0.0217	10679.7	24.0	R-513A
167.7	0.26	0.09	0.000087	0.0218	10633.5	24.0	R-513A
187.1	0.08	0.10	0.000037	0.0219	12967.9	30.0	R-513A
184.9	0.10	0.10	0.000042	0.0219	12952.6	28.0	R-513A
178.8	0.12	0.10	0.000047	0.0217	12929.5	27.0	R-513A
170.2	0.14	0.10	0.000052	0.0217	12896.7	27.0	R-513A
159.8	0.17	0.10	0.000057	0.0218	12850.2	28.0	R-513A
174.1	0.12	0.10	0.000038	0.0219	12997.6	30.0	R-513A
163.7	0.14	0.10	0.000042	0.0219	12966.5	29.0	R-513A
152.2	0.16	0.10	0.000046	0.0217	12923.1	28.0	R-513A
185.8	0.11	0.10	0.000034	0.0221	13308.7	30.0	R-513A
177.7	0.13	0.10	0.000038	0.0221	13284.5	28.0	R-513A
167.9	0.15	0.10	0.000042	0.0221	13251.9	26.0	R-513A
156.7	0.17	0.10	0.000046	0.0219	13207.1	25.0	R-513A
243.9	0.15	0.10	0.000085	0.0221	10042.7	24.0	R-513A
238.1	0.17	0.10	0.000092	0.0221	10037.1	23.0	R-513A

Table A.3-1. (continued)

Nu	x_q	P_r	Bo	B_{nd}	Re	U_c/%	fluid
225.2	0.21	0.10	0.000106	0.0221	10018.1	21.0	R-513A
211.1	0.26	0.10	0.000118	0.0221	9989.5	21.0	R-513A
196.3	0.31	0.10	0.000130	0.0219	9948.6	21.0	R-513A
180.5	0.38	0.10	0.000144	0.0217	9890.1	21.0	R-513A
265.2	0.17	0.10	0.000093	0.0221	9862.3	23.0	R-513A
262.0	0.19	0.10	0.000102	0.0221	9856.1	22.0	R-513A
250.8	0.24	0.10	0.000116	0.0221	9836.0	21.0	R-513A
236.9	0.29	0.10	0.000130	0.0221	9806.5	20.0	R-513A
221.4	0.35	0.10	0.000144	0.0219	9765.2	20.0	R-513A
204.2	0.42	0.10	0.000159	0.0219	9706.4	21.0	R-513A
273.5	0.18	0.10	0.000092	0.0223	9967.4	23.0	R-513A
273.2	0.21	0.10	0.000101	0.0223	9960.0	22.0	R-513A
265.1	0.26	0.10	0.000115	0.0221	9938.0	20.0	R-513A
252.3	0.31	0.10	0.000128	0.0221	9906.9	20.0	R-513A
236.5	0.36	0.10	0.000142	0.0219	9863.6	19.0	R-513A
218.5	0.44	0.10	0.000157	0.0219	9802.8	20.0	R-513A
279.1	0.20	0.10	0.000101	0.0223	9599.6	23.0	R-513A
277.9	0.22	0.10	0.000110	0.0223	9592.1	22.0	R-513A
269.2	0.28	0.10	0.000126	0.0223	9569.9	20.0	R-513A
255.4	0.33	0.10	0.000140	0.0221	9538.7	20.0	R-513A
239.4	0.39	0.10	0.000155	0.0221	9495.5	19.0	R-513A
220.9	0.47	0.10	0.000171	0.0219	9434.8	20.0	R-513A
258.8	0.19	0.10	0.000096	0.0223	9731.8	23.0	R-513A
255.0	0.21	0.10	0.000105	0.0223	9724.7	21.0	R-513A
243.2	0.26	0.10	0.000120	0.0221	9702.9	20.0	R-513A
229.2	0.31	0.10	0.000134	0.0221	9671.7	20.0	R-513A
213.6	0.37	0.10	0.000148	0.0219	9628.2	20.0	R-513A
196.8	0.45	0.10	0.000164	0.0219	9566.8	20.0	R-513A
187.4	0.18	0.10	0.000070	0.0225	7689.0	29.0	R-513A
268.3	0.24	0.10	0.000136	0.0223	7655.8	22.0	R-513A
265.4	0.27	0.10	0.000149	0.0223	7651.0	21.0	R-513A
255.6	0.34	0.10	0.000170	0.0223	7635.9	20.0	R-513A
243.6	0.42	0.10	0.000190	0.0223	7614.1	20.0	R-513A
230.0	0.50	0.10	0.000210	0.0221	7583.5	20.0	R-513A
214.6	0.60	0.10	0.000232	0.0219	7540.2	21.0	R-513A
251.5	0.14	0.11	0.000352	0.0230	8096.8	22.0	R-513A
241.7	0.29	0.11	0.000287	0.0228	8076.1	19.0	R-513A
226.2	0.40	0.11	0.000227	0.0228	8053.5	17.0	R-513A
203.6	0.47	0.11	0.000172	0.0228	8029.8	19.0	R-513A

Table A.3-1. (continued)

Nu	x_q	P_r	Bo	B_{nd}	Re	U_c/%	fluid
95.4	0.60	0.10	0.000057	0.0223	7811.5	26.0	R-513A
110.7	0.61	0.10	0.000056	0.0221	7791.2	30.0	R-513A
218.7	0.14	0.11	0.000064	0.0227	10291.5	28.0	R-513A
272.3	0.18	0.11	0.000109	0.0225	10235.3	21.0	R-513A
270.4	0.21	0.11	0.000119	0.0225	10227.2	20.0	R-513A
260.4	0.27	0.10	0.000135	0.0225	10202.2	19.0	R-513A
247.0	0.33	0.10	0.000151	0.0223	10166.6	19.0	R-513A
231.1	0.40	0.10	0.000167	0.0223	10116.7	19.0	R-513A
213.5	0.48	0.10	0.000185	0.0221	10046.3	19.0	R-513A
185.9	0.12	0.11	0.000054	0.0224	10276.3	28.0	R-513A
266.3	0.17	0.10	0.000107	0.0225	10226.4	21.0	R-513A
262.7	0.19	0.10	0.000117	0.0225	10219.3	20.0	R-513A
250.9	0.25	0.10	0.000133	0.0222	10196.3	19.0	R-513A
236.9	0.31	0.10	0.000149	0.0223	10162.5	19.0	R-513A
221.0	0.37	0.10	0.000165	0.0223	10114.4	19.0	R-513A
203.8	0.46	0.10	0.000182	0.0221	10046.0	19.0	R-513A
145.7	0.11	0.11	0.000041	0.0225	10406.6	29.0	R-513A
260.0	0.15	0.10	0.000104	0.0222	10362.5	21.0	R-513A
254.1	0.18	0.10	0.000113	0.0222	10356.8	20.0	R-513A
239.9	0.23	0.10	0.000129	0.0223	10335.4	19.0	R-513A
224.8	0.29	0.10	0.000144	0.0223	10302.5	19.0	R-513A
208.8	0.35	0.10	0.000160	0.0221	10255.0	19.0	R-513A
192.0	0.43	0.10	0.000176	0.0219	10186.5	19.0	R-513A
146.7	0.13	0.10	0.000045	0.0223	9688.8	29.0	R-513A
269.9	0.18	0.10	0.000120	0.0223	9640.0	21.0	R-513A
263.0	0.21	0.10	0.000130	0.0223	9633.2	20.0	R-513A
247.5	0.27	0.10	0.000149	0.0221	9610.6	19.0	R-513A
231.4	0.33	0.10	0.000166	0.0221	9577.1	18.0	R-513A
214.6	0.41	0.10	0.000184	0.0219	9529.2	19.0	R-513A
196.8	0.50	0.10	0.000203	0.0217	9460.9	19.0	R-513A
224.6	0.16	0.11	0.000068	0.0225	9810.0	29.0	R-513A
290.0	0.21	0.10	0.000122	0.0223	9752.1	21.0	R-513A
287.0	0.24	0.10	0.000133	0.0223	9743.4	20.0	R-513A
274.9	0.30	0.10	0.000152	0.0223	9717.4	19.0	R-513A
259.6	0.37	0.10	0.000170	0.0221	9680.6	19.0	R-513A
241.8	0.45	0.10	0.000188	0.0221	9629.3	19.0	R-513A
222.4	0.54	0.10	0.000208	0.0219	9557.1	19.0	R-513A
149.9	0.22	0.10	0.000060	0.0223	7112.6	30.0	R-513A
291.8	0.28	0.10	0.000165	0.0223	7080.6	22.0	R-513A

Table A.3-1. (continued)

Nu	x_q	P_r	Bo	B_{nd}	Re	U_c/%	fluid
285.5	0.32	0.10	0.000180	0.0221	7075.5	21.0	R-513A
271.5	0.40	0.10	0.000205	0.0221	7060.2	20.0	R-513A
256.6	0.49	0.10	0.000229	0.0221	7038.2	20.0	R-513A
240.8	0.59	0.10	0.000253	0.0219	7007.5	21.0	R-513A
223.7	0.72	0.10	0.000280	0.0219	6964.1	21.0	R-513A
187.2	0.21	0.10	0.000078	0.0223	7244.2	28.0	R-513A
286.3	0.28	0.10	0.000163	0.0223	7208.1	21.0	R-513A
283.6	0.32	0.10	0.000178	0.0223	7202.3	21.0	R-513A
274.4	0.40	0.10	0.000203	0.0221	7186.1	20.0	R-513A
262.6	0.49	0.10	0.000226	0.0221	7163.8	20.0	R-513A
248.9	0.59	0.10	0.000250	0.0219	7133.0	21.0	R-513A
233.0	0.71	0.10	0.000277	0.0219	7090.2	22.0	R-513A
263.2	0.21	0.10	0.000401	0.0221	6198.9	21.0	R-513A
250.3	0.38	0.10	0.000331	0.0219	6181.2	19.0	R-513A
233.5	0.50	0.10	0.000265	0.0219	6163.7	17.0	R-513A
211.8	0.59	0.10	0.000205	0.0219	6146.5	19.0	R-513A
189.1	0.33	0.07	0.000223	0.0190	4108.2	23.0	R-515B
193.7	0.42	0.07	0.000189	0.0188	4095.4	22.0	R-515B
196.9	0.49	0.07	0.000158	0.0188	4082.7	23.0	R-515B
198.7	0.55	0.07	0.000129	0.0188	4070.4	27.0	R-515B
174.6	0.10	0.08	0.000338	0.0196	5553.1	22.0	R-515B
177.3	0.24	0.08	0.000281	0.0196	5537.5	20.0	R-515B
177.5	0.35	0.08	0.000228	0.0194	5519.8	18.0	R-515B
173.2	0.43	0.08	0.000179	0.0194	5500.6	20.0	R-515B
222.6	0.15	0.07	0.000386	0.0192	4749.5	25.0	R-515B
215.9	0.31	0.07	0.000319	0.0190	4735.7	22.0	R-515B
205.2	0.43	0.07	0.000256	0.0191	4721.4	21.0	R-515B
189.7	0.52	0.07	0.000198	0.0191	4707.1	22.0	R-515B
87.5	0.66	0.07	0.000066	0.0187	4569.7	28.0	R-515B
153.7	0.17	0.07	0.000134	0.0188	5036.2	27.0	R-515B
159.2	0.22	0.07	0.000113	0.0188	5024.3	27.0	R-515B
163.7	0.27	0.07	0.000094	0.0188	5012.1	28.0	R-515B
218.5	0.21	0.07	0.000093	0.0187	6243.5	29.0	R-515B
196.2	0.25	0.07	0.000103	0.0186	6223.3	26.0	R-515B
175.3	0.30	0.06	0.000114	0.0186	6194.5	25.0	R-515B
155.1	0.36	0.06	0.000126	0.0184	6153.3	24.0	R-515B
304.9	0.23	0.07	0.000175	0.0189	5518.9	27.0	R-515B
290.8	0.27	0.07	0.000190	0.0189	5514.6	25.0	R-515B
263.8	0.36	0.07	0.000217	0.0188	5498.7	24.0	R-515B

Table A.3-1. (continued)

Nu	x_q	P_r	Bo	B_{nd}	Re	U_c/%	fluid
238.3	0.46	0.07	0.000243	0.0188	5473.6	23.0	R-515B
214.3	0.56	0.07	0.000268	0.0187	5437.2	23.0	R-515B
190.7	0.70	0.07	0.000296	0.0186	5384.4	23.0	R-515B
340.8	0.28	0.07	0.000197	0.0188	5037.0	26.0	R-515B
327.5	0.33	0.07	0.000214	0.0188	5031.7	25.0	R-515B
299.5	0.43	0.07	0.000245	0.0187	5015.0	23.0	R-515B
272.4	0.54	0.07	0.000273	0.0187	4990.7	22.0	R-515B
246.1	0.66	0.07	0.000302	0.0186	4956.5	22.0	R-515B
219.5	0.81	0.06	0.000334	0.0185	4908.1	21.0	R-515B
292.5	0.17	0.07	0.000153	0.0192	6319.2	25.0	R-515B
279.0	0.21	0.07	0.000167	0.0192	6315.8	23.0	R-515B
252.5	0.28	0.07	0.000191	0.0190	6299.0	21.0	R-515B
227.6	0.37	0.07	0.000213	0.0191	6270.8	21.0	R-515B
203.7	0.46	0.07	0.000235	0.0189	6228.6	20.0	R-515B
180.4	0.58	0.07	0.000260	0.0188	6166.4	20.0	R-515B
276.8	0.12	0.08	0.000121	0.0193	7884.4	24.0	R-515B
268.3	0.15	0.08	0.000132	0.0193	7881.5	22.0	R-515B
245.9	0.21	0.08	0.000151	0.0193	7861.6	21.0	R-515B
221.7	0.28	0.07	0.000169	0.0192	7826.1	20.0	R-515B
197.8	0.35	0.07	0.000187	0.0192	7771.6	20.0	R-515B
173.8	0.45	0.07	0.000206	0.0191	7690.4	19.0	R-515B
280.0	0.10	0.07	0.000087	0.0192	9565.4	26.0	R-515B
269.5	0.13	0.07	0.000095	0.0192	9560.3	24.0	R-515B
244.3	0.17	0.07	0.000108	0.0192	9533.8	22.0	R-515B
218.3	0.22	0.07	0.000121	0.0190	9488.8	21.0	R-515B
193.0	0.28	0.07	0.000134	0.0189	9421.0	20.0	R-515B
168.7	0.34	0.07	0.000147	0.0188	9320.9	19.0	R-515B
320.0	0.34	0.07	0.000237	0.0188	3539.5	30.0	R-515B
308.0	0.45	0.07	0.000270	0.0188	3534.2	29.0	R-515B
293.9	0.56	0.07	0.000302	0.0188	3525.8	29.0	R-515B
277.6	0.69	0.07	0.000334	0.0188	3513.5	29.0	R-515B
259.4	0.86	0.07	0.000370	0.0187	3495.6	30.0	R-515B
123.1	0.06	0.08	0.000089	0.0194	9535.8	25.0	R-515B
129.5	0.09	0.08	0.000075	0.0195	9515.4	23.0	R-515B
134.6	0.12	0.08	0.000062	0.0193	9493.1	23.0	R-515B
137.1	0.15	0.08	0.000051	0.0193	9470.0	26.0	R-515B
120.3	0.09	0.08	0.000041	0.0196	7256.6	30.0	R-450A
221.6	0.13	0.08	0.000103	0.0194	7231.8	23.0	R-450A
217.9	0.16	0.08	0.000113	0.0194	7230.2	21.0	R-450A

Table A.3-1. (continued)

Nu	x_q	P_r	Bo	B_{nd}	Re	U_c/%	fluid
206.9	0.21	0.08	0.000129	0.0194	7219.1	20.0	R-450A
194.7	0.27	0.08	0.000144	0.0194	7199.2	20.0	R-450A
181.2	0.33	0.08	0.000159	0.0193	7168.7	20.0	R-450A
166.7	0.41	0.07	0.000176	0.0191	7123.2	21.0	R-450A
126.0	0.13	0.08	0.000053	0.0196	6630.2	29.0	R-450A
239.0	0.18	0.08	0.000142	0.0194	6603.5	21.0	R-450A
233.7	0.21	0.08	0.000154	0.0194	6602.0	20.0	R-450A
220.9	0.29	0.08	0.000176	0.0194	6590.6	20.0	R-450A
207.0	0.36	0.08	0.000197	0.0192	6569.6	19.0	R-450A
192.1	0.45	0.08	0.000218	0.0192	6537.0	20.0	R-450A
176.1	0.56	0.07	0.000241	0.0191	6488.0	20.0	R-450A
209.2	0.09	0.08	0.000059	0.0193	8808.1	27.0	R-450A
209.7	0.10	0.08	0.000065	0.0193	8806.5	26.0	R-450A
203.9	0.13	0.08	0.000074	0.0191	8794.8	25.0	R-450A
193.6	0.17	0.07	0.000082	0.0191	8773.9	24.0	R-450A
181.0	0.21	0.07	0.000091	0.0192	8742.0	24.0	R-450A
166.1	0.25	0.07	0.000101	0.0190	8694.5	24.0	R-450A
186.6	0.15	0.07	0.000054	0.0189	8255.8	30.0	R-450A
171.9	0.17	0.07	0.000060	0.0189	8234.8	27.0	R-450A
156.9	0.20	0.07	0.000066	0.0188	8204.8	26.0	R-450A
141.6	0.23	0.07	0.000073	0.0188	8162.2	25.0	R-450A
203.5	0.28	0.09	0.000103	0.0210	4653.4	30.0	R-134a
254.4	0.35	0.09	0.000170	0.0208	4639.4	23.0	R-134a
252.0	0.40	0.09	0.000185	0.0208	4637.2	21.0	R-134a
245.2	0.48	0.09	0.000211	0.0208	4631.3	20.0	R-134a
237.0	0.57	0.08	0.000236	0.0208	4623.4	20.0	R-134a
227.5	0.67	0.08	0.000261	0.0208	4612.7	21.0	R-134a
216.8	0.80	0.08	0.000289	0.0207	4598.0	22.0	R-134a
181.0	0.13	0.09	0.000075	0.0210	6514.1	28.0	R-134a
260.4	0.18	0.08	0.000144	0.0208	6482.6	20.0	R-134a
258.5	0.22	0.08	0.000157	0.0208	6477.9	19.0	R-134a
249.8	0.29	0.08	0.000179	0.0208	6464.3	18.0	R-134a
238.2	0.37	0.08	0.000200	0.0207	6445.3	18.0	R-134a
224.5	0.46	0.08	0.000221	0.0207	6419.3	18.0	R-134a
209.1	0.57	0.08	0.000245	0.0205	6382.7	19.0	R-134a
254.9	0.20	0.08	0.000178	0.0208	4418.1	24.0	R-134a
251.9	0.25	0.08	0.000194	0.0208	4415.7	22.0	R-134a
244.4	0.34	0.08	0.000222	0.0208	4409.6	21.0	R-134a
236.2	0.43	0.08	0.000247	0.0208	4401.6	21.0	R-134a

Table A.3-1. (continued)

Nu	x_q	P_r	Bo	B_{nd}	Re	U_c/%	fluid
227.4	0.54	0.08	0.000274	0.0207	4391.2	22.0	R-134a
217.4	0.67	0.08	0.000303	0.0207	4376.9	24.0	R-134a
189.8	0.10	0.09	0.000080	0.0210	6100.5	30.0	R-134a
272.5	0.16	0.09	0.000156	0.0208	6072.8	21.0	R-134a
269.1	0.20	0.09	0.000170	0.0208	6068.4	20.0	R-134a
259.6	0.28	0.08	0.000194	0.0208	6056.9	19.0	R-134a
248.4	0.36	0.08	0.000217	0.0208	6041.2	19.0	R-134a
235.8	0.46	0.08	0.000240	0.0207	6019.9	19.0	R-134a
221.6	0.57	0.08	0.000265	0.0207	5990.3	20.0	R-134a
230.6	0.21	0.09	0.000179	0.0208	3728.4	25.0	R-134a
227.8	0.25	0.09	0.000195	0.0208	3726.8	24.0	R-134a
221.7	0.34	0.08	0.000223	0.0208	3723.1	22.0	R-134a
215.4	0.44	0.08	0.000249	0.0208	3718.5	23.0	R-134a
208.3	0.55	0.08	0.000275	0.0208	3712.4	23.0	R-134a
200.6	0.68	0.08	0.000305	0.0208	3704.4	25.0	R-134a
201.5	0.31	0.08	0.000189	0.0208	2590.4	29.0	R-134a
197.6	0.39	0.08	0.000211	0.0208	2589.1	28.0	R-134a
193.6	0.48	0.08	0.000233	0.0208	2587.4	29.0	R-134a
189.5	0.59	0.08	0.000258	0.0207	2585.3	30.0	R-134a
162.1	0.06	0.09	0.000239	0.0210	4487.0	17.0	R-134a
171.9	0.17	0.09	0.000217	0.0210	4482.3	17.0	R-134a
182.3	0.25	0.09	0.000196	0.0210	4476.3	16.0	R-134a
193.0	0.33	0.09	0.000177	0.0210	4469.6	17.0	R-134a
207.4	0.40	0.09	0.000155	0.0210	4460.2	21.0	R-134a
216.3	0.44	0.09	0.000143	0.0208	4454.3	25.0	R-134a
193.4	0.08	0.09	0.000276	0.0210	3457.3	20.0	R-134a
201.3	0.20	0.09	0.000249	0.0210	3454.3	19.0	R-134a
209.6	0.30	0.09	0.000225	0.0210	3450.8	20.0	R-134a
218.8	0.38	0.09	0.000202	0.0210	3447.0	21.0	R-134a
231.6	0.46	0.09	0.000176	0.0208	3441.9	25.0	R-134a
240.4	0.50	0.09	0.000162	0.0208	3438.7	29.0	R-134a
158.8	0.05	0.09	0.000167	0.0208	6618.6	19.0	R-134a
170.4	0.12	0.08	0.000151	0.0208	6607.9	18.0	R-134a
181.8	0.18	0.08	0.000136	0.0208	6594.4	18.0	R-134a
192.8	0.24	0.08	0.000122	0.0208	6579.0	19.0	R-134a
205.4	0.29	0.08	0.000106	0.0207	6557.3	22.0	R-134a
211.8	0.31	0.08	0.000097	0.0207	6543.6	26.0	R-134a
227.5	0.38	0.08	0.000124	0.0204	6400.3	27.0	R-134a
244.5	0.41	0.08	0.000124	0.0203	6380.2	28.0	R-134a

Table A.3-1. (continued)

Nu	x_q	P_r	Bo	B_{nd}	Re	U_c/%	fluid
150.4	0.07	0.09	0.000233	0.0210	2561.5	25.0	R-134a
158.4	0.17	0.09	0.000215	0.0210	2560.0	23.0	R-134a
167.5	0.25	0.09	0.000199	0.0210	2558.6	23.0	R-134a
177.7	0.33	0.09	0.000183	0.0210	2557.1	25.0	R-134a
193.3	0.40	0.09	0.000166	0.0208	2555.2	29.0	R-134a
167.3	0.06	0.09	0.000231	0.0210	4564.3	18.0	R-134a
176.3	0.16	0.09	0.000209	0.0210	4559.1	17.0	R-134a
185.7	0.25	0.09	0.000188	0.0208	4552.6	17.0	R-134a
195.0	0.32	0.09	0.000168	0.0208	4545.4	18.0	R-134a
207.0	0.39	0.08	0.000146	0.0208	4535.4	22.0	R-134a
213.9	0.42	0.08	0.000134	0.0208	4529.1	26.0	R-134a
216.4	0.49	0.08	0.000141	0.0205	4464.3	30.0	R-134a
165.4	0.06	0.09	0.000227	0.0210	4588.4	18.0	R-134a
174.4	0.16	0.09	0.000204	0.0210	4583.2	17.0	R-134a
184.0	0.24	0.09	0.000184	0.0208	4576.9	17.0	R-134a
193.4	0.31	0.09	0.000165	0.0208	4569.7	18.0	R-134a
205.6	0.38	0.08	0.000143	0.0208	4559.8	22.0	R-134a
212.8	0.41	0.08	0.000131	0.0208	4553.6	26.0	R-134a
160.8	0.06	0.09	0.000170	0.0210	6691.8	19.0	R-134a
171.5	0.13	0.09	0.000152	0.0210	6680.9	18.0	R-134a
181.9	0.19	0.09	0.000136	0.0208	6667.2	18.0	R-134a
191.7	0.24	0.09	0.000122	0.0208	6651.6	18.0	R-134a
202.4	0.30	0.08	0.000104	0.0208	6629.9	22.0	R-134a
207.5	0.32	0.08	0.000095	0.0208	6616.2	26.0	R-134a
223.9	0.39	0.08	0.000123	0.0204	6470.7	26.0	R-134a
240.2	0.42	0.08	0.000122	0.0204	6450.0	28.0	R-134a
160.3	0.06	0.09	0.000167	0.0210	6722.4	18.0	R-134a
171.2	0.13	0.09	0.000150	0.0210	6711.0	18.0	R-134a
181.6	0.19	0.09	0.000134	0.0208	6696.7	17.0	R-134a
191.2	0.24	0.08	0.000120	0.0208	6680.5	18.0	R-134a
201.4	0.29	0.08	0.000103	0.0208	6657.8	22.0	R-134a
205.9	0.32	0.08	0.000094	0.0207	6643.5	25.0	R-134a
220.8	0.38	0.08	0.000122	0.0204	6494.4	26.0	R-134a
236.4	0.41	0.08	0.000121	0.0204	6473.6	28.0	R-134a
261.0	0.47	0.08	0.000121	0.0203	6434.4	30.0	R-134a
182.1	0.08	0.09	0.000277	0.0210	3425.8	20.0	R-134a
189.9	0.20	0.09	0.000249	0.0210	3422.9	19.0	R-134a
198.3	0.29	0.09	0.000224	0.0210	3419.5	19.0	R-134a
207.2	0.38	0.09	0.000201	0.0210	3415.8	20.0	R-134a

Table A.3-1. (continued)

Nu	x_q	P_r	Bo	B_{nd}	Re	U_c/%	fluid
219.2	0.46	0.09	0.000174	0.0210	3410.8	24.0	R-134a
227.2	0.50	0.09	0.000159	0.0210	3407.6	29.0	R-134a
149.0	0.07	0.08	0.000236	0.0208	2613.7	25.0	R-134a
157.0	0.17	0.08	0.000218	0.0208	2612.1	23.0	R-134a
166.0	0.26	0.08	0.000201	0.0208	2610.4	23.0	R-134a
176.1	0.33	0.08	0.000186	0.0208	2608.7	24.0	R-134a
191.2	0.41	0.08	0.000168	0.0208	2606.5	28.0	R-134a
252.8	0.18	0.08	0.000169	0.0208	4663.7	23.0	R-134a
249.5	0.23	0.08	0.000184	0.0208	4661.2	22.0	R-134a
241.5	0.31	0.08	0.000211	0.0208	4654.7	20.0	R-134a
233.1	0.40	0.08	0.000235	0.0208	4646.2	20.0	R-134a
223.5	0.51	0.08	0.000261	0.0207	4634.8	21.0	R-134a
213.0	0.63	0.08	0.000288	0.0207	4619.2	22.0	R-134a
181.2	0.10	0.09	0.000076	0.0208	6297.1	28.0	R-134a
252.3	0.16	0.08	0.000147	0.0208	6266.6	20.0	R-134a
248.4	0.20	0.08	0.000161	0.0208	6262.4	19.0	R-134a
238.1	0.27	0.08	0.000183	0.0207	6249.8	18.0	R-134a
226.5	0.35	0.08	0.000205	0.0207	6232.1	18.0	R-134a
213.9	0.44	0.08	0.000227	0.0207	6207.6	18.0	R-134a
199.9	0.55	0.08	0.000251	0.0205	6173.4	19.0	R-134a
186.6	0.11	0.08	0.000078	0.0208	6309.8	29.0	R-134a
251.8	0.16	0.08	0.000147	0.0207	6276.8	20.0	R-134a
246.7	0.20	0.08	0.000161	0.0207	6272.1	19.0	R-134a
235.6	0.28	0.08	0.000184	0.0207	6258.7	18.0	R-134a
223.4	0.35	0.08	0.000205	0.0207	6239.8	18.0	R-134a
210.1	0.45	0.08	0.000227	0.0205	6213.9	18.0	R-134a
195.9	0.56	0.08	0.000251	0.0206	6177.4	19.0	R-134a
241.9	0.20	0.08	0.000169	0.0207	3901.0	26.0	R-134a
238.2	0.24	0.08	0.000184	0.0207	3899.3	24.0	R-134a
230.7	0.33	0.08	0.000210	0.0207	3895.1	23.0	R-134a
222.9	0.42	0.08	0.000235	0.0207	3889.9	22.0	R-134a
214.6	0.52	0.08	0.000260	0.0207	3882.9	23.0	R-134a
205.8	0.65	0.08	0.000288	0.0207	3873.5	24.0	R-134a
204.1	0.79	0.08	0.000191	0.0208	2659.5	29.0	R-134a
200.1	0.87	0.08	0.000213	0.0208	2658.1	28.0	R-134a
195.7	0.96	0.08	0.000236	0.0208	2656.3	29.0	R-134a
191.2	0.99	0.08	0.000262	0.0208	2654.0	30.0	R-134a